

**MEASUREMENT OF THE B_c^\pm MESON LIFETIME
USING $B_c^\pm \rightarrow J/\psi + l^\pm + X$ DECAYS**

by

Mark P. Hartz

BSE, University of Pennsylvania, 2000

Submitted to the Graduate Faculty of
the Department of Physics and Astronomy in partial fulfillment
of the requirements for the degree of

Doctor of Philosophy

University of Pittsburgh

2008

UNIVERSITY OF PITTSBURGH
DEPARTMENT OF PHYSICS AND ASTRONOMY

This dissertation was presented

by

Mark P. Hartz

It was defended on

November 11, 2008

and approved by

Professor Paul Shepard, Department of Physics and Astronomy

Professor Joe Boudreau, Department of Physics and Astronomy

Professor Adam Lebovich, Department of Physics and Astronomy

Professor Vittorio Paolone, Department of Physics and Astronomy

Professor Manfred Paulini, Carnegie Mellon University Department of Physics

Dissertation Director: Professor Paul Shepard, Department of Physics and Astronomy

Copyright © by Mark P. Hartz
2008

MEASUREMENT OF THE B_c^\pm MESON LIFETIME USING $B_c^\pm \rightarrow J/\psi + l^\pm + X$ DECAYS

Mark P. Hartz, PhD

University of Pittsburgh, 2008

This thesis describes a measurement of the average proper decay time of the B_c^\pm mesons, the ground state of bottom and charm quark bound states. The lifetime measurement is carried out in the decay modes $B_c^\pm \rightarrow J/\psi + e^\pm + X$ and $B_c^\pm \rightarrow J/\psi + \mu^\pm + X$, where the J/ψ decays as $J/\psi \rightarrow \mu^+\mu^-$ and the X are unmeasured particles such as ν_e or ν_μ . The data are collected by the CDF II detector which measures the properties of particles created in $\sqrt{s} = 1.96$ TeV $p\bar{p}$ collisions delivered by the Fermilab Tevatron. This measurement uses $\sim 1 \text{ fb}^{-1}$ of integrated luminosity. The measured average proper decay time of B_c^\pm mesons, $\tau = 0.475_{-0.049}^{+0.053}(\text{stat.}) \pm 0.018(\text{syst.})$ ps, is competitive with the most precise measurements in the world and confirms previous measurements and theoretical predictions.

TABLE OF CONTENTS

PREFACE	xxix
1.0 INTRODUCTION	1
2.0 THE STANDARD MODEL	4
2.1 Electroweak Interactions	6
2.2 Strong Interactions and Quantum Chromodynamics	10
2.3 Mixing in the Quark Sector	14
3.0 THEORETICAL CONSIDERATIONS	16
3.1 Calculations Within the Standard Model	16
3.1.1 Perturbative Calculations	17
3.1.2 Nonperturbative (QCD) Calculations	17
3.1.2.1 Heavy Quark Effective Theory	18
3.1.2.2 Nonrelativistic QCD	18
3.1.2.3 Lattice QCD	19
3.2 Application to B Hadrons	19
3.2.1 B Hadron Production in $p\bar{p}$ Collisions	19
3.2.2 B Hadron Masses, Decays and Lifetimes	22
3.3 The B_c Meson	22
3.3.1 Production of the B_c Meson	22
3.3.2 The B_c Meson Mass	24
3.3.3 The B_c Meson Decays and Lifetime	24
4.0 EXPERIMENTAL APPARATUS	31
4.1 The Accelerator Complex	31

4.1.1	The proton source and acceleration	31
4.1.2	Antiproton production and acceleration	33
4.1.3	The Tevatron	33
4.2	The CDF II Detector	35
4.2.1	Silicon strip detectors	37
4.2.1.1	The SVX II detector	38
4.2.1.2	The ISL detector	39
4.2.2	The COT drift chamber	39
4.2.3	Time-of-flight detector	43
4.2.4	Calorimetry	43
4.2.4.1	The CEM calorimeter	43
4.2.4.2	The CHA calorimeter	44
4.2.5	Muon detectors	45
4.2.5.1	The central muon detector	45
4.2.5.2	The central muon upgrade detector	45
4.2.5.3	The central muon extension	47
4.2.6	The CDF II trigger system	47
4.2.6.1	The level 1 trigger	49
4.2.6.2	The level 2 trigger	49
4.2.6.3	Level 3 Trigger	49
5.0	ANALYSIS PROCEDURE AND TECHNIQUES	50
5.1	Per event proper decay time measurements	52
5.2	Per event detector resolution	56
5.3	B_c Lifetime Distribution	56
5.4	Fitting Data	57
5.4.1	Fitting weighted events	58
5.4.2	Propagating parameters and errors	58
5.4.3	Extended likelihood fits	59
5.4.4	Probability Distribution for σ_{ct^*}	60
5.5	Likelihood Ratio Methods	60

5.6	Monte Carlo Simulations	61
6.0	$J/\psi + l^\pm$ CANDIDATE SELECTION	62
6.1	J/ψ Selection	62
6.1.1	Trigger and trigger path confirmation	64
6.1.2	Muon likelihood for J/ψ legs	64
6.1.3	COT and silicon hit requirements	67
6.1.4	The dimuon invariant mass	67
6.2	Generic Selection of $J/\psi + l^\pm$ Events	68
6.2.1	Third track selection	68
6.2.2	Cuts for the three track system	69
6.3	Selection Specific to the Muon Channel	73
6.4	Selection Specific to the Electron Channel	74
6.5	Validation of Selection	78
7.0	BACKGROUNDS	79
7.1	Misidentified J/ψ Background	80
7.1.1	Misidentified J/ψ normalization	80
7.1.2	Misidentified J/ψ ct^* fits	81
7.1.3	Misidentified J/ψ σ_{ct^*} fits	82
7.2	Hadrons Misidentified as Leptons Background	85
7.2.1	Probabilities for hadrons to be misidentified as leptons	86
7.2.1.1	Correction for the muon misidentification probability	86
7.2.2	Particle composition of the J/ψ +track samples	90
7.2.2.1	Two dimensional particle identification fits	92
7.2.2.2	One dimensional particle identification fits	93
7.2.2.3	The muon fraction in the electron channel	94
7.2.2.4	Z_e^{pull} and Z_μ^{pull} cut efficiencies	95
7.2.2.5	Final particle fractions	96
7.2.3	Misidentified lepton ct^* fits	96
7.2.4	Misidentified lepton σ_{ct^*} fits	103
7.2.5	Misidentified lepton normalization	105

7.3	$b\bar{b}$ Background	107
7.3.1	The $b\bar{b}$ PYTHIA sample and its tuning	107
7.3.2	$b\bar{b}$ tuning crosscheck	119
7.3.3	Normalization of the $b\bar{b}$ background	120
7.3.4	$b\bar{b}$ ct^* fits	120
7.3.5	$b\bar{b}$ σ_{ct^*} fits	120
7.4	Residual e^+e^- Background	126
7.4.1	e^+e^- identification efficiency	126
7.4.2	Sources of e^+e^-	127
7.4.3	Checking the veto efficiency with signed impact parameter	129
7.4.4	Residual e^+e^- normalization	131
7.4.5	Residual e^+e^- ct^* fit	134
7.4.6	Residual e^+e^- σ_{ct^*} fit	136
7.5	Prompt J/ψ Background	140
7.6	Backgrounds Summary	142
8.0	B_c LIFETIME FITTER	144
8.1	B_c signal ct^* PDF	144
8.2	B_c signal σ_{ct^*} PDF	145
8.3	Construction of Likelihood	146
8.3.1	Lifetime fitter checks	147
9.0	B_c AVERAGE LIFETIME FIT	152
9.1	Fit Results	152
9.2	Fit Result Cross-Checks	153
9.3	Combining the Electron and Muon Channel Fits	161
10.0	SYSTEMATIC UNCERTAINTIES	164
10.1	The B_c spectrum	165
10.2	B_c Decay Modes	165
10.3	Misidentified J/ψ ct^* model	168
10.4	$b\bar{b}$ Scale Factors	169
10.5	$b\bar{b}$ Track Parameter Errors	172

10.6	Resolution Functions	175
10.7	B_c σ_{ct^*} functional form	175
10.8	J/ψ +track Proton Fraction	179
10.9	Decay-in-Flight Correction	180
10.10	J/ψ mass sidebands and the misidentified J/ψ background	181
10.11	Misidentified Electron Method	185
10.12	e^+e^- veto efficiency	188
10.13	Silicon detector alignment	188
10.14	Combining Systematic Uncertainties	188
11.0	CONCLUSION	191
11.1	Comparison to Other Measurement	191
11.2	Comparison to Theoretical Predictions	192
11.3	Prospects for Future Measurements	194
11.4	Concluding Remarks	197
APPENDIX A. MONTE CARLO SIMULATION SAMPLES		198
A.1	BGenerator Sample of B_c Decays	198
A.2	PYTHIA $b\bar{b}$ Sample	201
A.3	PYTHIA e^+e^- Sample	201
APPENDIX B. ASSOCIATED DATA SAMPLES SELECTION		203
B.1	Conversion Electron Sample	203
B.2	Tagged D^0 Sample	204
B.3	Λ Sample	206
APPENDIX C. THIRD TRACK PROTON STUDIES		209
APPENDIX D. MISIDENTIFIED LEPTON FITS		213
D.1	Mass Fits for Electron Misidentification Probabilities	213
D.2	Mass Fits for Muon Misidentification Probabilities	227
D.3	$T_\pi^{pull}/Z_\pi^{pull}$ Fits for the Electron Channel	232
D.4	$T_\pi^{pull}/Z_\pi^{pull}$ Fits for the Muon Channel	239
D.5	Z_π^{pull} Fits for the Electron Channel	253
D.6	Z_π^{pull} Fits for the Muon Channel	260

BIBLIOGRAPHY 267

LIST OF TABLES

1	Table of elementary bosons in the standard model with electric charges and masses listed. The Higgs boson has not yet been discovered. There are 8 gluons, making an SU(3) color octet, that carry color charge.	5
2	Table of elementary fermions in the standard model with the electric charges and masses listed. All charges are for matter particles; anti-matter particles have opposite charge. All charges are given as multiples of the electron charge. All particles carry weak charge and the quarks carry strong charge. Quark masses, except for top, are approximate since confinement limits the ability to measure a bare quark mass.	6
3	Listing of ground state B hadrons, their quark composition and their relative production in $\sqrt{s} = 1.8 \text{ TeV}$ $p\bar{p}$ collisions and $Z \rightarrow b\bar{b}$ decays. The list does not include all B baryon states, and the relative productions of the baryons is unknown. Charge conjugate hadrons exist with the same production rates. . .	21
4	Estimates of the B_c lifetime using various theoretical approaches.	29
5	Branching fractions of the B_c through $B_s^{0(*)}$	29
6	Branching fractions of the B_c through charmonium.	30
7	Cuts applied to dimuon J/ψ leg candidates or the two particle J/ψ system to select J/ψ candidates.	63
8	Cuts applied to the third track and three track system, that are general to muon and electron final states.	68
9	Cuts applied to the third muon in muon channel candidates.	73
10	Cuts applied to the electron or three track system in $J\psi + e^\pm$ candidates. . .	74

11	Table of electron efficiency and $S^2/(S + B)$ for various p_T dependent electron likelihood ratio cuts.	76
12	Parameters from the ct^* fits to sideband J/ψ events.	83
13	Parameters from the σ_{ct^*} fits to sideband J/ψ events.	84
14	Parameters from the ct^* fits to reweighted sideband J/ψ +track events.	102
15	Parameters from the ct^* fits to reweighted J/ψ +track events.	104
16	Parameters from the σ_{ct^*} fits to reweighted J/ψ +track events.	106
17	Numbers used to determine the $b\bar{b}$ background normalization and the predicted normalizations (first and third columns in the last row).	123
18	Parameters from the $b\bar{b} ct^*$ fits.	124
19	Parameters from $b\bar{b} \sigma_{ct^*}$ fits.	125
20	Fitted parameters from the residual $e^+e^- ct^*$ fit.	137
21	Fitted parameters from the σ_{ct^*} fit of e^+e^- events in J/ψ sidebands.	138
22	Fitted parameters from the residual $e^+e^- \sigma_{ct^*}$ fit.	139
23	Fitted parameters describing σ_{ct^*} in fits of J/ψ +track data with $ct^* < 0$	142
24	Summary of background predictions and signal events.	142
25	Free parameters from the fits in both electron and muon channels. All errors are from the MIGRAD algorithm, except for the $c\tau$ errors which are calculated with the MINOS algorithm.	153
26	Constrained parameters from the fit of the electron channel events.	154
27	Continuation of constrained parameters from the fit of the electron channel events.	155
28	Constrained parameters from the fit of the muon channel events.	156
29	Continuation of constrained parameters from the fit of the muon channel events.	157
30	Shifts in the average proper decay length for systematic studies of the B_c spectrum.	167
31	Shifts in the average proper decay length for systematic studies of the B_c branching fractions.	169
32	Shifts in the average proper decay length for systematic studies of the shape of the ct^* distribution for misidentified J/ψ events.	171

33	Variation of the predicted $b\bar{b}$ normalization for variations in the factors that scale the relative fractions of QCD processes in the $b\bar{b}$ production.	171
34	Shifts in the average proper decay length for systematic studies of the tuning of the PYTHIA $b\bar{b}$ sample.	172
35	Shifts in the average proper decay length for systematic studies of the track parameters uncertainties in the PYTHIA $b\bar{b}$ sample.	174
36	Parameters describing the single Gaussian and double Gaussian resolution functions from fits of the J/ψ +track sample.	176
37	Shifts in the average proper decay length for systematic studies of the choice of resolution function used while modeling the prompt J/ψ and $B_c ct^*$	177
38	Parameters from the σ_{ct^*} fits of B_c events from BGENERATOR.	178
39	Shifts in the average proper decay length for systematic studies of the choice of σ_{ct^*} model for B_c decays.	179
40	Shifts in the average proper decay length for systematic studies of the choice of proton fraction model for third tracks in the J/ψ +track sample.	179
41	Shifts in the average proper decay length for systematic studies of the decay-in-flight correction for events falling outside the D^0 mass window.	180
42	Fitted parameters from sideband $J/\psi + \mu ct^*$ fits using only the upper sideband or both sidebands.	186
43	Shifts in the average proper decay length for systematic studies of the sideband J/ψ events used while determining the misidentified J/ψ background for the muon channel.	186
44	Shifts in the average proper decay length for systematic studies of the method for handling the Z_e cut in the misidentified electron calculation.	187
45	Shifts in the average proper decay length for systematic studies of the correction to the conversion veto efficiency in the $p_T = 2.0 = 2.5 \text{ GeV}/c$ region.	188
46	Summary of systematic uncertainties for the electron and muon channels listed in the columns labeled e and μ respectively. The columns labeled Total contain the combined systematic uncertainties of the two channels.	190
47	Listing of the measurements of the B_c average proper decay time τ	192

48	Estimates of the fraction of $J/\psi(\mu^+\mu^-) + l^\pm$ events from different B_c decays, where the branching fractions to the final states include all branching fractions to intermediate states.	200
49	Cuts applied to select photon conversion candidates.	204
50	Cuts applied to two track hadronic trigger datasets to skim D^{*+} tagged D^0 decays.	206
51	Cuts applied to two track hadronic trigger datasets to skim Λ decays.	208

LIST OF FIGURES

1	Inclusive decay modes of the B_c^- through decay of the b quark (a), decay of the c quark (b), and weak annihilation of the b and c quarks (c).	2
2	Picture of the shape that the potential for the complex scalar field should take for spontaneous symmetry breaking to be possible.	8
3	Diagrams of the electroweak interactions via the photon (γ) (a) and the massive W^\pm (b) and Z (c) bosons	9
4	Mesons in the spin 0 nonet.	11
5	Diagrams of the strong interactions via the gluons of QCD. Notice the gluons interact with themselves since they also carry color charge.	12
6	Qualitative picture of the strong field lines between two interacting quarks.	12
7	Running of the coupling constant α_s	13
8	Feynman diagrams for e^+e^- scattering at lowest order.	17
9	Representative leading order gluon fusion (a) and quark annihilation (b) diagrams for $b\bar{b}$ production. Representative next to leading order production through the scattering of a virtual b quark (c) or splitting of an excited gluon (d).	21
10	Representative Feynman diagrams of the lowest order in α_s processes that contribute to the production of B_c mesons in $p\bar{p}$ interactions. There are 36 diagrams in all.	23
11	Inclusive decays modes that determine the B_c meson total width. Decays can happen through the b quarks (a), the c quark, or weak annihilation of the b and c quarks (c).	25

12	A schematic of the Fermilab accelerator chain showing the progression of protons and antiprotons used in the Tevatron.	32
13	Integrated luminosity delivered by the Tevatron.	34
14	Isometric view of the CDF II detector. The detector components used in this thesis are labeled	35
15	Illustration of the relationship between η and θ	36
16	Arrangement of sensors in the five SVX II layers in an $r - \phi$ slice.	38
17	Radial and axial arrangement of silicon layers including the ISL.	39
18	One quarter $r - z$ side view of the COT showing its position relative to other detectors.	40
19	End view of three COT super cells.	41
20	Diagram of wavelength shifters (WLS) and light guides for scintillator layers in the central hadronic calorimeter.	44
21	A $r - \phi$ slice of the CMU cells stacked within a CMU wedge. Notice the offset of the sense wire in layers 1 and 3 versus layers 2 and 4. The cells are 6.35×2.68 cm in height and width.	46
22	Pseudorapidity coverage of the muon detectors including the CMP. The ϕ dependence is due to the constant CMP length and its box shape.	47
23	Side $r - z$ view of the CDF II detector showing the position and orientation of the CMX detector.	48
24	Evolution of the expected distribution of ct for B_c events as non-ideal effects are added. (a) An ideal distribution follows an exponential decay law. (b) Unmeasured particles from the B_c decay smear the distribution. (c) Additional smearing of the distribution is due to the detector measurement resolution. (d) The addition of background sources obscures the B_c events.	51
25	Diagram showing a simplified flow of the measurement procedure.	53
26	Example of event with a hadron misidentified as a muon that might be preferentially selected by the dimuon trigger.	65

27	(a) Two dimensional plots of $S^2/(S + B)$ for muon channel candidates given cuts for the minimum muon likelihood on CMU and CMX muons. (b) Zooming in shows a peek near a value of 0.06 for both muon types.	66
28	Fitted dimoun mass distributions, with red shaded J/ψ signal region. Plot (a) does not include the trigger confirmation for the J/ψ legs, while plot (b) does.	67
29	Comparison of the three track vertex probabilities for simulated muon channel events events from B_c decays (a) and $b\bar{b}$ production (b).	69
30	$S^2/(S + B)$ for muon channel candidates as a function of the minimum vertex probability.	70
31	Opening angle $\Delta\phi$ between the J/ψ and third muon for simulated signal events (a) and simulated $b\bar{b}$ background events (b).	71
32	Evaluation of $S^2/(S + B)$ for the choice of $\Delta\phi$ cut carried out for the B_c cross section measurement. A loose cut of $< \pi/2$ was chosen.	71
33	Simulated σ_{Lxy} for B_c events. A loose cut of $< 90 \mu\text{m}$ removes very little signal in electron channel (a) or muon channel (b) events.	72
34	$J/\psi + \mu^\pm$ mass distribution for simulated B_c events. Most events fall in a 4-6 GeV/ c^2 window.	72
35	Electron likelihood ratio for electrons from photon conversion.	76
36	p_T dependent electron likelihood ratio cut (a) and the electron efficiency as a function of p_T (b).	77
37	Exponential fits of the true ct of simulated B_c for the electron (a) and muon (b) channels after all analysis cuts are applied. The input average proper decay length for the simulated events is $140 \mu\text{m}$	78
38	Fitted J/ψ mass for B_c candidates in the electron (a) and muon (b) channels.	81
39	Fitted ct^* distributions for sideband J/ψ events in the electron channel (a) and muon channel (b).	82
40	Fitted σ_{ct^*} distributions for sideband J/ψ events in the electron (a) and muon (b) channels.	84

41	Fits of the tagged D^0 mass distributions where the pion leg has $p_T = 3 - 4$ GeV/ c . (a) No lepton identification requirement is applied to the pion leg. (b) The pion leg is identified as a CMUP muon.	87
42	Fits of the Λ mass distributions where the p^- leg has $p_T = 2 - 3$ GeV/ c . (a) No lepton identification requirement is applied to the p^- leg. (b) The p^- leg passes the electron likelihood ratio cut.	88
43	Probabilities for positively charged (a) and negatively charged (b) hadrons to be misidentified as electrons.	88
44	Probabilities for hadrons to be misidentified as muons.	89
45	D^0 mass fits from the BGENERATOR sample of D^0 decays, including parent K^- (a), K^+ (b), and π^\pm (c) and daughter K^- (d), K^+ (e), and π^\pm (f) fits.	89
46	T_π^{pull} (a) and Z_π^{pull} (b) projections for an example two dimensional fit of third tracks in the electron channel J/ψ +track sample.	93
47	Example of a Z_π^{pull} of the third tracks in the muon channel J/ψ +track sample.	94
48	Efficiencies for particle types to pass the $Z_e^{pull} > -1.3$ (a) and $Z_\mu^{pull} > -1.0$ (b) cuts.	96
49	Particle fractions for third tracks in the electron channel J/ψ +track sample grouped in $q = -1, ct^* < 0 \mu\text{m}$ (a), $q = 1, ct^* < 0 \mu\text{m}$ (b), $q = -1, 0 < ct^* < 150 \mu\text{m}$ (c), $q = 1, 0 < ct^* < 150 \mu\text{m}$ (d), $q = -1, ct^* > 150 \mu\text{m}$ (e), and $q = 1, ct^* > 150 \mu\text{m}$ (f) bins.	97
50	Particle fractions for third tracks in the muon channel J/ψ +track sample grouped in $q = -1, ct^* < 0 \mu\text{m}$ (a), $q = 1, ct^* < 0 \mu\text{m}$ (b), $q = -1, 0 < ct^* < 150 \mu\text{m}$ (c), $q = 1, 0 < ct^* < 150 \mu\text{m}$ (d), $q = -1, ct^* > 150 \mu\text{m}$ (e), and $q = 1, ct^* > 150 \mu\text{m}$ (f) bins.	98
51	Fitted J/ψ mass peaks for electron (a) and muon channel (b) J/ψ +track samples.	99
52	Fitted $1/W_{MM}(ct_i^*)$ for the muon channel sideband J/ψ +track events.	100
53	Fit functions overlaid on the reweighted ct^* distributions for electron (a) and muon (b) channel sideband J/ψ +track events.	101
54	Fitted functions overlaid on the reweighted ct^* distributions for electron (a) and muon (b) channel J/ψ +track events.	104

55	Fitted functions overlaid on the reweighted σ_{ct^*} distributions for electron (a) and muon (b) channel sideband J/ψ +track events.	105
56	Fitted functions overlaid on the reweighted σ_{ct^*} distributions for electron (a) and muon (b) channel J/ψ +track events.	106
57	Diagram showing how a $b\bar{b}$ event makes it into the B_c candidate sample.	108
58	Leading order gluon fusion (a) and $q\bar{q}$ annihilation (b) and next to leading order scattering of a virtual b quark (c) and splitting of an excited gluon (d) QCD processes for $b\bar{b}$ production.	109
59	Distributions of $d_0^{\mu-J/\psi} > 0.01$ for the four non-prompt sources: B_c decays (a), $b\bar{b}$ (b), misidentified third muons (c), and misidentified J/ψ (d).	111
60	Comparisons between QCD production processes of the mean values for the measured quantities $\Delta\phi$ (a), $\Delta\eta$ (b), Δp_T (c), J/ψ p_T (d), and third muon p_T (e).	112
61	Comparisons between QCD production processes of the root mean squared values for the measured quantities $\Delta\phi$ (a), $\Delta\eta$ (b), Δp_T (c), J/ψ p_T (d), and third muon p_T (e).	113
62	Fitted $\Delta\phi$ distributions for flavor creation (a), flavor excitation (b), and gluon splitting (c) events from the PYTHIA $b\bar{b}$ sample.	114
63	Fitted $\Delta\phi$ distributions for events modeling misidentified third muons (a) and misidentified J/ψ (b).	115
64	Fitted $B^\pm \rightarrow J/\psi + K^\pm$ mass distributions for data (a), flavor creation (b), flavor excitation (c) , and gluon splitting (d).	117
65	Fitted $\Delta\phi$ for $J/\psi + \mu^\pm$ events.	118
66	Impact parameter of the third lepton with respect to the J/ψ for the “unvertexed” electron (a) and muon (b) channel samples.	119
67	Electron channel fitted $B^\pm \rightarrow J/\psi + K^\pm$ mass distributions for data (a), flavor creation (b), flavor excitation (c), and gluon splitting (d).	121
68	Muon channel fitted $B^\pm \rightarrow J/\psi + K^\pm$ mass distributions for data (a), flavor creation (b), flavor excitation (c), and gluon splitting (d).	122

69	Fitted ct^* distributions of the PYTHIA $b\bar{b}$ events for the electron (a) and muon (b) channels.	123
70	Fitted σ_{ct^*} distributions of the PYTHIA $b\bar{b}$ events for the electron (a) and muon (b) channels.	125
71	Efficiency for identifying $J/\psi + e$ events where the electron comes from an e^+e^- pair. Efficiencies come from a PYTHIA Monte Carlo simulation.	127
72	R_{ee} of e^+e^- pairs in PYTHIA.	128
73	R_{ee} of identified e^+e^- pairs in $J/\psi + e^\pm$ candidate events in data.	129
74	Illustration of a photon conversion where the photon originates at the primary vertex.	130
75	d_0^{sign} for electrons in “unvertexed” $J/\psi + e^\pm$ events from the sources: conversion electrons in PYTHIA (a), light neutral meson decays in PYTHIA (b), $b\bar{b}$ events in PYTHIA (c), misidentified electron events (d), misidentified J/ψ events (e), and B_c decays in the BGENERATOR sample (f). For each plot the number of events with $d_0^{sign} > 0$ and < 0 are listed.	132
76	d_0^{sign} for electrons in “unvertexed” $J/\psi + e^\pm$ events in data.	133
77	Efficiency of the e^+e^- veto in data determined using d_0^{sign} asymmetries, compared to the efficiency from PYTHIA.	133
78	e^+e^- veto efficiency as a function of ct^* (left) and σ_{ct^*} (right).	134
79	Fit ct^* for sideband $J/\psi + e$ events overlaid on the sub-sample where the electrons are identified as e^+e^- electrons.	135
80	Fitted function overlaid on the ct^* distribution of identified e^+e^- reweighted for veto efficiencies. Red is the constrained misidentified J/ψ component.	136
81	Fitted function overlaid on the σ_{ct^*} of identified e^+e^- events in the J/ψ mass sidebands reweighted for veto efficiencies.	138
82	Fitted function overlaid on the σ_{ct^*} distribution of identified e^+e^- events in the J/ψ mass signal region reweighted for veto efficiencies.	139
83	Fitted σ_{ct^*} projections for $ct^* < 0$ sideband $J/\psi + \text{track}$ events for the electron channel (a) and muon channel (b).	141

84	Fitted σ_{ct^*} projections for $ct^* < 0$ J/ψ +track events for the electron channel (a) and muon channel (b).	141
85	Comparison of predicted and measured $J/\psi + e^\pm$ (a) and $J/\psi + \mu^\pm$ (b) mass distributions for non-prompt events.	143
86	K factor distribution for the electron (a) and muon (a) channels where events are from the BGENERATOR sample of B_c decays.	145
87	Pulls of measured $c\tau$ for ~ 1000 simple Monte Carlo trials with input $c\tau$ values of 80 (a), 140 (b), and 200 (c) μm . Fits were carried out with the electron channel fitter.	149
88	Pulls of measured $c\tau$ for ~ 1000 simple Monte Carlo trials with input $c\tau$ values of 80 (a), 140 (b), and 200 (c) μm . Fits were carried out with the muon channel fitter.	150
89	Fit of ct for $B^\pm \rightarrow J/\psi + K^\pm$ candidates.	151
90	ct^* fit projections for the electron channel (a,c) and muon channel (b,d) fits. The backgrounds are plotted as a single function (a) and (b) and broken out (c) and (d).	158
91	σ_{ct^*} fit projections for the electron channel (a,c) and muon channel (b,d) fits. The backgrounds are plotted as a single function in (a) and (b) and broken out in (c) and (d).	159
92	Fitted σ_{ct^*} functions compared to the σ_{ct^*} distributions from the BGENERATOR sample of B_c decays for the electron (a) and muon (b) channels.	160
93	Predicted $J/\psi + l$ mass distributions for the electron channel (a) and the muon channel (b). The histograms for the predicted components are stacked.	161
94	$-2\ln(L)$ contours for the electron and muon channels. For each point, the $c\tau$ is fixed while the other parameters are minimized with MIGRAD.	162
95	Combined likelihood for the electron and muon channels.	163
96	Comparison of B_c and B meson p_T spectra that are used while generating events in BGENERATOR.	166
97	Comparison of electron (a) and muon (b) channel K factor distributions for simulated B_c events with varied p_T spectra.	167

98	Comparison of the electron (a) and muon (b) channel K factor for default and adjusted branching fractions.	168
99	Fitted ct^* distributions for sideband J/ψ +track events for the electron channel (a) and muon channel (b) cuts.	170
100	ct^* distributions for electron (a) and muon (b) channel sideband $J/\psi+l$ events with the adjusted functions from the sideband J/ψ +track samples.	170
101	Comparison of track parameter errors for J/ψ legs in J/ψ +track samples for both PYTHIA and data. Variables are $\cot(\theta)$ error (a), curvature error (b), z_0 error (c), d_0 error (d), and ϕ_0 error (e).	173
102	Comparison of track parameter errors for J/ψ legs in J/ψ +track samples for both PYTHIA and data after reweighting is applied to the PYTHIA sample. Variables are $\cot(\theta)$ error (a), curvature error (b), z_0 error (c), d_0 error (d), and ϕ_0 error (e).	174
103	Plot of single and double Gaussian resolution functions for the electron (a) and muon (b) channels.	176
104	Fits σ_{ct^*} distributions for B_c events from BGENERATOR for electron (a) and muon (b) channel final states.	178
105	Fit of J/ψ candidate mass distribution for $J/\psi + \mu$ events.	181
106	Invariant mass of third muon and oppositely charged J/ψ legs for events in the J/ψ sideband region.	182
107	Fit of the J/ψ mass for $J/\psi + \mu$ events split into two types. (a) The third muon does not reconstruct to within 50 MeV/ c^2 of the J/ψ mass with the oppositely charged J/ψ leg. (b) The third muon does reconstruct to within 50 MeV/ c^2 of the J/ψ mass with the oppositely charged the J/ψ leg.	183
108	Fit of the J/ψ mass for $J/\psi + \mu$ events where the third muon does reconstruct to within 50 MeV/ c^2 of the J/ψ mass with the oppositely charged the J/ψ leg. An additional Gaussian is added to fit the bump in the lower sideband.	184
109	Fitted ct^* for sideband $J/\psi + \mu$ events using only the upper sideband (a) and using both sidebands (b).	185

110	Comparison of the B_c average proper decay time for the CDF Run I, D0 Run II, and CDF Run II experiments. The weighted average is taken assuming no correlations in the uncertainties.	193
111	Reconstructed $J/\psi + \pi^\pm$ for B_c candidates.	196
112	Comparison of the B_c and B meson spectra used when generating events with BGENERATOR.	199
113	$\Delta\cot(\theta)$ for conversion pair candidates.	205
114	Left: Invariant mass difference between the D^{*+} and D^0 systems. Right: Invariant mass of the D^0 system after all cuts are applied.	207
115	Invariant mass of Λ^0 candidates after selection is applied.	208
116	Proton fraction of third tracks in the PYTHIA J/ψ +track sample.	210
117	Pull of measured $B_c c\tau$ in toy Monte Carlos where the model for proton fractions is varied.	211
118	Pull of measured $B_c c\tau$ in toy Monte Carlos where the model for proton fractions is varied after the $Z_\mu > -1.0$ has been applied.	212
119	Fitted D^0 mass peaks where the π^+ leg meets the third track requirements. Broken into p_T bins of 2 – 3 GeV/ c (top left), 3 – 4 GeV/ c (top right), 4 – 5 GeV/ c (middle left), 5 – 7 GeV/ c (middle right), and > 7 GeV/ c (bottom).	215
120	Fitted D^0 mass peaks where the π^- leg meets the third track requirements. Broken into p_T bins of 2 – 3 GeV/ c (top left), 3 – 4 GeV/ c (top right), 4 – 5 GeV/ c (middle left), 5 – 7 GeV/ c (middle right), and > 7 GeV/ c (bottom).	216
121	Fitted D^0 mass peaks where the K^+ leg meets the third track requirements. Broken into p_T bins of 2 – 3 GeV/ c (top left), 3 – 4 GeV/ c (top right), 4 – 5 GeV/ c (bottom left), and > 5 GeV/ c (bottom right).	217
122	Fitted D^0 mass peaks where the K^- leg meets the third track requirements. Broken into p_T bins of 2 – 3 GeV/ c (top left), 3 – 4 GeV/ c (top right), 4 – 5 GeV/ c (bottom left), and > 5 GeV/ c (bottom right)	218
123	Fitted Λ mass peaks where the p^+ leg meets the third track requirements. Broken into p_T bins of 2 – 3 GeV/ c (left) and > 3 GeV/ c (right).	219

124	Fitted Λ mass peaks where the p^- leg meets the third track requirements. Broken into p_T bins of 2 – 3 GeV/ c (top left), 3 – 4 GeV/ c (top right), 4 – 5 GeV/ c (bottom left), and > 5 GeV/ c (bottom right)	220
125	Fitted D^0 mass peaks where the π^+ leg passes electron selection. Broken into p_T bins of 2 – 3 GeV/ c (top left), 3 – 4 GeV/ c (top right), 4 – 5 GeV/ c (middle left), 5 – 7 GeV/ c (middle right), and > 7 GeV/ c (bottom).	221
126	Fitted D^0 mass peaks where the π^- leg passes electron selection. Broken into p_T bins of 2 – 3 GeV/ c (top left), 3 – 4 GeV/ c (top right), 4 – 5 GeV/ c (middle left), 5 – 7 GeV/ c (middle right), and > 7 GeV/ c (bottom).	222
127	Fitted D^0 mass peaks where K^+ leg passes electron selection. Broken into p_T bins of 2 – 3 GeV/ c (top left), 3 – 4 GeV/ c (top right), 4 – 5 GeV/ c (bottom left), and > 5 GeV/ c (bottom right).	223
128	Fitted D^0 mass peaks where K^- leg passes electron selection. Broken into p_T bins of 2 – 3 GeV/ c (top left), 3 – 4 GeV/ c (top right), 4 – 5 GeV/ c (bottom left), and > 5 GeV/ c (bottom right)	224
129	Fitted Λ mass peaks where p^+ leg passes electron selection. Broken into p_T bins of 2 – 3 GeV/ c (left) and > 3 GeV/ c (right).	225
130	Fitted Λ mass peaks where p^- leg passes electron selection. Broken into p_T bins of 2 – 3 GeV/ c (top left), 3 – 4 GeV/ c (top right), 4 – 5 GeV/ c (bottom left), > 5 GeV/ c (bottom right)	226
131	Fitted D^0 mass peaks where the π^\pm leg meets the third track requirements. Broken into p_T bins of 3 – 4 GeV/ c (top left), 4 – 5 GeV/ c (top right), 5 – 7 GeV/ c (bottom left), and > 7 GeV/ c (bottom right).	228
132	Fitted D^0 mass peaks where the K leg meets the third track requirements. Broken into p_T and q bins of 3 – 5 GeV/ c and $q = 1$ (top left), > 5 GeV/ c and $q = 1$ (top right), 3 – 5 GeV/ c and $q = -1$ (bottom left), and > 5 GeV/ c and $q = -1$ (bottom right).	229
133	Fitted D^0 mass peaks where the π^\pm leg meets the third muon requirements. Broken into p_T bins of 3 – 4 GeV/ c (top left), 4 – 5 GeV/ c (top right), 5 – 7 GeV/ c (bottom left), and > 7 GeV/ c (bottom right).	230

134	Fitted D^0 mass peaks where the K leg meets the third muon requirements. Broken into p_T and q bins of $3 - 5$ GeV/ c and $q = 1$ (top left), > 5 GeV/ c and $q = 1$ (top right), $3 - 5$ GeV/ c and $q = -1$ (bottom left), and > 5 GeV/ c and $q = -1$ (bottom right).	231
135	Z_{π}^{pull} (left) and TOF_{π}^{pull} (right) projections of fits of particle fractions in the $p = 2.0 - 2.5$ GeV/ c (top) and $p = 2.5 - 3.0$ GeV/ c (bottom) momentum bins for positively charged third tracks and J/ψ +track $ct^* < 0$ μm	233
136	Z_{π}^{pull} (left) and TOF_{π}^{pull} (right) projections of fits of particle fractions in the $p = 2.0 - 2.5$ GeV/ c (top) and $p = 2.5 - 3.0$ GeV/ c (bottom) momentum bins for negatively charged third tracks and J/ψ +track $ct^* < 0$ μm	234
137	Z_{π}^{pull} (left) and TOF_{π}^{pull} (right) projections of fits of particle fractions in the $p = 2.0 - 2.5$ GeV/ c (top) and $p = 2.5 - 3.0$ GeV/ c (bottom) momentum bins for positively charged third tracks and J/ψ +track $0 < ct^* < 150$ μm	235
138	Z_{π}^{pull} (left) and TOF_{π}^{pull} (right) projections of fits of particle fractions in the $p = 2.0 - 2.5$ GeV/ c (top) and $p = 2.5 - 3.0$ GeV/ c (bottom) momentum bins for negatively charged third tracks and J/ψ +track $0 < ct^* < 150$ μm	236
139	Z_{π}^{pull} (left) and TOF_{π}^{pull} (right) projections of fits of particle fractions in the $p = 2.0 - 2.5$ GeV/ c (top) and $p = 2.5 - 3.0$ GeV/ c (bottom) momentum bins for positively charged third tracks and J/ψ +track $ct^* > 150$ μm	237
140	Z_{π}^{pull} (left) and TOF_{π}^{pull} (right) projections of fits of particle fractions in the $p = 2.0 - 2.5$ GeV/ c (top) and $p = 2.5 - 3.0$ GeV/ c (bottom) momentum bins for negatively charged third tracks and J/ψ +track $ct^* > 150$ μm	238
141	Z_{π}^{pull} (left) and TOF_{π}^{pull} (right) projections of fits of particle fractions in the $p = 2.0 - 2.25$ GeV/ c (top) and $p = 2.25 - 2.5$ GeV/ c (bottom) momentum bins for positively charged third tracks and J/ψ +track $ct^* < 0$ μm	240
142	Z_{π}^{pull} (left) and TOF_{π}^{pull} (right) projections of fits of particle fractions in the $p = 2.5 - 2.75$ GeV/ c (top) and $p = 2.75 - 3.0$ GeV/ c (bottom) momentum bins for positively charged third tracks and J/ψ +track $ct^* < 0$ μm	241

143	Z_{π}^{pull} (left) and TOF_{π}^{pull} (right) projections of fits of particle fractions in the $p = 2.0 - 2.25$ GeV/ c (top) and $p = 2.25 - 2.5$ GeV/ c (bottom) momentum bins for negatively charged third tracks and J/ψ +track $ct^* < 0$ μm	242
144	Z_{π}^{pull} (left) and TOF_{π}^{pull} (right) projections of fits of particle fractions in the $p = 2.5 - 2.75$ GeV/ c (top) and $p = 2.75 - 3.0$ GeV/ c (bottom) momentum bins for negatively charged third tracks and J/ψ +track $ct^* < 0$ μm	243
145	Z_{π}^{pull} (left) and TOF_{π}^{pull} (right) projections of fits of particle fractions in the $p = 2.0 - 2.25$ GeV/ c (top) and $p = 2.25 - 2.5$ GeV/ c (bottom) momentum bins for positively charged third tracks and J/ψ +track $0 < ct^* < 150$ μm	244
146	Z_{π}^{pull} (left) and TOF_{π}^{pull} (right) projections of fits of particle fractions in the $p = 2.5 - 2.75$ GeV/ c (top) and $p = 2.75 - 3.0$ GeV/ c (bottom) momentum bins for positively charged third tracks and J/ψ +track $0 < ct^* < 150$ μm	245
147	Z_{π}^{pull} (left) and TOF_{π}^{pull} (right) projections of fits of particle fractions in the $p = 2.0 - 2.25$ GeV/ c (top) and $p = 2.25 - 2.5$ GeV/ c (bottom) momentum bins for negatively charged third tracks and J/ψ +track $0 < ct^* < 150$ μm	246
148	Z_{π}^{pull} (left) and TOF_{π}^{pull} (right) projections of fits of particle fractions in the $p = 2.5 - 2.75$ GeV/ c (top) and $p = 2.75 - 3.0$ GeV/ c (bottom) momentum bins for negatively charged third tracks and J/ψ +track $0 < ct^* < 150$ μm	247
149	Z_{π}^{pull} (left) and TOF_{π}^{pull} (right) projections of fits of particle fractions in the $p = 2.0 - 2.25$ GeV/ c (top) and $p = 2.25 - 2.5$ GeV/ c (bottom) momentum bins for positively charged third tracks and J/ψ +track $ct^* > 150$ μm	248
150	Z_{π}^{pull} (left) and TOF_{π}^{pull} (right) projections of fits of particle fractions in the $p = 2.5 - 2.75$ GeV/ c (top) and $p = 2.75 - 3.0$ GeV/ c (bottom) momentum bins for positively charged third tracks and J/ψ +track $ct^* > 150$ μm	249
151	Z_{π}^{pull} (left) and TOF_{π}^{pull} (right) projections of fits of particle fractions in the $p = 2.0 - 2.25$ GeV/ c (top) and $p = 2.25 - 2.5$ GeV/ c (bottom) momentum bins for negatively charged third tracks and J/ψ +track $ct^* > 150$ μm	250
152	Z_{π}^{pull} (left) and TOF_{π}^{pull} (right) projections of fits of particle fractions in the $p = 2.5 - 2.75$ GeV/ c (top) and $p = 2.75 - 3.0$ GeV/ c (bottom) momentum bins for negatively charged third tracks and J/ψ +track $ct^* > 150$ μm	251

153	The fraction of $p = 2 - 3$ GeV/ c third tracks that are protons for the muon channel J/ψ +track sample.	252
154	Fitted Z_{π}^{pull} distributions for $q = 1$ and $J/\psi + track$ $ct^* < 0$ μm . Broken into third track momentum bins of 3.0 – 3.5 GeV/ c (top left), 3.5 – 4.0 GeV/ c (top right), 4.0 – 5.0 GeV/ c (middle left), 5.0 – 6.5 GeV/ c (middle right), and > 6.5 GeV/ c (bottom).	254
155	Fitted Z_{π}^{pull} distributions for $q = -1$ and $J/\psi + track$ $ct^* < 0$ μm . Broken into third track momentum bins of 3.0 – 3.5 GeV/ c (top left), 3.5 – 4.0 GeV/ c (top right), 4.0 – 5.0 GeV/ c (middle left), 5.0 – 6.5 GeV/ c (middle right), and > 6.5 GeV/ c (bottom).	255
156	Fitted Z_{π}^{pull} distributions for $q = 1$ and $J/\psi + track$ $0 < ct^* < 150$ μm . Broken into third track momentum bins of 3.0 – 3.5 GeV/ c (top left), 3.5 – 4.0 GeV/ c (top right), 4.0 – 5.0 GeV/ c (middle left), 5.0 – 6.5 GeV/ c (middle right), and > 6.5 GeV/ c (bottom).	256
157	Fitted Z_{π}^{pull} distributions for $q = -1$ and $J/\psi + track$ $0 < ct^* < 150$ μm . Broken into third track momentum bins of 3.0 – 3.5 GeV/ c (top left), 3.5 – 4.0 GeV/ c (top right), 4.0 – 5.0 GeV/ c (middle left), 5.0 – 6.5 GeV/ c (middle right), and > 6.5 GeV/ c (bottom).	257
158	Fitted Z_{π}^{pull} distributions for $q = 1$ and $J/\psi + track$ $ct^* > 150$ μm . Broken into third track momentum bins of 3.0 – 3.5 GeV/ c (top left), 3.5 – 4.0 GeV/ c (top right), 4.0 – 5.0 GeV/ c (middle left), 5.0 – 6.5 GeV/ c (middle right), and > 6.5 GeV/ c (bottom).	258
159	Fitted Z_{π}^{pull} distributions for $q = -1$ and $J/\psi + track$ $ct^* > 150$ μm . Broken into third track momentum bins of 3.0 – 3.5 GeV/ c (top left), 3.5 – 4.0 GeV/ c (top right), 4.0 – 5.0 GeV/ c (middle left), 5.0 – 6.5 GeV/ c (middle right), and > 6.5 GeV/ c (bottom).	259

160	Fitted Z_{π}^{pull} distributions for $q = 1$ and $J/\psi + track\ ct^* < 0\ \mu\text{m}$. Broken into third track momentum bins of 3.0 – 3.5 GeV/c (top left), 3.5 – 4.0 GeV/c (top center), 4.0 – 4.5 GeV/c (top right), 4.5 – 5.0 GeV/c (middle right), 5.0 – 6.0 GeV/c (middle center), 6.0 – 7.0 GeV/c (middle right), and > 7.0 GeV/c (bottom).	261
161	Fitted Z_{π}^{pull} distributions for $q = -1$ and $J/\psi + track\ ct^* < 0\ \mu\text{m}$. Broken into third track momentum bins of 3.0 – 3.5 GeV/c (top left), 3.5 – 4.0 GeV/c (top center), 4.0 – 4.5 GeV/c (top right), 4.5 – 5.0 GeV/c (middle right), 5.0 – 6.0 GeV/c (middle center), 6.0 – 7.0 GeV/c (middle right), and > 7.0 GeV/c (bottom).	262
162	Fitted Z_{π}^{pull} distributions for $q = 1$ and $J/\psi + track\ 0 < ct^* < 150\ \mu\text{m}$. Broken into third track momentum bins of 3.0 – 3.5 GeV/c (top left), 3.5 – 4.0 GeV/c (top center), 4.0 – 4.5 GeV/c (top right), 4.5 – 5.0 GeV/c (middle right), 5.0 – 6.0 GeV/c (middle center), 6.0 – 7.0 GeV/c (middle right), and > 7.0 GeV/c (bottom).	263
163	Fitted Z_{π}^{pull} distributions for $q = -1$ and $J/\psi + track\ 0 < ct^* < 150\ \mu\text{m}$. Broken into third track momentum bins of 3.0 – 3.5 GeV/c (top left), 3.5 – 4.0 GeV/c (top center), 4.0 – 4.5 GeV/c (top right), 4.5 – 5.0 GeV/c (middle right), 5.0 – 6.0 GeV/c (middle center), 6.0 – 7.0 GeV/c (middle right), and > 7.0 GeV/c (bottom).	264
164	Fitted Z_{π}^{pull} distributions for $q = 1$ and $J/\psi + track\ ct^* > 150\ \mu\text{m}$. Broken into third track momentum bins of 3.0 – 3.5 GeV/c (top left), 3.5 – 4.0 GeV/c (top center), 4.0 – 4.5 GeV/c (top right), 4.5 – 5.0 GeV/c (middle right), 5.0 – 6.0 GeV/c (middle center), 6.0 – 7.0 GeV/c (middle right), and > 7.0 GeV/c (bottom).	265
165	Fitted Z_{π}^{pull} distributions for $q = -1$ and $J/\psi + track\ ct^* > 150\ \mu\text{m}$. Broken into third track momentum bins of 3.0 – 3.5 GeV/c (top left), 3.5 – 4.0 GeV/c (top center), 4.0 – 4.5 GeV/c (top right), 4.5 – 5.0 GeV/c (middle right), 5.0 – 6.0 GeV/c (middle center), 6.0 – 7.0 GeV/c (middle right), and > 7.0 GeV/c (bottom).	266

PREFACE

As with most endeavours in life, there are a number of people without whom completing this document would not have been possible. I extend my thanks to all who contributed to this work and would like to give special thanks to the following people. I thank my advisor, Professor Paul Shepard, for guidance, insight and encouragement throughout my career as a graduate student. Over the course of our six years working together he has exhibited many qualities that I hope to emulate in my career as a scientist.

I would also like to thank Professor Joe Boudreau, for always being available to discuss the intricacies of data analysis at the CDF experiment. His encyclopedic knowledge of analysis methods and techniques, in addition to his vast knowledge of physical processes, was an indispensable resource throughout my PhD studies.

I appreciate the contributions from all of the members of my thesis committee. I thank Professor Adam Lebovich for his willingness to answer any question regarding the dirty details of QCD, and in a manner that an experimentalist could understand, Professor Vittorio Paolone for helping me to formulate my ideas in a manner that all physicists can understand, and Professor Manfred Paulini for his constant encouragement and insights.

Much of a PhD students time is spent in an office, sitting before a computer, writing software to make measurements. It is no surprise then that my office mate, Dr. Chunlei Lui, played an important role in my time as a PhD student at Fermilab. We shared many a discussion on topics ranging from likelihood fit techniques to politics to sports. Whether for the purpose of working or avoiding work, our discussions were always enlightening.

The most challenging time for a PhD student is probably the first year of graduate school, with its nearly overwhelming array of difficult courses. Without the support of fellow students such as Ben Brown, Dr. Emily Chapman, and Jon Gaffney I may never have

emerged from the flood of seemingly endless homework assignments. I would like to thank them and all of the students with whom I shared the formative years of my PhD career.

Any physics result that comes out of the CDF experiment at Fermilab is the result of countless hours of work by scientists, engineers and technicians from the CDF collaboration and the various divisions of Fermilab, including the accelerator and computing divisions. I appreciate all of the work that these people have put into making Fermilab one of the greatest places for scientific research in the world.

There are number of educators who encouraged my love of math and science before my time in graduate school and I thank them all. In particular, I would like to thank my high school math and physics teachers, Mr. Mountz and Mr. Zervanos. They taught math and physics with a passion that was passed on to many students.

Of course, any person's successes in life are largely influenced his family. I thank my parents, Patricia and Barry Hartz, for all of the love and support they have given me throughout my life. They have always allowed me to pursue my interests and goals while providing me with encouragement at every step. I thank my older sister Karen Hartz, who has always been a role model for achieving success and happiness through independence. My younger brothers, John, Justin and Andrew, have all played an important role in my maturation. I thank John for keeping me down to earth, Justin for keeping me in touch with my carefree fun loving side and Andrew for providing an example of how broad ones horizons can be. I would also like to thank my Grandmother, aunts, uncles and cousins for all of the support and encouragement they have provided throughout my life and during my time as a PhD student.

1.0 INTRODUCTION

The $B_c^+ = \bar{b}c$ and $B_c^- = b\bar{c}$ are the ground state of the meson formed by the bound state of an antibottom \bar{b} and a charm c quark or its charge conjugate. The B_c^\pm provides a unique laboratory for the study of quantum chromodynamics (QCD) since it is composed of two heavy quarks but decays via the weak force. This allows for the application of nonrelativistic QCD (NRQCD), which is normally applied to $b\bar{b}$ and $c\bar{c}$ systems that decay by the strong and electromagnetic forces, while calculating quantities such as weak decay form factors. The average proper decay time (lifetime) of the B_c^\pm is a physical property of the B_c^\pm meson that can be measured and used to test the applications of NRQCD while calculating the properties of weak decays.

The B_c^\pm decays through either of the constituent quarks or by the annihilation of the constituent quarks to a virtual W boson, as illustrated in Figure 1. The decays through the c quark account for the largest fraction of decay modes since the transition from c to s quarks has a large associated CKM matrix element. The decays through the b quark are suppressed by the CKM matrix element, but can offer useful experimental signatures since the decay products often include a J/ψ ($c\bar{c}$) mesons that decays to $\mu^+\mu^-$. The decay modes $B_c^\pm \rightarrow J/\psi + e^\pm + X$ and $B_c^\pm \rightarrow J/\psi + \mu^\pm + X$, where the J/ψ decays to $\mu^+\mu^-$ and X are unmeasured particles, are used in this measurement of the B_c^\pm lifetime described in this thesis.

The B_c^\pm lifetime has previously been measured using semileptonic decays to J/ψ by CDF Run I, $\tau = 0.46_{-0.16}^{+0.18}(stat.) \pm 0.03(syst.)$ ps [1], CDF Run II, $\tau = 0.463_{-0.065}^{+0.073}(stat.) \pm 0.036(syst.)$ ps [2], and D0 Run II, $\tau = 0.448_{-0.036}^{+0.038}(stat.) \pm 0.032(syst.)$ ps [3]. These measurements are consistent with the theoretical predictions, which suggest a lifetime of 0.4 to 0.7 ps depending on the theoretical approach [4, 5, 6, 7].

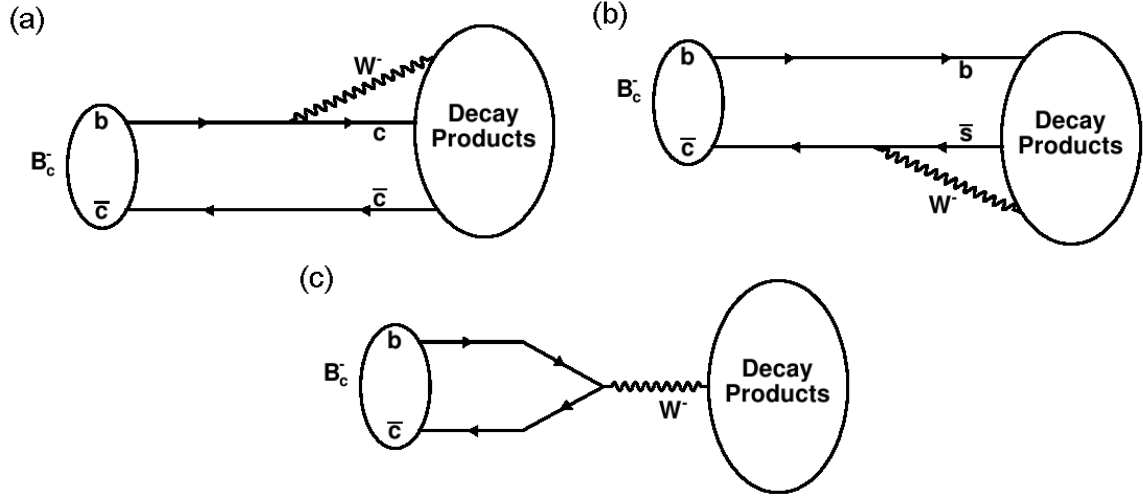


Figure 1: Inclusive decay modes of the B_c^- through decay of the b quark (a), decay of the c quark (b), and weak annihilation of the b and c quarks (c).

The lifetime measurement uses events created in $\sqrt{s} = 1.96$ TeV $p\bar{p}$ collisions. The properties of the particles created in the collisions are measured by the CDF II detector [8]. An integrated luminosity of $\sim 1 \text{ fb}^{-1}$, collected between February 2002 and February 2006, is used for the measurement. Since the production of B_c^\pm mesons is suppressed by a factor of ~ 1000 relative to $c\bar{c}$ and $b\bar{b}$ production, the background sources of B_c^\pm candidates can be significant and must be accurately modeled. The measurement procedure consists of constructing models for the B_c^\pm background sources, as well as modeling the unmeasured particles X in the decay of B_c^\pm to the final states of interest. The signal and background models are used to construct a fitter that measures the B_c^\pm lifetime when applied to candidate events in data.

The thesis is organized as follows. Chapter 2 provides an introduction to the standard model of particle physics, and Chapter 3 discusses the portion of the standard model describing hadrons containing b quarks including the B_c^\pm meson. Chapter 4 contains a description of the experimental apparatus used in the measurement, and Chapter 5 includes a discussion of the various experimental techniques used to study the collected data. The selection criteria

for candidate B_c^\pm events are discussed in Chapter 6. The modeling of background contributions are presented in Chapter 7, and the combination of background and signal models to construct a lifetime fitter is discussed in Chapter 8. The measured value of the B_c^\pm average proper decay time (lifetime) is presented in Chapter 9, and systematic uncertainties in the measurement are discussed in Chapter 10. Chapter 11 discusses the measurement in the context of previous B_c^\pm measurements and theoretical expectations.

2.0 THE STANDARD MODEL

The current best understanding of fundamental particles and their interactions is described by the standard model (SM) of particle physics, which was developed in the 1960s and 1970s to explain a number of mysteries concerning the interactions of fundamental particles including explanations for the origin of particle masses and the menagerie of hadrons discovered in the 1950s and 1960s. The SM builds upon the relativistic theory of quantum mechanics originally developed by Dirac [9] and expanded on by others [10, 11, 12]. Since its inception it has been confirmed by nearly all experimental tests, the lone exception being the discovery of masses and mixing amongst the neutrinos. In fact, over the last 30 years the Standard Model has been experimentally tested for fractional deviations from theory as small as 10^{-11} [13] and no significant deviation has yet been found.

The Standard Model consists of fields describing structureless elementary particles and their interactions. The particles can be classified as those with integer multiples of \hbar spin called bosons and those with half-integer multiple spin called fermions. The bosons, listed in Table 1, are typically described as the force carriers for the three elementary forces in the standard model. The photon (γ) is a massless spin 1 boson that mediates the electromagnetic force, the Z and W^\pm are massive spin 1 bosons that mediate the weak force, and the strong force is mediated by an octet of massless spin 1 bosons that carry strong charge themselves called gluons (g).

The fermions, listed in Table 2, are the particles that make up matter and can be broken into those that interact via the strong force, quarks, and those that do not, leptons. The quarks carry charge for all three forces and are always found in bound states. Leptons are classified as charged leptons, which carry electromagnetic and weak charge, and neutrinos which only carry weak charge. Within the fermions the particles are classified in three gen-

Name	Force Carried	Charge	Mass	Interacts With
Photon (γ)	Electromagnetic	0	0	All charged particles
W^\pm	Weak	± 1	$80.4 \text{ GeV}/c^2$	Left handed leptons and quarks
Z	Weak	0	$91.2 \text{ GeV}/c^2$	Left handed leptons and quarks
Gluon (g)	Strong	0	0	Quarks
Higgs (H^0)	-	0	$> 114 \text{ GeV}/c^2$	Massive bosons and fermions

Table 1: Table of elementary bosons in the standard model with electric charges and masses listed. The Higgs boson has not yet been discovered. There are 8 gluons, making an SU(3) color octet, that carry color charge.

erations, each containing two quarks, a charged lepton and a neutrino. The first generation contains the electron (e), its associated neutrino (ν_e) and the up (u) and down (d) quarks. Ordinary matter consists primarily of particles in the first generation. As one moves to the second and third generations, the masses of the particles increase. Among the second and third generations, the quarks and charged leptons are not stable particles and eventually decay through the electroweak interaction. The neutrinos were originally assumed to be massless, but experimental results have shown that they have a mass hierarchy, although their masses are much smaller than the other fermions. Recent measurements of neutrino mixing show large mixing angles, implying that the mass eigenstates should be thought of separately from the flavor eigenstates. When studying most properties of the quark and charged lepton sectors of the SM, however, the neutrinos can be treated as massless and neutrino mixing can be ignored.

All particles within the SM have antimatter partners with the same mass but opposite charge, although the γ and Z bosons are their own antiparticles. The antiparticles are usually denoted by changing the sign of the charge, $e^- \rightarrow e^+$, or by including a bar over the particle, $p \rightarrow \bar{p}$. For electromagnetic and strong interactions, processes are symmetric under exchange of particles and antiparticles. For the weak interaction the symmetry only holds when a reflection of parity is included, and even then, the symmetry is only approximate.

The interactions of fermions via the electromagnetic and weak forces are unified in the electroweak theory where an additional scalar boson, the Higgs boson, is introduced. The

Generation	Leptons			Quarks		
	Flavor	Charge	Mass	Flavor	Charge	Mass
1	Electron (e)	-1	$0.511 \text{ MeV}/c^2$	Up (u)	$2/3$	$1.5 - 4 \text{ MeV}/c^2$
	e Neutrino (ν_e)	0	$< 3 \text{ eV}/c^2$	Down (d)	$-1/3$	$4 - 8 \text{ MeV}/c^2$
2	Muon (μ)	-1	$106 \text{ MeV}/c^2$	Charm (c)	$2/3$	$1.2 - 1.4 \text{ GeV}/c^2$
	μ Neutrino (ν_μ)	0	$< 0.2 \text{ MeV}/c^2$	Strange (s)	$-1/3$	$80 - 130 \text{ MeV}/c^2$
3	Tau (τ)	-1	$1.78 \text{ GeV}/c^2$	Top (t)	$2/3$	$178 \text{ GeV}/c^2$
	τ Neutrino (ν_τ)	0	$< 18 \text{ MeV}/c^2$	Bottom (b)	$-1/3$	$4.1 - 4.4 \text{ GeV}/c^2$

Table 2: Table of elementary fermions in the standard model with the electric charges and masses listed. All charges are for matter particles; anti-matter particles have opposite charge. All charges are given as multiples of the electron charge. All particles carry weak charge and the quarks carry strong charge. Quark masses, except for top, are approximate since confinement limits the ability to measure a bare quark mass.

standard model Higgs boson remains undetected with an experimental lower limit on its mass of $114 \text{ GeV}/c^2$ [14] from direct searches. Global fits of measured quantities in the electroweak theory place an upper limit on the mass of $193 \text{ GeV}/c^2$ [15]. Given these limits, if the Standard Model Higgs boson does exist, it should be discovered at the current or next generation of high energy experiments.

The interactions of quarks via the strong force are described by the theory of quantum chromodynamics (QCD). The nature of the strong interactions leads to the experimentally observed fact that quarks are always found in composite particles, either $1/2$ integer spin baryons or integer spin mesons, that are collectively called hadrons. The proton of ordinary matter, the lightest of the baryons and only stable hadron, is a bound state of two u quarks and a d quark.

2.1 ELECTROWEAK INTERACTIONS

The interactions of particles via the electromagnetic and weak forces are unified in the electroweak theory developed by Weinberg, Salam and Glashow [16, 17, 18]. The initial

configuration of the theory describes an $SU(2)_L \times U(1)_Y$ gauge group that represents the fermions' local gauge symmetry in the Lagrangian. To account for parity violation in the weak interaction, the $SU(2)_L$ symmetry only applies to the left-handed fermions and makes transformations within the quark doublets:

$$\begin{pmatrix} u \\ d \end{pmatrix}_L \begin{pmatrix} c \\ s \end{pmatrix}_L \begin{pmatrix} t \\ b \end{pmatrix}_L \quad (2.1)$$

and lepton doublets:

$$\begin{pmatrix} \nu_e \\ e \end{pmatrix}_L \begin{pmatrix} \nu_\mu \\ \mu \end{pmatrix}_L \begin{pmatrix} \nu_\tau \\ \tau \end{pmatrix}_L \quad (2.2)$$

The $U(1)$ symmetry has a corresponding gauge boson B , while the $SU(2)_L$ gauge bosons are described by the three component isospin triplet W^a . For the theory to be renormalizable B and W^a should be massless, but observations of weak decays show that the mediating bosons of the weak force do have considerable mass. This problem is solved by the so-called Higgs mechanism [19], where the presence of an additional scalar field can lead to massive bosons if the symmetry of the scalar field's potential is broken. In the case of electroweak symmetry breaking, a complex scalar field ϕ with a quartic potential like that in Figure 2 is introduced. The ϕ field interacts with the gauge bosons and transforms under the $SU(2)_L$ symmetry so it is written as:

$$\phi = \begin{pmatrix} \phi^+ \\ \phi^0 \end{pmatrix} \quad (2.3)$$

As ϕ settles to small variations around one of its minima, the symmetry of its potential is broken and the field can be written as variations around the minimum, the vacuum expectation value $v/\sqrt{2}$:

$$\phi = \begin{pmatrix} 0 \\ \frac{v+H^0}{\sqrt{2}} \end{pmatrix} \quad (2.4)$$

Under this symmetry breaking, the interaction terms between the gauge bosons, B and W^a , and ϕ lead to three massive bosons called the W^\pm and Z as well as a massless boson that is labeled the photon. The field H^0 , called the Higgs boson, has a mass that depends on the exact shape of the ϕ potential. The fermion masses can also be accommodated by including

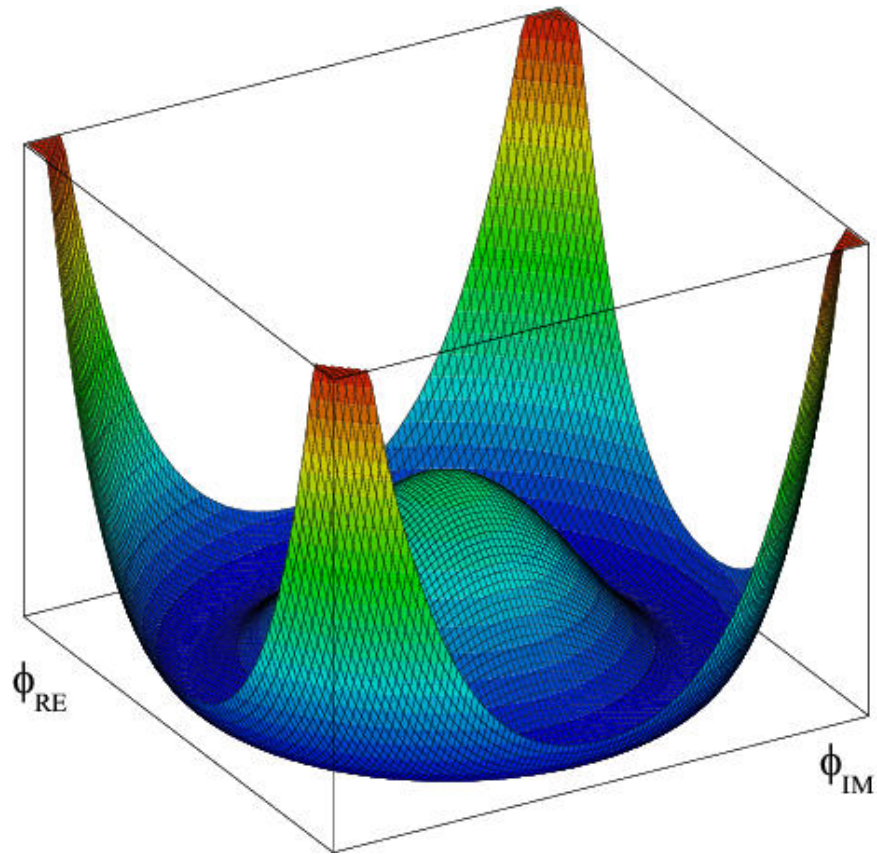


Figure 2: Picture of the shape that the potential for the complex scalar field should take for spontaneous symmetry breaking to be possible.

interaction terms between the fermion fields and ϕ . The theory after symmetry breaking includes interaction terms between the fermions/gauge bosons and H^0 , which provide the avenue for the discovery of H^0 .

After the symmetry breaking, the theory contains interaction terms between the new gauge bosons and the fermions that are described by the diagrams in Figure 3. The scale of the coupling between the charged particles and the photon is given by the fine structure constant:

$$\alpha = \frac{e^2}{\hbar c} \approx \frac{1}{137} \quad (2.5)$$

Within factors and for small energies relative to the Z and W^\pm masses, the coupling of the fermions to the massive gauge bosons is suppressed relative to the photon coupling by the inverse mass of the gauge boson squared.

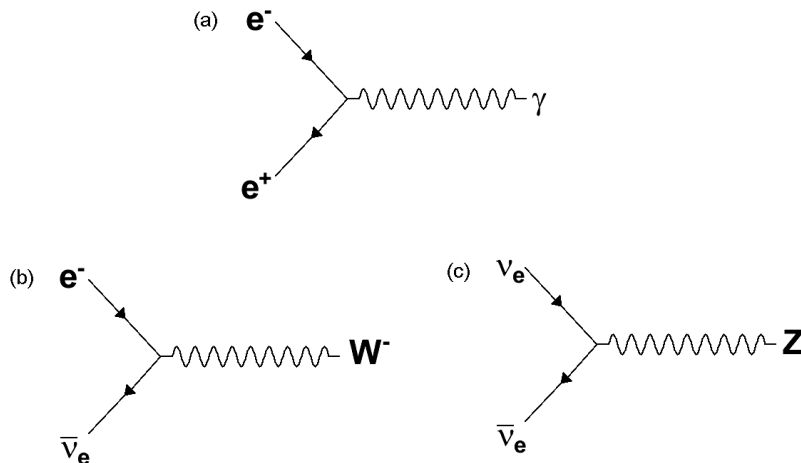


Figure 3: Diagrams of the electroweak interactions via the photon (γ) (a) and the massive W^\pm (b) and Z (c) bosons

Since the weak interaction via the W^\pm is the only interaction that couples to particles of different flavor, it is solely responsible for flavor changing processes in the Standard Model. The electromagnetic and strong interactions will only produce flavors in particle-antiparticle pairs, where the total flavor is null, or leave flavor unchanged between initial and final states.

2.2 STRONG INTERACTIONS AND QUANTUM CHROMODYNAMICS

The theory of quarks and the strong interaction, also known as quantum chromodynamics (QCD), grew out of the study of the large number of mesons and baryons discovered in the 1940s-60s. Physicists found that mesons could be classified in groups defined by symmetries under transformations of charge and a new quantum number called strangeness. Figure 4 shows this symmetry for spin 0 mesons. This classification scheme, known as the quark model and developed by Gell-Mann and Nishijima [20], explains the symmetry by postulating three types of quarks, u , d and s , that form the mesons in quark-antiquark pairs and baryons in triplets of quarks or antiquarks.

The presence of one baryon, the Δ^{++} , introduced a problem for the quark model since it is composed of three u quarks with parallel spin in seeming violation of the Pauli exclusion principle. This was solved by the introduction of an $SU(3)$ gauge degree of freedom for quarks that would eventually be identified as the color symmetry of the strong force [21, 22]. Associated with this symmetry is the octet of vector gauge bosons that are now called the gluons.

When high energy hadron collisions were interpreted to show point-like constituents within hadrons such as the proton, the quarks, till then a theoretical construct, were identified as fundamental particles that make up the mesons and baryons. The later discovery of the c , b and t quarks combined with u , d and s quarks as well as the postulated $SU(3)$ color symmetry form the modern theory of QCD in the Standard Model.

In QCD, the quarks belong to color triplets of the $SU(3)$ representation where the color charges are defined as red (r), yellow (y) and blue (b). The gauge bosons are the octet of gluons that mediate the color interaction and carry color charge as well. The interactions of the theory are shown in Fig 5 and include gluon-gluon interactions since they carry color charge as well. The fact that color is not observed directly in nature means there must be an exact color symmetry for observable states in QCD. These color singlet states exist for qqq and $q\bar{q}$ combinations with the irreducible representations:

$$3 \otimes 3 \otimes 3 = 1 \oplus 8 \oplus 8 \oplus 10 \tag{2.6}$$

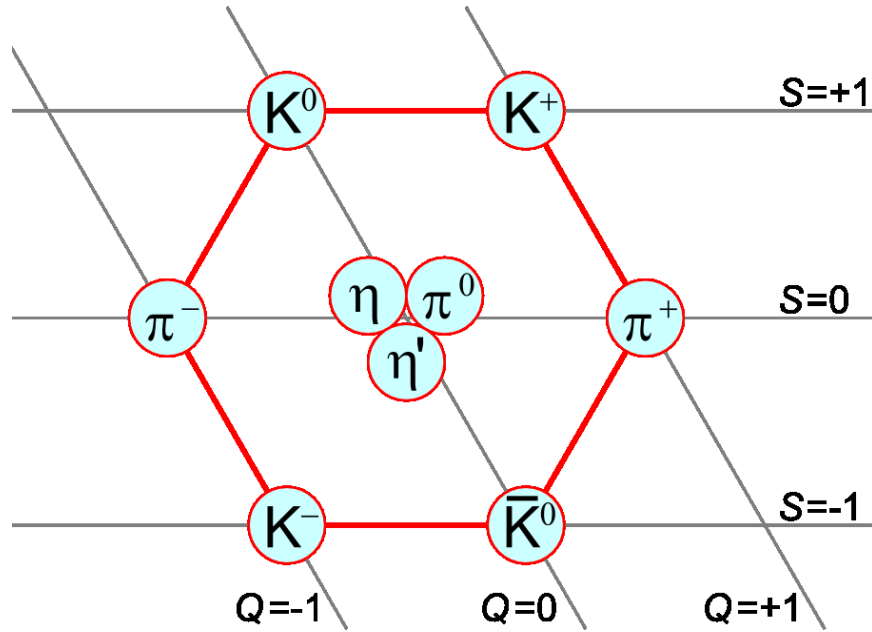


Figure 4: Mesons in the spin 0 nonet.

$$3 \otimes 3^* = 1 \oplus 8 \tag{2.7}$$

Here the antiquarks belong to the complex conjugate representation 3^* . There are no color singlet representations for qq or $qqqq$ and these types of states have not been observed.

The limitation of QCD states to color singlets is referred to as quark confinement since it means quarks are always observed as constituents of qqq or $q\bar{q}$ bound states. An explanation of confinement as a dynamical consequence of QCD is beyond the reach of calculations but it is possible to postulate a qualitative explanation. Since the gluons carry charge, they interact with each other in addition to interacting with the quarks. Figure 6 shows an approximate description of field lines between two quarks interacting via the strong force. One can see that the fields lines tend to bunch together compared to the electric interaction. This is due to the fact that the gluons carry charge and interact. If the quarks are separated, the amount of energy in the strong field increases until there is enough energy to produce a $q\bar{q}$ pair from the vacuum. Two new mesons form from the original $q\bar{q}$ pair and the new $q\bar{q}$ pair,

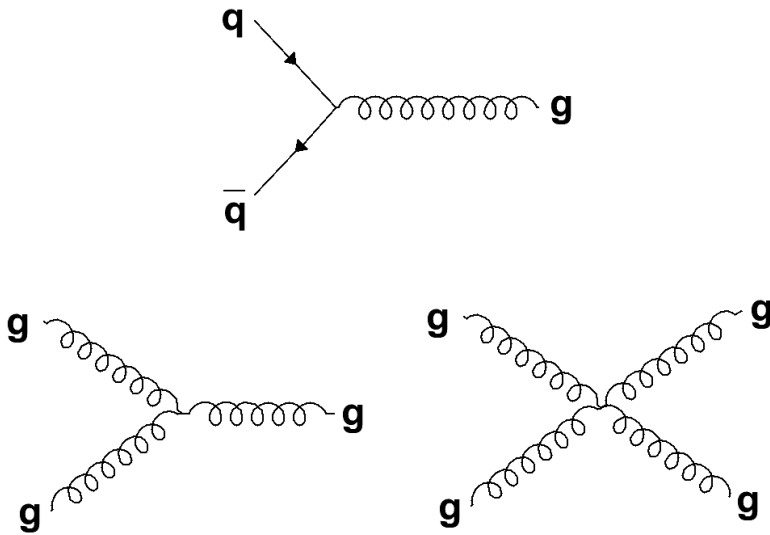


Figure 5: Diagrams of the strong interactions via the gluons of QCD. Notice the gluons interact with themselves since they also carry color charge.

preserving confinement.

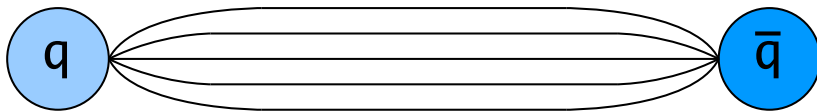


Figure 6: Qualitative picture of the strong field lines between two interacting quarks.

The confinement of quarks in color singlet states characterizes the theory at small energy (long distance) scales. The inability to derive a quantitative description of confinement stems from that fact that the coupling constant of the strong force α_s is of order 1 for the binding energy scales within hadrons. If one looks at higher energies however, one sees a running of the coupling constant towards lower values as shown in Figure 7. This property, known as asymptotic freedom, means quarks will couple "weakly" in high energy interactions and

the theory can be treated with a perturbative expansion in powers of the coupling constant α_s [23].

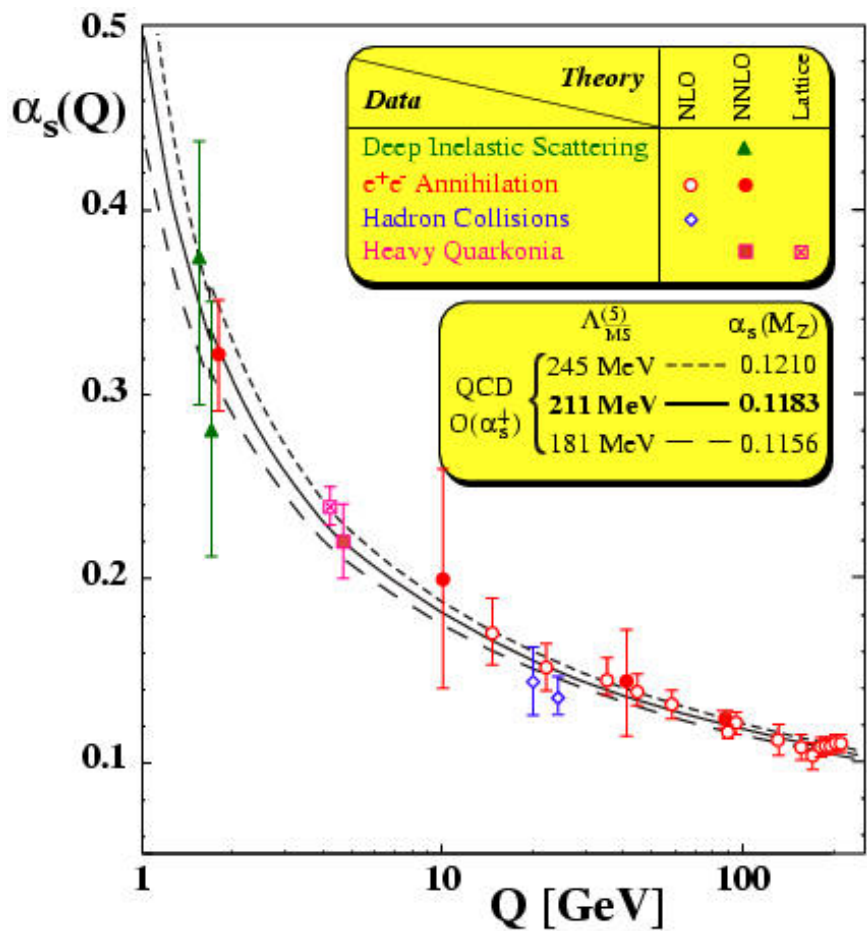


Figure 7: Running of the coupling constant α_s .

The interplay between the short distance perturbative asymptotic freedom and the long distance, nonperturbative confinement of QCD plays an important role in understanding the phenomenology of the theory. While experiments often probe strongly interacting particles at energy scales where asymptotic freedom applies, these particles are still the color singlets of the theory and must be handled in the nonperturbative regime. The theoretical methods for handling these two aspects of the theory are discussed in the next chapter.

2.3 MIXING IN THE QUARK SECTOR

The three $SU(2)_L$ doublets for the three quark generations shown in (2.1) allow transitions from one quark type to another within the doublet, but do not allow for transitions between generations. Since stable s or b quarks are not seen in nature, an explanation for their decay is needed. The solution is to discard the assumption that the quark eigenstates for the weak interaction are the same as the quark mass eigenstates.

The idea of mixing between the weak and mass eigenstates was first proposed by Cabibbo who postulated the universality of the weak interaction among fermions and a mixing angle θ_C between the down and strange quarks to explain the $\sim 1/4$ rate of transitions when there is a change in strangeness [24]. The concept was extended to three quark generations by Kobayashi and Maskawa [25] by introduction of the Cabibbo-Kobayashi-Maskawa (CKM) matrix which relates the weak ($|d\rangle$) and mass ($|d'\rangle$) eigenstates for the down-type quarks:

$$\begin{bmatrix} V_{ud} & V_{us} & V_{ub} \\ V_{cd} & V_{cs} & V_{cb} \\ V_{td} & V_{ts} & V_{tb} \end{bmatrix} \begin{bmatrix} |d\rangle \\ |s\rangle \\ |b\rangle \end{bmatrix} = \begin{bmatrix} |d'\rangle \\ |s'\rangle \\ |b'\rangle \end{bmatrix} \quad (2.8)$$

The magnitudes of the elements in the CKM matrix have been measured, and exhibit a pattern of diagonal elements of ~ 1 and off-diagonal elements $\ll 1$ [15]:

$$\begin{bmatrix} 0.9730 - 0.9746 & 0.2174 - 0.2241 & 0.0030 - 0.0044 \\ 0.213 - 0.226 & 0.968 - 0.975 & 0.039 - 0.044 \\ 0.0 - 0.08 & 0.0 - 0.11 & 0.07 - 0.9993 \end{bmatrix} \quad (2.9)$$

Since transitions between quark flavors is proportional to the matrix elements squared, one can see that those transitions between flavors within a generation are preferred since they depend on the diagonal elements of the matrix. On the other hand, transitions between generations are suppressed by the magnitudes of the off-diagonal elements of the matrix. This feature is of particular interest when comparing for the decay rates of the c quark, which decays within its generation, and b quark, which decays between generations. Since V_{cs} is ~ 1 and V_{cb} is ~ 0.04 , the decay width of the c quarks is larger, despite its smaller mass.

The particles described by the Standard Model are generally not stable and will decay to other particles within a given period of time according to an exponential decay law. The exponential law describes the fact that particles have no memory so the probability for a particle to decay at any instant is a constant. Given the CKM matrix, it is possible to give a general description of the decays of hadrons. Hadrons can be broken into ground states and excited states based on their orbital configurations. The orbitally excited hadrons decay to the ground state hadrons through the emission of photons or pions. The lifetimes of excited states are short since the strength of the strong interaction sets a time scale of $< 10^{-20}$ s. For ground state hadrons, the decay depends on the compositions. Mesons that contain a $q\bar{q}$ pair of the same flavor are referred to as quarkonium and decay via the strong and electromagnetic interactions by annihilation. As with the the orbitally excited states, the typical time scale for the decays is $< 10^{-20}$ s. For ground state baryons and mesons with quarks of differing flavor, the only modes of decay involve changes in flavor that must be determined by the weak interaction and the CKM matrix. Given the relative weakness of the weak force, the flavor changing decays of the ground states will take place at the time scale of 10^{-10} s, considerably longer than for excited states and quarkonium.

3.0 THEORETICAL CONSIDERATIONS

The previous chapter describes the general properties of the various sectors of the Standard Model. To make connections with experimental results, it is necessary to apply tools to calculate predictions for observables from the Standard Model. This chapter describes the generic tools for calculating observables in the perturbative regime that includes calculations of electroweak interactions and strong interactions in the limit of asymptotic freedom. This is followed by a discussion of methods used for calculations in the nonperturbative region of QCD. The final sections discuss the application of perturbative and nonperturbative methods to mesons containing b quarks and the special case of the B_c meson.

3.1 CALCULATIONS WITHIN THE STANDARD MODEL

The typical observables of interest in the standard model are quantities such as production cross sections, lifetimes and masses for composite particles. In general, the calculation of an observable depends on the amplitude for some transition between initial and final states and a factor that accounts for the available phase space. The amplitude is written in terms of the two states $\langle S_{in}|$ and $|S_{out}\rangle$ and some transition operator \mathcal{T} as

$$A = \langle S_{in}|\mathcal{T}|S_{out}\rangle. \tag{3.1}$$

The evaluation of A is generally broken into two steps: the determination of the operator \mathcal{T} and evaluation of the matrix elements for \mathcal{T} taken between the input and output states. The techniques described in subsequent sections will include methods for determining the operators and calculating the matrix elements.

3.1.1 Perturbative Calculations

In electroweak interactions or the asymptotically free regime of the strong interaction, the strength of the coupling between the fermions and the gauge bosons is small enough that an expansion in powers of the coupling allows for a perturbative solution. In this case it is useful to expand the operators for a given observable in powers of the coupling constant, keeping only those terms necessary for the desired precision, and evaluate matrix elements for each term in the expansion.

The most common procedure for such expansions uses the Feynman diagrams and rules that allow the terms in the expansion to be expressed as diagrams of the particle interactions where the number of vertices in the diagrams give the power of the expansion in the coupling parameter. Figure 8 shows lowest order diagrams for e^+e^- scatter through the electromagnetic force. The presence of two vertices in each diagram means that the amplitude is proportional to the square of the coupling parameter. The Feynman rules that accompany the diagram are a prescription for writing the integral used to calculate the matrix elements based on the configuration of particle lines and vertices in the diagrams.

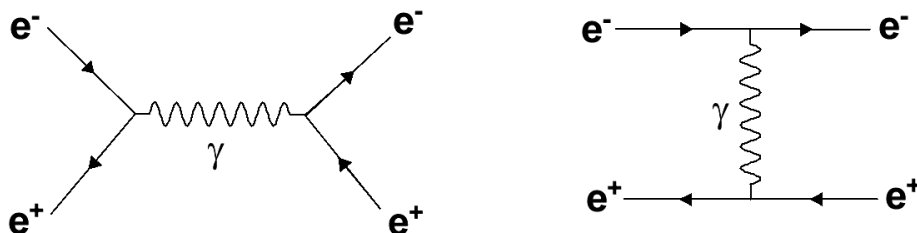


Figure 8: Feynman diagrams for e^+e^- scattering at lowest order.

3.1.2 Nonperturbative (QCD) Calculations

Calculations in QCD are complicated by the fact that a given system is usually characterized by multiple energy scales, some of which fall in the non-perturbative regime. An example is the collision of two protons with kinetic energies much larger than the binding energy of the

proton. The interactions of the quarks and gluons within a proton are of an energy scale that must be treated nonperturbatively, whereas hard interactions between the quarks or gluons of the colliding protons involves large energy transfers and can be treated perturbatively.

An important question is whether it is possible to separate the nonperturbative and perturbative mathematics when calculating the observables of such a system? In general this can be done by describing the system in terms of noninteracting currents that describe nonperturbative and perturbative physics. This concept, called factorization [26], is useful for isolating the nonperturbative behavior of a system and treating it with special theoretical tools. It will only work when the system can be accurately described by noninteracting currents. For example, it may be applicable in two body decays where the final state particles carry large momentum and quickly move away from each other.

Once the nonperturbative part of a calculation is isolated, special approaches are needed for its calculations. The following sections describe a number of approaches that are relevant to the properties of systems containing heavy quarks, quarks whose mass is much greater than the typical binding energy of QCD, $\Lambda_{QCD} \sim 0.2 GeV$.

3.1.2.1 Heavy Quark Effective Theory In meson systems where one of the quarks is significantly heavier than the other, the heavy quark can be thought of as a stationary source of the strong field. Making this assumption, it is possible to integrate out the large frequency component of the heavy quark field and disentangle the long distance and short distance processes using an expansion in the inverse of the heavy quark mass. This leaves an effective field theory that can be used for the calculation of matrix elements [27]. To lowest order, the heavy quark plays a role similar to the proton's in a hydrogen atom.

3.1.2.2 Nonrelativistic QCD In systems with two heavy quarks (b or c quarks) the typical velocity of the quarks is small enough to treat nonrelativistically at lowest order. This is true of the $b\bar{b}$ system where v^2/c^2 is ~ 0.1 [28]. In NRQCD the Lagrangian is broken into three parts.

$$\mathcal{L}_{b\bar{b}} = \mathcal{L}_{light} + \mathcal{L}_{heavy} + \delta\mathcal{L} \tag{3.2}$$

Here \mathcal{L}_{light} is a fully relativistic Lagrangian that describes the gluons and light quarks, \mathcal{L}_{heavy} describes a Schrodinger field theory for the heavy quark dynamics and $\delta\mathcal{L}$ includes correction terms that reproduce the full effects of the relativistic theory [29]. While an infinite number of terms is necessary to exactly recover the fully relativistic theory, the terms can be ordered according to velocity scaling rules and only those necessary for a given precision kept.

3.1.2.3 Lattice QCD One method for finding numerical solutions in a gauge theory is to move the theory onto a discrete space-time lattice with a lattice spacing of a . The equations of motion for the theory can then be solved numerically on the lattice, and by increasing the size of the lattice and decreasing the spacing, one can hope to accurately model the continuous theory. The application of this approach to QCD is called Lattice QCD (LQCD). When dealing with hadrons containing heavy quarks, it is often useful to use LQCD in conjunction with one of the previously described effective field theories. This allows for better control of the systematic uncertainties inherent to calculations in LQCD [30].

3.2 APPLICATION TO B HADRONS

As discussed in previous sections, the quarks of the standard model are confined to color singlets. Of particular interest for these color singlet states are their production, mass and decay properties. The production and mass are governed by the dynamics of QCD and the bare quark masses, while the decays also depend on the dynamics of the weak interaction for baryons and mesons containing quarks of differing flavor. A discussion of these properties in hadrons containing a b quark and light quarks (u , d and s quarks) and the methods for calculating the observables of interest follows.

3.2.1 B Hadron Production in $p\bar{p}$ Collisions

The description of the production of B hadrons in $p\bar{p}$ collisions can be broken into parts: a description of the quark and gluon components of the protons, the production of $b\bar{b}$ pairs

from the interactions of the partons and the hadronization of the b quarks to form B hadrons.

The production of $b\bar{b}$ pairs necessarily depends on the center of mass energy at which the $p\bar{p}$ collisions takes place. The protons can be thought of as composite objects containing valence quarks, the u and d quarks, and particles that represent the strong interactions within the protons, virtual gluons and quarks. At sufficiently high energies, the interactions are between the quark and gluon components, the partons, of the proton instead of the proton as a whole. To characterize the interaction it is necessary to use parton distribution functions which describe the fraction of the proton's momentum carried by the quark flavors and gluons within the proton. In subsequent sections of this text the CTEQ5L [31] parton distribution functions, which are based on a global analysis of experimental results involving collisions of protons and anti-protons, are used.

Given parton distributions that describes the composite structure of the proton, it is possible to give the correct weighting to the Feynman diagrams that describe the production of $b\bar{b}$ pairs. To model $b\bar{b}$ production that is consistent with data, it is necessary to include more than the lowest order diagrams. The leading order in α_s (LO) and typical next to leading order (NLO) diagrams are shown in Figure 9. The relative contributions of these terms depends on the parton distribution function.

The hadronization or fragmentation of b quarks into B hadrons is a long distance (small energy) process that cannot be treated perturbatively in QCD. The process can be described qualitatively as the bare quark field creating $q\bar{q}$ pairs which combines with the b quarks to form hadrons. For the analysis described in this text, the fragmentation in $b\bar{b}$ simulated data is carried out using the Lund string scheme [32], [33]. This model represents the strong field between the produced $b\bar{b}$ pair as a string. As the $b\bar{b}$ move apart, the string breaks by the introduction of a $q\bar{q}$ pair which can take part in the fragmentation. This process continues until there is no longer sufficient energy for the breaking of strings. Table 3 lists many of the ground state B hadrons produced during the hadronization of the b quarks.

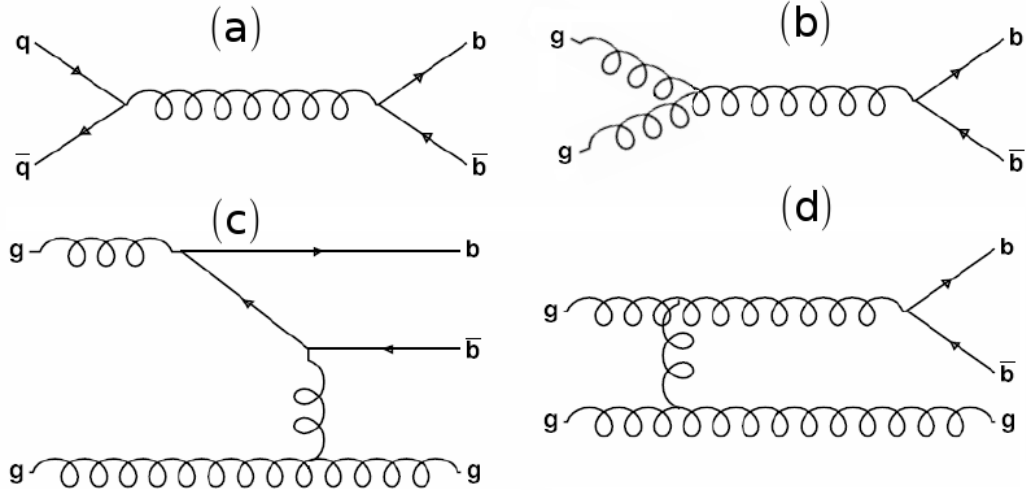


Figure 9: Representative leading order gluon fusion (a) and quark annihilation (b) diagrams for $b\bar{b}$ production. Representative next to leading order production through the scattering of a virtual b quark (c) or splitting of an excited gluon (d).

B Hadron	Quark Composition	Production Fraction (%) [15]
B^0 or B_d	db	39.7 ± 1.0
B^+ or B_u	$u\bar{b}$	39.7 ± 1.0
B_s^0	$s\bar{b}$	10.7 ± 1.1
B_c^+	$c\bar{b}$	$\ll 1$
B Baryons		9.9 ± 1.7
Λ_b^0	udb	
Ξ_b^0	usb	
Ξ_b^-	dsb	

Table 3: Listing of ground state B hadrons, their quark composition and their relative production in $\sqrt{s} = 1.8 \text{ TeV}$ $p\bar{p}$ collisions and $Z \rightarrow b\bar{b}$ decays. The list does not include all B baryon states, and the relative productions of the baryons is unknown. Charge conjugate hadrons exist with the same production rates.

3.2.2 B Hadron Masses, Decays and Lifetimes

The masses and decays of the B hadrons are generally treated in the framework of HQET. In particular, the ratio of lifetimes for different B hadrons are well determined in the heavy quark expansion: $\tau_{B_s}/\tau_{B_d} = 1.00 \pm 0.01$, $\tau_{B_u}/\tau_{B_d} = 1.06 \pm 0.01$ and $\tau_{\Lambda_b}/\tau_{B_d} = 0.86 \pm 0.05$ [34]. These results show good agreement with current worlds averages of measurements of the lifetimes [35, 36].

3.3 THE B_C MESON

The B_c meson, the ground state of $b\bar{c}$ and $\bar{b}c$ bound states, represents a unique laboratory for the study of QCD and weak decays. This is because the B_c is the only meson that contains two heavy quarks and decays weakly. Of particular interest is the calculation of weak decay form factors in a doubly heavy system. As discussed in Section 3.1.2.2, the presence of two heavy quarks allows for a treatment of the system in the framework of NRQCD where a number of approaches including potential models, operator product expansions, and QCD sum rules can be tested.

The following sections contain a discussion of the theoretical approaches for calculating properties of the B_c meson including: B_c production, the mass of the B_c meson, and its decay properties. The theoretical predictions in these areas are important for the measurement of the B_c lifetime and discussed in detail in the following sections. Where applicable, a discussion of experimental results is included as well.

3.3.1 Production of the B_c Meson

The mechanism for the production of the B_c meson should not be assumed *a priori* to be the same as that for mesons with a b quark and a light quark. In the latter case the B meson forms when a $b\bar{b}$ pair is produced and the two b quarks subsequently fragment. This involves the production of $q\bar{q}$ pairs from the energy stored in the color field which hadronize with the $b\bar{b}$ pair. For the production of B_c to take place through the fragmentation of a $b\bar{b}$ pair, a $c\bar{c}$ pair

will have to be created during the fragmentation. In the Lund string model for fragmentation, the approximate ratios of $q_i\bar{q}_i$ pairs produced are $u : d : s : c \approx 1 : 1 : 0.3 : 10^{-11}$ [37]. This suggests that B_c production through fragmentation of $b\bar{b}$ (or $c\bar{c}$) will be quite rare compared to the production of the lighter B mesons.

Another possible mode of production is through the coupling $W^+ \rightarrow c\bar{b}$. This production, however, is suppressed relative to strong production by the weak coupling and the CKM matrix element $|V_{cb}| \sim 0.04$ [38].

The dominant mode of production for B_c in hadron collisions is through the hard production of both a $b\bar{b}$ and $c\bar{c}$ pair where two of the different flavors form a color singlet. In $p\bar{p}$ collisions, the initial and final states will be $g + g \rightarrow B_c + b + \bar{c}$ and $q + \bar{q} \rightarrow B_c + b + \bar{c}$. Figure 10 shows 2 of the 36 Feynman diagrams that contribute to B_c production. The cross section for B_c and its excited states calculated for $p\bar{p}$ collisions at $\sqrt{s} = 1.8 \text{ TeV}$ is 5.3 nb [38]. This compares to the measured $b\bar{b}$ cross section for $\sqrt{s} = 1.8 \text{ TeV}$ $p\bar{p}$ collisions of $\sim 2.5 \mu\text{b}$ for the $p_T > 6.0 \text{ GeV}/c$ region [39]. From this one can expect a suppression of ~ 1000 in the B_c production rate compared to B mesons containing a light quark.

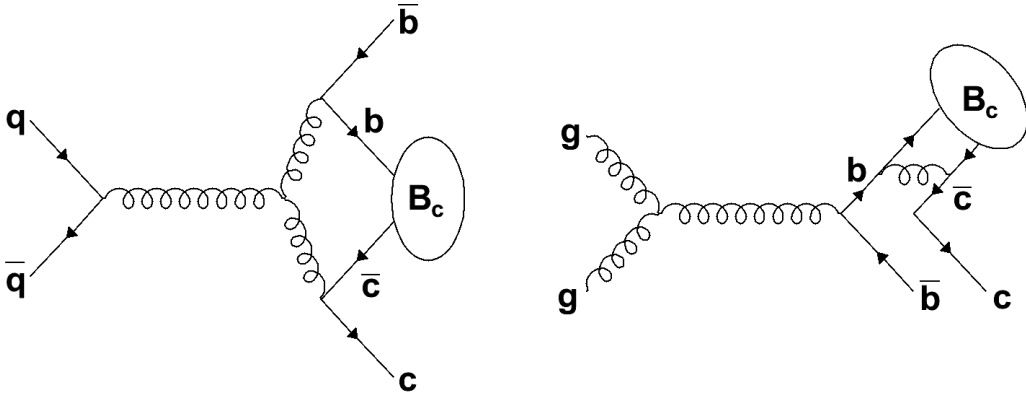


Figure 10: Representative Feynman diagrams of the lowest order in α_s processes that contribute to the production of B_c mesons in $p\bar{p}$ interactions. There are 36 diagrams in all.

A measurement of the production of $B_c^\pm \rightarrow J/\psi + l^\pm + X$ relative to $B^\pm \rightarrow J/\psi + K^\pm$ was carried out using CDF Run I data and found to be ~ 0.13 [1]. Given the hadronization of b to B^+ $\sim 40\%$ of the time and a branching fraction of $\sim 0.1\%$ for $B^\pm \rightarrow J/\psi + K^\pm$ [15],

one still needs to know the $B_c^\pm \rightarrow J/\psi + l^\pm + X$ branching fraction to obtain the rate of B_c production relative to $b\bar{b}$ production. Theoretical calculations suggest that B_c decays semileptonically with a J/ψ in the final state $\sim 2\%$ of the time [40]. Applying the numbers recovers a relative production of 1.2×10^{-3} which is consistent with the theoretical prediction.

The relatively low rate of B_c production relative to $b\bar{b}$ production suggests that the largest backgrounds for a measurement B_c properties will come from $b\bar{b}$. A suppression factor of ~ 1000 will be required to bring the backgrounds down to the signal size.

3.3.2 The B_c Meson Mass

The mass of the B_c meson is considerably heavier than B mesons with light quarks due to the mass of the c quark compared to the light quark masses. The mass can be calculated in the framework of lattice QCD to be $6.304 \pm 0.004 \pm 0.011_{-0.000}^{+0.018} \text{ GeV}/c^2$ [41]. Calculations using non-relativistic potential models give similar values in the range $6.247 - 6.286 \text{ GeV}/c^2$ [42]. The mass of the B_c has been measured in $B_c^\pm \rightarrow J/\psi\pi^\pm$ decays at CDF to be $6.2756 \pm 0.0029(\text{stat.}) \pm 0.0025(\text{syst.}) \text{ GeV}/c^2$, which is in good agreement with theoretical predictions [43].

A precise and accurate value of the B_c mass plays an important role in a measurement of the lifetime using semileptonic decays for two reasons. The semileptonic nature of the decay means there will be missing momentum leading to an inability to fully reconstruct the B_c mass for B_c candidate events. Since the formula for proper decay time contains a factor of the particle mass, the precisely measured mass from hadronic decays should be used. The value for the mass also sets the upper end of the partially reconstructed mass distribution for semileptonic decays.

3.3.3 The B_c Meson Decays and Lifetime

As discussed previously, the lifetime of B mesons, where the second quark is light compared to the b quark, can be evaluated in the spectator model where corrections are calculated using the heavy quark expansion. For the B_c meson this approach no longer works since the mass of the c quark ($\sim 1.2 \text{ GeV}/c^2$) is of the same order as the b quark mass ($\sim 4.3 \text{ GeV}/c^2$).

A different approach is needed when working with this doubly heavy system.

Before proceeding with a discussion of quantitative methods for calculating the B_c decays and lifetime, it is useful to make some qualitative statements about the expected results. Figure 11 shows the modes that should determine the B_c decay width: decay of the c quark to an s quark and a virtual W boson, decay of the b quark to a c quark and a virtual W and annihilation of the b and c quarks to a virtual W boson. The transition $c \rightarrow s$ is within a single $SU(2)$ doublet and is proportional to the diagonal V_{cs} term in the CKM matrix, whereas the $b \rightarrow c$ transition is between doublets and is proportional to the off-diagonal term $V_{bc} \sim 0.04$. Because of this the typical lifetime of weakly decaying D mesons (consisting of a c and a lighter quark) is shorter than that of B mesons; ~ 40 ps compared to ~ 150 ps. By this reasoning one expects the largest contribution to the B_c decay width to come from decays of the c quark and a B_c lifetime that is closer to that of the D mesons than the B mesons.

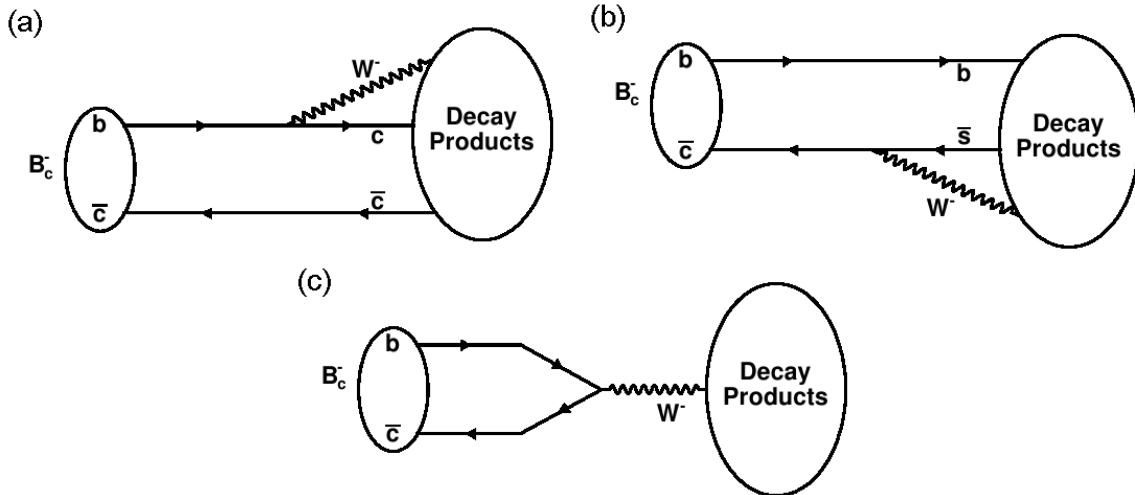


Figure 11: Inclusive decays modes that determine the B_c meson total width. Decays can happen through the b quarks (a), the c quark, or weak annihilation of the b and c quarks (c).

Calculation of the decays and lifetime of the B_c should begin by separating the contributions from the annihilation mode from the b and c decay modes. For the case of the

annihilation mode, one can estimate the width in the exclusive approach. The total width is simply a sum over final states with quarks or leptons given by the expression:

$$\Gamma_{ann.} = \sum_{i=l,q} G_F^2 |V_{bc}|^2 f_{B_c}^2 M_{B_c} m_i (1 - m_i^2/M_{B_c}^2) C_i \quad (3.3)$$

Here G_F is the Fermi coupling constant, V_{bc} is the CKM matrix element for b to c quark transitions, f_{B_c} is the leptonic decay constant, M_{B_c} is the B_c meson mass, m_i is the mass of the final state, and C_i is a factor that is different for the cases of leptons or quarks in the final state. In the case of leptons $C_i = 1$, but when the final state is contains c and s quarks $C_i = 3|V_{cs}|^2 a_1^2$, where the factor of 3 accounts for quark colors, V_{cs} is the CKM matrix element, and $a_1 = 1.22 \pm 0.04$ [40] accounts for hard gluon corrections. The quantity f_{B_c} is estimated to be $\sim 300 \text{ MeV}$ in potential models [44] or QCD sum rules [45]. The sum is dominated by the transitions to the heavy c and τ generations due to helicity suppression of decays to the lighter quarks and leptons.

Study of the decays of the B_c through the b and c quarks requires a different approach. A first rough estimate of the B_c lifetime can be carried out by estimating the partial widths for decays through the b and c quark using the lifetimes of the B and D mesons. For the c quark decay an additional factor must be added to account for the much smaller phase space in decays of the D mesons compared to the B_c . The formula for the total width is then:

$$\frac{1}{\tau_{B_c}} = \frac{1}{\tau_B} + \frac{0.6}{\tau_D} + \Gamma_{anni}. \quad (3.4)$$

This method of estimating the lifetime gives 0.4 ps [4], which is consistent with the previous qualitative exercise.

More advanced calculations of the b and c quark contributions to the total width depend on the doubly heavy nature of the B_c which suggest a treatment using NRQCD since the total energy of the system is dominated by the rest energies of the b and c quarks. The methods for calculating the decay widths may be either inclusive, where the total widths for the b or c quark transitions are calculated, or exclusive, where the widths are determined by calculating and summing over all final states. Exclusive results are of particular interest since they include calculations of the branching fractions which are a useful input to any analysis that will measure properties of the B_c in data.

Calculation of the lifetime in the inclusive approach has been carried out using the optical theorem and an operator product expansion (OPE) [5]. From the optical theorem, which relates the cross section to the imaginary part of the forward scattering amplitude, the total width is written as:

$$\Gamma_{B_c} = \frac{1}{2M_{B_c}} \langle B_c | \mathcal{T} | B_c \rangle \quad (3.5)$$

Here, \mathcal{T} is the transition operator and is defined as:

$$\mathcal{T} = Im \ i \int d^4x T H_{eff}(x) H_{eff}(0) \quad (3.6)$$

One can see that \mathcal{T} depends on a non-local operator product. Since the energy released in heavy quark decays is large, the non-local operator can be represented by virtual particles which carry large energy and, according to the uncertainty principle, exist only over short distances. By this reasoning, it is possible to expand the non-local operator product in terms of local operators. This is referred to as the operator product expansion (OPE). For the case of non-relativistic B_c decays, the terms in the expansion of \mathcal{T} are ordered by powers of the quark velocity v and those necessary for the desired degree of precision are kept.

After the expansion of \mathcal{T} using the OPE it is necessary to evaluate the matrix elements from equation 3.5. Once again, this is carried out in the non-relativistic limit by reasoning that anti-quarks cannot be produced in a system containing a non-relativistic quark, and vice versa. With this reasoning it is possible to integrate out the anti-quark component of the spinor, which can be treated perturbatively, leaving only a two spinor to describe the quark component. The resulting matrix elements are evaluated using potential models for the bound state.

The estimate of the B_c lifetime in this approach depends on a number of input quantities, including heavy quark masses, $|V_{cb}|$ and f_{B_c} . Applying best values yields a lifetime of 0.52 ps where the mass of the c quark is the largest source of uncertainty and is set to 1.5 GeV/c^2 . For values ranging from 1.4 to 1.6 GeV/c^2 the calculated lifetime falls in the range 0.4-0.7 ps [5].

Another approach for estimating the b and c quark contributions to the B_c lifetime is the use of QCD sum rules [46] to estimate the semileptonic decay widths and the factorization approach [47] which allows for evaluation of the hadronic modes based on the semileptonic

modes [6]. This exclusive approach provides branching fractions in addition to an estimate of a lifetime.

A complete explanation of the QCD sum rules method falls beyond the scope of this paper, but detailed introductions do exist [48]. The method begins with the correlation function of quark currents which, through the dispersion relation, is related to the hadronic states. In the limit of large momentum transfers the correlation function can be evaluated using pQCD and the OPE. One then has a relation between the hadronic states and calculable quantities.

In the cited paper [6], the QCD sum rules are applied to the calculation of the semileptonic form factors for the decay of the heavy quarks, and the semileptonic widths are calculated. The hadronic decay widths are obtained using the assumption of factorization between the weak transition of the heavy quark, which is described by the QCD sum rules applied to the semileptonic decay, and the hadronic final state. The largest sources of uncertainty in the calculation of the semileptonic decay widths are the heavy quark masses, which are determined by the sum rules for heavy quarkonia. The calculated lifetime also depends on the the scale for estimating the hard gluon corrections to the effective Hamiltonian in the factorization approach. The predicted lifetime is 0.48 ± 0.05 ps.

A number of methods for estimating the lifetime of the B_c meson are described in the previous paragraphs. Table 4 gives a summary of lifetime estimates in the literature. All estimates point to a B_c lifetime that is considerably shorter than the other B mesons. In each case, theoretical uncertainties arise from the choice of scales within the approach, whether it is the c quark mass or the scale of hard gluon corrections. A precise measurement of the B_c lifetime will not only test the general methods described, but also the assumptions that must be applied in each method.

The previously described QCD sum rules method for calculating the B_c lifetime used the exclusive approach of including widths for all dominant final states [49]. The calculation of final state widths is of particular importance since an estimate of B_c branching fractions to the specific final states is input to any study of the B_c in data. In particular, the choice of final state in which to search for the B_c will depend on the fraction of B_c decays to that final state.

Lifetime Calculation Approach	Calculated Value
Estimate from B , D meson Decays	0.4 ps [4]
Optical Theorem, OPE, Potential Models	0.4 – 0.7 ps [5]
Three Point QCD Sum Rules	0.48 ± 0.05 ps [6]
Light Front Constituent Quark Model	0.59 ± 0.06 ps [7]

Table 4: Estimates of the B_c lifetime using various theoretical approaches.

Since the total decay width of the B_c is dominated by the c quark decay, one should expect that decays to B_s have the dominant branching fractions. According to calculations, this is true as $B_c^\pm \rightarrow B_s^{0(*)} + \pi^\pm/\rho^\pm$ account for 20 – 40% of decays. Various estimates of these branching fractions are shown in Table 5.

Decay Mode	Branching Fraction(%)		
	[49]	[50]	[51]
$B_s^{0*} + \rho^\pm$	20.2	11	16.8
$B_s^0 + \rho^\pm$	7.2	2.3	3.86
$B_s^{0*} + \pi^\pm$	6.5	2.1	1.2
$B_s^0 + \pi^\pm$	16.4	3.9	1.56

Table 5: Branching fractions of the B_c through $B_s^{0(*)}$.

In all models, the decay to $B_s^{0*} + \rho^\pm$ is found to have the largest branching fraction, but this is not a useful channel from an experimental perspective since ρ decays typically include a π^0 which is difficult to reconstruct experimentally. The channel $B_c^\pm \rightarrow B_s^0 + \pi^\pm$ does not share this problem, but reconstruction of B_s^0 presents its own difficulties. The most promising mode for reconstructing B_s^0 is through $D_s^\pm(\phi + \pi^\pm) + \pi^\mp$, but the branching fraction for $B_s^0 \rightarrow D_s^\pm + \pi^\mp$ is only $\sim 3\%$, while the branching fraction for $D_s^\pm \rightarrow \phi + \pi^\pm$ is only $\sim 4\%$. This leaves a total suppression due to branching fractions relative to B_c production of 2×10^{-4} in the most optimistic case.

If decays through the c quark that leave a B_s^0 in the final state do not offer a promising experimental signature for a lifetime measurement, what about decays through the b quark where there is a J/ψ in the final state? Decay modes with J/ψ have often been preferred in experiments since J/ψ decays to the clean signature of two muons 5% of the time and the

J/ψ has a relatively narrow peak. From Table 6 one can see that the $B_c^\pm \rightarrow J/\psi + e/\mu^\pm + \nu_{e/\mu}$ decays dominate the branching fractions through the b quark with charmonium in the final state. If one reconstructs the J/ψ using the two muon final state, the total suppression due to branching fractions relative to B_c production is 1×10^{-3} , since J/ψ decays to two muons $\sim 5\%$ of the time. The disadvantage of this channel is that the semileptonic decay leads to an unmeasured neutrino in the final state, so any analysis of the data will have to account for the missing neutrino. The fully reconstructed $J/\psi + \pi^\pm$ does not suffer from this problem, but is suppressed in the branching fractions by another factor of 10.

Decay Mode	Branching Fraction(%)		
	[49]	[50]	[51]
$J/\psi + \rho^\pm$	0.40	0.49	0.31
$J/\psi + \pi^\pm$	0.13	0.17	0.11
$J/\psi + e/\mu^\pm + \nu_{e/\mu}$	1.9	2.07	1.44

Table 6: Branching fractions of the B_c through charmonium.

The calculations of the B_c branching fractions tell us that the combination of $B_c \rightarrow J/\psi + l + \nu$ modes, where l can be an electron or a muon, should give at least 10 times the statistics of the most abundant fully reconstructed modes. In addition, the presence of the J/ψ , which decays to two muons, will provide an experimental signature for triggering, which is an important aspect of experimental physics in $p\bar{p}$ collisions that will be discussed in the next chapter. For these reasons the $B_c \rightarrow J/\psi + l + \nu$ decay modes offer the first chance to study the B_c lifetime in an experiment with limited statistics.

4.0 EXPERIMENTAL APPARATUS

The B_c mesons studied in this thesis are created by the collision of protons and antiprotons ($p\bar{p}$) at a center of mass energy of $\sqrt{s} = 1.96$ TeV. The particle accelerator complex, located at the Fermi National Accelerator Laboratory (Fermilab), includes the Tevatron, a synchrotron with superconducting magnets, that accelerates the protons and antiprotons. The the p and \bar{p} beams circulate in opposite directions within the Tevatron and the beams are focused for collisions at the locations of two multipurpose particle detectors. Of these two, the CDF II detector provides the measurements used in this thesis. The accelerator complex and the various parts of the CDF II detector necessary for measuring the B_c lifetime are discussed in detail in the following sections.

4.1 THE ACCELERATOR COMPLEX

The Fermilab accelerator complex, which produces and accelerates the p and \bar{p} particles, has components used for p acceleration, \bar{p} production and acceleration, and acceleration and collisions of both p and \bar{p} beams. Figure 12 shows a schematic of the accelerator chain.

4.1.1 The proton source and acceleration

The protons used for collisions begin as hydrogen (H) atoms with an electron added to form H^- . The ions are accelerated to 750 keV/ c^2 and transferred to the Linac where they are accelerated to 400 MeV/ c^2 [52]. After acceleration in the Linac, the H^- ions are transferred to the Booster proton synchrotron [53] where the electrons are stripped and the protons

FERMILAB'S ACCELERATOR CHAIN

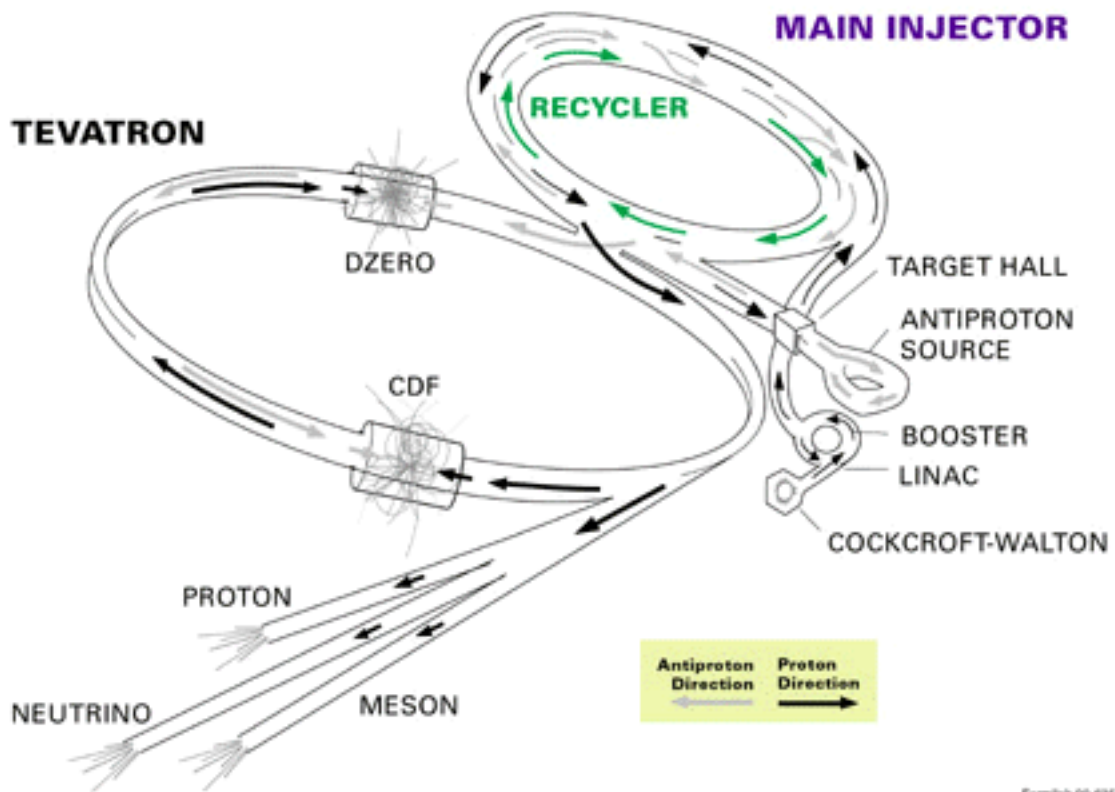


Figure 12: A schematic of the Fermilab accelerator chain showing the progression of protons and antiprotons used in the Tevatron.

are accelerated to an energy of $8 \text{ GeV}/c^2$. The protons are then transferred to the Main Injector [54], a synchrotron that accelerates the protons to $120 \text{ GeV}/c^2$, after which they are used for antiproton production or collisions in the Tevatron.

4.1.2 Antiproton production and acceleration

The production of antiprotons [55] begins with $120 \text{ GeV}/c^2$ protons from the Main Injector that are extracted and collided with a fixed nickel target. The shower of particles from the collisions are bent in a dipole magnetic field that selects $\sim 8 \text{ GeV}/c$ negative particles and sends them to the Debuncher. There the particles beams are cooled to reduce the beam size and momentum spread. The antiprotons are then transferred to the Accumulator where they collect until transfer to the Recycler, which is located in the same ring as the Main Injector, for long term storage. From the Recycler, the antiprotons can be transferred to the Main Injector and accelerated to $150 \text{ GeV}/c^2$ in preparation for injection into the Tevatron.

4.1.3 The Tevatron

The Tevatron [56] receives $150 \text{ GeV}/c^2$ proton and antiproton beams from the Main Injector. A given injection of beams into the Tevatron is called a store, and under typical operating conditions a store will circulate within the Tevatron for about 24 hours before the beams are dropped in preparation for injection of a new store. A new Tevatron store begins with the injection of protons from the Main Injector, followed by the injection of antiprotons. The beams are then accelerated from 150 to $960 \text{ GeV}/c^2$, also known as flattop. After acceleration the beams are tuned and scraped to minimize the beam losses and halos. Finally the beams are focused at the CDF II and D0 detectors to initiate collisions between the protons and antiprotons.

The rate of interactions depends on the luminosity of the beams, which is measured instantaneously and integrated over the course of a store. The formula for instantaneous luminosity is given as

$$L = f \frac{N_p N_{\bar{p}}}{A}. \quad (4.1)$$

N_p and $N_{\bar{p}}$ are the number of proton and antiproton particles, f is the revolution frequency, and A is the cross sectional area of the interaction region. The instantaneous luminosity has units of $\text{cm}^{-2}\text{s}^{-1}$. A typical store has an average instantaneous luminosity of $\sim 1 \times 10^{32} \text{ cm}^{-2}\text{s}^{-1}$ and an integrated luminosity of $\sim 5 \times 10^{36} \text{ cm}^{-2}$. The integrated luminosity for a typical store is $\sim 5 \text{ pb}^{-1}$ ($1 \text{ b} = 10^{-24} \text{ cm}^2$). The cross section for a given interaction type is expressed in barns, and cross section for B_c production is $\sim 5 \text{ nb}$. The expected number of B_c produced for a given integrated luminosity is simply the integrated luminosity multiplied by the cross section. For 1 fb^{-1} of integrated luminosity, $\sim 5 \times 10^6 B_c$ mesons are produced. The integrated luminosity delivered by the Tevatron to the CDF and D0 experiments is shown in Figure 13. The measurement discussed in this thesis uses the first 1 fb^{-1} of luminosity integrated between February 2002 and February 2006.

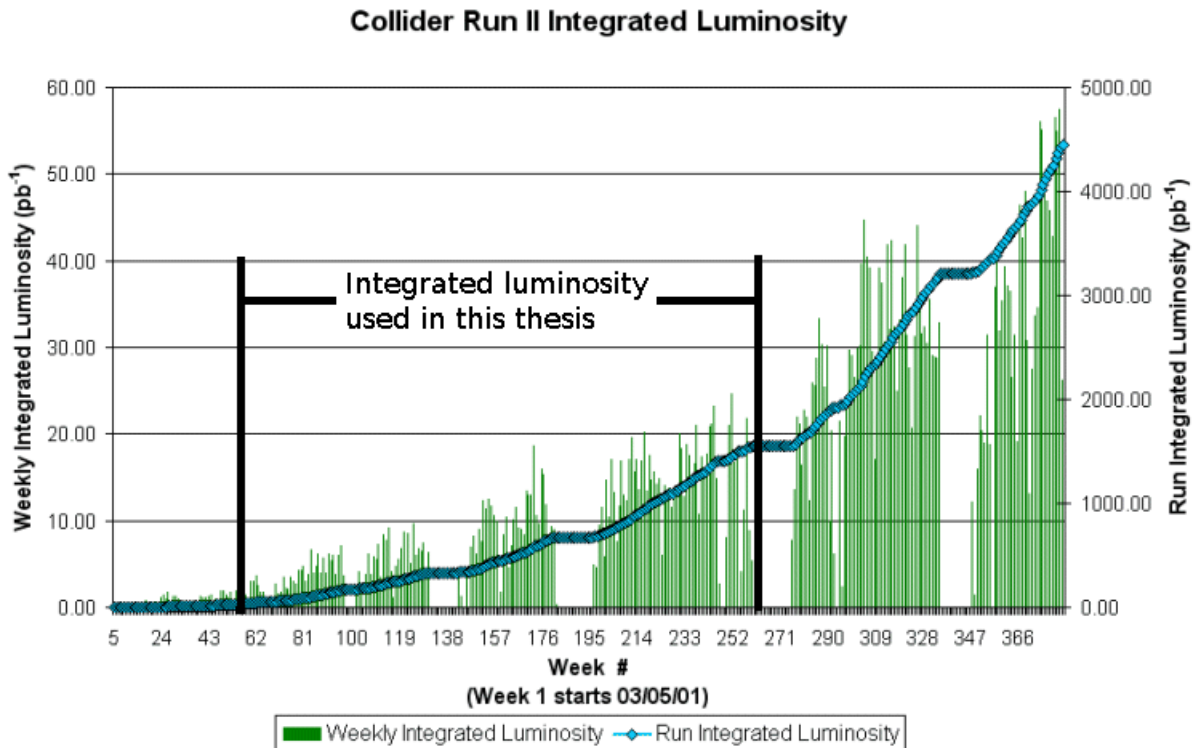


Figure 13: Integrated luminosity delivered by the Tevatron.

4.2 THE CDF II DETECTOR

Particles created in the Tevatron's $p\bar{p}$ collisions are measured by the CDF II Detector, which provides the data for this analysis. The CDF II is a multipurpose detector designed for tracking of charged particles, energy measurement of electromagnetically and strongly interacting particles, particle identification, and muon detection among other capabilities. Figure 14 shows an isometric view of the detector where subsystems used in this analysis have been labeled. The details of the detector subsystems are discussed in subsequent sections.

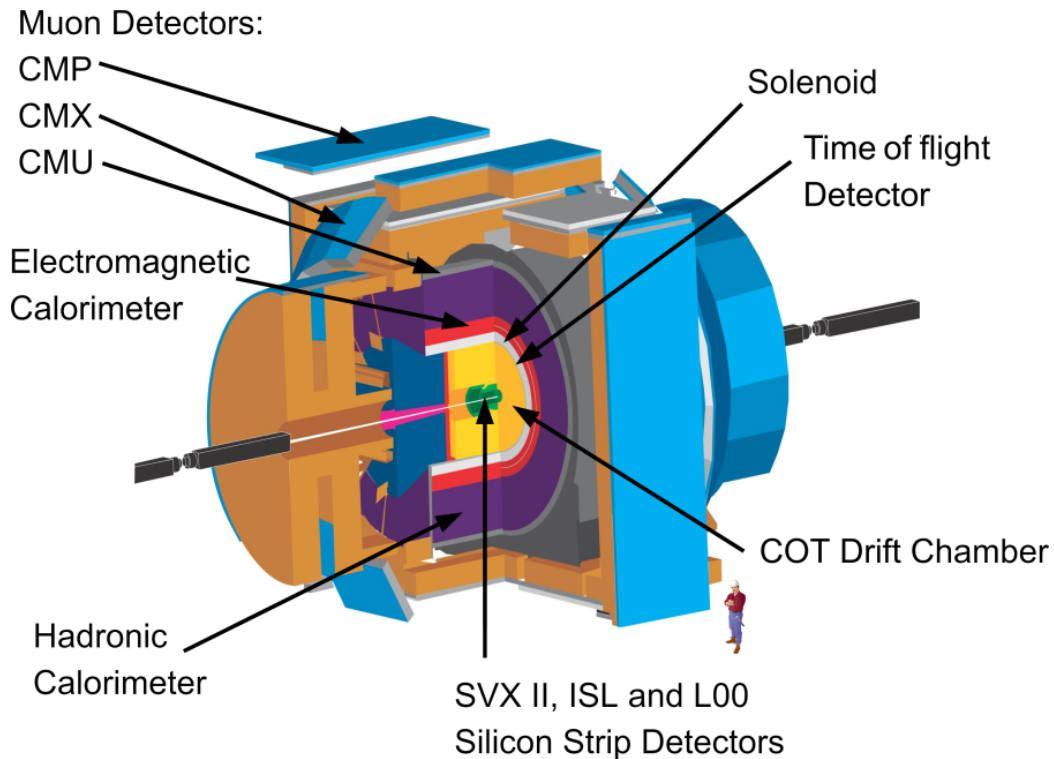


Figure 14: Isometric view of the CDF II detector. The detector components used in this thesis are labeled

The detector exhibits an approximate azimuthal symmetry around the axis defined by the direction of the beams, leading to the choice of coordinates r , ϕ , and η or z . The coordinates r and ϕ are the radius and angle in the plane perpendicular to the direction of

the beam. The coordinate η is the pseudorapidity and is defined as

$$\eta = -\ln\left[\tan\left(\frac{\theta}{2}\right)\right]. \quad (4.2)$$

Here, θ is the angle relative to the beam axis and $\theta = 0$ is the direction of the proton beam. Figure 15 illustrates the relationship between η and θ . In the limit of relativistic particles, the pseudorapidity approximates the rapidity of the particle which is

$$y = \frac{1}{2}\ln\left(\frac{E + p_L}{E - p_L}\right). \quad (4.3)$$

In some instances the Cartesian coordinates, where x and y describe the azimuthal plane perpendicular to the beam and z describes the beam axis and increases in value in the direction of the protons, are used to describe positions as well. The point of origin for all coordinates is the center of the detector.

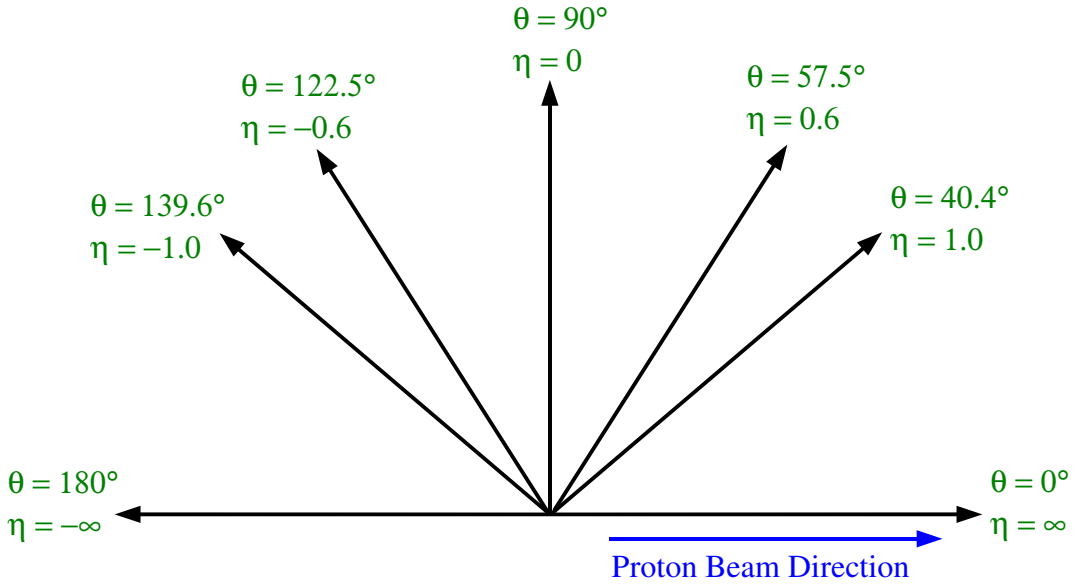


Figure 15: Illustration of the relationship between η and θ .

Typically particles of interest have momentum of ~ 1 GeV/c or greater. At the corresponding velocities, a number of particles will usually travel through the detector before

decaying. These "stable" particles include: π^\pm , K^\pm , K_L^0 , p^\pm , e^\pm , μ^\pm , and γ . Of particular interest are the trajectories of charged "stable" particles, which are tracked by the detector and used for the reconstruction events in this analysis.

4.2.1 Silicon strip detectors

Silicon strip sensors are solid state devices that make precision position measurements of ionizing particles as they pass through the sensor. The sensor consists of a silicon wafer with p-n junctions between the bulk and strips near the surface. The application of a bias voltage between the surfaces serves to increase the size of the depletion region of the p-n junctions, leaving the bulk depleted of free charge carriers. When a charged particle passes through the wafer, it excites electron hole pairs that separate and drift to the surfaces of the sensor where the charge is collected by the strips. The collected charge is typically amplified by amplifiers located on the sensor and read out by electronics that include a storage pipeline for the charge and convert the analog charge to a digital signal. The positions of the strips and the collected charge are used to construct "hits" that provide a position measurement of the particle in the coordinate perpendicular to the orientation of the strip.

The inner most detector subsystems of the CDF II Detector, the silicon strip detectors, make precision measurements of charged particle positions near the $p\bar{p}$ interaction point. The three silicon detector systems cover varying ranges of r : the layer 00 (L00) has a single detector layer at a radius of ~ 1.35 cm, the SVX II [57] consists of five layers between radii of ~ 2.5 and ~ 10.6 cm, and the intermediate silicon layers [58] (ISL) are 3 layers between radii of ~ 20 and ~ 29 cm. Measurements from the SVX II and ISL detectors are used in this analysis, and descriptions of these detectors follow.

The silicon detectors provide precise measures of charged particle trajectories (tracks). For particles with a momentum projected on the $r - \phi$ plane of $p_T = 2$ GeV/ c^2 , the measurement resolution of the particles impact parameter relative to the $p\bar{p}$ interaction point (including the uncertainty on the position of the interaction point) is ~ 45 μm when all silicon detector systems are used and ~ 65 μm when only the SVX II and ISL detectors are used [59]. The SVX II and ISL detectors also provide important z hits that help determine η

and the z momentum of tracks. In this analysis discussed in this thesis the silicon detectors provide precise measurements of decay vertices for B_c candidate events.

4.2.1.1 The SVX II detector The SVX II, the workhorse of the CDF II silicon trackers, consists of 5 layers of double sided silicon strip sensors arranged in concentric cylinders of increasing radius with a length of 90 cm in the z direction. Figure 16 shows the arrangement of the sensors in an azimuthal slice. The sensors have strip pitches ranging from $60 \mu\text{m}$ to $140 \mu\text{m}$ depending on radius. The double sided sensors have strips on both sides of the silicon to allow for two position measurements at each layer. All layers have strips parallel to the beam direction for ϕ measurements. Three layers have strips perpendicular to the z direction to measure z position, while the remaining two have small angle stereo strips that are tilted 1.2° relative to the ϕ strips. Hits in the small angle stereo sensors help remove the ambiguity involved in matching ϕ and z hits where there is more than one particle leaving hits in a given sensor.

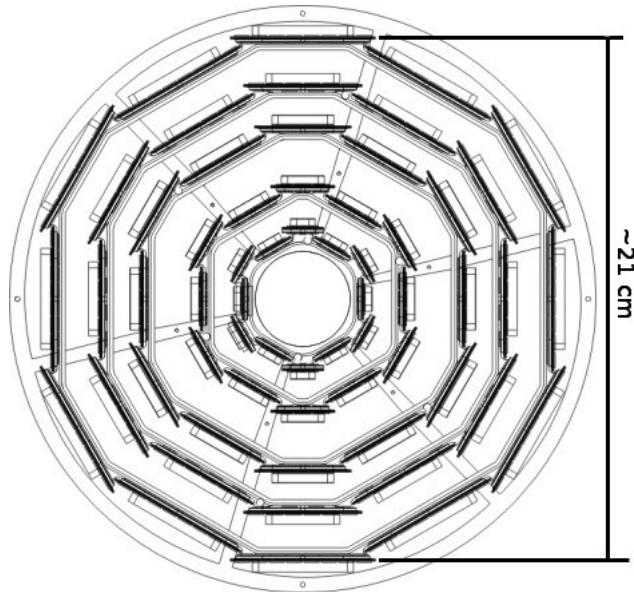


Figure 16: Arrangement of sensors in the five SVX II layers in an $r - \phi$ slice.

The SVX II is unique among the silicon detectors because its hits are read out and used as part of the trigger to identify events with displaced vertices. This feature and other features of the CDF II trigger are discussed in section 4.2.6.

4.2.1.2 The ISL detector The ISL detector serves as an extension of the SVX II to larger radius, and allows for better matching of hits between the silicon detectors and the central outer tracker (COT), a drifter chamber tracker that covers the r range beyond the silicon. As with the SVX II the ISL is approximately symmetric for rotations in ϕ . The arrangement of ISL layers relative to the SVX II can be seen in Figure 17. The ISL sensors are double sided with ϕ and 1.2° small angle stereo strips spaced with a pitch of $112 \mu\text{m}$.

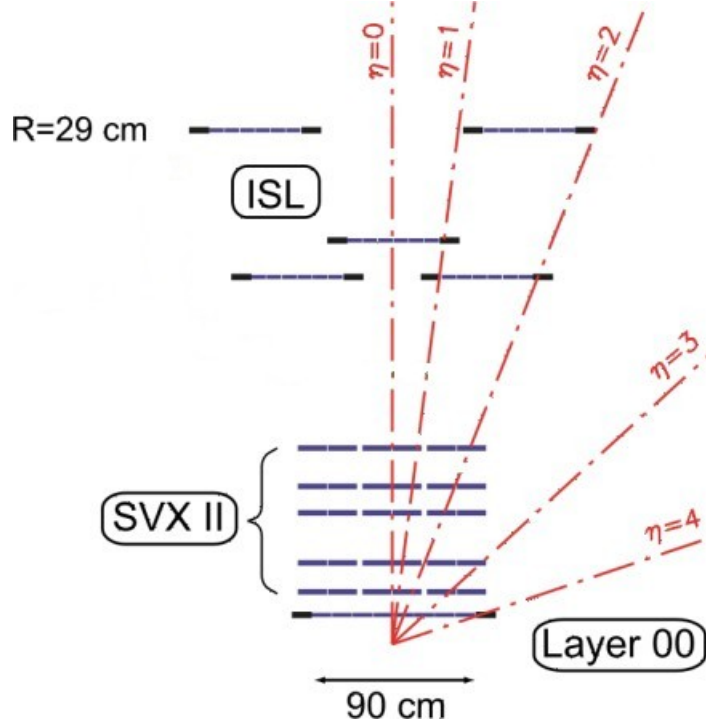


Figure 17: Radial and axial arrangement of silicon layers including the ISL.

4.2.2 The COT drift chamber

The COT [60] drift chamber, ranging $40 < r < 140 \text{ cm}$ and $|z| < 155 \text{ cm}$, collects electrons from the ionization of an argon/methane gas mixture by charged particles as they pass through the 1.4 T magnetic field in which the tracking detectors are immersed. Figure 18 shows the position of the COT relative to other detectors. The COT consists of potential wires, sense wires, and field sheets that span its 310 cm length arranged in super cells as illustrated in Figure 19. Voltages applied to the potential wires and field sheets create an

electric field configuration so the ionized charge collects on the sense wires. The collected charge is amplified and digitized by readout electronics before being sent to the data acquisition system. Half of the super cells within the COT are tilted at 2° relative to the z axis to give small angle stereo information, allowing for z position measurements. The remaining super cells are parallel to the z axis to give measurements of position in the $r - \phi$ plane. The super cells are arranged in 8 super layers that cover all ϕ values and increasing r values.

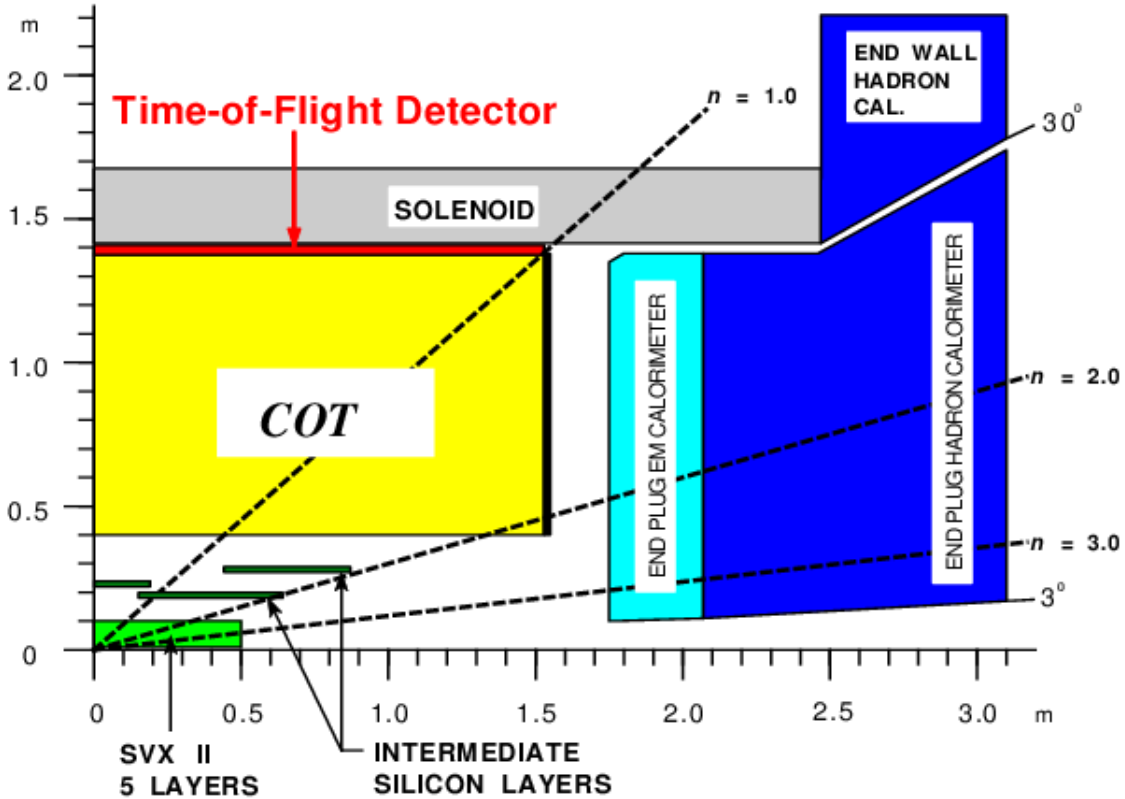


Figure 18: One quarter $r - z$ side view of the COT showing its position relative to other detectors.

The COT hits play the dominant role in measurements of particle momentum in the transverse direction, which is determined by the curvature of the particles path as it passes through the magnetic field. The transverse momentum p_T resolution has a p_T dependence described by

$$\delta p_T = 0.001 p_T^2. \quad (4.4)$$

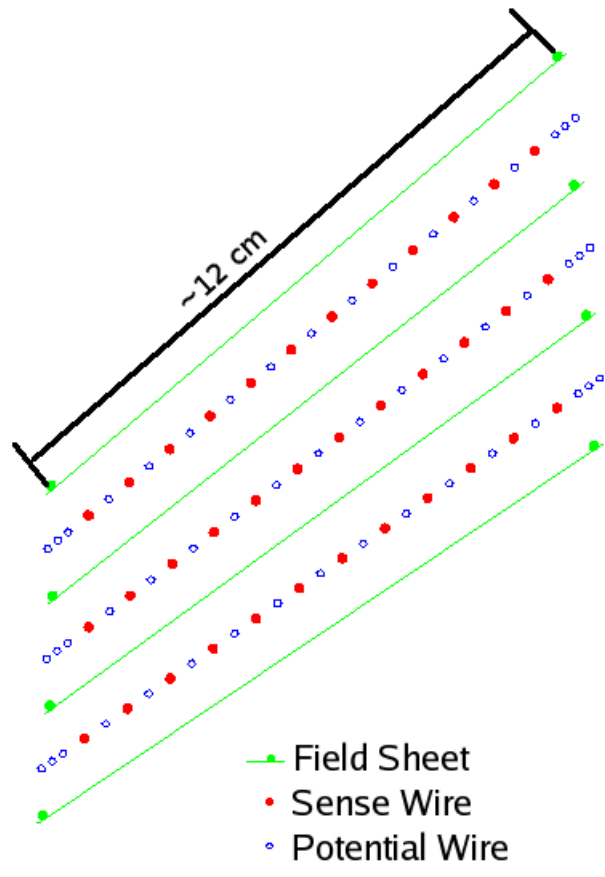


Figure 19: End view of three COT super cells.

The combination of z and small angle stereo hit information from the silicon detectors and the small angle stereo super layers also allows for the calculation of p_z from the polar angle θ and p_T :

$$p_z = p_T / \tan(\theta). \quad (4.5)$$

The COT hit information also contributes to the measurement of track positions near the interaction point, but such measurements are dominated by information from the silicon detectors.

In addition to measuring the position and momentum of charged particles as they pass through the detector, the COT also plays an important role in the identification of charged particles. Since the curvature of its trajectory in the magnetic field only reveals the particles momentum, additional information is needed to determine its mass. The Bethe-Bloch formula relates the energy loss per unit of distance traveled (dE/dx) of a charged particle passing through a medium to the properties of the medium and the velocity of the particle [61] and can be written as

$$dE/dx = \frac{4\pi N e^2}{m_e c^2 \beta^2} z^2 \left[\ln\left(\frac{2m_e c^2 \beta^2 \gamma^2}{I}\right) - \beta^2 - \frac{\delta(\beta)}{2} \right]. \quad (4.6)$$

N is the electron number density in medium, e is the electron charge, and m_e is the electron mass. z is the charge of incident particle, β is v/c of the incident particle γ is $1/\sqrt{1-\beta^2}$ of the incident particle, I is the mean excitation energy of atoms in the medium, and $\delta(\beta)$ is a correction for large β values.

Within the COT ionized charge is collected on the sense wires and converted to a digital signal, where the length of the digital pulse is related to the total charge. From a comparison of the pulse lengths the particle leaves as it travels through the detector, it is possible to measure its energy loss over a short distance. The energy loss measurements are usually compared to the expected value for a given particle type of a given momentum and divided by the measurement resolution to give a pull distributions with $\sigma \cong 1$ for a sample of particles of the same type. The resolution of the COT allows for a separation of 1.25σ between pions and kaons with momentums 2 GeV/c [62].

4.2.3 Time-of-flight detector

The time-of-flight (TOF) detector [63] consists of scintillator bars located just beyond the COT in r and contributes to particle identification. As with dE/dx , it is possible to extract the particle mass from the momentum by measuring the particle velocity. For the TOF detector this is done by measuring the time it takes for the particle to travel from the interaction vertex to the TOF detector:

$$m = \frac{p}{c} \sqrt{\frac{c^2 t^2}{L^2} - 1}. \quad (4.7)$$

Here, L is the distance traveled as determined by the tracking system, and t is the time of travel as measured by the TOF detector. The measured elapsed time t depends on t_0 , the nominal time of the $p\bar{p}$ interaction, and the measured time at which the scintillator fires. The time t has a number of corrections applied to achieve the timing resolution necessary for separating pions and kaons. The calibrated TOF system provides a resolution of ~ 100 ps [64] which corresponds to a separation of $\sim 1\sigma$ between pions and kaons at $p=3$ GeV/c.

4.2.4 Calorimetry

Beyond the tracking system and solenoid are the calorimeter systems which destructively measure the energy carried by particles from each interaction. In the central region, particles first encounter the central electromagnetic calorimeter (CEM) followed by the central hadronic calorimeter (CHA).

4.2.4.1 The CEM calorimeter The lead/scintillator CEM, which begins at $r = 1.7$ m and covers $z = \pm 2.5$ m, consists of 31 layers of 5 mm thick polystyrene scintillator interleaved with 30 layers of 1/8 in thick lead [65]. The CEM is arranged in towers that subtend 15° of ϕ and ~ 0.11 in η [8]. The light from the scintillators is collected by acrylic wave shifters and is transmitted through acrylic light guides to photomultiplier tubes located beyond the calorimetry. The CEM provides an energy resolution for electromagnetic showers of $\sigma_E/E = 0.14\sqrt{E}$.

The central preshower detector (CPR) is radially located before the central calorimeter and measures early particle showers. In this capacity it allows for better separation be-

tween pions and other particles [8]. Originally the CPR was a wire chamber, but in 2004 it was upgraded to the CPR2, a scintillator tile detector [66]. The central electromagnetic strip chamber (CES), located at the average position of maximum shower development between the eighth lead and ninth scintillator layers of the CEM, provides shower position measurements [65].

4.2.4.2 The CHA calorimeter The steel/scintillator CHA, with the same tower geometry as the CEM, contains the particle showers that penetrate beyond the CEM. It consists of 32 layers of 2.5 cm thick steel and 1.0 cm thick polystyrene scintillator [67]. The light collection, illustrated in Figure 20, is similar to that in the CEM. The CHA provides a depth of 4.7 radiation lengths for pions [68].

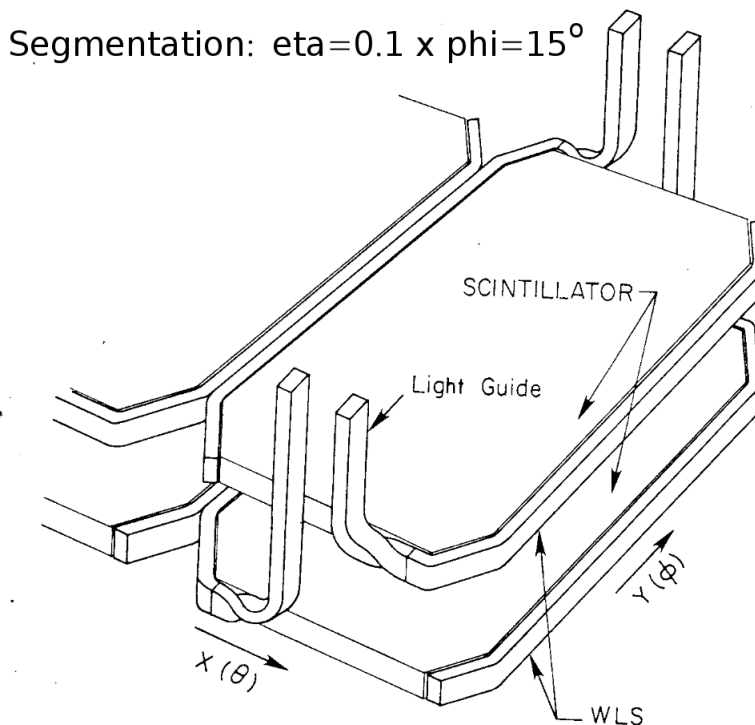


Figure 20: Diagram of wavelength shifters (WLS) and light guides for scintillator layers in the central hadronic calorimeter.

The hadronic and electromagnetic calorimetry provide measurements of the energy de-

posited as particles interact. In addition, the details of the showers created by the interacting particles can be used to identify certain particle types, such as electrons.

4.2.5 Muon detectors

Among the “stable” charged particles, the muons have the smallest cross section to interact with materials in the tracking and calorimeter. Hence, most muons survive to the region beyond the calorimetry with only some amount of multiple Coulomb scattering. For this reason, the outermost CDF II detectors in r are the muon detectors. These detectors match hits to tracks that are extrapolated from the tracking region. Since other types of particles usually do not survive to the muon detectors, hits in the muon detector can be used to identify the matching track as a muon.

4.2.5.1 The central muon detector The central muon detector [69] (CMU), installed at the outer radius of the central hadronic calorimeter wedges, covers $|\eta| < 0.6$ with 226 cm long 12.6° wedges covering the positive and negative z regions. Each wedge consists of 4 layers of 6.35×2.68 cm single wire drift cells containing a stainless steel $50 \mu\text{m}$ sense wire. The the cells are arranged with an offset between the first/third layers and the second/fourth layers, as shown in Figure 21, so the side of the cell through which the particle passes can be determined by the charge arrival times at the wires. The difference in arrival times allows for a measurement of the particles path in the $r - \phi$ plane using hits in the four layers. The CMU hits, which are called a stub, are matched to a track from the tracking system, and the slope of the stub relative to the radial direction gives an estimate the particles deflection due to the magnetic field, which is a measurement of the particles momentum. The z position of the stub is determined by comparing the charge collected at both z ends of the CMU cells.

4.2.5.2 The central muon upgrade detector The central muon upgrade detector (CMP) offers coverage in the same $|\eta| < 0.6$ as the CMU. Arranged in a box that surrounds the central region of the detector, the CMP consists of single wire drift cells stacked in four layers, much like the CMU. Since the CMP sits behind an additional 60 cm of steel, there

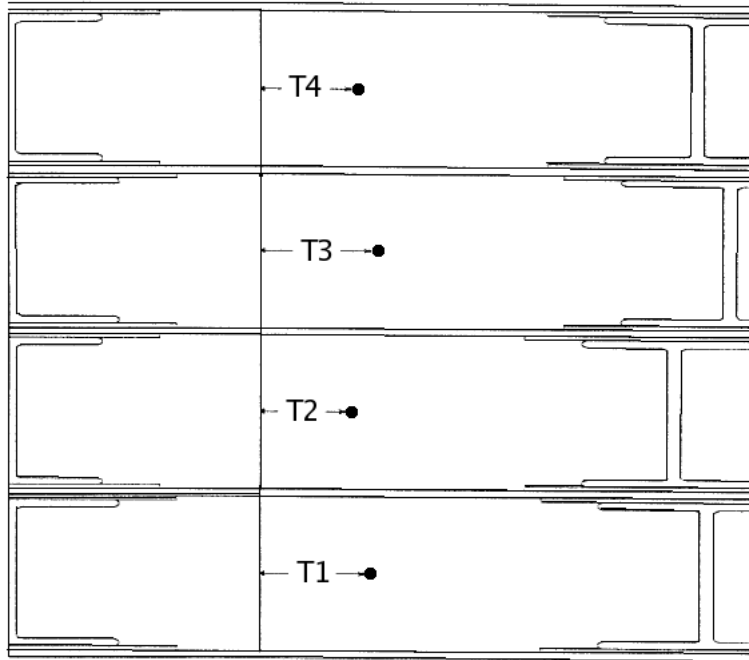


Figure 21: A $r - \phi$ slice of the CMU cells stacked within a CMU wedge. Notice the offset of the sense wire in layers 1 and 3 versus layers 2 and 4. The cells are 6.35×2.68 cm in height and width.

are considerably fewer kaons and pions that penetrate to the CMP compared to the CMU. The length of the CMP cells are constant, so the η coverage shows a ϕ dependence due to its box shape as Figure 22 illustrates.

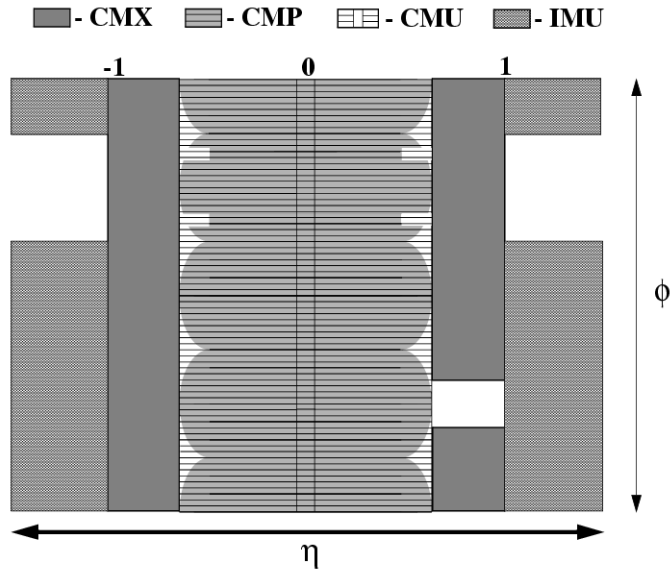


Figure 22: Pseudorapidity coverage of the muon detectors including the CMP. The ϕ dependence is due to the constant CMP length and its box shape.

4.2.5.3 The central muon extension The Central Muon Extension detector (CMX) extends the CDF II muon coverage to the $0.6 < |\eta| < 1.0$ region. The CMX consists of 4 layer stacks of single wire drift tubes arranged in ϕ wedges, similar to the CMU. Figure 23 shows the orientation and position of the CMX detector in a side view of the CDF II detector. There is no additional shielding added between the CMX and the interaction point as the long path through the calorimetry and the intervening detector supports offer sufficient shielding [8].

4.2.6 The CDF II trigger system

The Tevatron provides $p\bar{p}$ collisions at a rate of 2.7 MHz with a typical CDF II event size of ~ 200 kB. Since the CDF II detector only writes about 20 MB/s to tape, it is necessary to reject 99.995% of the $p\bar{p}$ collisions. This is accomplished by a three level trigger system

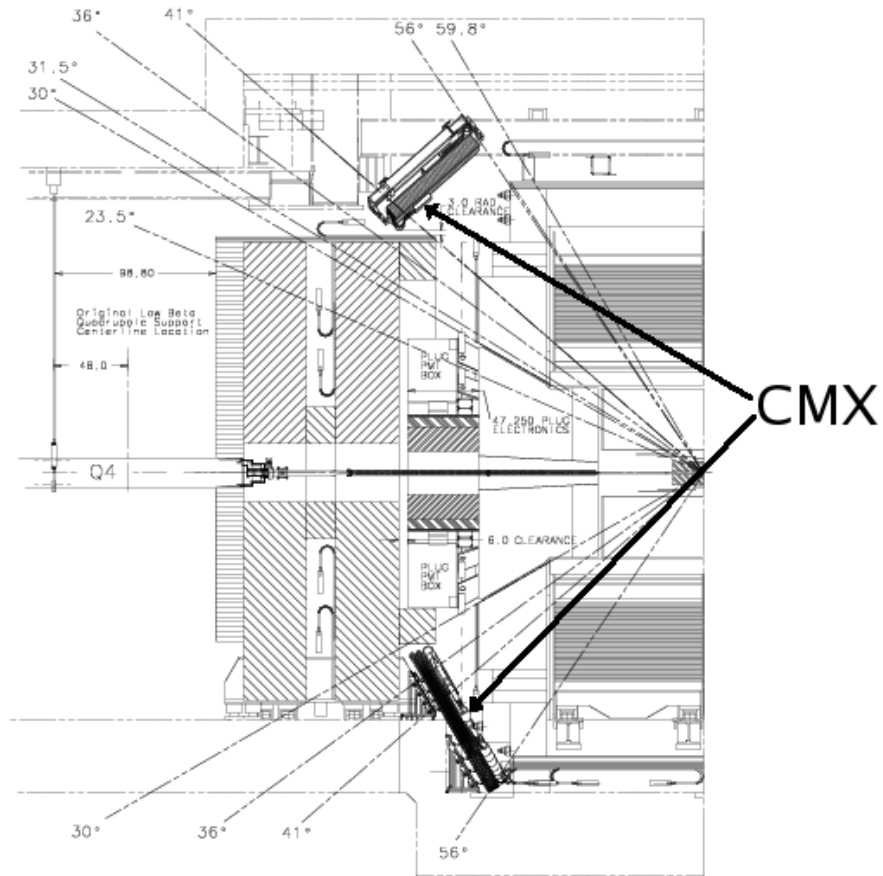


Figure 23: Side $r - z$ view of the CDF II detector showing the position and orientation of the CMX detector.

where the first two levels use dedicated hardware to choose or reject events and the third level uses a computer farm built with commercial computer hardware.

4.2.6.1 The level 1 trigger The level 1 trigger is a dedicated hardware trigger that makes decisions using information from the COT, calorimeters and muon detectors. The extremely fast tracker (XFT), a pattern recognition system for fast COT track reconstruction using dedicated hardware, provides the tracks for the level 1 trigger [70]. The decision time is fixed at 5 μ s, requiring a 42 buffer deep pipeline for the storage of events while decisions are made. The typical and the accept rate is ~ 20 kHz, and the maximum accept rate is 50 kHz. For the analysis discussed in this thesis, events originate from one of two level 1 triggers: two XFT tracks with $p_T > 1.5$ GeV/ c are matched with stubs in the CMU detector, or one XFT track with $p_T > 1.5$ GeV/ c is matched with a CMU stub while another with $p_T > 2.0$ GeV/ c is matched with a CMX stub.

4.2.6.2 The level 2 trigger After an event is accepted by the level 1 trigger, it is passed to the level 2 trigger [71]. The level 2 trigger uses the same information as the level 1 trigger with additional track position information in the form of the silicon vertex tracker (SVT). The SVT applies pattern recognition to SVX II silicon hits that are matched to XFT tracks and calculates impact parameters for tracks [72]. Events with displaced vertices are chosen by requiring SVT tracks with impact parameters that are not consistent with zero. For the case of the dimuon triggers used to collect signal candidates in this analysis, the SVT is not used at level 2, but SVT triggered events are used in some studies of related data samples in this analysis. The level 2 system typically has an output rate of 200-800 Hz.

4.2.6.3 Level 3 Trigger The level 3 trigger system [73] runs on standard computer hardware and uses reconstructed information from all parts of the CDF II detector. The typical output rate for level 3 is ~ 100 Hz. For the J/ψ trigger used in this analysis, there is very little additional selection applied by the level 3 trigger.

5.0 ANALYSIS PROCEDURE AND TECHNIQUES

The measurement of the B_c lifetime in $B_c^\pm \rightarrow J/\psi(\mu^+\mu^-) + l^\pm + X$ decays includes a number of steps, most of which address the non-ideal nature of the data used for the measurement. In the ideal situation, where the proper decay time of a B_c event can be measured perfectly with no background sources, the proper decay time distribution of an ensemble of events is described by an exponential decay law:

$$F(t) = \frac{1}{\tau} e^{-\frac{t}{\tau}}. \quad (5.1)$$

Here, τ is the average proper decay time of the events and $t > 0$. Figure 24 illustrates the ideal distribution along with distributions that model non-ideal effects seen in data including: unmeasured particles from the B_c decay chain that cause an incorrect measurement of the lorentz boost, detector measurement resolution effects, and the presense of backgrounds events.

A measurement of the lifetime must model all of the non-ideal effects in such a manner that a fit to the data can extract the true B_c average proper decay time (lifetime). Figure 25 illustrates the procedure for such a measurement. B_c candidates are selected using criteria that maximize the signal significance with some feedback from the evaluation of the systematic uncertainties in the analysis. The selection, which is discussed in detail in Chapter 6, chooses candidates events in which two muon candidates reconstruct to the mass of the J/ψ and a third lepton candidate appears to originate from the same vertex as the J/ψ . The lifetime model for B_c events, discussed in Chapter 8, accounts for unmeasured particles from the B_c decay and is determined using simulated B_c events. The backgrounds sources are identified and modeled using data where possible and simulated events otherwise. The backgrounds, which are discussed in detail in Chapter 7, are:

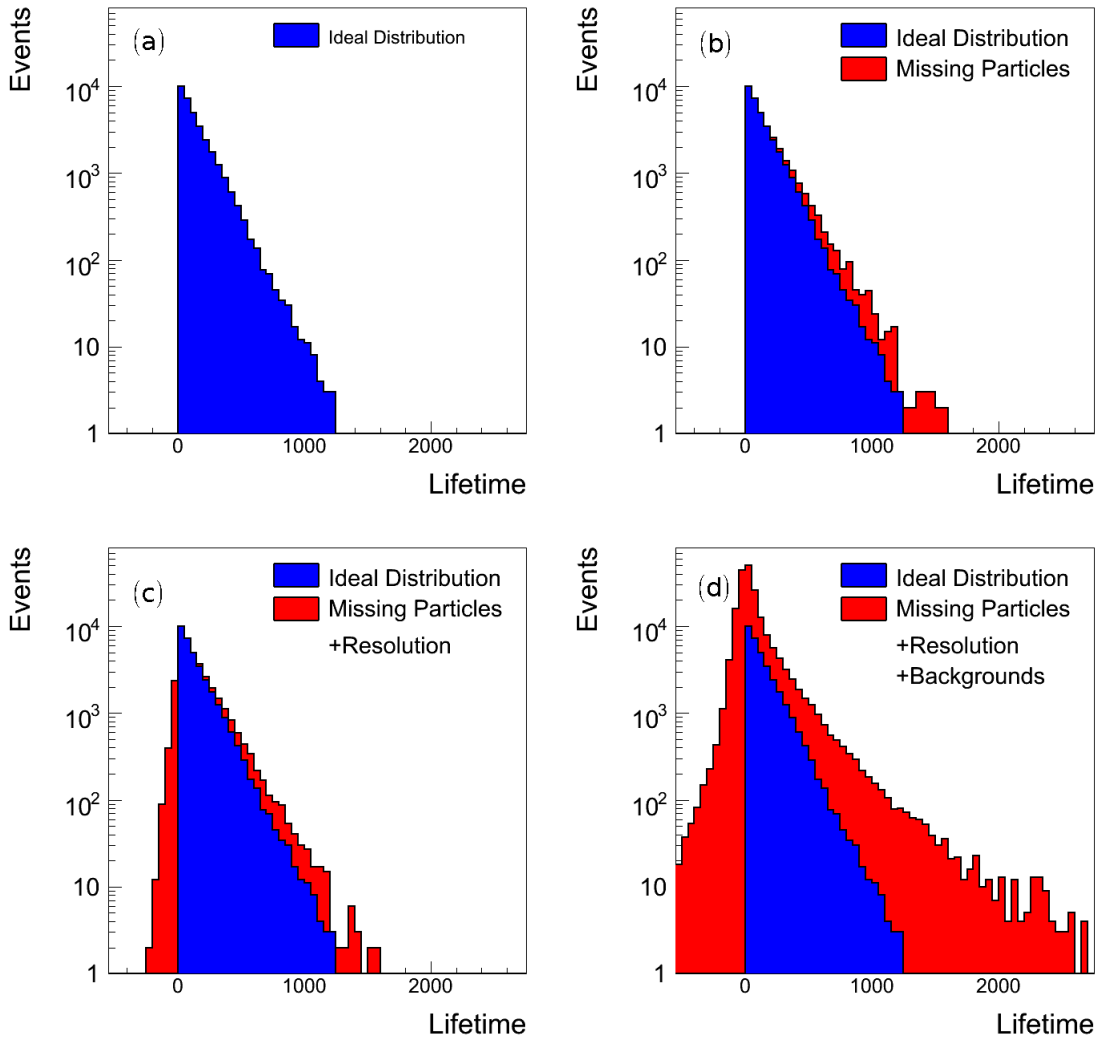


Figure 24: Evolution of the expected distribution of ct for B_c events as non-ideal effects are added. (a) An ideal distribution follows an exponential decay law. (b) Unmeasured particles from the B_c decay smear the distribution. (c) Additional smearing of the distribution is due to the detector measurement resolution. (d) The addition of background sources obscures the B_c events.

- Misidentified Leptons – The third lepton candidate is a hadron that is misidentified as a lepton.
- Misidentified J/ψ – The J/ψ candidate is the result of random combinations of particles or physics backgrounds such as Drell-Yan dimuon production.
- $b\bar{b}$ – The J/ψ and third lepton candidates originate from opposite b jets.
- Residual e^+e^- – Unique to final states with an electron, the electron candidate is produced when a photon converts or a light neutral meson decays to produce an e^+e^- pair.
- Prompt J/ψ – Additional prompt J/ψ candidates are present due to prompt charmonium production. If a lepton is produced as well, a $J/\psi + l$ candidate can be present.

The B_c signal model and background models are used to construct a lifetime fitter that is applied to the selected signal candidates in data to measure the lifetime, as described in Chapter 9. Systematic uncertainties are evaluated in Chapter 10 using variations in the signal and background models, with a feedback to event selection to allow for the minimization of systematic uncertainties.

The various steps in the analysis are carried out using a number of experimental techniques and procedures that are outlined in the following sections.

5.1 PER EVENT PROPER DECAY TIME MEASUREMENTS

A measurement of the average lifetime of the B_c must begin with a definition of the per event quantities that can be measured and used to measure the average lifetime. As discussed in the previous chapter, particles passing through the detector have their track trajectories measured by the silicon and COT detectors. Ignoring energy loss, the trajectory is described by a helix, where the curvature is a measurement of the particles p_T . The parameters describing the helix are:

- d_0 – the distance of the closest approach to the z axis
- z_0 – the z position at the closest approach to the z axis

Data for Measurement Modeling Signal and Background

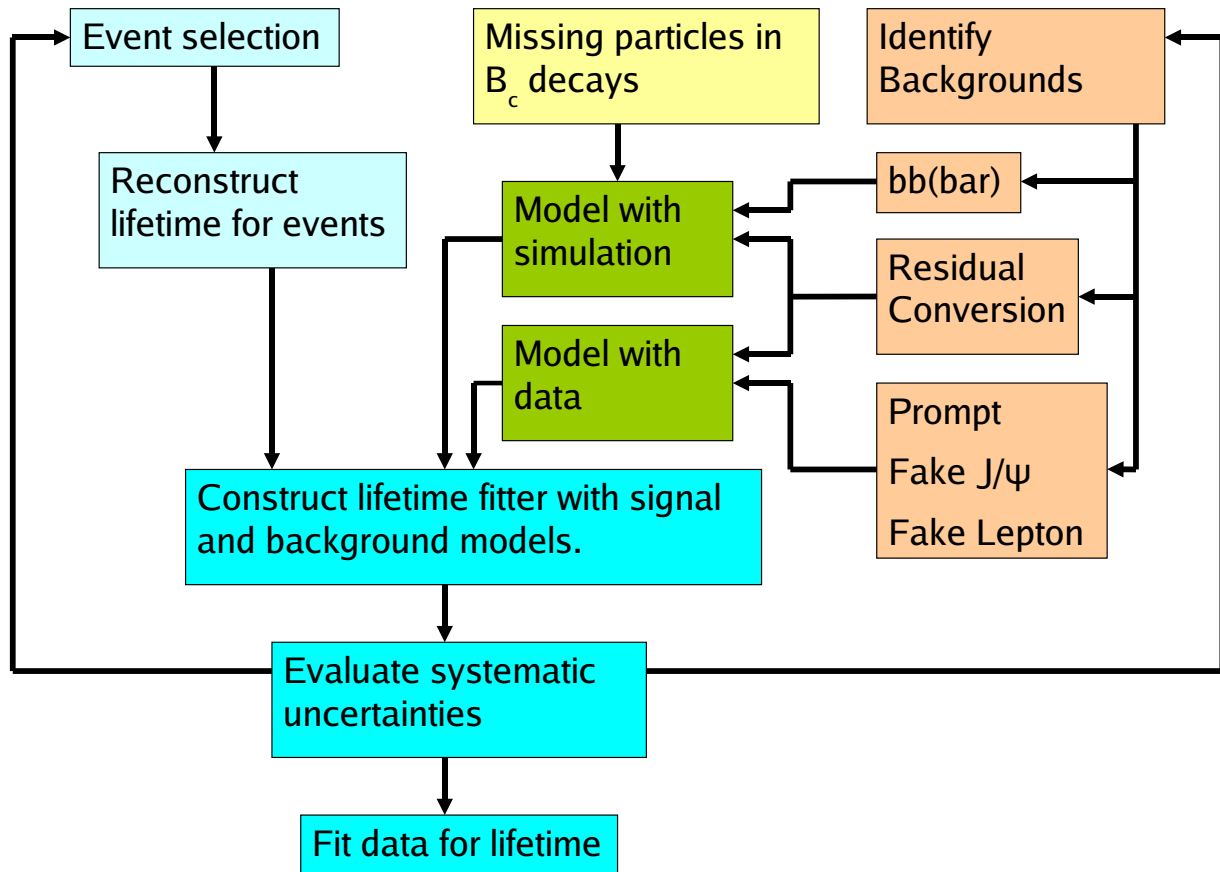


Figure 25: Diagram showing a simplified flow of the measurement procedure.

- ϕ_0 – the azimuthal angle describing the direction of the track at the closest approach to the z axis
- $\cot(\theta)$ – the cotangent of the polar angle describing the track direction
- C – The curvature of the track which is the inverse of the radius of the trajectory in the $r - \phi$ plane

The helix parameters are determined by fits to hits within the silicon and COT detectors, and a corresponding error matrix describes the uncertainty in these parameters. Given a particle type hypothesis for a track, it is refitted, accounting for energy loss in the tracking volume [74].

For two or more tracks, it is possible to define a vertex when the tracks intersect within a reasonable interval of their measured uncertainties. For a real particle, the vertex describes the position in the detector at which the particle decays into other particles. The uncertainty on the vertex position is determined by propagating the uncertainties for the parameters that describe the helices of the individual tracks.

Measuring the proper decay time of a particle requires knowledge of the point of origin as well as the point of decay. When particles originate from the primary $p\bar{p}$ interaction point, a precise measurement of the interaction point gives the particle’s point of origin. The beamline, the path the p and \bar{p} beams take through the detector is stable over short periods of time and is fitted using minimum bias triggered events where the primary vertices are reconstructed from tracks in the event [75]. A precise measure of the x and y position of the primary vertex in a given event is determined by the beamline position at the z position of the tracks of interest in the event. Even if the tracks of interest originate from a displaced vertex, a B_c^\pm decay for example, the determined x and y position of the interaction point shows negligible bias since the slope of the beamline relative to the z axis is quite small.

With methods for measuring the distance traveled by particles before decaying and the momentum of the “stable” decay products, it is possible to reconstruct the proper time the particle survives before decaying to “stable” particles. From relativistic kinematics, the displacement of a particle before decaying (over a short distance where the trajectory can

be approximated by a straight line), its momentum, and its proper decay time are related:

$$m \frac{\vec{X}_{dv} - \vec{X}_{pv}}{t} = \vec{P}. \quad (5.2)$$

Here, the momentum and displacement are measured in the same frame, the lab frame. The subscripts dv and pv stand for the displaced and primary vertices. The vector and magnitude of the transverse component of the momentum are defined as \vec{p}_T and p_T respectively. Taking the dot product of both sides of the equation with the transverse momentum vector and then dividing by the magnitude yields

$$m \frac{(\vec{X}_{dv} - \vec{X}_{pv}) \cdot \vec{p}_T}{p_T t} = p_T. \quad (5.3)$$

For real particle decays, the transverse distance traveled before decaying in the lab frame can be written as $L_{xy} = (\vec{X}_{dv} - \vec{X}_{pv}) \cdot \vec{p}_T / p_T$ since the momentum and displacement vectors are in the same direction. Therefore, the proper decay length for the particle, ct , using the measured quantities L_{xy} and p_T and the particle's mass is written as

$$ct = \frac{mcL_{xy}}{p_T}. \quad (5.4)$$

For the specific case of $B_c^\pm \rightarrow J/\psi + l^\pm + X$ decays, the unmeasured particles in the decay, X , mean that the momentum of the B_c is not fully reconstructed. It is necessary to define a pseudo-proper decay length ct^* in terms of the transverse momentum of the measured particles, $p_T(J/\psi l)$:

$$ct^* = \frac{M(B_c)c(\vec{X}_{dv}(J/\psi l) - \vec{X}_{pv}) \cdot \vec{p}_T(J/\psi l)}{p_T(J/\psi)} \cdot \frac{\vec{p}_T(J/\psi l)}{p_T(J/\psi l)}. \quad (5.5)$$

In this case the L_{xy} and p_T are defined using the three track, $J/\psi l$ vertex, and ct^* is can be written as

$$ct^* = \frac{M(B_c)cL_{xy}(J/\psi l)}{p_T(J/\psi l)}. \quad (5.6)$$

The missing momentum also precludes fully reconstructing $M(B_c)$ for each event, so the value determined from exclusive $B_c^\pm \rightarrow J/\psi + \pi^\pm$ decays, $6.2756 \pm 0.0029(stat.) \pm 0.0025(syst.)$ GeV/ c^2 [43], is used instead. Given that the three track vertex is the B_c decay position, ct^*

can be related to ct by correcting for the difference in the three track p_T and the p_T of the B_c^\pm meson. A factor K is defined to account for the missing particles and relates ct to ct^* :

$$ct^* = ct \times \frac{\vec{P}(B_c)}{p_T(J/\psi l)} \cdot \frac{p_T(J/\psi l)}{p_T(J/\psi l)} = \frac{ct}{K}. \quad (5.7)$$

K cannot be measured using the data and must be determined from a realistic Monte Carlo simulation of expected signal events.

5.2 PER EVENT DETECTOR RESOLUTION

In addition to measuring a per event ct^* it is also possible to measure the uncertainty of the ct^* measurement for each event, σ_{ct^*} , by propagating the uncertainties on the L_{xy} and p_T measurements. Given an ideal probability distribution for ct^* with no detector resolution effects, $F_{ideal}(ct^*)$, one expects the measured distribution to exhibit a smearing that depends on σ_{ct^*} :

$$F_{meas}(ct^*, \sigma_{ct^*}) = F_{ideal}(ct^*) \otimes G(ct^*, \sigma_{ct^*}; s_1..s_n). \quad (5.8)$$

Here, $G(ct^*, \sigma_{ct^*}; s_1..s_n)$ is the resolution function and is typically modeled by the sum of one or more Gaussian distributions with widths that depends on σ_{ct^*} and parameters $s_1..s_n$ that scale the σ_{ct^*} for each Gaussian component. In this analysis, a single Gaussian is used to model the resolution and that choice is studied as part of the systematic uncertainty evaluation.

5.3 B_c LIFETIME DISTRIBUTION

As discussed previously, the ct^* of signal events can be related to ct by a factor K which can only be determined for signal events in a Monte Carlo simulation of B_c decays. Since the measured quantity is ct^* , it is necessary to formulate the probability distribution of ct^* in B_c decays such that it is parameterized by the average lifetime τ . Beginning with the ideal

decay law the effect of unmeasured particles is added using the K factor distribution from the Monte Carlo signal events. The decay law is

$$F_{B_c}(ct) = \frac{1}{c\tau} e^{-\frac{ct}{c\tau}}. \quad (5.9)$$

If $H(K)$ is the distribution of K factors from the Monte Carlo, the probability distribution for ct^* depends on $H(K)$ and is parameterized by τ :

$$F_{B_c}(ct^*) = \int dK H(K) \frac{K}{c\tau} e^{-\frac{Kct^*}{c\tau}}. \quad (5.10)$$

The distribution is also smeared to account for detector resolution:

$$F_{B_c}(ct^*, \sigma_{ct^*}) = \int dK H(K) \frac{K}{c\tau} e^{-\frac{Kct^*}{c\tau}} \theta(ct^*) \otimes G(ct^*, \sigma_{ct^*}; s). \quad (5.11)$$

5.4 FITTING DATA

The analysis procedure requires fitting models to data for the purpose of constraining background models and eventually extracting a value for the average B_c lifetime. Unless otherwise specified, all fits are carried out using the unbinned maximum likelihood method outlined here.

Suppose a background shows a ct^* distribution that can be described by the probability distribution function (PDF) $F(ct^*, \sigma_{ct^*}; P_0, P_1, \dots, P_n)$, where P_0, P_1, \dots, P_n are parameters that must be determined by a fit to the data. If there are N events in the sample used to model the background, the likelihood is defined as

$$L = \prod_{i=1}^N F(ct_i^*, \sigma_{ct_i^*}; P_0, P_1, \dots, P_n). \quad (5.12)$$

Since the likelihood will be maximized, it is important that the probability function is normalized so the maximum cannot change by adjusting the normalization. One typically works with $-2\ln(L)$:

$$-2\ln(L) = -2 \sum_{i=1}^N \ln[F(ct_i^*, \sigma_{ct_i^*}; P_0, P_1, \dots, P_n)]. \quad (5.13)$$

This quantity is minimized while varying the parameters to give the values that best describe the sample. Typically the minimization is carried out with the MIGRAD or MINOS algorithms from the MINUIT fitting software [76]. In addition to providing best values for $P_0..P_x$, the fit also provides an error matrix that describes the uncertainties for the parameter values, including their correlations.

A number of extensions and refinements of the fitting procedure are discussed here.

5.4.1 Fitting weighted events

In some cases the fitted events need to be weighted by some efficiency $\epsilon(ct^*)$ that depends on the variable that is being fitted. Since the likelihood method involves a product over the unweighted events, it is necessary to write the unweighted probability distribution in terms of the distribution for weighted events, $F_W(ct^*)$, and the inverse of the efficiency:

$$L = \prod_{i=1}^N \frac{A(P_0, P_1, \dots, P_n)}{\epsilon(ct_i^*)} F_W(ct_i^*, \sigma_{ct^*i}; P_0, P_1, \dots, P_n). \quad (5.14)$$

Here A normalizes the weighted PDF divided by the efficiency to give the normalized unweighted PDF. If $\epsilon(ct^*)$ is determined beforehand, a fit of the unweighted events in such a matter determines P_0, P_1, \dots, P_n for the weighted distribution.

5.4.2 Propagating parameters and errors

Often it is necessary to propagate parameters determined by one fit into another. An example of this is fitting a background component using sidebands and then propagating the background model into a fit of the signal region. In this situation, the likelihood function includes a term to constrain the parameters from the previous fit:

$$L = e^{-\frac{1}{2} P_{bg}^T C_{bg}^{-1} P_{bg}} \prod_{i=1}^N F_{sig}(ct_i^*, \sigma_{ct^*i}; P_0, P_1, \dots, P_n) + F_{bg}(ct_i^*, \sigma_{ct^*i}; P_0^{bg}, P_1^{bg}, \dots, P_m^{bg}). \quad (5.15)$$

P_{bg} is a vector containing the differences between the previously measured values of the parameters and the values in the current fit, $(\bar{P}_m^{bg} - P_m^{bg})$. C_{bg} is the covariance matrix, the square of the error matrix that describes the uncertainties for the parameters \bar{P}_m^{bg} . When

$-2\ln(L)$ is evaluated, the parameter constraint becomes an additive quadratic term that is minimal for no change in the parameters. The parameters, however, can be adjusted from the previously fitted values if the increase in the quadratic constraint is smaller than the decrease in the rest of the likelihood function.

5.4.3 Extended likelihood fits

Components of the PDF in likelihood fits should be normalized such that their sum cannot grow arbitrarily, otherwise the fitter will do just that. This can be done by normalizing each component to integrate to 1 and multiplying components by parameters that are defined to be fractions that sum to 1. An example is

$$L = \prod_{i=1}^N [f_1 F_1(x_i) + (1 - f_1)(f_2 F_2(x_i) + (1 - f_2)F_3(x_i))]. \quad (5.16)$$

In this instance the parameters f_1 and f_2 are constrained to values between 0 and 1 and the multiplicative factors for F_1 , F_2 , and F_3 sum to 1 by definition. Another approach for constraining the normalization is the extended likelihood method where the likelihood is written in terms of absolute normalizations:

$$L = \frac{N^{(N_1+N_2+N_3)} e^{-N}}{(N_1 + N_2 + N_3)!} \prod_{i=1}^N [N_1 F_1(x_i) + N_2 F_2(x_i) + N_3 F_3(x_i)]. \quad (5.17)$$

Each component is normalized by the total number of events N_1 , N_2 , and N_3 , and the likelihood includes a Poisson constraint of the fitted number of events $N_1 + N_2 + N_3$ to the total number of events N seen in the sample being fitted.

5.4.4 Probability Distribution for σ_{ct^*}

As discussed previously, the PDFs that describe ct^* include smearing functions that depend on σ_{ct^*} . For fits with more than one component, it may be the case that the distribution of σ_{ct^*} varies for the various components. In such a case it is necessary to include the PDF for σ_{ct^*} in the fit or a bias may be introduced [77]. An example is

$$L = \prod_{i=1}^N [f_1 E_1(\sigma_{ct_i^*}) F_1(ct_i^*, \sigma_{ct_i^*}) + (1 - f_1) E_2(\sigma_{ct_i^*}) F_2(ct_i^*, \sigma_{ct_i^*})]. \quad (5.18)$$

Here, E_1 and E_2 are the σ_{ct^*} PDFs of the two components. The form of $E(\sigma_{ct_i^*})$ is determined by a separate fit to the $\sigma_{ct_i^*}$ distribution only.

5.5 LIKELIHOOD RATIO METHODS

It is often necessary to differentiate between two classes of events based on detector information. Where the classes are identified using more than one measured quantity, a likelihood ratio can be constructed to combine multiple measurements into a single quantity that discriminates between the classes of events. For example, assume one wants to differentiate between signal S and background B events using the measured quantities x_0, x^1, \dots, x_n which have been chosen because the distribution for signal and background events differs for each measured quantity. The probability distributions for the measured quantities, $S_0(x_0), S_1(x_1), \dots, S_n(x_n)$ for signal events and $B_0(x_0), B_1(x_1), \dots, B_n(x_n)$ for background events, are determined using samples of the signal and background types of events. The likelihood ratio is defined in a related sample for a given event:

$$L = \frac{\prod_{j=0}^n S_j(x_j)}{\prod_{j=0}^n S_j(x_j) + \prod_{j=0}^n B_j(x_j)}. \quad (5.19)$$

For signal events, the likelihood ratio will tend towards a value of 1, and the purity of signal events can be enhanced by rejecting events with a likelihood ratio below a given value.

5.6 MONTE CARLO SIMULATIONS

When it is not possible to isolate samples of events using data, simulated events are used. The Monte Carlo simulations used in this analysis are created by generating particles produced in $p\bar{p}$ collisions and simulating the decays and interactions of the particles as they pass through the CDF II detector.

Two separate programs provide differing levels of sophistication while generating the particles produced in $p\bar{p}$ collisions. PYTHIA [37] models the physical processes of $b\bar{b}$ production in $p\bar{p}$ collisions, including $2 \rightarrow 2$ processes with initial and final state radiation. The b quark fragmentation to form B mesons and jets is carried out using the phenomenological Lund string model [32]. BGENERATOR [78] offers an alternative and simpler approach to the generation of B mesons. Instead of generating $b\bar{b}$ and modeling the fragmentation, BGENERATOR takes as its input a p_T and η spectrum of the B meson and generates the mesons directly. This simple approach allows for much faster generation of events, but the events are less realistic as they do not include fragmentation particles and the correlations between the two b jets is not properly modeled.

Short lived particles (particles that typically decay before interacting with detector material) are decayed according to decay tables by the EVTGEN program [79]. The decay tables include the branching fractions for a given particle to decay to a given final state as well as the physics model to use in the decay. The branching fractions are measured quantities where available and theoretical predictions where measurements have not yet been made.

Particles that live long enough to pass through the detector have their interactions with the detector simulated by the CDFSIM program [80]. This program uses GEANT3 [81] to simulate particle interactions with the detector material. The performance of the simulation is tested by comparing the simulated detector response to what is seen in data and found to be in good agreement with data [82]. In addition to simulating the detector response, the selection of events by the trigger is simulated [83].

6.0 $J/\psi + l^\pm$ CANDIDATE SELECTION

The $J/\psi + l^\pm$ candidate events are selected using a number of criteria, consisting of cuts on measured quantities chosen to maximize the number of signal events S relative to background events B and minimize the systematic uncertainties of the average lifetime measurement. The J/ψ decaying to two oppositely charged muons provides a clean channel for identification of J/ψ candidates and the offline selection criteria for the J/ψ are largely determined by the dimuon trigger. The selection of the third lepton candidates and the properties of the three track system require more detailed studies to determine the optimal balance between signal versus background and to minimize systematic uncertainties. Since two final states are studied, $J/\psi + e^\pm$ and $J/\psi + \mu^\pm$, the candidates are split into two samples with similar, but different selection criteria. From this point forward the final states are referred to as the electron channel and muon channel.

In the process of defining the event selection, Monte Carlo simulation samples of B_c signal and $b\bar{b}$ background events are used to evaluate the efficiency of cuts. A description of these samples can be found in Appendix A. Data samples of conversion electrons and pions from $D^0 \rightarrow K\pi$ decays are also used while optimizing cuts, and a description of those samples is given in Appendix B.

6.1 J/ψ SELECTION

Interactions are selected by the J/ψ dimuon trigger that includes a number of trigger paths, all of which select two oppositely charged muon candidates with an invariant mass close to the J/ψ mass. For this analysis, the two trigger paths with the highest rates are used:

1. CMUCMU1.5 Path – This path selects events with two oppositely charged $p_T > 1.5$ GeV/ c XFT tracks that are matched to $p_T > 1.5$ GeV/ c CMU stubs. The stub matching requires the position of the track extrapolated to the CMU radius to be within 30 cm of the CMU stub. The two muon candidates are required to have $\Delta\phi < 120^\circ$ and invariant mass between 2.7 and 4.0 GeV/ c^2 .
2. CMU1.5_CMX2 Path – This path requires one XFT track with $p_T > 1.5$ GeV/ c that matches a $p_T > 1.5$ GeV/ c CMU stub and an oppositely charged XFT track with $p_T > 2.0$ GeV/ c that matches a $p_T > 1.5$ GeV/ c CMX stub. The CMU stub matching is the same as for the CMUCMU1.5 path, while the CMX matching requires the extrapolated track to be within 50 cm of the stub. The $\Delta\phi$ and invariant mass requirements are the same as the CMUCMU1.5 path.

The offline selection of $J/\psi \rightarrow \mu^+\mu^-$ candidates is summarized in Table 7. The first five entries match the trigger selection and ensure the J/ψ candidate includes the trigger tracks. The remaining cuts either minimize backgrounds or improve the quality of the tracks that make the J/ψ candidate. A detailed description of the most important cuts follows.

Selection Requirement	Value
Two Muons	CMU+CMU or CMU+CMX, opposite charge
Trigger Confirmation	J/ψ legs for muon channel candidates only
Trigger Path Selection	CMUCMU1.5 or CMU1.5_CMX2 Trigger Path
CMU Muon p_T	> 1.5 GeV/ c
CMX Muon p_T	> 2.0 GeV/ c
Muon Likelihood	> 0.06
COT Hits	2 Stereo + 2 Axial Super layers (5 hits each SL)
Silicon Hits	≥ 3 hits in ϕ layers (SVX+ISL)
J/ψ Mass	$ M_{J/\psi} - 3.09687 \text{ GeV}/c^2 < 0.05 \text{ GeV}/c^2$

Table 7: Cuts applied to dimuon J/ψ leg candidates or the two particle J/ψ system to select J/ψ candidates.

6.1.1 Trigger and trigger path confirmation

Since the candidate selection requires a third muon for the muon channel, care is taken to ensure the presence of the third muon was not required for the event to pass the trigger. One type of muon channel background consists of events where a hadron is misidentified as a muon. If one of the J/ψ muons does not satisfy the trigger requirements, the likelihood of selecting the event will increase if the event contains a hadron misidentified as a muon. This scenario, illustrated in Figure 26, introduces a bias in the hadron misidentification probability that is used to model this background (see Section 7.2). By requiring that the J/ψ legs are sufficient for the event to pass the trigger, any possible bias is avoided. This is done by verifying that the track and stub information of the offline J/ψ muons match the triggered objects for each event. Since this bias does not exist where the third track is an electron, the trigger confirmation is not applied for electron channel candidates.

In addition to the CMUCMU1.5 or CMU1.5_CMX2 paths described above, the trigger includes lower frequency paths that generally have higher p_T requirements for the muons. If an event were to pass one of these other paths while failing the two higher frequency paths, trigger confirmation becomes considerably more complicated. To avoid this complication, each event must pass either the CMUCMU1.5 or CMU1.5_CMX2 trigger path.

6.1.2 Muon likelihood for J/ψ legs

CDF Note 7043 [84] describes a method developed by CDF collaborators for calculating a likelihood ratio for identifying muon candidates detected by the CMU and CMX detectors. The likelihood ratio uses five measured quantities:

1. $\Delta(r\phi)$ – the azimuthal separation between the muon stub and extrapolated track positions at the muon chamber in units of distance
2. $\Delta\phi$ – the opening angle between the direction of the extrapolated track and the muon stub projected onto the $r - \phi$ plane
3. ΔZ – the separation between the z position of the extrapolated track and muon stub
4. E_{em} – the energy deposited in the electromagnetic calorimeter by the muon candidate
5. E_{had} – the energy deposited in the hadronic calorimeter by the muon candidate

Trigger Bias Scenario

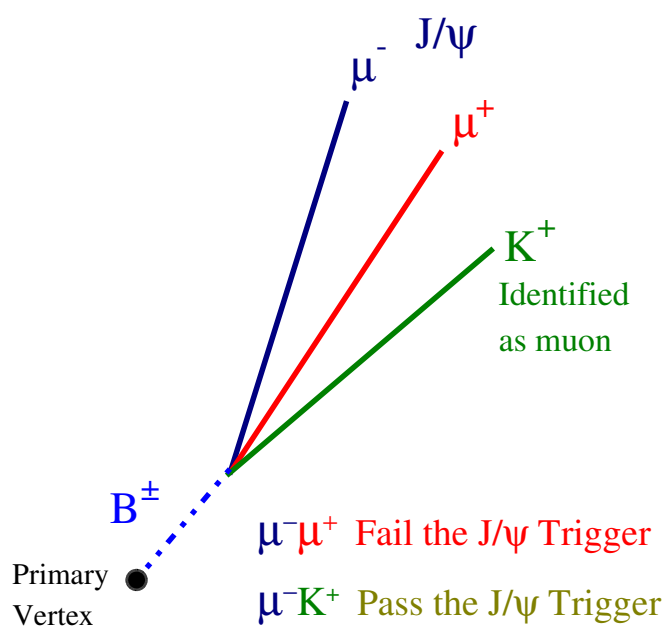


Figure 26: Example of event with a hadron misidentified as a muon that might be preferentially selected by the dimuon trigger.

The signal distributions for each measured quantity are modeled with muons from J/ψ decays, while the background distributions are modeled with pions from K_s^0 , kaons from D^0 , and protons from Λ decays.

The value of the likelihood ratio cut is determined by studying the quantity $S^2/(S+B)$, where S is the expected number of signal events and B is the expected number of background events. The likelihood ratio is calculated for all J/ψ legs in the muon channel sample and the signal and background components of the muon channel sample are calculated for different values of the likelihood ratio cut. Figure 27 shows the optimized quantity $S^2/(S+B)$ as the likelihood ratio cut varies independently for CMU and CMX muons. The optimal point of the cut, where $S^2/(S+B)$ is at its maximum, is > 0.06 , which is lower than one might expect. However, this merely indicates that the muons from J/ψ candidates are already quite pure.

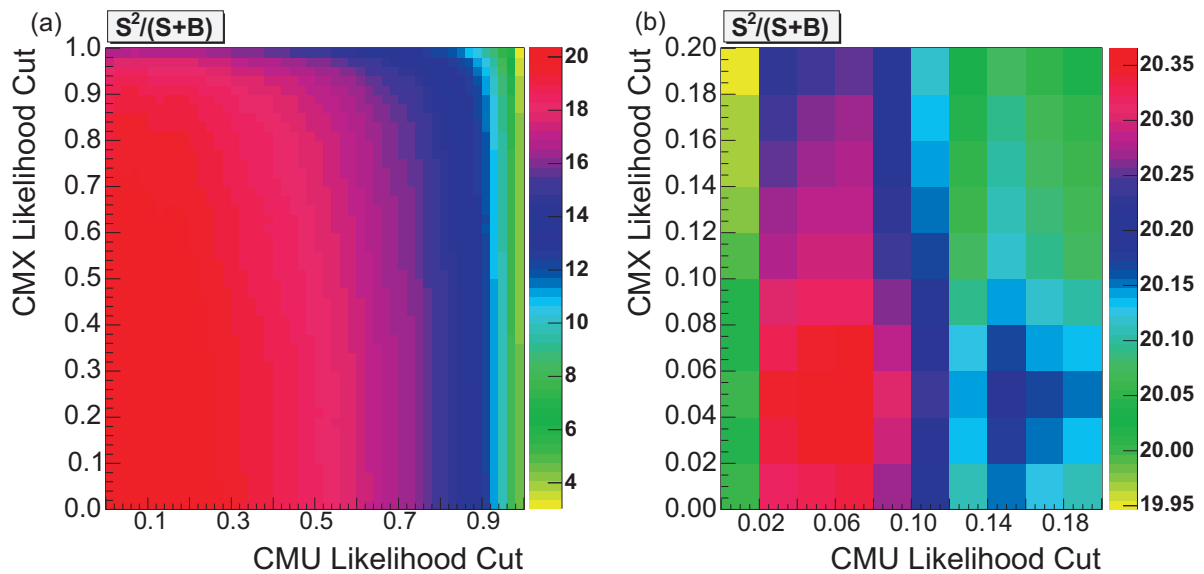


Figure 27: (a) Two dimensional plots of $S^2/(S+B)$ for muon channel candidates given cuts for the minimum muon likelihood on CMU and CMX muons. (b) Zooming in shows a peak near a value of 0.06 for both muon types.

6.1.3 COT and silicon hit requirements

Requirements on the number of hits in the COT and silicon detectors used in track reconstruction prevent the inclusion of poor quality tracks. Tracks must have COT hits in at least two ϕ and small angle stereo super layers, with at least five hits in each super layer [85]. The choice of at least three silicon ϕ hits in the SVX and ISL insures quality measurements of displaced vertices.

6.1.4 The dimuon invariant mass

If two muons originate from the decay of a J/ψ , the reconstructed invariant mass of the dimuon system will be the J/ψ mass. Figure 28 illustrates the J/ψ mass peak in dimuon candidates without and with trigger confirmation. Within the $\pm 50 \text{ MeV}/c^2$ window there are ~ 7 million J/ψ events over a background of $\sim 700,000$. The trigger confirmation removes only a small fraction of J/ψ events.

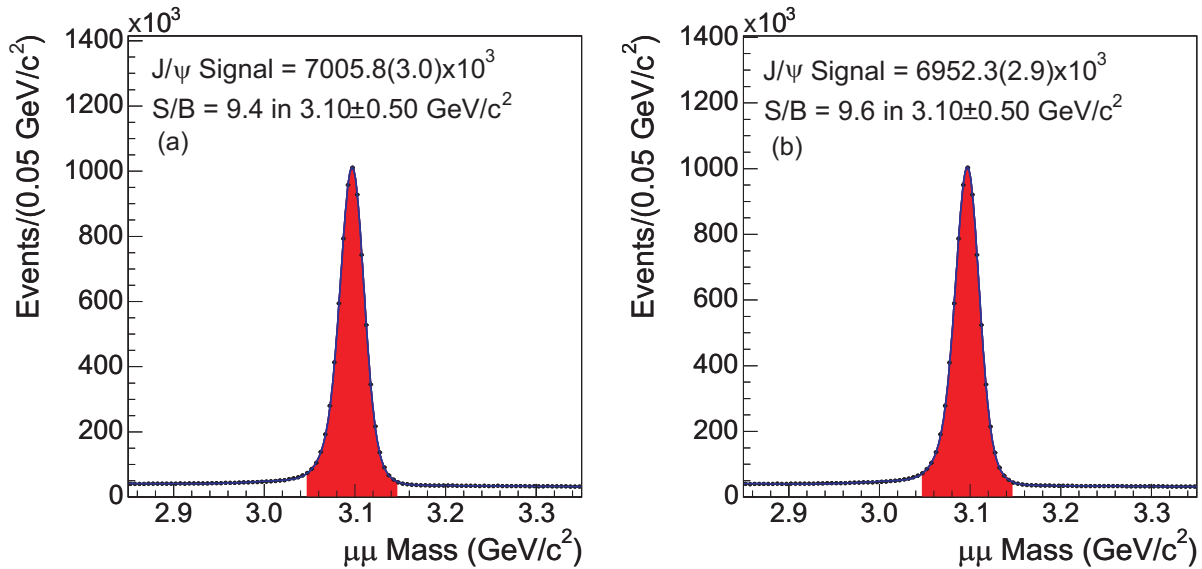


Figure 28: Fitted dimuon mass distributions, with red shaded J/ψ signal region. Plot (a) does not include the trigger confirmation for the J/ψ legs, while plot (b) does.

6.2 GENERIC SELECTION OF $J/\psi + l^\pm$ EVENTS

The addition of a third lepton to the J/ψ systems provides candidate events for $B_c^\pm \rightarrow J/\psi + l^\pm + X$ decays. Events are selected based on the properties of the third lepton as well as the properties of the three track system. Table 8 summarizes selection criteria common to both electron channel and muon channel final states. A detailed discussion of these global selection cuts follows.

Selection Requirement	Value
Third lepton COT Hits	2 Stereo + 2 Axial Superlayers (5 hits each SL)
Third lepton dE/dx Hits	> 42 Hits
Silicon Hits	≥ 3 hits in ϕ layers
$J/\psi + l^\pm$ Vertex Probability	> 0.001
$J/\psi + l^\pm$ $\Delta\phi$	$< \pi/2$
$J/\psi + l^\pm$ $\sigma_{L_{xy}}$	$< 90 \mu\text{m}$
$J/\psi + l^\pm$ Mass	$ M_{J/\psi+l} - 5.0 \text{ GeV}/c^2 < 1.0 \text{ GeV}/c^2$
$J/\psi + K^\pm$ Mass Veto	$ M_{J/\psi+K} - 5.279 \text{ GeV}/c^2 > 0.05 \text{ GeV}/c^2$

Table 8: Cuts applied to the third track and three track system, that are general to muon and electron final states.

6.2.1 Third track selection

The silicon and COT hit requirements for the third track are the same as those used for the J/ψ legs. In addition, since the dE/dx of the third track is used, there is a requirement for at least 43 COT hits with dE/dx information, matching the requirement used in the calibration of the dE/dx [86].

6.2.2 Cuts for the three track system

A number of cuts are applied to the three track system to optimize the signal component and minimize systematic uncertainties. Sources of backgrounds for $J/\psi + l^\pm$ candidates include events where the J/ψ muons and the third lepton do not originate from the same decay vertex, specifically the $b\bar{b}$ and residual e^+e^- backgrounds. To reject events where this appears to be the case, the χ^2 vertex probability is used. Figure 29 shows the distribution of vertex probability for simulated B_c events, which is relatively flat compared to simulated $b\bar{b}$ events that peak sharply near 0. Figure 30 illustrates the $S^2/(S+B)$ for vertex probability cuts greater than the plotted value, and a conservative cut of > 0.001 is chosen.

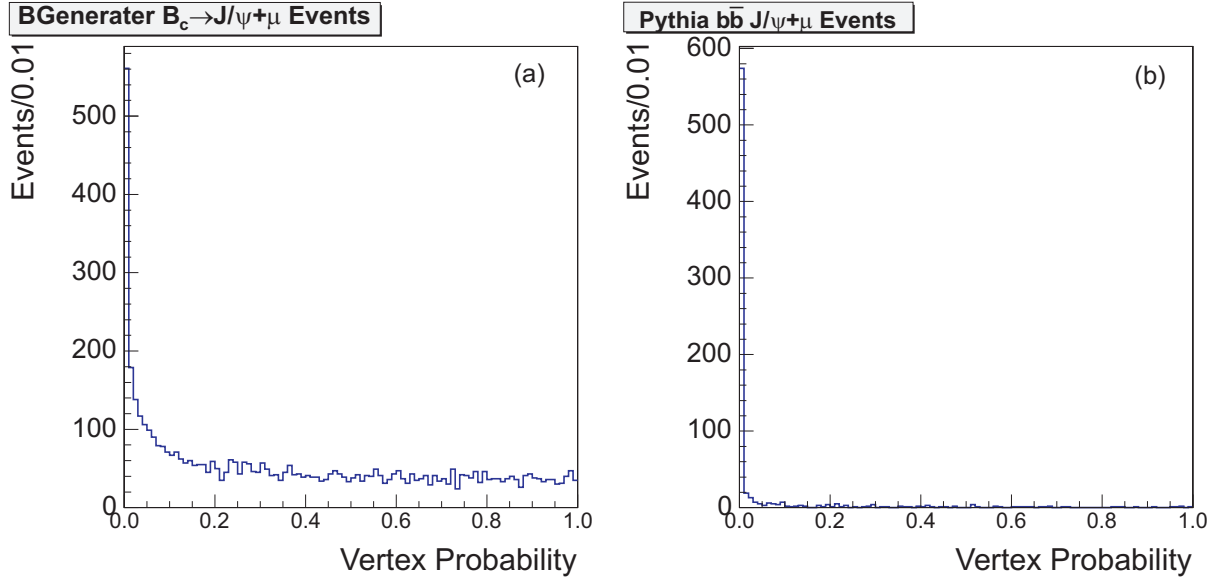


Figure 29: Comparison of the three track vertex probabilities for simulated muon channel events from B_c decays (a) and $b\bar{b}$ production (b).

The opening angle between the J/ψ and the third lepton in the $r - \phi$ plane, $\Delta\phi$, offers another variable to differentiate between signal and background, particularly $b\bar{b}$ events. Figure 31 illustrates the typically small values of $\Delta\phi$ for B_c events compared to $b\bar{b}$ events with large opening angles, as one would expect for particles from two different b jets. The optimization of the $\Delta\phi$ cut value was carried out for the previous measurement of the B_c cross section [87], see Figure 32, and the conservative cut of $\Delta\phi < \pi/2$ is used for this analysis as

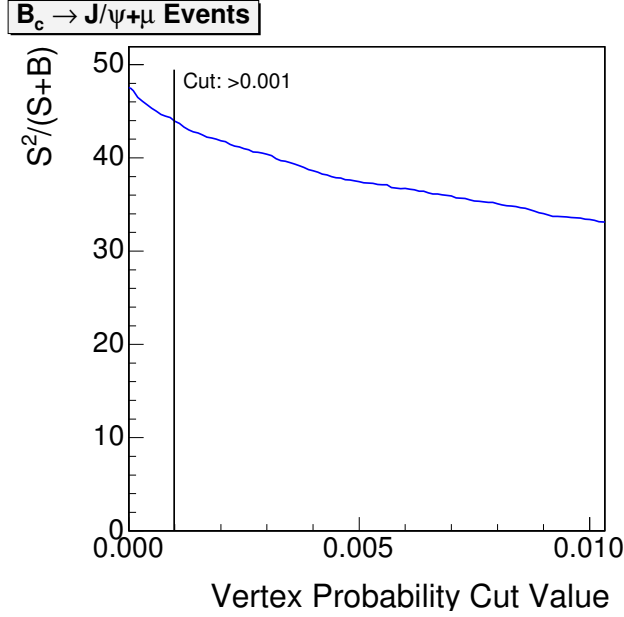


Figure 30: $S^2/(S + B)$ for muon channel candidates as a function of the minimum vertex probability.

well.

The measurement of σ_{ct^*} , for a given event is largely dependent on the measured $\sigma_{L_{xy}}$. To avoid uncertainties in modeling tails in the $\sigma_{L_{xy}}$ for simulated events, a loose cut of $\sigma_{L_{xy}} < 90 \mu\text{m}$ is applied. Figure 33 illustrates that the cut has little effect on the simulated samples of B_c signal events.

In signal events, the mass of the $J/\psi + l^\pm$ system is spread below the nominal B_c mass due to the undetected neutrino or other particles in the decay. Figure 34 shows the expected mass distribution for simulated signal events. Requiring events in a 4-6 GeV/c^2 window keeps most of the signal events. One easily removed source of background events are $B^\pm \rightarrow J/\psi + K^\pm$ decays where the kaon is misidentified as a lepton. To remove this background, events with a $J/\psi + K^\pm$ reconstructed mass within a $50 \text{ MeV}/c^2$ of the nominal B^\pm mass are rejected.

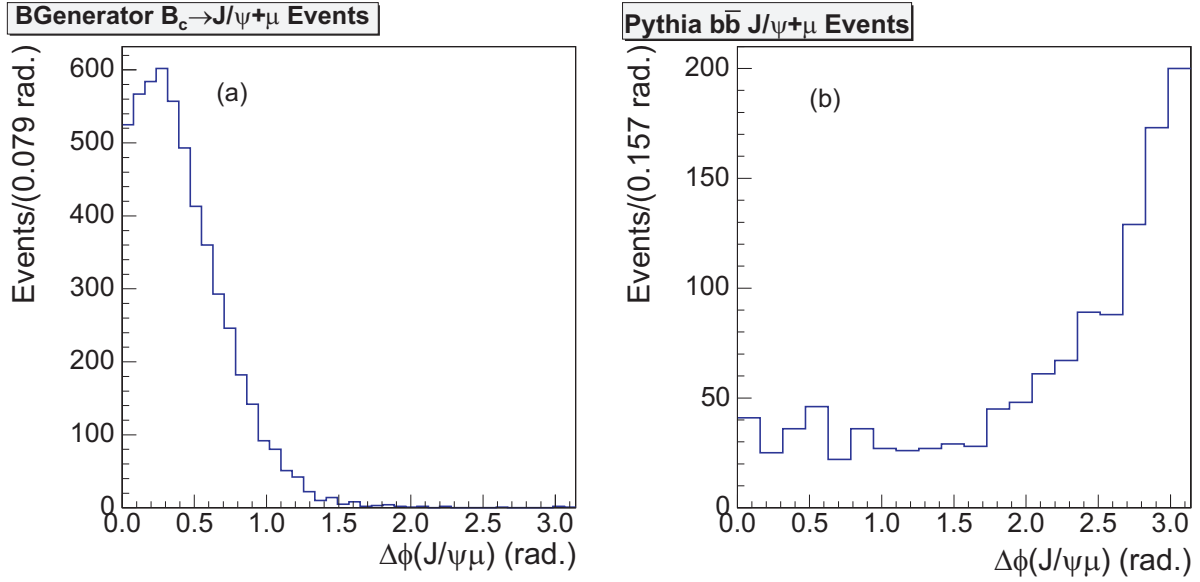


Figure 31: Opening angle $\Delta\phi$ between the J/ψ and third muon for simulated signal events (a) and simulated $b\bar{b}$ background events (b).

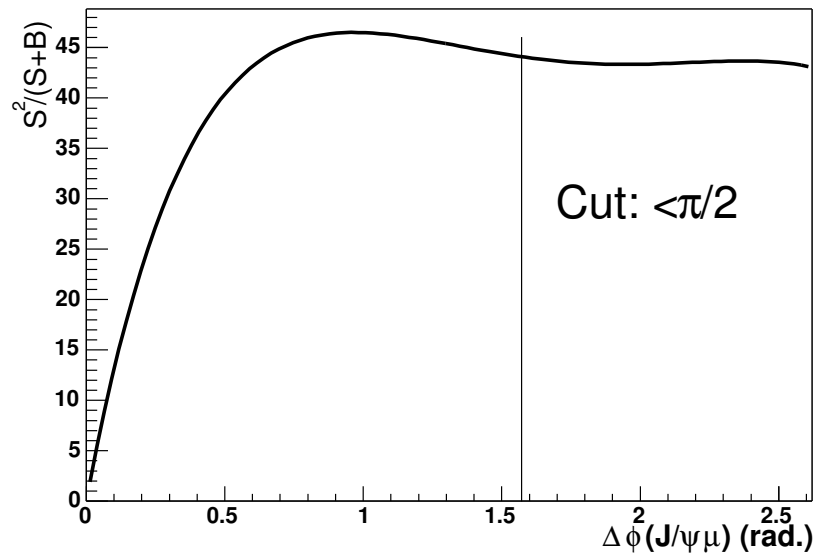


Figure 32: Evaluation of $S^2/(S + B)$ for the choice of $\Delta\phi$ cut carried out for the B_c cross section measurement. A loose cut of $< \pi/2$ was chosen.

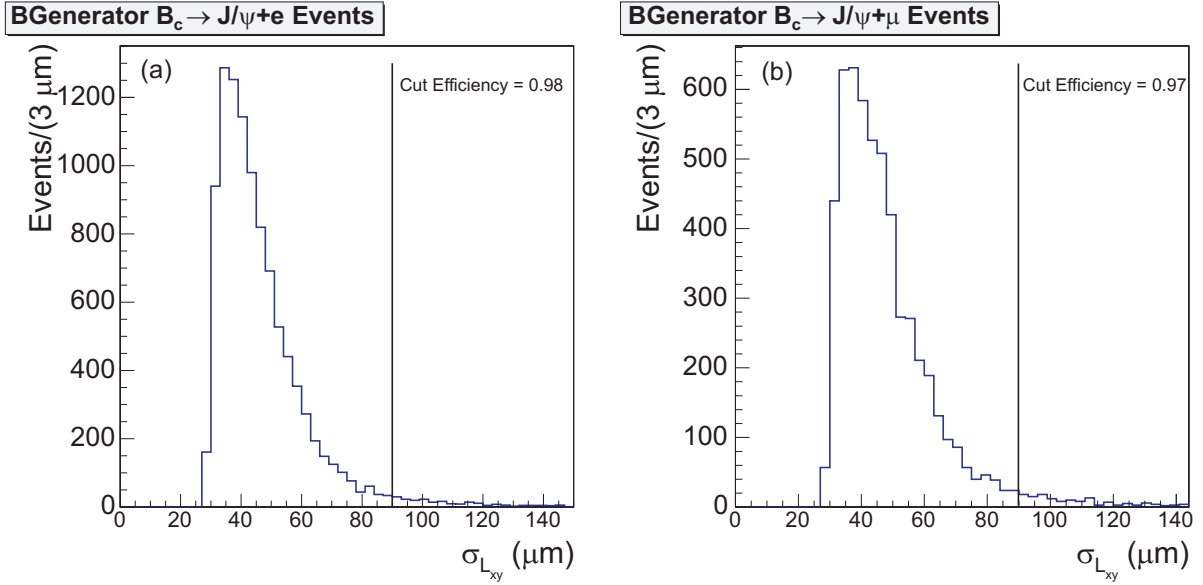


Figure 33: Simulated σ_{Lxy} for B_c events. A loose cut of $< 90 \mu\text{m}$ removes very little signal in electron channel (a) or muon channel (b) events.

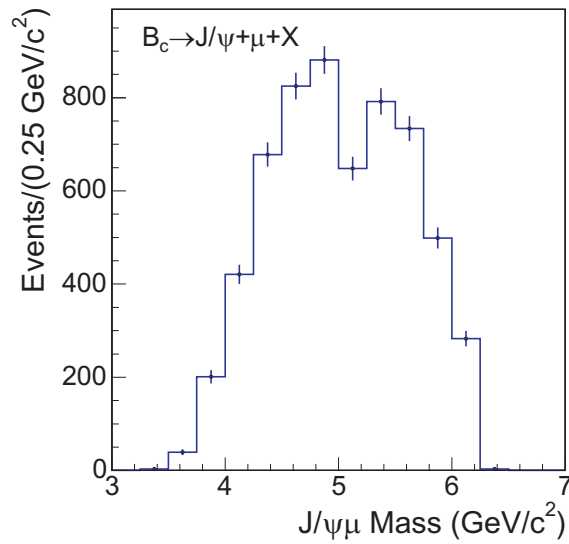


Figure 34: $J/\psi + \mu^\pm$ mass distribution for simulated B_c events. Most events fall in a 4-6 GeV/c^2 window.

6.3 SELECTION SPECIFIC TO THE MUON CHANNEL

The selection specific to the muon channel, outlined in Table 9 follows closely that outlined in the previous B_c cross section measurement [87]. To minimize the possibility of hadrons punching through the calorimeter to be misidentified as muons, the third muon must be matched to stubs in both the CMU and CMP detectors, and therefore fiducial to those detectors. The $r - \phi$ position of the CMU stub should match to the position of the extrapolated track with $\chi^2 < 9.0$. The p_T of the track is required to be greater than 3.0 GeV/ c since the efficiency for CMUP muons has been shown to fall off below 3.0 GeV/ c [88]. The muon track is required to be an XFT trigger track, since related data samples used to study muon misidentification rates consists largely of XFT trigger tracks.

Selection Requirement	Value
Third μ Type	CMUP (CMUP Fiducial)
Third μ Stub Matching	CMU $\chi^2(\text{X Pos.}) < 9.0$
Third μ Trigger Requirement	Is XFT
Third μ Isolation at CMU	No extrapolated track within 40 cm (xy) at CMU radius
Third μ p_T	> 3.0 GeV/ c
Third μ dE/dx Cut	$Z_\mu^{pull} > -1.0$

Table 9: Cuts applied to the third muon in muon channel candidates.

To minimize the probability that an additional track in the event donates a stub to the track of interest, hence minimizing dependencies on the density of tracks in the event, it is required that no other track with $p_T > 0.4$ GeV/ c extrapolate to within 40 cm of the track of interest at the CMU radius. As an exception, the J/ψ legs may extrapolate to within 40 cm since their stubs are already associated with a track. The choice of this cut is documented in the cross section analysis [87].

A cut of > -1.0 is applied to the Z_μ^{pull} distribution where the pull is evaluated with a

muon hypothesis. The definition of the Z_μ^{pull} is

$$Z_\mu = \frac{\ln(dE/dx_{meas})}{\ln(dE/dx_\mu)}, \quad (6.1)$$

$$Z_\mu^{pull} = \frac{Z_\mu}{\sigma_{Z_\mu}}.$$

The quantity dE/dx_μ is the expected dE/dx for a muon with the muon candidate's momentum, and the quantity σ_{Z_μ} is the expected uncertainty in the Z_μ measurement. This cut removes a large number of kaons and protons that are candidates to be misidentified as a muon, minimizing systematic uncertainties related to the misidentification background. A more detailed discussion of the motivation for this cut can be found in Appendix C.

6.4 SELECTION SPECIFIC TO THE ELECTRON CHANNEL

The selection specific to the electron channel, outlined in Table 10, closely follows that outlined in the B_c cross section measurement by CDF collaborators using this channel [89].

Selection Requirement	Value
Fiducial Requirement	In CES Fiducial Region
Electron p_T	$> 2.0 \text{ GeV}/c$
Electron dE/dx Cut	$Z_e^{pull} > -1.3$
Electron Likelihood Ratio	$> p_T$ Dependent Cut
e^+e^- Veto	$ \Delta(\cot(\theta)) > 0.05 \parallel \Delta_{xy} < -0.03 \text{ cm} \parallel \Delta_{xy} > 0.05 \text{ cm}$
$J/\psi e$ p_T	$> 5 \text{ GeV}/c$

Table 10: Cuts applied to the electron or three track system in $J\psi + e^\pm$ candidates.

The electrons are selected using a likelihood ratio based on calorimeter information that was developed by CDF collaborators for lepton based B meson tagging [90]. The likelihood ratio uses the following measured quantities to discriminate between electrons and hadrons:

- E_{had}/E_{em} – ratio of energy deposited in the hadronic calorimeters relative to the energy deposited in the electromagnetic calorimeter for the two towers associated with the electron candidate
- E_{em}/p – ratio of the energy deposited in the electromagnetic calorimeter to the momentum of the electron candidate
- CES χ_x^2 – a χ^2 from a comparison of CES wire view of the shower profile to the profile from a test beam of electrons
- CES χ_z^2 – a χ^2 from a comparison of CES strip view of the shower profile to the profile from a test beam of electrons
- CES $q\Delta X/\sigma_x$ – the transverse distance between the CES cluster and the track extrapolated to the CES, multiplied by charge to sign it, and divided by the expected variation
- CES $q\Delta Z/\sigma_z$ – same as the previous variable, but the distance is in the $r - z$ plane
- E_{CES}/p^* – the wire cluster pulse height in the CES, scaled by $p^* = 10(p/10)^\alpha$. Here α is a momentum dependent term that allows for valid comparisons when energies are less than $10 \text{ GeV}/c^2$.
- Corrected Q_{CPR} – the pulse height in the CPR corrected for $\sin(\theta)$ dependence.

The likelihood ratio was also developed to include dE/dx information, but for this measurement the dE/dx has been removed from the likelihood ratio and a cut on dE/dx is applied separately.

The performance of the likelihood ratio is studied using a sample of electrons from photon conversion, which is described in Appendix B. The likelihood ratio values for electrons are shown in Figure 35 with the expected peak near 1. The choice of cut for the likelihood ratio depends on the efficiency for electrons and hadrons to pass a given cut value. The rate of hadrons that pass the cut determines the electron misidentification background, and is estimated using pions identified as products of D^0 meson decays, as described in Appendix B. The $S^2/(S + B)$ is studied for a number of p_T dependent cuts as outlined in Table 11. The optimal choice of cuts is one that aims for flat (in p_T) 80% efficient electron selection while imposing maximum and minimum cut values of 0.6 and 0.9. Figure 36 illustrates the p_T dependent cut and shows the efficiency of the cut as a function of p_T .

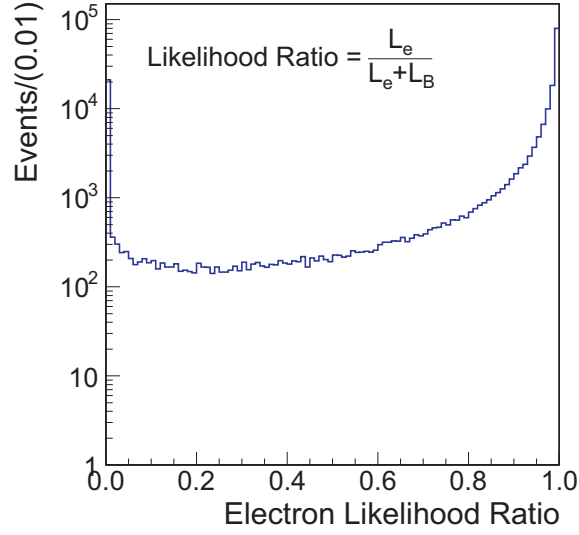


Figure 35: Electron likelihood ratio for electrons from photon conversion.

Cut Scenario	Average e Efficiency	$S^2/(S + B)$
70% Eff.	70.0%	81.5
Cut = 0.8	77.6%	83.8
Cut = 0.9	71.9%	81.2
75% Eff., Max Cut=0.85	77.7%	84.3
75% Eff., Max Cut=0.9	76.6%	84.3
80% Eff., Max Cut=0.8	81.3%	84.4
80% Eff., $0.6 < \text{Cut} < 0.9$	79.5%	85.2
80% Eff., $0.6 < \text{Cut} < 0.85$	80.0%	84.7
85% Eff., Cut > 0.6	81.5%	83.9

Table 11: Table of electron efficiency and $S^2/(S + B)$ for various p_T dependent electron likelihood ratio cuts.

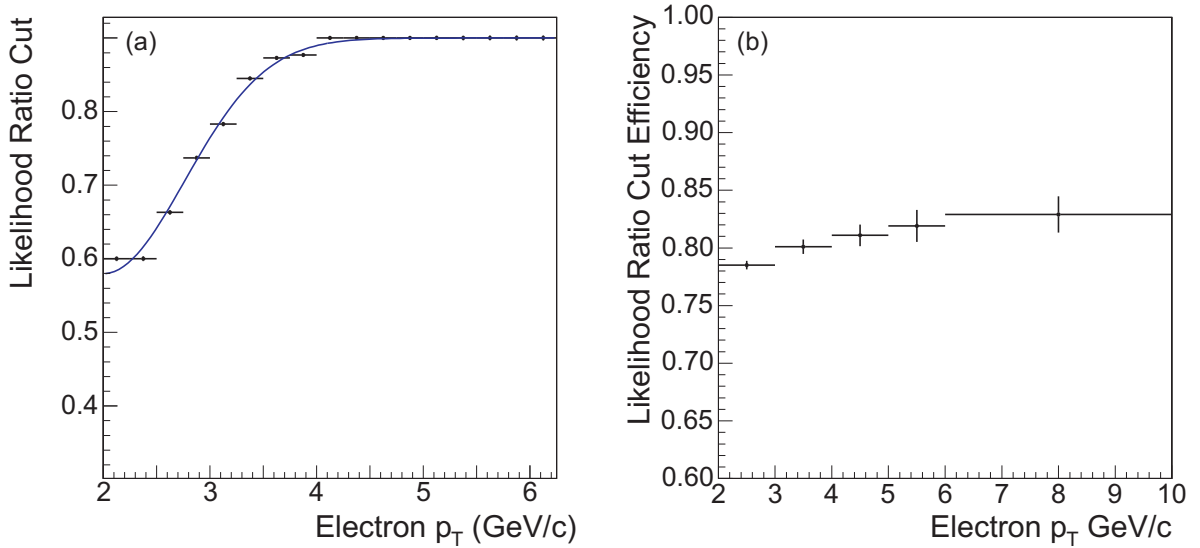


Figure 36: p_T dependent electron likelihood ratio cut (a) and the electron efficiency as a function of p_T (b).

The p_T cuts for the electron and $J/\psi + e^\pm$ system, as well as the dE/dx and the e^+e^- veto follow the cuts developed by CDF collaborators for previous measurements of the B_c cross section [89] and lifetime [91]. The requirement of electron $p_T > 2.0$ GeV/ c is largely driven by the inability of the electron likelihood ratio to differentiate hadrons and electrons at low p_T , as well as lower e^+e^- electron veto efficiency at lower momentum. The $J/\psi + e^\pm$ p_T cut removes 28% of the background from events where the J/ψ is not real, while only removing 14% of signal events. The dE/dx cut removes large fractions of pions, kaons and protons that could be misidentified as electrons. The e^+e^- veto cuts removes electrons that are part of e^+e^- candidate pairs that come from photon conversion or the decay of light neutral mesons. Since the e^+e^- pairs originate from the same point and have a small opening angle, events are rejected if the pair's separation Δ_{xy} in the $r - \phi$ plane and the polar opening angle θ are small.

6.5 VALIDATION OF SELECTION

To ensure that the event selection does not bias the lifetime distribution of B_c candidate events, the selection cuts are applied to a realistic Monte Carlo simulation of B_c events and the true lifetime ct of surviving events is fitted with an exponential decay law. The fitted average proper decay lengths, illustrated in Figure 37, are $c\tau = 139.0 \pm 1.4 \mu\text{m}$ and $c\tau = 139.4 \pm 1.8 \mu\text{m}$ for the electron and muon channels respectively, and are in good agreement with the average proper decay length input to the simulation of $140 \mu\text{m}$.

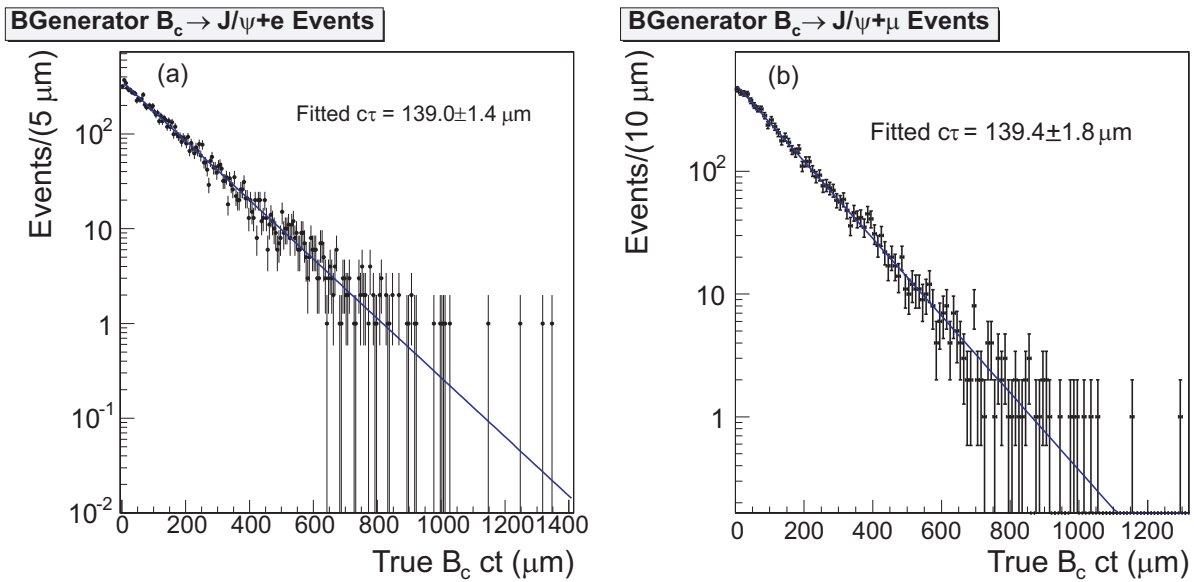


Figure 37: Exponential fits of the true ct of simulated B_c for the electron (a) and muon (b) channels after all analysis cuts are applied. The input average proper decay length for the simulated events is $140 \mu\text{m}$.

7.0 BACKGROUNDS

Due to the undetected particles in the $J/\psi + l^\pm + X$ final state, it is not possible to reconstruct the B_c mass peak. Hence, there are no mass sideband regions available to constrain background sources of $J/\psi + l^\pm$ events. Consequently, the background is categorized by various sources, and each source is modeled using either related data or simulated events. The models provide determinations of the normalization and the ct^* and σ_{ct^*} distributions for each background that can be used in the B_c average lifetime fit.

The background sources of $J/\psi + l^\pm$ are generally present in both muon and electron final state, the lone exception being electrons from photon conversion. The background sources are classified as:

- Hadrons Misidentified as Leptons – events with a J/ψ candidate and a third track that is typically from a long lived hadron (π , K or p). This third track can be misidentified as a lepton. For muons this may happen when the hadron punches through the calorimetry or decays to a muon. For electrons the hadrons can leave signatures in the calorimetry that look sufficiently like an electron's to pass the electron likelihood ratio cut.
- Misidentified J/ψ – events where the J/ψ candidate is not a true J/ψ . Sources can be Drell-Yan dimuon production or random combinations of tracks in the event.
- $b\bar{b}$ – The event contains two b quark jets. One jet produces a J/ψ and the other produces a lepton. The J/ψ and lepton have a small probability of appearing to originate from a common vertex, but $b\bar{b}$ production is three orders of magnitude larger than B_c production.
- Residual e^+e^- – Electrons or positrons are produced in e^+e^- pairs when photons convert or light neutral mesons decay, and they can appear in the same event as a J/ψ . The residual background consists of events that survive the e^+e^- veto due to imperfect

efficiency. This background is only present for the electron channel.

- Prompt J/ψ – prompt J/ψ production with an additional lepton in the final state.

The methods for modeling each of these backgrounds are discussed in detail in the following sections. Each background model includes the background normalization and templates for the ct^* and σ_{ct^*} distributions that are propagated in the B_c lifetime fit.

7.1 MISIDENTIFIED J/ψ BACKGROUND

The misidentified J/ψ background consists of events where two tracks are identified as muons and have an invariant mass in the J/ψ mass window but do not originate from the decay of a J/ψ . If the misidentified J/ψ candidate is associated with a third lepton candidate, it will be selected for the B_c candidate sample. The sources of misidentified J/ψ include Drell-Yan production and random combinations of tracks in the event.

The background is modeled by using the same selection requirements that are used for B_c candidates, but moving the J/ψ mass window by plus or minus $0.15 \text{ GeV}/c^2$ in order to sample the upper and lower J/ψ mass sidebands. These sideband events are used to determine the normalization for the misidentified J/ψ background as well as models for its ct^* and σ_{ct^*} distributions.

7.1.1 Misidentified J/ψ normalization

Figure 38 shows the fitted J/ψ mass distribution from electron channel and muon channel B_c candidate events where the J/ψ mass cut has been removed. The signal component of the fits is constrained by the fits of the high statistics J/ψ candidate samples previously shown in Figure 28. The background component is assumed to be linear. The fit of the electron channel sample shows no pathologies and can be used to measure 325.2 ± 10.0 background events under the J/ψ mass peak. The fit of the muon channel sample shows some structure in the lower sideband. Due to this, the fitted background measurement under the mass peak, 127 ± 5 events, shows some disagreement with 141.5 ± 8.4 events obtained by counting events

in the sidebands and dividing by two. For the B_c lifetime measurement, the value from counting, 141.5 ± 8.4 events, is used; and the behaviour in the lower sideband is studied as part of the evaluation of systematic uncertainties.

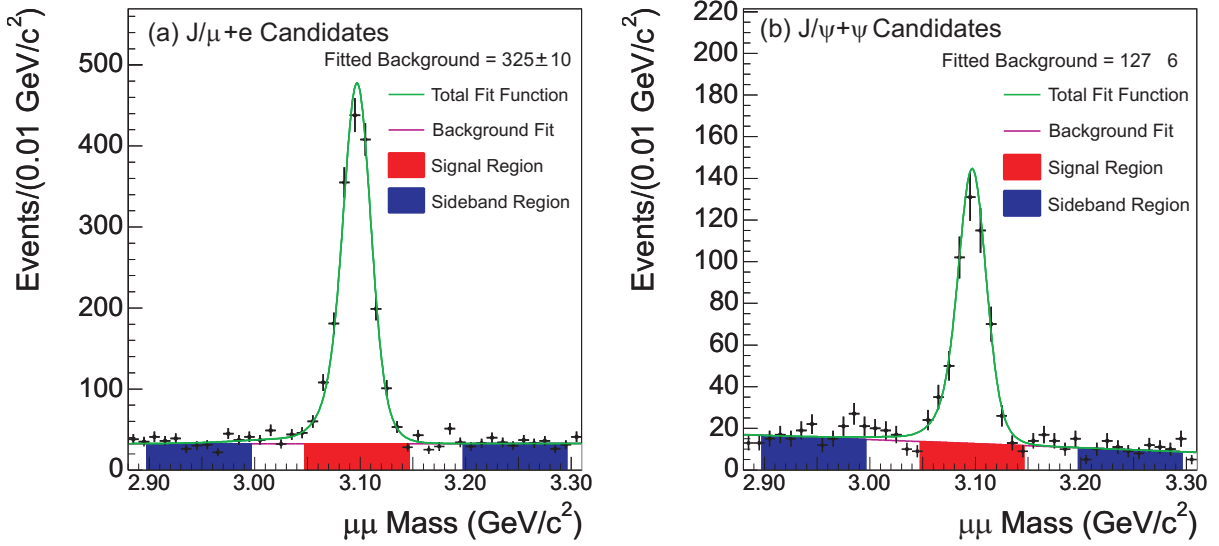


Figure 38: Fitted J/ψ mass for B_c candidates in the electron (a) and muon (b) channels.

7.1.2 Misidentified J/ψ ct^* fits

The ct^* of misidentified J/ψ events is modeled by fitting the events in the J/ψ sideband regions. A PDF consisting of one Gaussian, one positive exponential, and two negative exponential components is used for the electron channel fit. The muon channel events are fitted with the same function but for the exclusion of one of the negative exponential components. The form of the PDF is

$$F_{MJ}(ct^*, \sigma) = [f_0\delta(ct^*) + \frac{f_+}{c\tau_+}e^{\frac{-ct^*}{c\tau_+}}\theta(ct^*) + \frac{f_{++}}{c\tau_{++}}e^{\frac{-ct^*}{c\tau_{++}}}\theta(ct^*) + \frac{f_-}{c\tau_-}e^{\frac{ct^*}{c\tau_-}}\theta(-ct^*)] \quad (7.1)$$

$$\otimes \frac{1}{\sqrt{2\pi s\sigma}}e^{-\frac{1}{2}\left(\frac{ct^*}{s\sigma}\right)^2}.$$

The functions $\delta(ct^*)$ and $\theta(ct^*)$ are the Dirac delta and Heaviside step functions respectively. The forms of the PDFs are chosen to model the expected contributions of the events in data.

The delta function models the promptly produced component, the negative exponentials model the component from B decays, and the positive exponential models events with a negative ct^* ¹. The resulting fits to data are shown in Figure 39 and the fitted parameters are listed in Table 12.

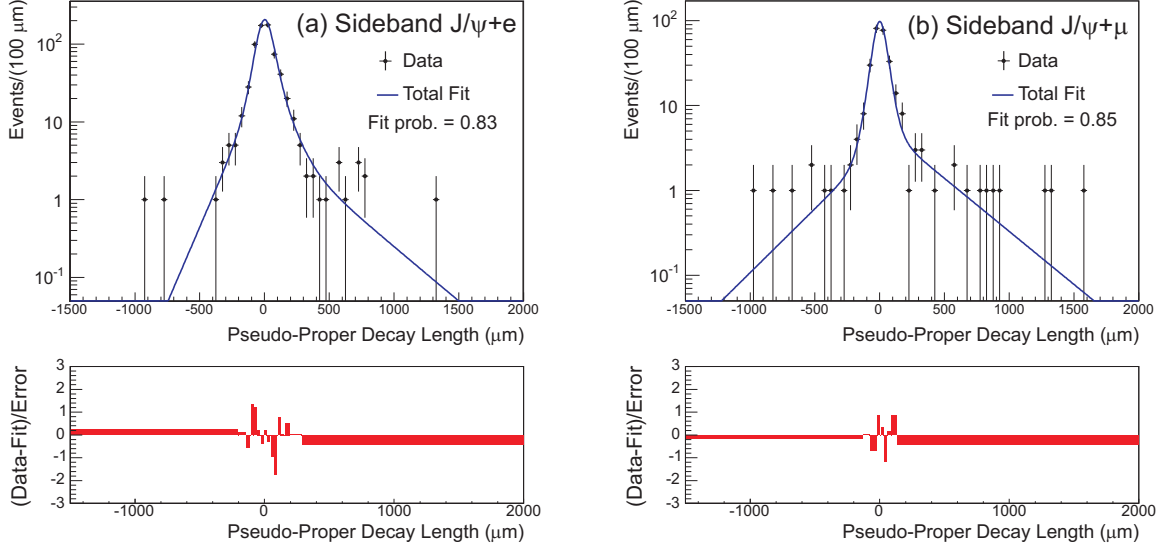


Figure 39: Fitted ct^* distributions for sideband J/ψ events in the electron channel (a) and muon channel (b).

7.1.3 Misidentified J/ψ σ_{ct^*} fits

The σ_{ct^*} of the sideband events is fitted with an empirically chosen function that is used for both channels:

$$P_{MJ}(\sigma_{ct^*}) = \frac{1}{\sqrt{2\pi}P_0} e^{-\frac{1}{2}\left(\frac{\sigma}{P_0}\right)^2} \otimes \left[\frac{1}{P_1} e^{-\frac{(\sigma_{ct^*}-P_2)}{P_1}} \theta(\sigma_{ct^*} - P_2) \right]. \quad (7.2)$$

The form of the function is chosen to allow fits that agree with data while having a small number of parameters. This functional form has the added benefit that the overall properties

¹Events with negative ct^* can be produced by combinations of tracks that do not originate from the same decay vertex or tracks from a partially reconstructed decay. Recall that L_{xy} is constructed by taking the dot product of the displacement vector and momentum vector in the $r - \phi$ plane. If the angle between these vectors is $> \pi/2$, L_{xy} and subsequently ct^* are negative.

Parameter	Electron Channel		Muon Channel	
	Fit Value	Error	Fit Value	Error
s	1.30	0.06	1.32	0.10
f_0	0.664	0.062	0.790	0.061
f_+	0.056	0.029	0.141	0.031
$c\tau_+$ (μm)	310	97	347	168
f_{++}	0.111	0.033	-	-
$c\tau_{++}$ (μm)	112	24	-	-
f_-	0.168	0.047	0.069	0.023
$c\tau_-$ (μm)	82	22	288	85

Table 12: Parameters from the ct^* fits to sideband J/ψ events.

of the function are not very sensitive to small changes of the parameters in the regions of allowed values. The fitted σ_{ct^*} distributions are shown in Figure 40 and the fitted parameters are listed in Table 13.

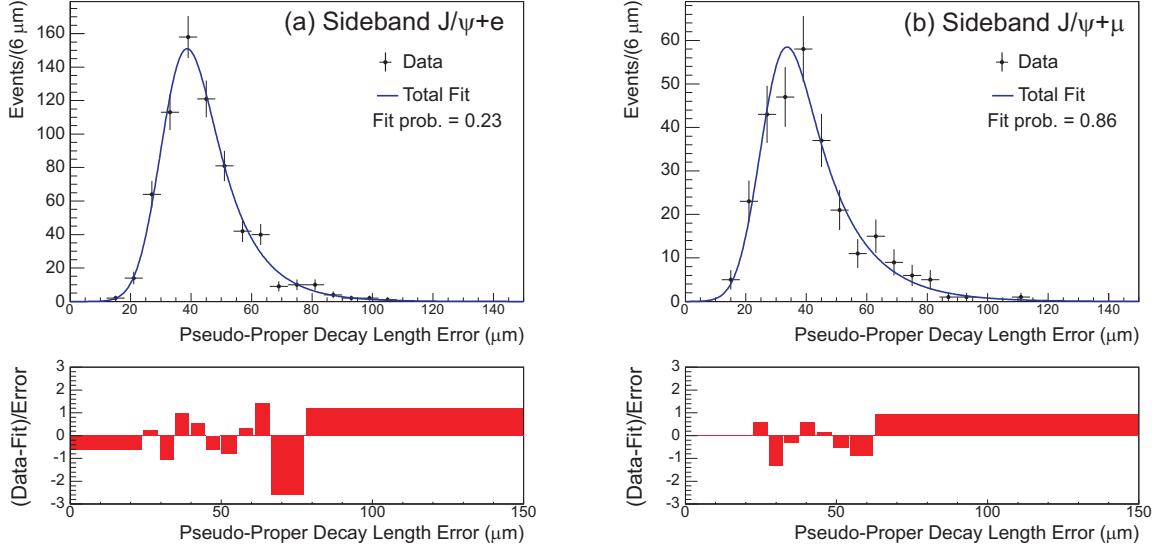


Figure 40: Fitted σ_{ct^*} distributions for sideband J/ψ events in the electron (a) and muon (b) channels.

Parameter	Electron Channel		Muon Channel	
	Value	Error	Value	Error
P_0 (μm)	6.93	0.46	6.67	0.79
P_1 (μm)	11.5	0.7	14.3	1.3
P_2 (μm)	32.3	0.6	26.6	1.0

Table 13: Parameters from the σ_{ct^*} fits to sideband J/ψ events.

7.2 HADRONS MISIDENTIFIED AS LEPTONS BACKGROUND

Events with a J/ψ and a hadron where the hadron is mistakenly identified as a lepton are labeled as the misidentified lepton background. The background is modeled with a sample of J/ψ +hadron events that are reweighted to account for the probability that the hadron is misidentified as a lepton.

Determination of the misidentified lepton background begins with samples of events with a J/ψ and an additional track such that the three track system meets all of the $J/\psi + l^\pm$ selection requirements except for the lepton identification on the third track (electron likelihood ratio for the electron channel and CMUP stubs for the muon channel). These events are labeled the J/ψ +track sample. Two samples are constructed, one based on the cuts for the electron channel and the other based on the cuts for the muon channel.

For the muon channel J/ψ +track sample, muons are removed by vetoing events where the third track has an associated CMUP muon stub. Events where the electron likelihood ratio for the third track is > 0.7 are also vetoed to remove electrons. This leaves a sample that consists of long lived hadrons (pions, kaons, and protons). Leptons are not removed from the electron channel J/ψ +track sample since the $Z_e^{pull} > 1.3$ cut enhances their contribution to the sample. Instead the contribution from leptons is measured and accounted for.

The determination of average misidentification probabilities for third tracks is done in two steps. First the probability that a given hadron type of a given p_T will be misidentified as a lepton is measured using separate data samples where hadrons can be positively identified. Next the particle composition of third tracks in the J/ψ +track samples is measured using dE/dx and TOF information. Combining the probabilities that a track is a certain particle type, $f_{\pi\dots p}$, with the misidentification probability for each type, $\epsilon_{\pi\dots p}^{misid}$, gives a weighting that is applied on a per event basis to the J/ψ +track sample:

$$W = \epsilon_\pi^{misid} f_\pi + \epsilon_K^{misid} f_K + \epsilon_p^{misid} f_p. \quad (7.3)$$

The reweighted J/ψ +track samples are used as models of the misidentified lepton backgrounds.

7.2.1 Probabilities for hadrons to be misidentified as leptons

The probability that a hadron is identified as a lepton is measured in samples where the hadron is positively identified as a decay product in a fully reconstructed system of particles with a narrow mass peak. For the case of pions and kaons, the decay chain $D^{*+} \rightarrow D^0 \pi^+ \rightarrow \pi^+ K^- \pi^+ + \text{charge conjugate}$ is used. Here the charge of the soft pion from the $D^{*\pm}$ decay is used to identify which of the D^0 decay products is a pion. The decay $\Lambda \rightarrow p^+ \pi^- + \text{charge conjugate}$ is used for protons. The proton is identified as the decay product with the higher momentum. The selection of these samples is outlined in Appendix B. When the D^0 and Λ events have been selected and reconstructed, selection identical to the J/ψ +track third track selection is applied to the decay product that has been identified as a pion, kaon, or proton. The number of events in the reconstructed mass peak, N_{parent} , is measured. Lepton identification is then applied to the decay product and the number of events in the reconstructed mass peak, $N_{daughter}$, is measured. For the electron channel the lepton identification is the electron likelihood ratio cut, and for the muon channel the lepton identification is the requirements of CMUP stubs and the stub matching. The ratio of $N_{daughter}/N_{parent}$ gives an measurement of the misidentification probability. This procedure is carried out for particles classified by particle type, charge, and p_T .

Figure 41 illustrates the D^0 mass fits with π^\pm D^0 decay products in the $p_T = 3 - 4$ GeV/ c range that are used to measure the probability that pions are misidentified as muons. Figure 42 illustrates the Λ mass fits with p^- decay products in the $p_T = 2 - 3$ GeV/ c range that are used to measure the probability that protons are misidentified as electrons. The full set of mass fits for all particle types, charges, and p_T ranges is presented in Appendix D. Figures 43 and 44 summarize the misidentification probabilities for electrons and muons, respectively. The probability for protons to be identified as muons was studied as part of the cross section measurement and an upper limit of 3.4×10^{-4} at a 95% confidence level was determined [87].

7.2.1.1 Correction for the muon misidentification probability A significant portion of pions and kaons that are identified as muons are particles that decay-in-flight inside

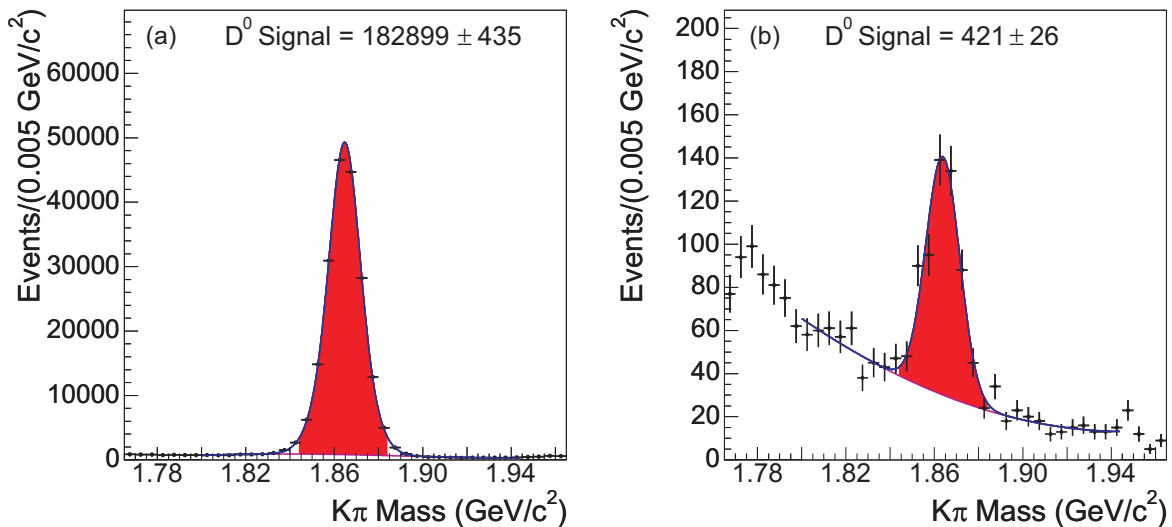


Figure 41: Fits of the tagged D^0 mass distributions where the pion leg has $p_T = 3 - 4$ GeV/c. (a) No lepton identification requirement is applied to the pion leg. (b) The pion leg is identified as a CMUP muon.

the tracking volume. When the decay-in-flight is reconstructed as a single track it may contain hits from both the original hadron and the muon. Since the muon is lighter and a portion of the momentum is carried by the neutrino in the decay, the measured momentum for such a track differs from the pion momentum. If the momentum measurement deviates too far from the pion momentum, the reconstructed D^0 mass no longer falls in the mass window and the event is not counted as part of the daughter distribution used to measure the misidentification probability. Since no such mass cut exists in the J/ψ +track sample, a correction should be applied to account for events moving out of the mass window.

The correction is carried out using a realistic BGENERATOR Monte Carlo simulation of D^0 decays. The parent and daughter mass peaks for simulated events are fitted in the same manner as data, as illustrated in Figure 45. Using the truth information in the simulation, it is possible to identify the decay-in-flight events where the D^0 mass falls outside of the signal mass window.

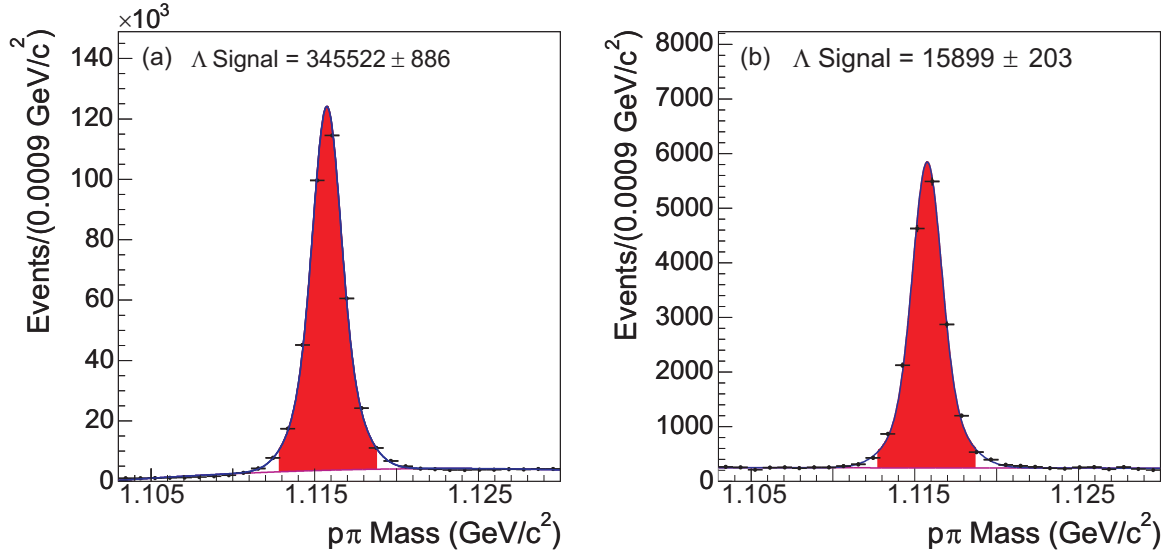


Figure 42: Fits of the Λ mass distributions where the p^- leg has $p_T = 2 - 3 \text{ GeV}/c$. (a) No lepton identification requirement is applied to the p^- leg. (b) The p^- leg passes the electron likelihood ratio cut.

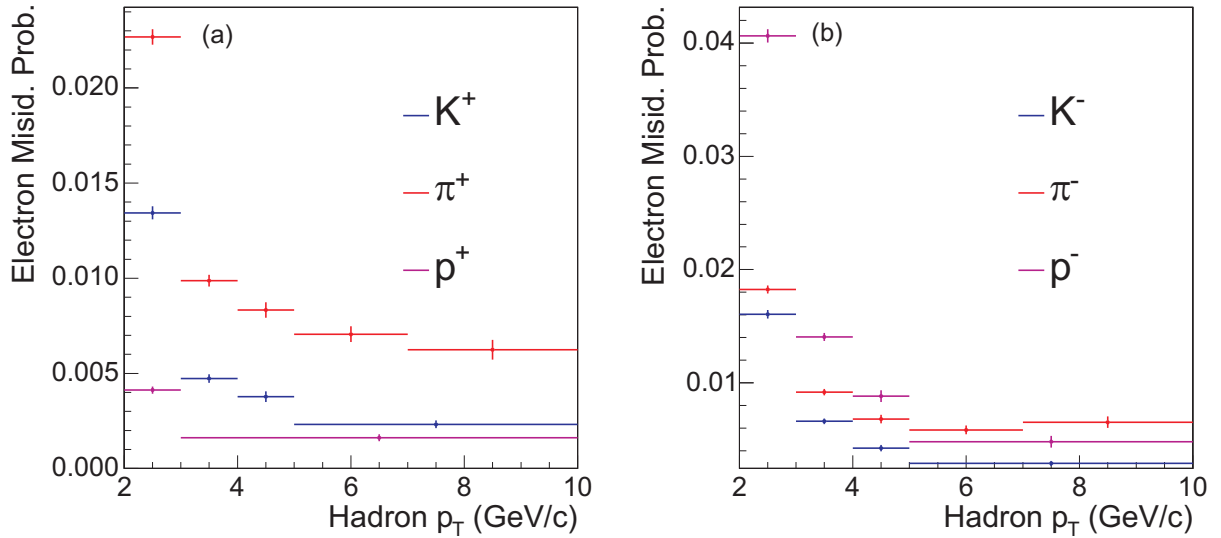


Figure 43: Probabilities for positively charged (a) and negatively charged (b) hadrons to be misidentified as electrons.

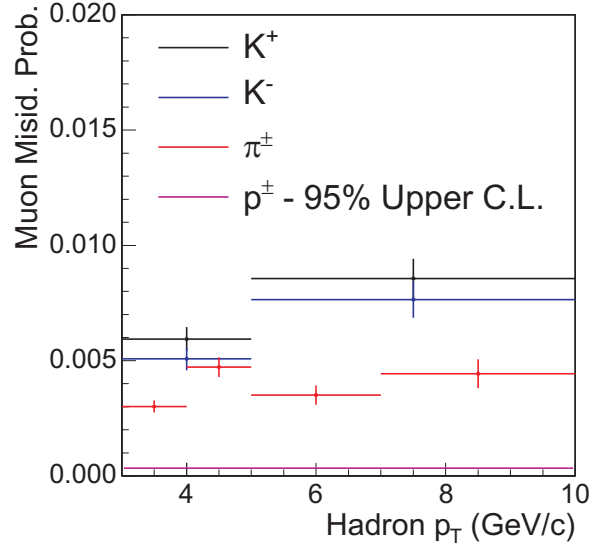


Figure 44: Probabilities for hadrons to be misidentified as muons.

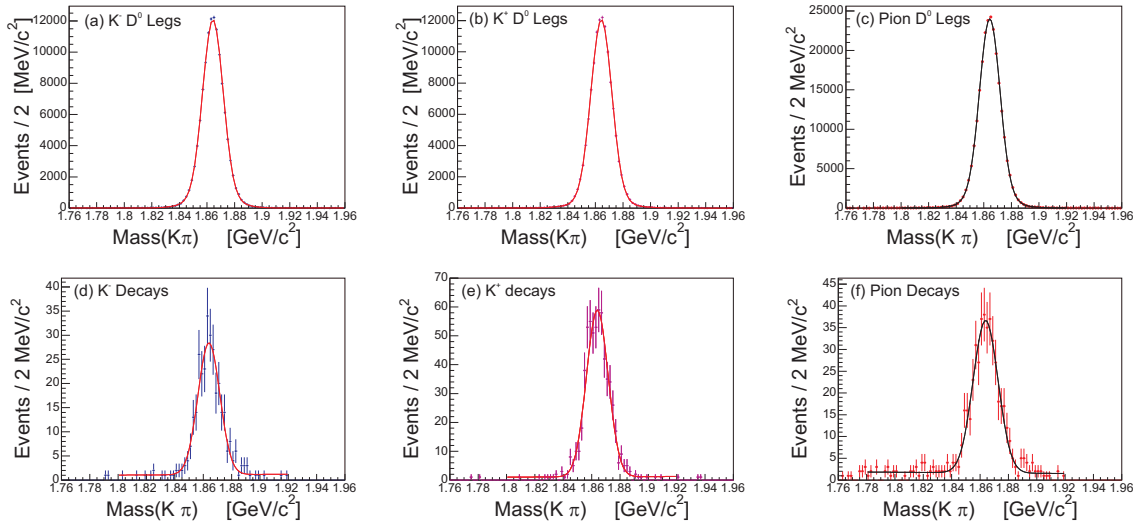


Figure 45: D^0 mass fits from the BGENERATOR sample of D^0 decays, including parent K^- (a), K^+ (b), and π^\pm (c) and daughter K^- (d), K^+ (e), and π^\pm (f) fits.

The correction for data is constructed using the equation

$$N_{out}^{data} = N_{out}^{sim} \times \frac{N_{parent}^{data}}{N_{parent}^{sim}}. \quad (7.4)$$

N_{out}^{data} is the expected number of decay-in-flight events that fall outside of the mass window in the daughter distribution in data, N_{parent}^{data} is the number of events in the mass window in the parent distribution in data, N_{out}^{sim} is the number of decay-in-flight events that fall outside of the mass window in the simulated daughter distribution, and N_{parent}^{sim} is the number of events in the mass window in the simulated parent distribution. The ratio of events in the data and simulation parent distributions is used to normalize the simulated number of events falling outside the of the mass window to data, giving a count of the events falling outside of the mass window in data. Ideally one would like to normalize to data using the total number of decay-in-flight events in the simulation and data, but the number in data cannot be measured separately from events where the hadron punches through the calorimeter. The parent distributions can be thought of as samples of events that are candidates to decay-in-flight. Since the decay-in-flight probability is determined by the pion and kaon lifetimes, which are both well measured and modeled in the simulation, the ratio of candidates for decay-in-flight offers a reasonable proxy for the ratio of the total number of decays-in-flight.

Multiplicative corrections that are applied to the misidentification probabilities were calculated as part of the cross section analysis, and the values for K^- , K^+ , and π^\pm are 1.16 ± 0.04 , 1.09 ± 0.02 , and 1.24 ± 0.06 , respectively [87]. These corrections are applied to the muon misidentification probabilities used in this thesis.

7.2.2 Particle composition of the J/ψ +track samples

Having determined the probabilities for a hadron to be misidentified as a lepton, it is necessary to determine the composition of third tracks in the J/ψ +track sample so the proper particle dependent misidentification probabilities can be applied. This is carried out using dE/dx and TOF information. Pull distributions, given a pion hypothesis, are defined for the

dE/dx and TOF measurements on third tracks:

$$Z_\pi = \frac{\ln(dE/dx_{meas})}{\ln(dE/dx_\pi)}, \quad (7.5)$$

$$Z_\pi^{pull} = \frac{Z_\pi}{\sigma_{Z_\pi}},$$

$$T_\pi^{pull} = \frac{TOF_{meas} - TOF_\pi}{\sigma_{TOF_\pi}}. \quad (7.6)$$

dE/dx_{meas} and TOF_{meas} are the measured quantities. dE/dx_π and TOF_π are the expected values for a pion with the track's properties, and σ_{Z_π} and σ_{TOF_π} are the expected measurement resolutions for a pion with the track's properties. Tracks created by pions should be distributed normally, and tracks from other particles will have distributions offset according to the particle's mass.

The Z_π^{pull} and T_π^{pull} distributions of third tracks in the J/ψ +track sample are fitted in a number of bins to account for dependencies in the particle fractions. Events are binned based on charge and momentum of the third track. Additional binning is applied based on ct^* since the physics sources of J/ψ +track events varies with the proper decay time of the events. The ct^* bins are:

1. $ct^* < 0 \mu\text{m}$ – This region consists mostly of prompt J/ψ that originate from the same vertex as a third track.
2. $0 < ct^* < 150 \mu\text{m}$ – This region contains prompt J/ψ +track events, events where the J/ψ and track come from different b jets, and events where both come from the same b jet.
3. $ct^* > 150 \mu\text{m}$ – This region contains mostly J/ψ +track from a single b jet.

For third track momentums below 3 GeV/ c , the TOF separation is enough to differentiate kaons and protons, and two dimensional fits are carried out using T_π^{pull} and Z_π^{pull} . For events with third track momentums above 3 GeV/ c , TOF adds little separating power to the fits and Z_π^{pull} only fits are used. The fraction of protons typically cannot be determined by the $p_T > 3.0$ GeV/ c fits, so the model for proton fractions outlined in Appendix C is used and the effect of this constraint is studied as a systematic uncertainty.

Muons are not removed from the electron channel J/ψ +track sample, and a method must be applied to determine the muon fraction, since muons are nearly identical to pions in the TOF_{π}^{pull} and Z_{π}^{pull} distributions. The muon fraction is identified by counting the number of CMU and CMX muons and applying known muon efficiencies, fiducial regions and misidentification probabilities to determine a total muon count.

The fits to determine the particle fractions for the third tracks are carried out before the Z_e^{pull} and Z_{μ}^{pull} cuts are applied to the J/ψ +track samples for the electron and muon channels respectively. This is done to avoid the obvious biases that would be introduced in the Z_{π}^{pull} distributions if the cuts were applied. Since the cuts are ultimately applied to the third tracks, the particle fractions must be recalculated using the expected efficiency for each particle type as determined by the conversion, tagged D^0 , and Λ samples that are outlined in Appendix B.

7.2.2.1 Two dimensional particle identification fits The two dimensional T_{π}^{pull} and Z_{π}^{pull} fits require templates that model each particle type and are determined using electrons from the conversion electron sample, pions and kaons from the tagged D^0 sample, and protons from the Λ sample. The functional form of the template is the same for each particle type and includes the product of two one dimensional functions, each of which is the sum of two Gaussians:

$$F_{particle}(Z_{\pi}^{pull}, T_{\pi}^{pull}) = \left[\frac{f_{T1}}{\sqrt{2\pi}\sigma_{T1}} e^{-\frac{1}{2} \frac{(T_{\pi}^{pull} - P_{T1})^2}{\sigma_{T1}^2}} + \frac{(1 - f_{T1})}{\sqrt{2\pi}\sigma_{T2}} e^{-\frac{1}{2} \frac{(T_{\pi}^{pull} - P_{T2})^2}{\sigma_{T2}^2}} \right] \times \quad (7.7)$$

$$\left[\frac{f_{Z1}}{\sqrt{2\pi}\sigma_{Z1}} e^{-\frac{1}{2} \frac{(Z_{\pi}^{pull} - P_{Z1})^2}{\sigma_{Z1}^2}} + \frac{(1 - f_{Z1})}{\sqrt{2\pi}\sigma_{Z2}} e^{-\frac{1}{2} \frac{(Z_{\pi}^{pull} - P_{Z2})^2}{\sigma_{Z2}^2}} \right].$$

The parameters with subscripts $T1$, $T2$, $Z1$, and $Z2$ are determined separately for each particle type and, along with the covariance matrices, propagated forward to the two dimensional fits of the third tracks in the J/ψ +track sample.

The third tracks in the J/ψ +track sample are fitted with a function of the form

$$F_{total}(Z_{\pi}^{pull}, T_{\pi}^{pull}) = f_{\pi} F_{\pi}(Z_{\pi}^{pull}, T_{\pi}^{pull}) + f_K F_K(Z_{\pi}^{pull}, T_{\pi}^{pull}) + \quad (7.8)$$

$$f_p F_p(Z_{\pi}^{pull}, T_{\pi}^{pull}) + f_e F_e(Z_{\pi}^{pull}, T_{\pi}^{pull}).$$

The parameters f_π , f_K , f_p , and f_e are the fractions for each particle type, and the functions $F_\pi(Z_\pi^{pull}, T_\pi^{pull})$, $F_K(Z_\pi^{pull}, T_\pi^{pull})$, $F_p(Z_\pi^{pull}, T_\pi^{pull})$, and $F_e(Z_\pi^{pull}, T_\pi^{pull})$ are of the form described in Eq. (7.7). Their parameters are constrained by the values and covariance matrices from the fits of tracks in the conversion electron, tagged D^0 , and Λ samples. Figure 46 shows the T_π^{pull} and Z_π^{pull} projections for one of the two dimensional fits. A full listing of the fit projections for can be found in Appendix D.

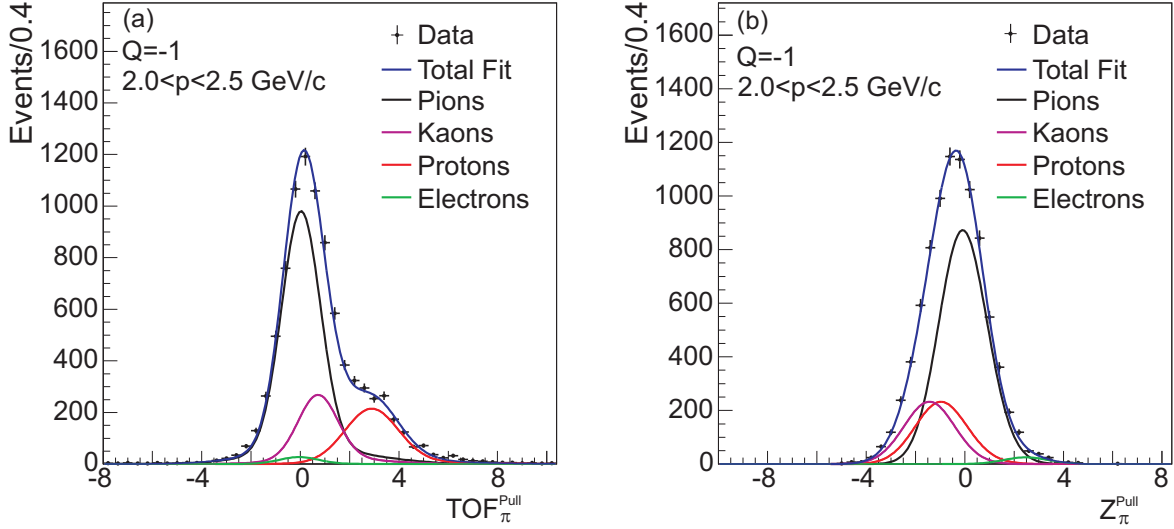


Figure 46: T_π^{pull} (a) and Z_π^{pull} (b) projections for an example two dimensional fit of third tracks in the electron channel J/ψ +track sample.

7.2.2.2 One dimensional particle identification fits For bins with $p > 3.0$ GeV/c, one dimensional Z_π^{pull} fits are carried out. As with the two dimensional fits, the templates for each particle type are fitted using the samples described in Appendix B. The one dimensional functions is the sum of two Gaussians:

$$F_{particle}(Z_{pull}) = \left[\frac{f_{Z1}}{\sqrt{2\pi}\sigma_{Z1}} e^{-\frac{1}{2} \frac{(Z_\pi^{pull} - P_{Z1})^2}{\sigma_{Z1}^2}} + \frac{(1 - f_{Z1})}{\sqrt{2\pi}\sigma_{Z2}} e^{-\frac{1}{2} \frac{(Z_\pi^{pull} - P_{Z2})^2}{\sigma_{Z2}^2}} \right]. \quad (7.9)$$

The fits of the third tracks in the J/ψ +track sample are carried out in a similar fashion to the two dimensional fits with a function of the form:

$$F_{total}(Z_\pi^{pull}) = f_\pi F_\pi(Z_\pi^{pull}) + f_K F_K(Z_\pi^{pull}) + f_p F_p(Z_\pi^{pull}) + f_e F_e(Z_\pi^{pull}). \quad (7.10)$$

The parameter f_p sets the fraction of protons and is constrained according to the PYTHIA based model outlined in Appendix C. All other fractions are determined solely by the fit. For the case of the muon channel J/ψ +track events, the electron component is not included since electrons have been removed. Figure 47 shows an example of a Z_π^{pull} fit. All other fits projections are shown in Appendix D.

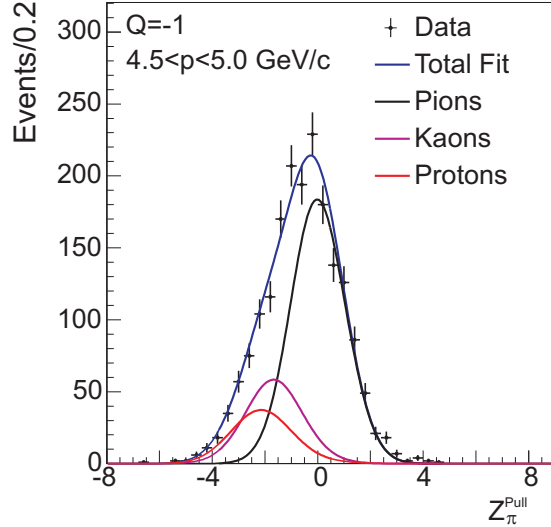


Figure 47: Example of a Z_π^{pull} of the third tracks in the muon channel J/ψ +track sample.

7.2.2.3 The muon fraction in the electron channel The fraction of muons in the electron channel J/ψ +track sample is assumed to be a component of the measured pion fractions since muons and pions have nearly identical TOF and dE/dx distributions. To determine the muon fraction, muons are identified as third tracks with associated hits in the CMU and CMX detectors. If the muon identification had perfect efficiency and coverage and zero misidentification probabilities, this method would give the number of muons in the sample. Since this is not the case, limitations of the measurements can be accounted for to make a determination the actual number of muons in the sample. One can write an equation for the number of identified muons, N_μ^{id} , for a given detector based on the true number of muons, N_μ , the fraction of muons in the detector fiducial, f_{fid} , the muon identification

efficiency, ϵ_{id} , the pion and kaon fractions in the sample, f_π and f_K , the pion and kaon muon misidentification rates, r_π and r_K , and the total number of events in the sample, N_T :

$$N_\mu^{id} = N_\mu \epsilon_{id} f_{fid} + N_T (f_\pi r_\pi f_{fid} + f_K r_K f_{fid}). \quad (7.11)$$

ϵ_{id} and r_π and r_K have been measured for the CMU and CMX detectors by CDF collaborators [88]. N_T , N_μ^{id} and f_{fid} are all measured in the J/ψ +track sample, and f_π and f_K are measured by the T_π^{pull} and Z_π^{pull} fits. Since the measured f_π is actually the true f_π plus the muon fraction, it should be replaced with $f_\pi - N_\mu/N_T$. Applying this transformation to f_π and solving the equation for N_μ yields:

$$N_\mu = \frac{N_\mu^{id}/f_{fid} - N_T(f_\pi r_\pi + f_K r_K)}{\epsilon_{id} - r_\pi} \quad (7.12)$$

This equation is applied for each momentum, charge, and ct^* to determine the number of muons that can be subtracted from the pion component. The data is split into $|\eta| < 0.6$, where the CMU detector is used, and $|\eta| > 0.6$, where the CMX detector is used.

7.2.2.4 Z_e^{pull} and Z_μ^{pull} cut efficiencies The particle fractions for the J/ψ +track samples after the Z_e^{pull} and Z_μ^{pull} cuts have been applied can be obtained by determining the efficiency of the cuts for each particle type and recalculating the fractions based on the efficiencies. The efficiencies are determined for electrons using the conversion sample, pions and kaons using the tagged D^0 sample, protons using the Λ sample, and muons using the J/ψ sample by applying the Z_e^{pull} or Z_μ^{pull} cut to the particle being studied. The momentum dependent efficiencies are shown in figure 48. Given the efficiencies and the fractions measured before the Z^{pull} cuts, f_π , f_K , etc., the fractions can be recalculated using the efficiencies:

$$f_\pi^z = \frac{\epsilon_\pi^z f_\pi}{\epsilon_\pi^z f_\pi + \epsilon_K^z f_K + \epsilon_p^z f_p + \epsilon_e^z f_e}. \quad (7.13)$$

Here, f_π^z is the expected pion fraction after the cut, and the $\epsilon_{\pi\dots e}^z$ are the measured cut efficiencies for each particle type.

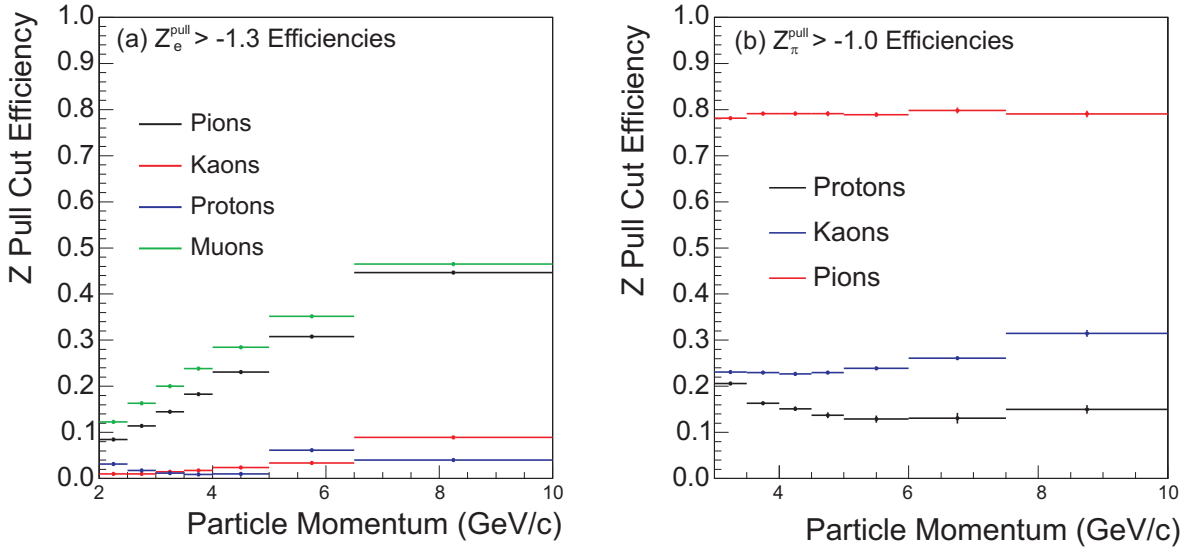


Figure 48: Efficiencies for particle types to pass the $Z_e^{pull} > -1.3$ (a) and $Z_\mu^{pull} > -1.0$ (b) cuts.

7.2.2.5 Final particle fractions The two dimensional T_π^{pull} and Z_π^{pull} fits and the one dimensional Z_π^{pull} fits are carried out for third tracks grouped into samples based on charge, momentum, and ct^* . The resulting particles fractions for third tracks are plotted in Figures 49 and 50 for the electron channel and muon channel, respectively.

7.2.3 Misidentified lepton ct^* fits

If the measured lepton misidentification probabilities and third track particle fractions are known, the J/ψ +track samples can be reweighted to determine the misidentified lepton background normalization and ct^* and σ_{ct^*} distributions. The samples of J/ψ +track events to which the weighting is applied contain both signal and background J/ψ events that are vertexed with a third track. Events with a misidentified J/ψ as well as a misidentified lepton are included as part of the misidentified J/ψ background determination, and this type of events should be subtracted from the misidentified lepton background to avoid double counting. This is done by first applying the weighting method used for J/ψ +track candidates

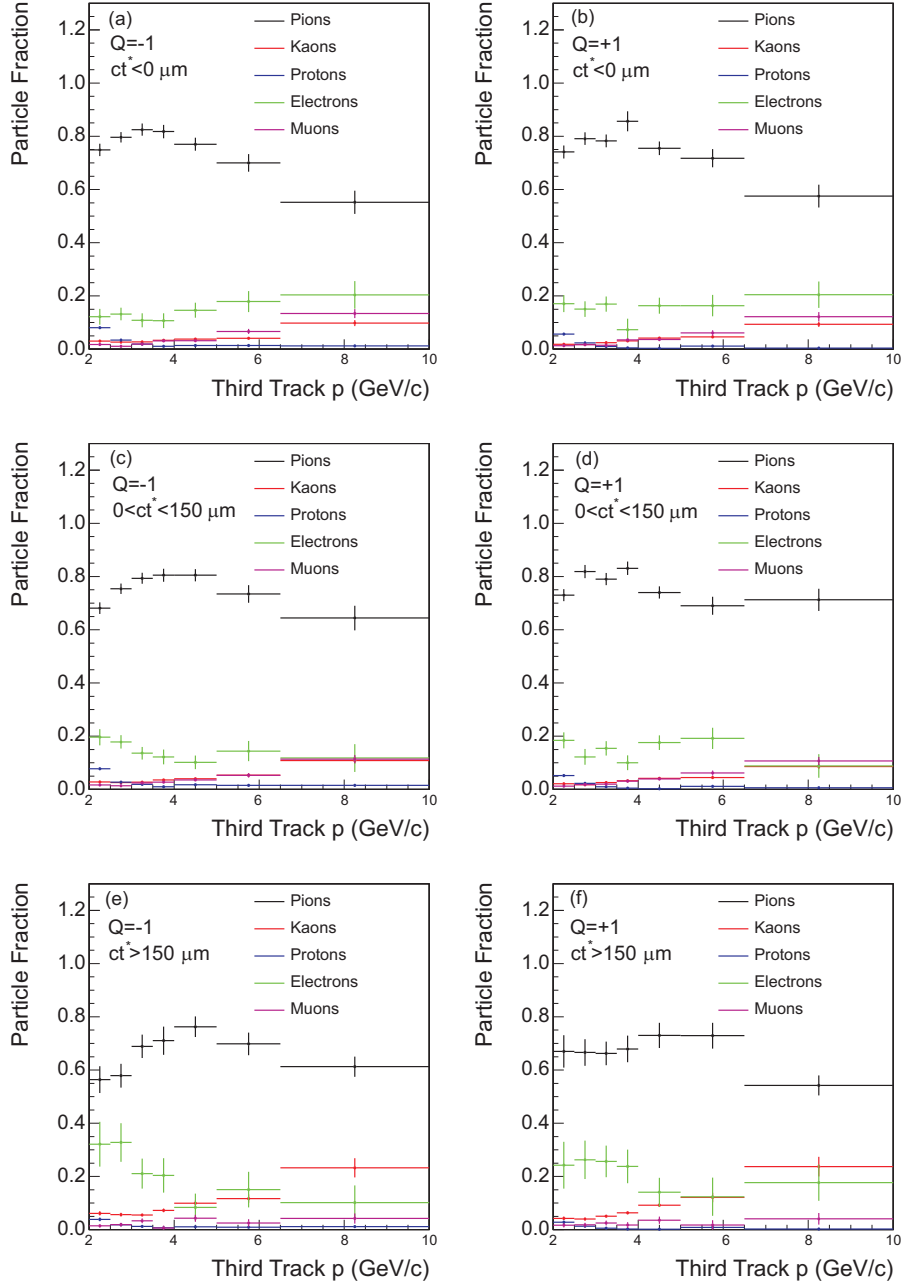


Figure 49: Particle fractions for third tracks in the electron channel J/ψ +track sample grouped in $q = -1$, $ct^* < 0 \mu\text{m}$ (a), $q = 1$, $ct^* < 0 \mu\text{m}$ (b), $q = -1$, $0 < ct^* < 150 \mu\text{m}$ (c), $q = 1$, $0 < ct^* < 150 \mu\text{m}$ (d), $q = -1$, $ct^* > 150 \mu\text{m}$ (e), and $q = 1$, $ct^* > 150 \mu\text{m}$ (f) bins.

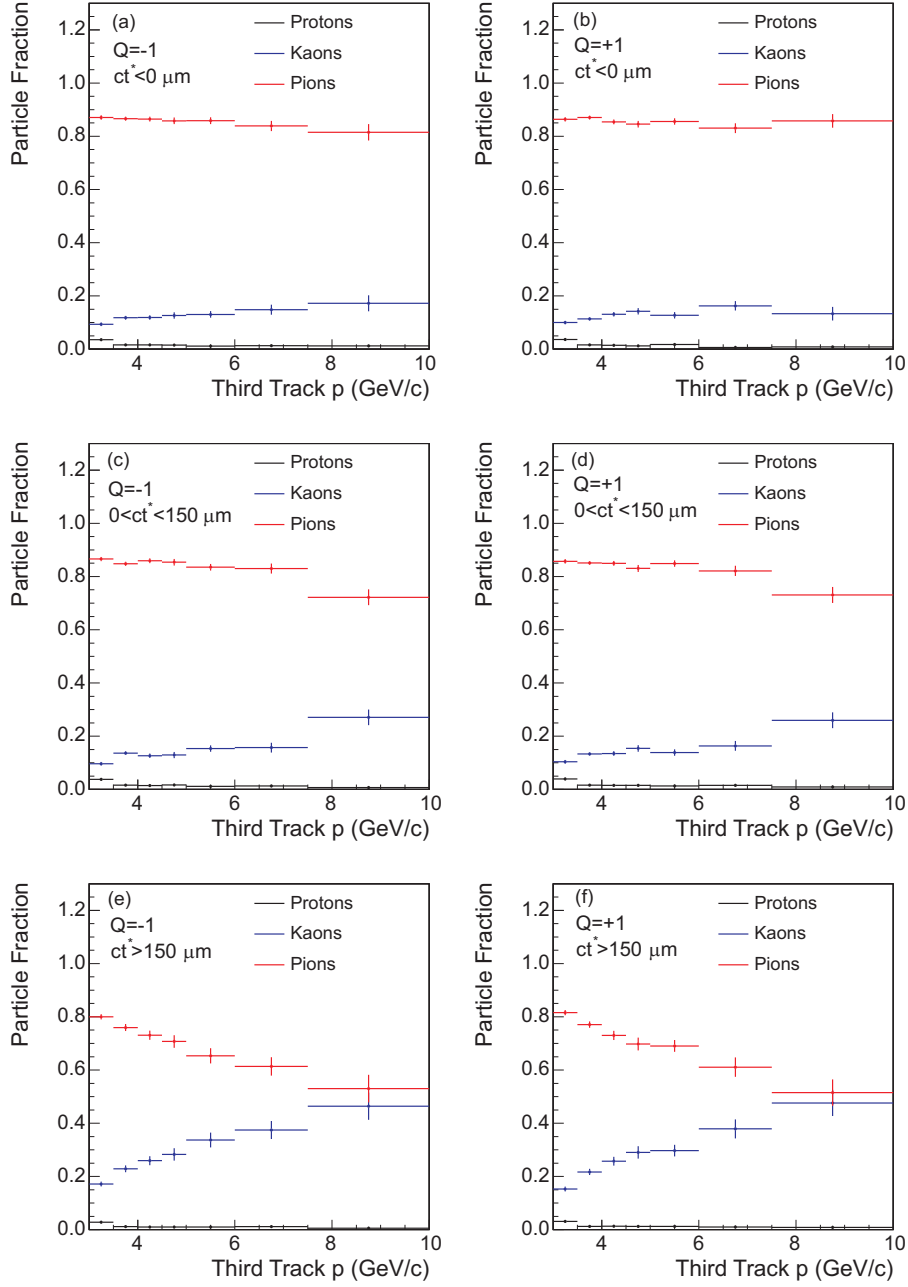


Figure 50: Particle fractions for third tracks in the muon channel J/ψ +track sample grouped in $q = -1$, $ct^* < 0 \mu\text{m}$ (a), $q = 1$, $ct^* < 0 \mu\text{m}$ (b), $q = -1$, $0 < ct^* < 150 \mu\text{m}$ (c), $q = 1$, $0 < ct^* < 150 \mu\text{m}$ (d), $q = -1$, $ct^* > 150 \mu\text{m}$ (e), and $q = 1$, $ct^* > 150 \mu\text{m}$ (f) bins.

but with the J/ψ mass window shifted to the sideband regions. The ct^* and σ_{ct^*} of events from the sidebands are fitted and the parameters are propagated to the fits of the J/ψ signal region to constrain the contributions from events with a misidentified J/ψ . The fitted J/ψ mass peaks for the J/ψ +track samples with the signal and sideband regions highlighted can be seen in Figure 51.

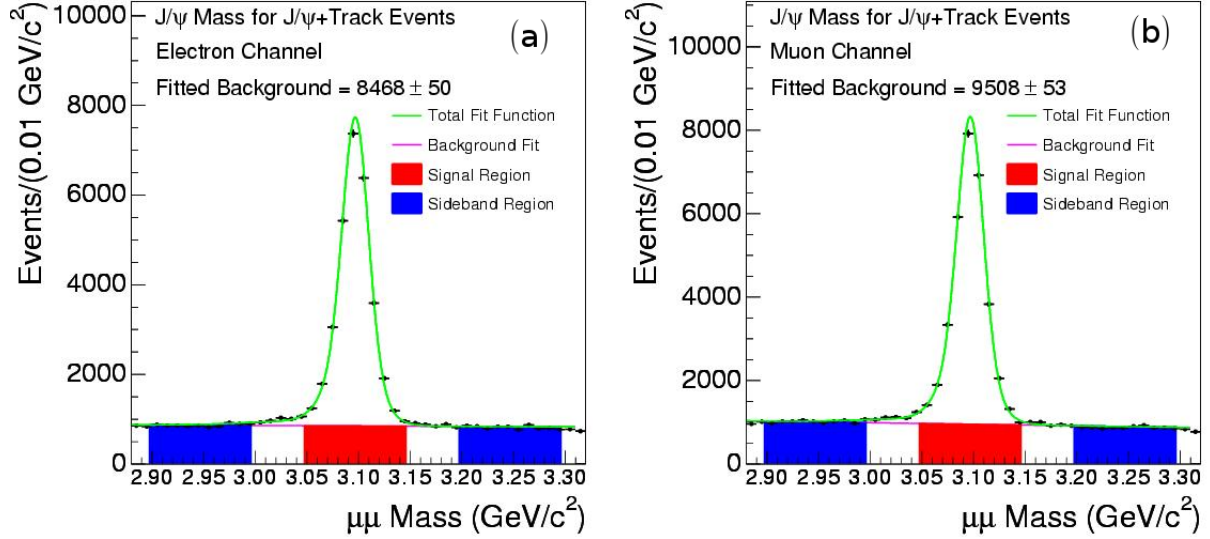


Figure 51: Fitted J/ψ mass peaks for electron (a) and muon channel (b) J/ψ +track samples.

Since the J/ψ +track events need to be weighted to model the misidentified lepton background, the method outlined in Section 5.4.1 for likelihood fits of a weighted sample is used. For the case of the sideband events, the PDF for the ct^* distributions is defined as:

$$L = e^{-\frac{1}{2}V_W^T C_w^{-1} V_W} \prod_i \frac{A(\sigma_{ct^*i})}{W_{MM}(ct_i^*)} F_{MM}(ct_i^*, \sigma_{ct^*i}) \quad (7.14)$$

The index i is over the sideband J/ψ +track events, $F_{MM}(ct_i^*, \sigma_{ct^*i})$ is the PDF that describes the reweighted sample, and $1/W_{MM}(ct_i^*)$ is the inverse of the ct^* dependent misidentification weighting. $1/W_{MM}(ct_i^*)$ is determined by calculating the average weighting for the sample in bins of ct^* and fitting the distribution. Figure 52 shows an example of the fitted $1/W_{MM}(ct_i^*)$ for the muon channel sideband J/ψ +track sample. The parameters that describe $1/W_{MM}(ct_i^*)$ are constrained by V_W , the vector describing the displacement of the

parameters from their previously fitted values, and C_W , the covariance matrix describing the uncertainty of the fitted parameters. By dividing $F_{MM}(ct_i^*, \sigma_{ct^*i})$ by $W_{MM}(ct_i^*)$, a PDF is constructed that describes the unweighted sample in terms of the PDF that describes the reweighted sample. This PDF must be normalized to one, so $A(\sigma_{ct^*i})$, which also depends on the parameters in the fit, is defined to satisfy the condition

$$\int_{-\infty}^{\infty} \frac{A(\sigma_{ct^*i})}{W_{MM}(ct_i^*)} F_{MM}(ct^*, \sigma_{ct^*i}) d(ct^*) = 1. \quad (7.15)$$

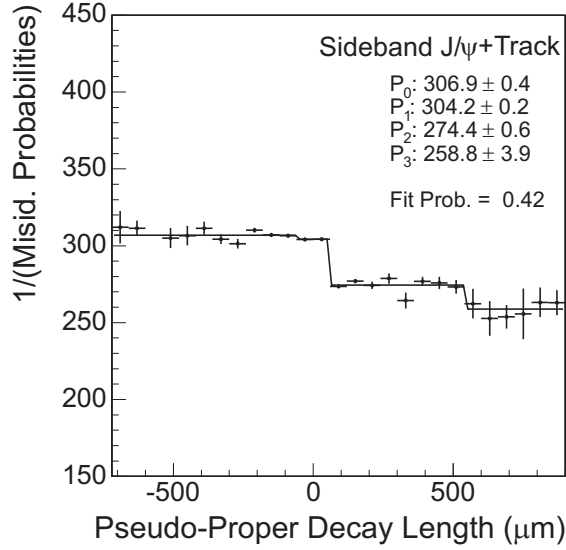


Figure 52: Fitted $1/W_{MM}(ct_i^*)$ for the muon channel sideband J/ψ +track events.

$F_{MM}(ct^*, \sigma_{ct^*i})$ is written in terms of the fit parameters as:

$$F_{MM}(ct^*, \sigma) = [f_0 \delta(ct^*) + \frac{f_1}{c\tau_1} e^{-\frac{ct^*}{c\tau_1}} \theta(ct^*) + \frac{f_2}{c\tau_2} e^{\frac{ct^*}{c\tau_2}} \theta(ct^*) + \frac{f_3}{c\tau_3} e^{-\frac{ct^*}{c\tau_3}} \theta(ct^*) + \frac{f_5}{c\tau_5} e^{\frac{ct^*}{c\tau_5}} \theta(-ct^*)] \otimes \frac{1}{\sqrt{2\pi s\sigma}} e^{-\frac{1}{2}(\frac{ct^*}{s\sigma})^2} \quad (7.16)$$

The parameters $c\tau_{1..5}$ are decay constants for positive and negative lifetime components of the background, $f_{1..5}$ are the fractions for the various components and s is the scaling for the measured per event σ_{ct^*} . $\delta(ct^*)$ is the Dirac delta function, and $\theta(ct^*)$ is the Heaviside step

function. The functional form of this PDF is motivated by the expectation of prompt and exponential components for the background, although the specific combination of terms is chosen for the best empirical result.

The weighted sideband events for both the muon and electron channels are fitted and the resulting $F_{MM}(ct_i^*, \sigma_i)$ distributions overlaid on the reweighted events are shown in Figure 53. The fitted parameter values for both channels are listed in Table 14.

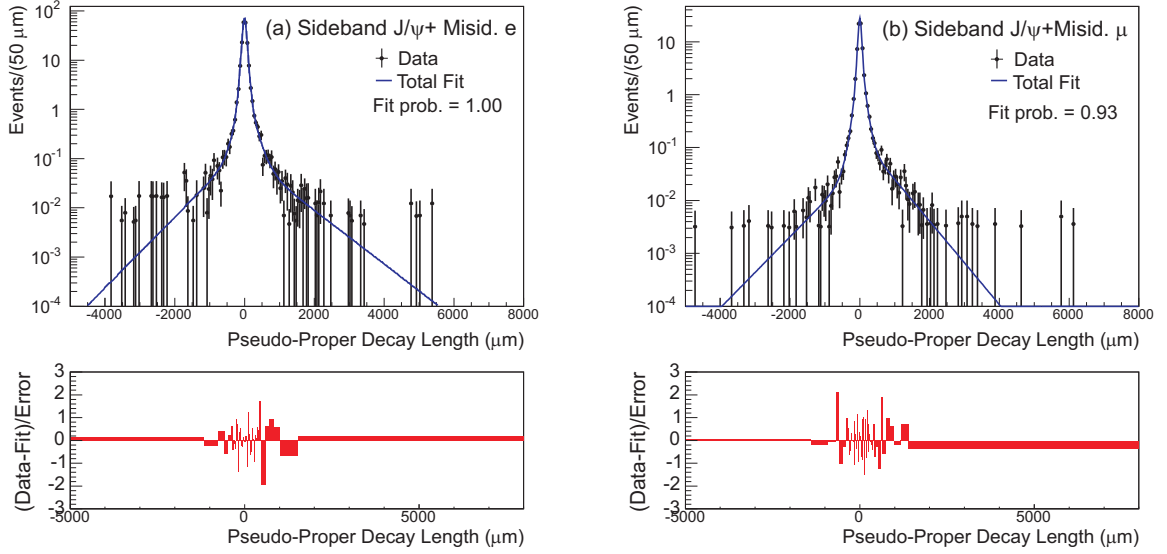


Figure 53: Fit functions overlaid on the reweighted ct^* distributions for electron (a) and muon (b) channel sideband J/ψ +track events.

With a functional form and fitted parameters to describe the events with misidentified J/ψ and misidentified leptons, it is possible to fit events in the signal region while constraining the component from misidentified J/ψ . The likelihood function for the signal region contains terms for events with misidentified and true J/ψ , as well as constraints for parameters determined by the fit of the sideband events and the weighting function:

$$L = e^{-\frac{1}{2}V_W^T C_W^{-1} V_W} e^{-\frac{1}{2}V_{MM}^T C_{MM}^{-1} V_{MM}} \prod_i [f_{sig} \frac{A_{ML}(\sigma_{ct^*i})}{W_{ML}(ct^*)} F_{ML}(ct_i^*, \sigma_{ct^*i}) + (1 - f_{sig}) \frac{A_{MM}(\sigma_{ct^*i})}{W_{MM}(ct^*)} F_{MM}(ct_i^*, \sigma_{ct^*i})]. \quad (7.17)$$

Parameter	Electron Channel		Muon Channel	
	Fit Value	Error	Fit Value	Error
s	1.167	0.024	1.104	0.023
f_0	0.600	0.357	0.730	0.029
$c\tau_1$ (μm)	797	254	87.4	7.1
f_1	0.0088	0.0044	0.126	0.012
$c\tau_2$ (μm)	46.2	12.2	67.8	20.4
f_2	0.157	0.041	0.080	0.041
$c\tau_3$ (μm)	164	75	551	47
f_3	0.043	0.003	0.024	0.003
$c\tau_4$ (μm)	126	72	127	54
f_4	0.039	0.004	0.028	0.019
$c\tau_5$ (μm)	51.0	13.2	647	133
f_5	0.140	0.029	0.008	0.003

Table 14: Parameters from the ct^* fits to reweighted sideband J/ψ +track events.

$F_{MM}(ct_i^*, \sigma_{ct^*i})$ and $1/W_{MM}(ct^*)$ have the same definition as the previous fit, and the parameters that describe them are constrained by V_{MM} and C_{MM} . V_{MM} is a vector that contains the difference between the parameters and their previously fitted values. C_{MM} is the covariance matrix that describes the uncertainties on the previously fitted values of the parameters. $1/W_{ML}(ct^*)$ is defined in the same manner as $1/W_{MM}(ct^*)$, but using events in the J/ψ signal region. V_W and C_W constrain the parameters that describe $1/W_{ML}(ct^*)$. $A_{ML}(\sigma_{ct^*i})$ and $A_{MM}(\sigma_{ct^*i})$ normalize the true and misidentified J/ψ terms, respectively, while f_{sig} defines the fraction of true J/ψ events. $F_{ML}(ct_i^*, \sigma_i)$ is the PDF for the true J/ψ component and is described in terms of its parameters:

$$F_{ML}(ct^*, \sigma_{ct^*}) = [f_0 \delta(ct^*) + \frac{f_+}{c\tau_+} e^{\frac{-ct^*}{c\tau_+}} \theta(ct^*) + \frac{f_{++}}{c\tau_{++}} e^{\frac{-ct^*}{c\tau_{++}}} \theta(ct^*) + \frac{f_-}{c\tau_-} e^{\frac{ct^*}{c\tau_-}} \theta(-ct^*)] \quad (7.18)$$

$$\otimes \frac{1}{\sqrt{2\pi s\sigma}} e^{-\frac{1}{2}(\frac{ct^*}{s\sigma_{ct^*}})^2}.$$

The parameters $c\tau_{+,++, -}$ are positive or negative lifetime decay constants, while $f_{0,+,++, -}$ constrain the relative fractions for components in the function. s scales the per event σ_{ct^*} to give the width of the experimental resolution function. The functional form of one prompt component and two positive lifetime components is expected as the J/ψ in the sample can be created at the primary interaction point (prompt) or through B decays (long lived). An additional negative lifetime component is added to improve agreement with data.

The likelihood function is fitted to the J/ψ +track samples, giving parameters for $F_{ML}(ct^*, \sigma)$ which describes the ct^* distributions of the misidentified lepton background. Figure 54 shows the resulting $F_{FL}(ct^*, \sigma)$ and $F_{MM}(ct^*, \sigma)$ functions overlaid on the weighted ct^* distributions from the J/ψ +track samples. The fitted parameters for $F_{ML}(ct^*, \sigma)$ are listed in Table 15.

7.2.4 Misidentified lepton σ_{ct^*} fits

The fits of the σ_{ct^*} distributions follow the same procedure as that used for fitting ct^* . The misidentified and true J/ψ events are both fitted with a PDF of the form:

$$P_{XX}(\sigma) = \frac{1}{\sqrt{2\pi P_0}} e^{-\frac{1}{2}(\frac{\sigma_{ct^*}}{P_0})^2} \otimes \left[\frac{P_5}{P_1} e^{-\frac{(\sigma_{ct^*} - P_2)}{P_1}} \theta(\sigma_{ct^*} - P_2) \right. \quad (7.19)$$

$$\left. + \frac{(1 - P_5)}{P_3} e^{-\frac{(\sigma_{ct^*} - P_4)}{P_3}} \theta(\sigma_{ct^*} - P_4) \right].$$

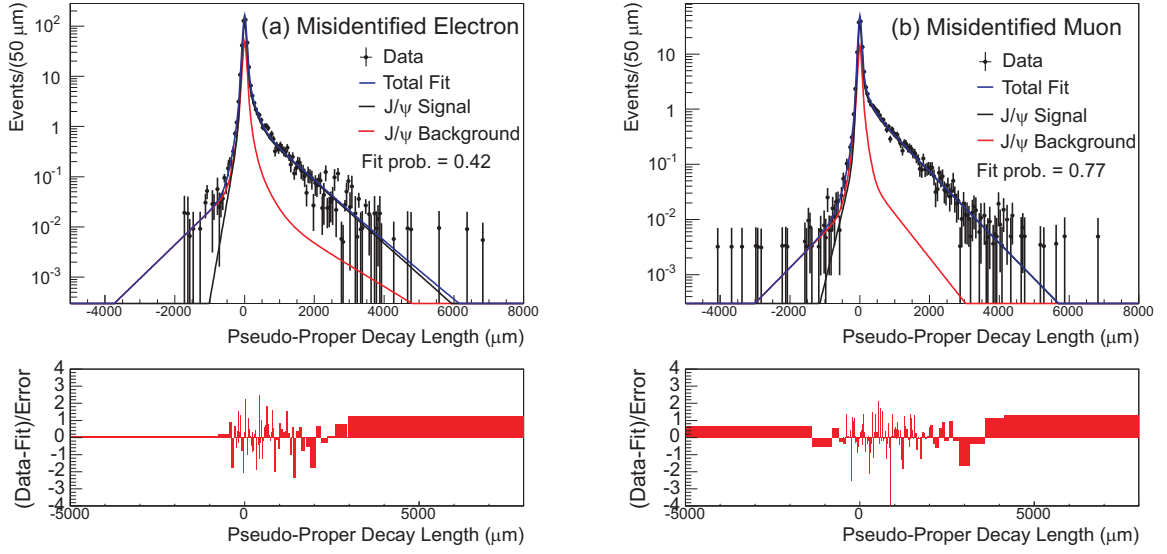


Figure 54: Fitted functions overlaid on the reweighted ct^* distributions for electron (a) and muon (b) channel J/ψ +track events.

	Electron Channel		Muon Channel	
Parameter	Fit Value	Error	Fit Value	Error
s	1.274	0.016	1.180	0.013
f_0	0.831	0.017	0.715	0.013
$c\tau_{++} (\mu\text{m})$	675	45	674	29
f_{++}	0.064	0.007	0.197	0.017
$c\tau_{+} (\mu\text{m})$	138	25	161	45
f_{+}	0.083	0.008	0.078	0.011
$c\tau_{-} (\mu\text{m})$	114	31	168	49
f_{-}	0.019	0.007	0.009	0.004

Table 15: Parameters from the ct^* fits to reweighted J/ψ +track events.

The form of this PDF is chosen empirically to allow for good agreement with the data. The resulting fits of the weighted σ_{ct^*} distributions for the J/ψ sideband regions are shown in Figure 55. The subsequent fits of the J/ψ signal region are shown in Figure 56 and the fitted parameters for events with true J/ψ are listed in Table 16.

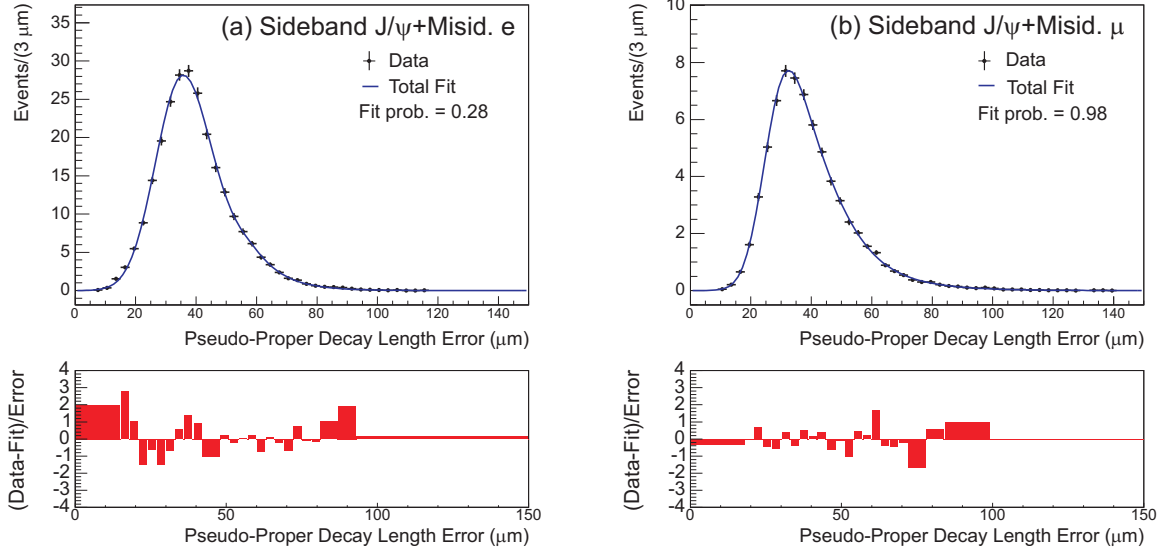


Figure 55: Fitted functions overlaid on the reweighted σ_{ct^*} distributions for electron (a) and muon (b) channel sideband J/ψ +track events.

7.2.5 Misidentified lepton normalization

The normalization of the misidentified lepton sample is evaluated by applying the weighting to events in the J/ψ +track sample and subtracting out 1/2 times the weighted normalization of the J/ψ sideband regions to avoid double counting with the misidentified J/ψ background. The statistical error on the number of events in the J/ψ +track sample as well as the errors for the lepton misidentification probabilities and particle fractions are propagated to the error estimates for the normalizations. The calculated normalizations are 312.0 ± 4.1 and 96.1 ± 4.6 events for the electron and muon channels, respectively.

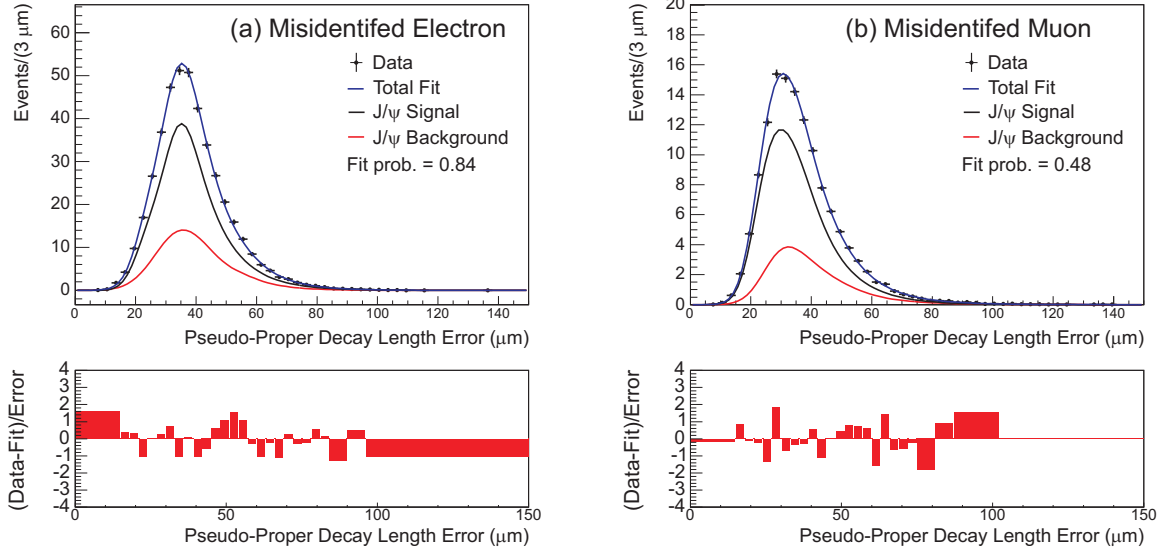


Figure 56: Fitted functions overlaid on the reweighted σ_{ct^*} distributions for electron (a) and muon (b) channel J/ψ +track events.

	Electron Channel		Muon Channel	
Parameter	Fit Value	Error	Fit Value	Error
P_0 (μm)	4.37	0.15	4.83	0.21
P_1 (μm)	10.48	1.67	11.68	0.44
P_2 (μm)	22.52	0.39	22.81	0.54
P_3 (μm)	10.43	0.41	8.74	1.57
P_4 (μm)	32.17	0.311	31.70	1.67
P_5 (μm)	0.352	0.043	0.800	0.081

Table 16: Parameters from the σ_{ct^*} fits to reweighted J/ψ +track events.

7.3 $b\bar{b}$ BACKGROUND

Events where the J/ψ and the third lepton are produced in the decay chains of different b quarks are the source of $b\bar{b}$ background events. As illustrated in Figure 57, these types of events are selected when the third lepton happens to point back to the vertex of the two muons that form the J/ψ candidate. Since the event selection also includes the $\Delta\phi < \pi/2$ cut between the J/ψ and third lepton, there must be a source of $b\bar{b}$ with small opening angle for this background to be significant.

The $b\bar{b}$ background cannot be modeled directly with data, so a realistic Monte Carlo simulation of $b\bar{b}$ events generated in PYTHIA is used. The PYTHIA sample is tuned and validated with data samples that are similar to the samples used in the lifetime measurement but that have been adjusted to enhance the $b\bar{b}$ components. The tuned PYTHIA sample is then used to determine the number of $b\bar{b}$ events in the B_c candidate samples and to model the ct^* and σ_{ct^*} distributions of $b\bar{b}$ background events.

7.3.1 The $b\bar{b}$ PYTHIA sample and its tuning

The PYTHIA sample, as described in Appendix A, includes the production of $b\bar{b}$ by $2 \rightarrow 2$ processes with initial and final state radiation where the CTEQ5L parton distributions that model the proton structure are used [31]. Figure 58 illustrates some of the production processes that PYTHIA models. In general, the $b\bar{b}$ production is classified into three groups of QCD processes:

- Flavor Creation (FC) – A $q\bar{q}$ pair annihilates or a gg pair fuses to form a $b\bar{b}$ pair in the final state. In these event the subsequent b quark jets are typically back to back.
- Flavor Excitation (FE) – A virtual b quark in the initial state scatters into the final state. The $b\bar{b}$ pair can have a smaller opening angle than in FC production.
- Gluon Splitting (GS) – A gluon in the initial state scatters and splits leaving a $b\bar{b}$ pair in the final state. This category also includes any $b\bar{b}$ production through a parton shower. Since the $b\bar{b}$ originates from a single parton, the pair can have a small opening angle.

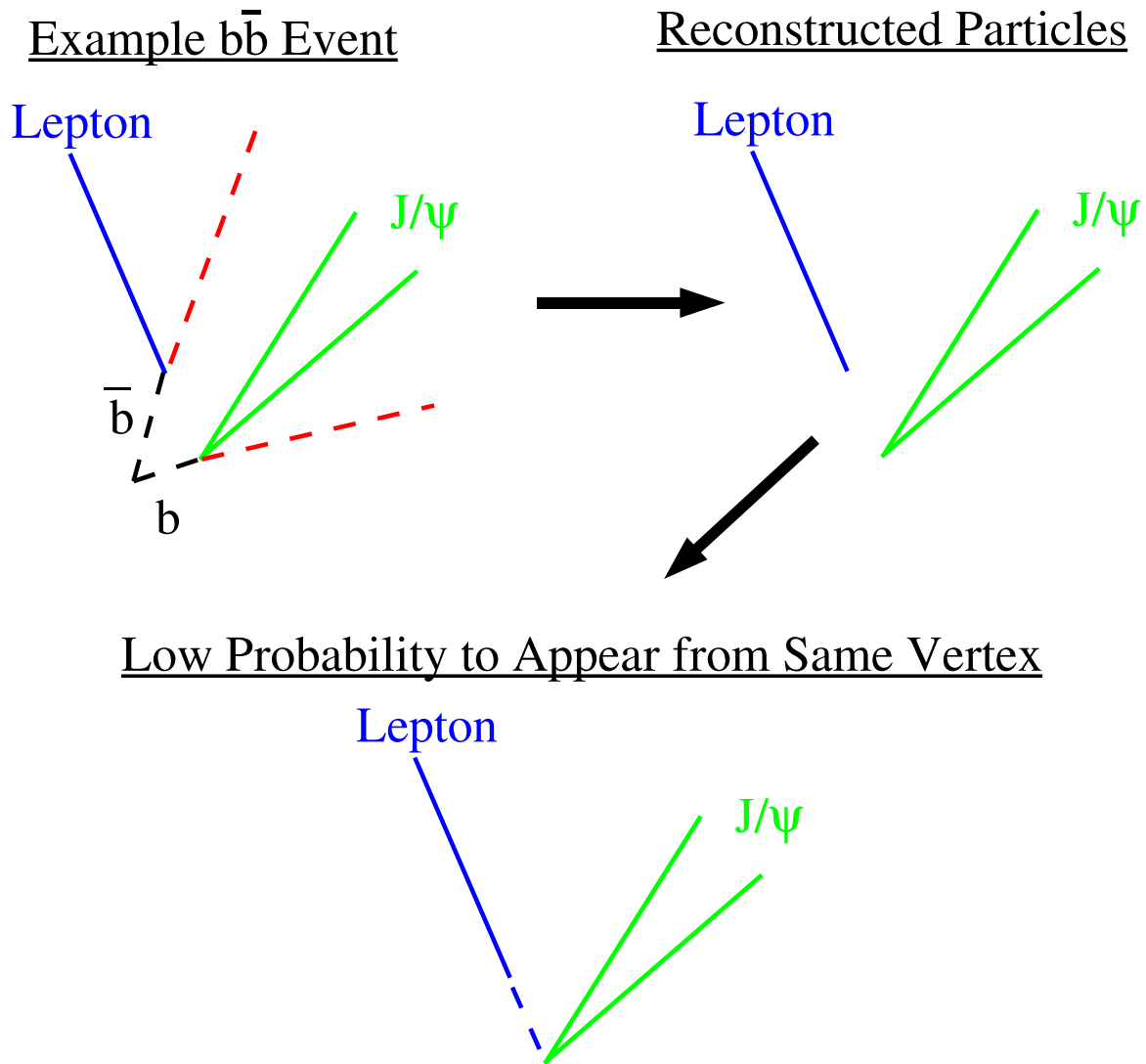


Figure 57: Diagram showing how a $b\bar{b}$ event makes it into the B_c candidate sample.

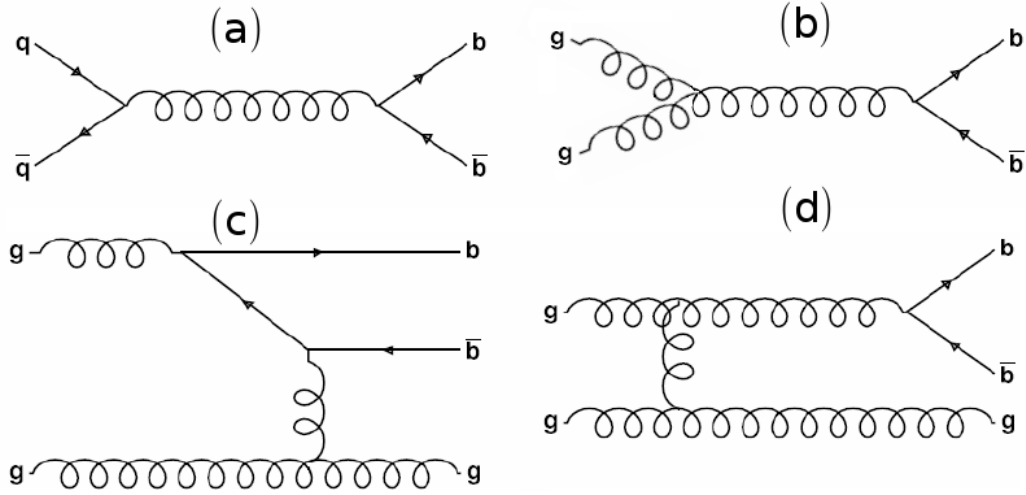


Figure 58: Leading order gluon fusion (a) and $q\bar{q}$ annihilation (b) and next to leading order scattering of a virtual b quark (c) and splitting of an excited gluon (d) QCD processes for $b\bar{b}$ production.

The properties of the $b\bar{b}$ events as determined by the PYTHIA sample depend on the relative fractions of FC, FE, and GS in the sample. Since the relative production is not strongly constrained by theory or experiment, studies comparing the PYTHIA sample to data determine the tuning of the relative fractions of FC, FE, and GS in the sample and the uncertainties in these tuned fractions. Typically these types of studies look at measured quantities that depend on the correlations of the two b quarks, such as the opening angle or difference in transverse momentum. Previous studies of $b\bar{b}$ production in data compared to simulation with specific parton distribution models used correlated measurements and suggest an enhancement of the GS component for the best agreement [92, 93].

A sample that is similar to the B_c candidate $J/\psi + l^\pm$ sample is used to study and tune the PYTHIA sample. Beginning with the $J/\psi + l^\pm$ candidates, the vertex probability and $\Delta\phi$ cuts are removed to enhance the $b\bar{b}$ contribution. Since the residual conversion background is also enhanced in this case, only $J/\psi + \mu^\pm$ events are used. This “unvertexed” sample is enhanced in $b\bar{b}$, but it contains two sources of events that are difficult to model: promptly produced J/ψ and B_c decays. To remove the prompt J/ψ events, a significance cut is applied

to the L_{xy} of the J/ψ vertex, $L_{xy}/\sigma_{L_{xy}} > 3.0$. Removal of the B_c component is possible after the definition of the variable $d_0^{\mu-J/\psi}$, the impact parameter of the third muon with respect to the J/ψ vertex. Figure 59 illustrates $d_0^{\mu-J/\psi}$ for $J/\psi + \mu^\pm$ sources, and one can see that B_c events are sharply peaked near zero, while the distribution for $b\bar{b}$ events is quite broad. The cut $d_0^{\mu-J/\psi} > 0.01$ cm removes nearly all of the B_c contribution while removing only $\sim 1/6$ of the $b\bar{b}$.

Given the “unvertexed” sample of $J/\psi + \mu^\pm$ events, one must determine the measured quantities that can be studied to best understand the relative normalizations of the production processes in the PYTHIA sample. Possible variables are:

- $\Delta\phi$ – the azimuthal opening angle between the J/ψ and the third muon
- $\Delta\eta$ – the pseudorapidity difference between the J/ψ and the third muon
- Δp_T – the p_T difference between the J/ψ and the third muon
- $p_T^{J/\psi}$ – the J/ψ p_T
- p_T^μ – the third muon p_T

Figures 60 and 61 show the mean and root mean square values, respectively, for each of the QCD production mechanisms, for each variable listed above. It is clear that based on the first two moments of the distributions that $\Delta\phi$ offers the most discriminating power between the QCD processes, and it is used for the study and tuning of the PYTHIA sample.

Figure 62 shows the fitted $\Delta\phi$ distributions for the different QCD processes in the PYTHIA sample. The goal is to fit the $\Delta\phi$ distribution in data using these templates, while allowing the relative amounts of the QCD processes to vary. This is complicated by a couple of issues. First, $b\bar{b}$ events are not the only source of $J/\psi + \mu^\pm$ events in the “unvertexed” sample. Events with misidentified J/ψ and misidentified third muons also contribute. These sources of events can be modeled using the same methods used for the B_c lifetime measurement. Figure 63 shows the fitted $\Delta\phi$ distributions for misidentified J/ψ and misidentified muon events. The predicted contributions from misidentified J/ψ and third muons are 97.0 ± 7.0 and 61.8 ± 3.4 events, respectively.

The second complication to the $\Delta\phi$ fitting procedure is the method to be used for setting the normalization of the $b\bar{b}$ components. One possibility is to allow the normalizations of

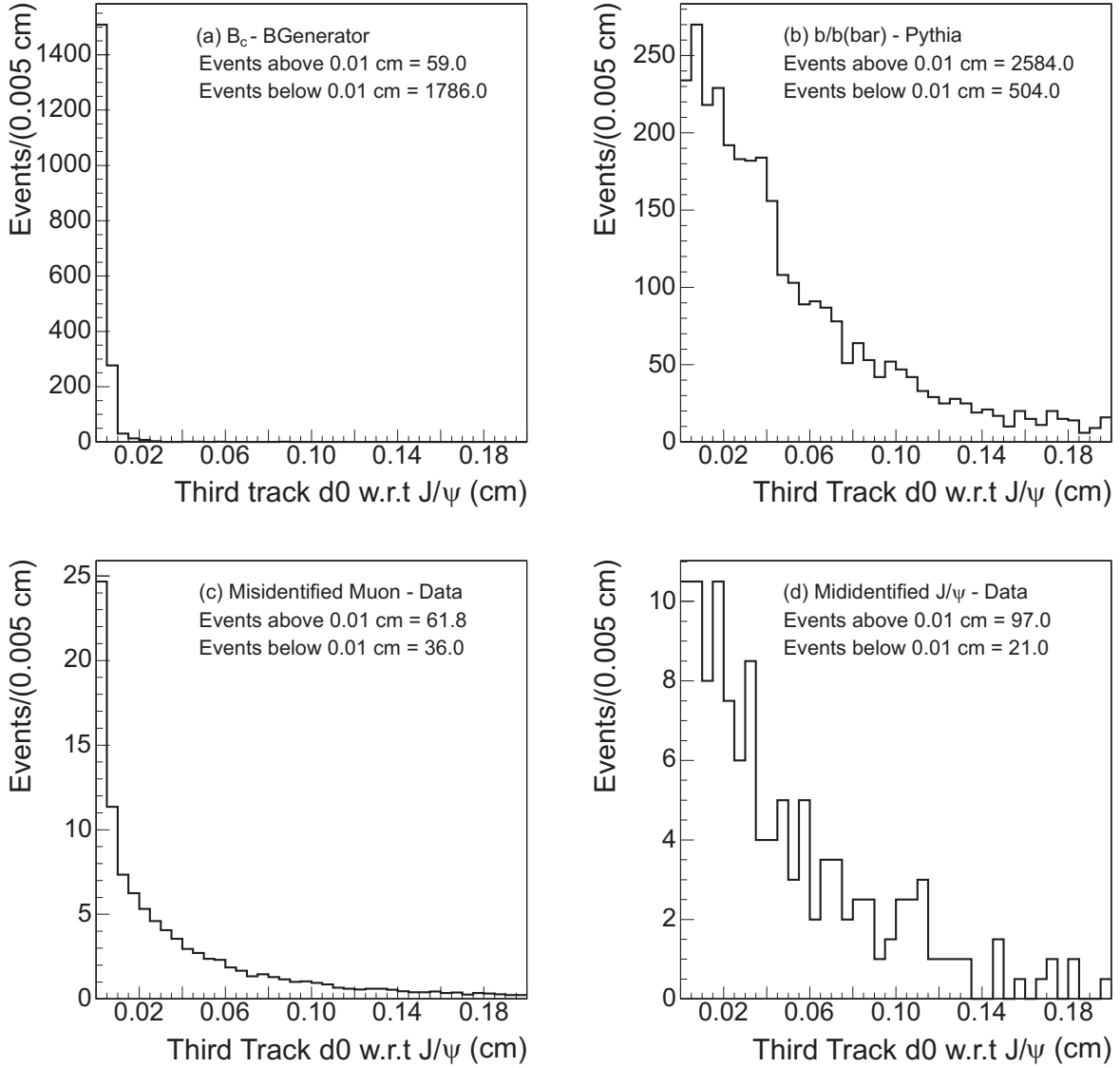


Figure 59: Distributions of $d_0^{\mu-J/\psi} > 0.01$ for the four non-prompt sources: B_c decays (a), $b\bar{b}$ (b), misidentified third muons (c), and misidentified J/ψ (d).

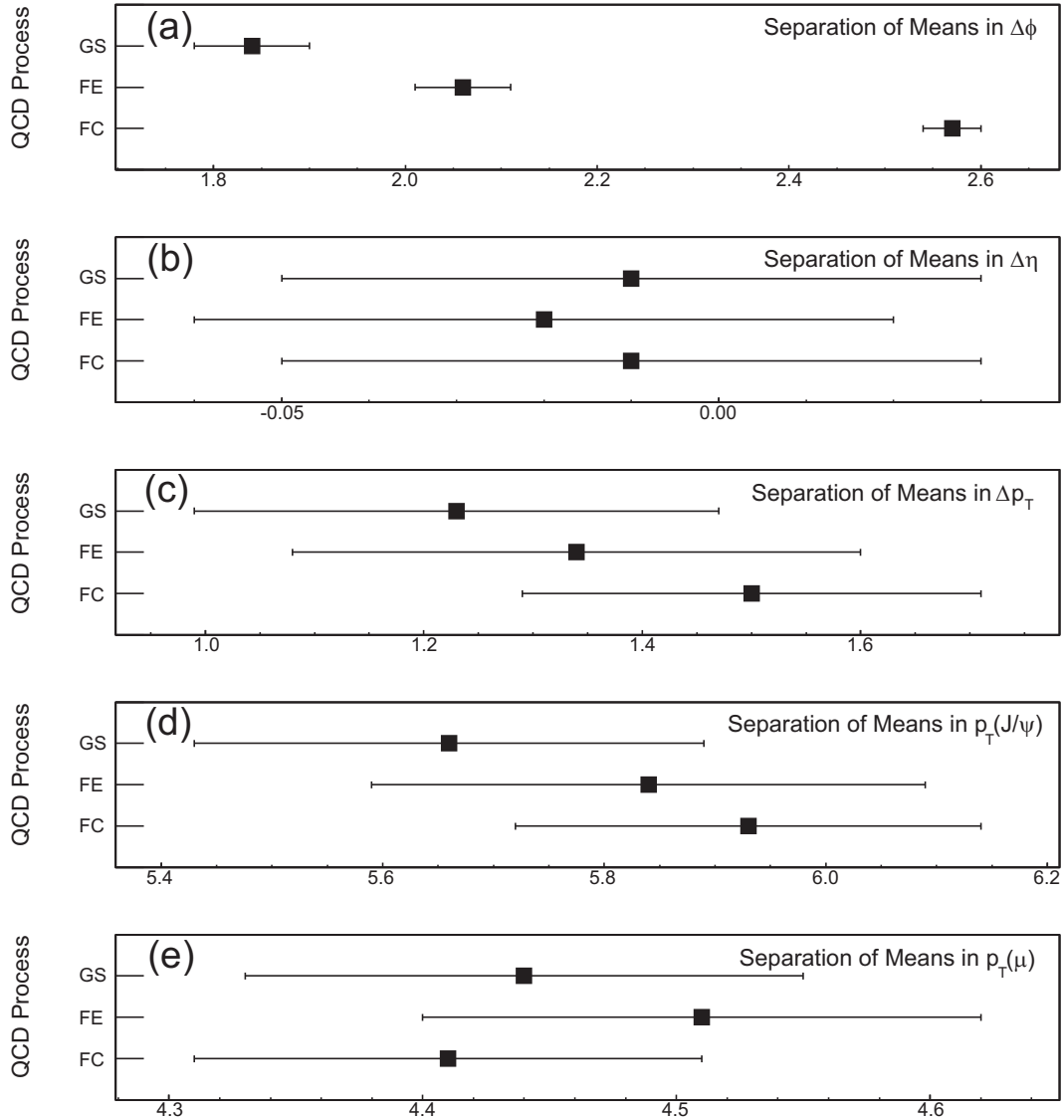


Figure 60: Comparisons between QCD production processes of the mean values for the measured quantities $\Delta\phi$ (a), $\Delta\eta$ (b), Δp_T (c), $J/\psi p_T$ (d), and third muon p_T (e).

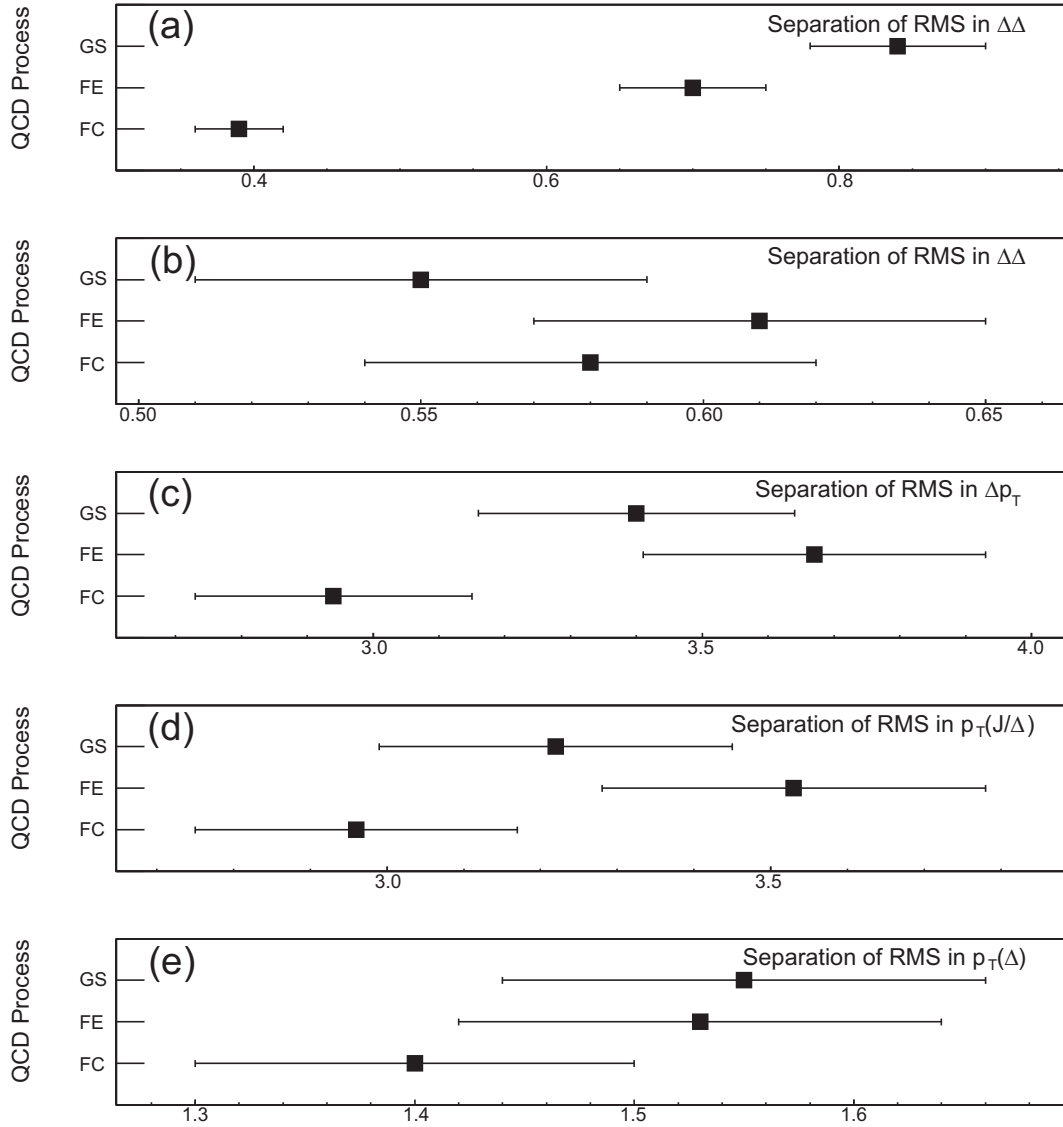


Figure 61: Comparisons between QCD production processes of the root mean squared values for the measured quantities $\Delta\phi$ (a), $\Delta\eta$ (b), Δp_T (c), $J/\psi p_T$ (d), and third muon p_T (e).

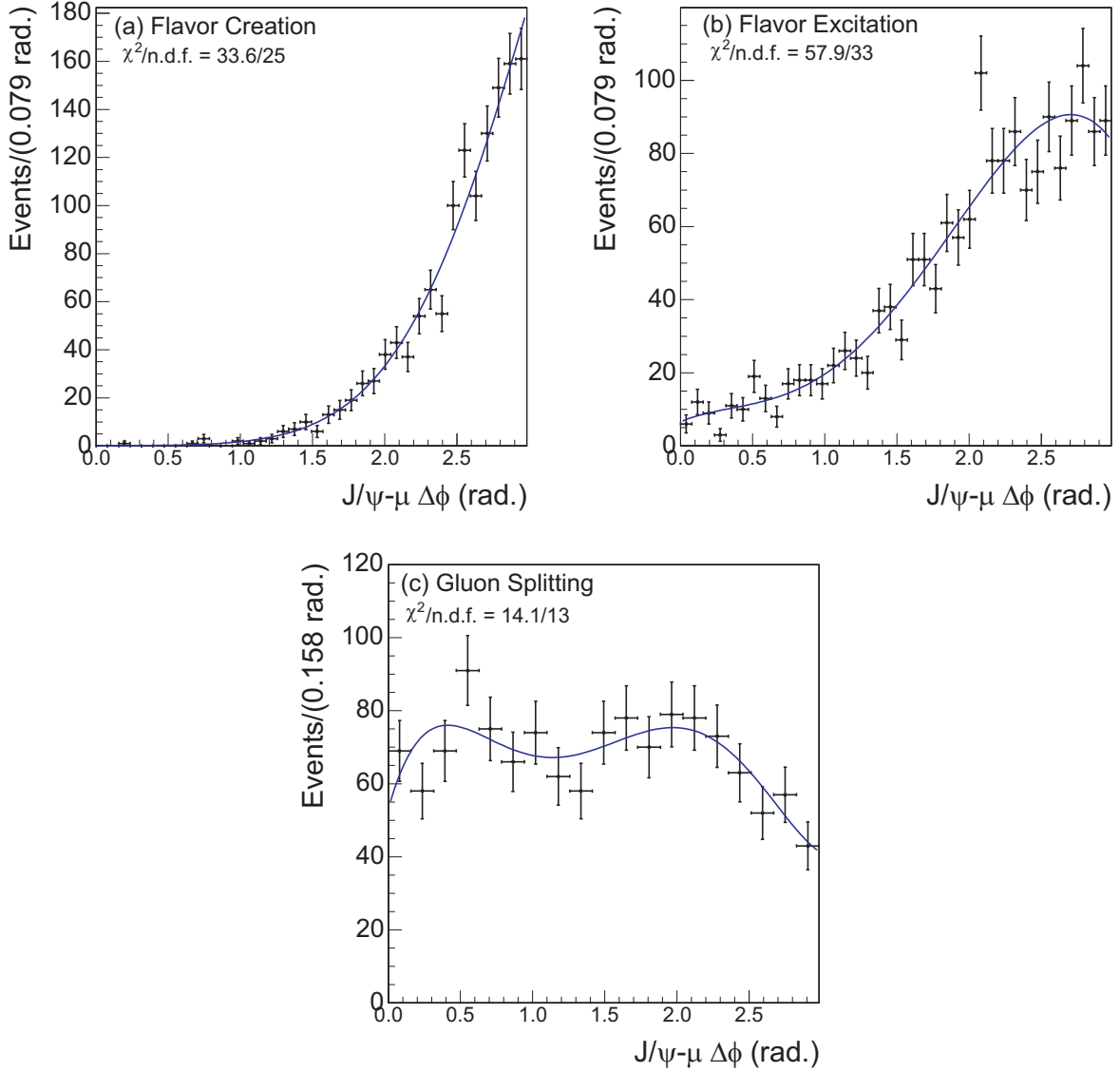


Figure 62: Fitted $\Delta\phi$ distributions for flavor creation (a), flavor excitation (b), and gluon splitting (c) events from the PYTHIA $b\bar{b}$ sample.

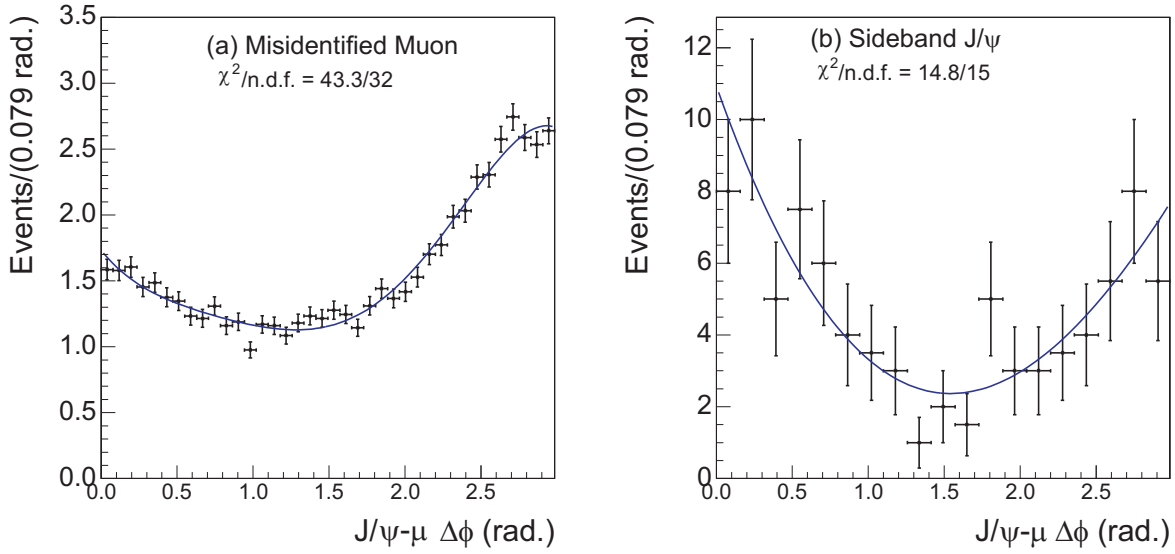


Figure 63: Fitted $\Delta\phi$ distributions for events modeling misidentified third muons (a) and misidentified J/ψ (b).

all three QCD process to float freely in the $\Delta\phi$ fit. This method, however, differs from the normalization method used in the lifetime measurement, where the rate of $J/\psi + \mu^\pm$ from $b\bar{b}$ relative to $B^\pm \rightarrow J/\psi + K^\pm$ decays is measured in the PYTHIA sample, and the normalization of the $b\bar{b}$ component in data is determined by this relative rate multiplied by the number of $B^\pm \rightarrow J/\psi + K^\pm$ decays in data. By this method the normalization is written as:

$$N_{b\bar{b}} = C_{norm} (S_{FC} N_{b\bar{b}}^{FC} + S_{FE} N_{b\bar{b}}^{FE} + S_{GS} N_{b\bar{b}}^{GS}) \times \frac{N_{B^\pm}^{data}}{S_{FC} N_{B^\pm}^{FC} + S_{FE} N_{B^\pm}^{FE} + S_{GS} N_{B^\pm}^{GS}} \quad (7.20)$$

Here, S_{FE} and S_{GS} scale the normalization of the FE and GS $b\bar{b}$ components, respectively, while S_{FC} is defined as $3 - S_{FE} - S_{GS}$ since the presence of the scale factors in the numerator and denominator eliminates one degree of freedom. $N_{B^\pm}^{FE}$, $N_{B^\pm}^{FC}$, and $N_{B^\pm}^{GS}$ are the fitted numbers of $B^\pm \rightarrow J/\psi + K^\pm$ for each QCD process in the PYTHIA sample, while $N_{B^\pm}^{data}$ is the number in data. $N_{b\bar{b}}^{FE}$, $N_{b\bar{b}}^{FC}$, and $N_{b\bar{b}}^{GS}$ are the number of $J/\psi(\mu^+\mu^-) + \mu^\pm$ in the PYTHIA sample before any scaling is applied. C_{norm} is a parameter that accounts for the uncertainties in the simulation of J/ψ and muon production in B decays relative to the $B^\pm \rightarrow J/\psi + K^\pm$

branching fraction and should be 1 if the rates in the PYTHIA sample match the physical values perfectly. Using this method of constraining the normalization has the advantage of ensuring a reasonable method for normalizing $b\bar{b}$ candidates for the lifetime measurement. The fitted N_{B^\pm} distributions are shown in Figure 64.

The fit to the $\Delta\phi$ distribution is carried out with the “unvertexed” $J/\psi + \mu^\pm$ events selected from 360 fb^{-1} of integrated luminosity. The fit uses an extended likelihood for N_{data} events in data of the form:

$$\begin{aligned}
-2\ln(L) = & \sum_i^{N_{data}} [N_{FE}F_{FE}(\Delta\phi_i) + N_{FC}F_{FC}(\Delta\phi_i) + N_{GS}F_{GS}(\Delta\phi_i) + \\
& N_{MJ}F_{MJ}(\Delta\phi_i) + N_{MM}F_{MM}(\Delta\phi_i)] + 2(N_{b\bar{b}} + N_{MJ} + N_{MM}) + \\
& 2\ln(N_{data}!) + V_p^T C_p^{-1} V_p + \\
& \frac{(N_{MJ} - \bar{N}_{MJ})^2}{E_{MJ}^2} + \frac{(N_{MM} - \bar{N}_{MM})^2}{E_{MM}^2} + \sum_j \frac{P_{bbnorm}^j - \bar{P}_{bbnorm}^j}{E_{bbnorm}^{j2}}
\end{aligned} \tag{7.21}$$

The previously shown fitted templates are described by the $F_{FE\dots MM}(\Delta\phi_i)$ functions, while the normalization of each component is given by $N_{FE\dots MM}$. Here, the MJ and MM subscripts refer to the misidentified J/ψ and third muon sources, respectively. The parameters describing the $F_{FE\dots MM}(\Delta\phi_i)$ templates are allowed to vary from their previously fitted values in the vector $V_p^i = P^i - \bar{P}^i$. The covariance matrix that describes the uncertainties in the previously fitted parameters is C_p . The normalizations N_{MJ} and N_{MM} are constrained within their uncertainties, while the normalizations N_{FE} , N_{GS} , N_{FC} and $N_{b\bar{b}}$ are determined by Eq. (7.20). The quantities P_{bbnorm}^j used in the normalization Eq. (7.20) are allowed to vary around their measured values, \bar{P}_{bbnorm}^j , while constrained by their uncertainties E_{bbnorm}^j .

Figure 65 shows the fitted $\Delta\phi$ distribution. The parameters that are used to tune the sample for the lifetime measurement are S_{FE} , S_{GS} and C_{norm} and their fitted values are:

$$S_{FE} = 0.83 \pm 0.34 \tag{7.22}$$

$$S_{GS} = 1.42 \pm 0.21 \tag{7.23}$$

$$C_{norm} = 1.05 \pm 0.10 \tag{7.24}$$

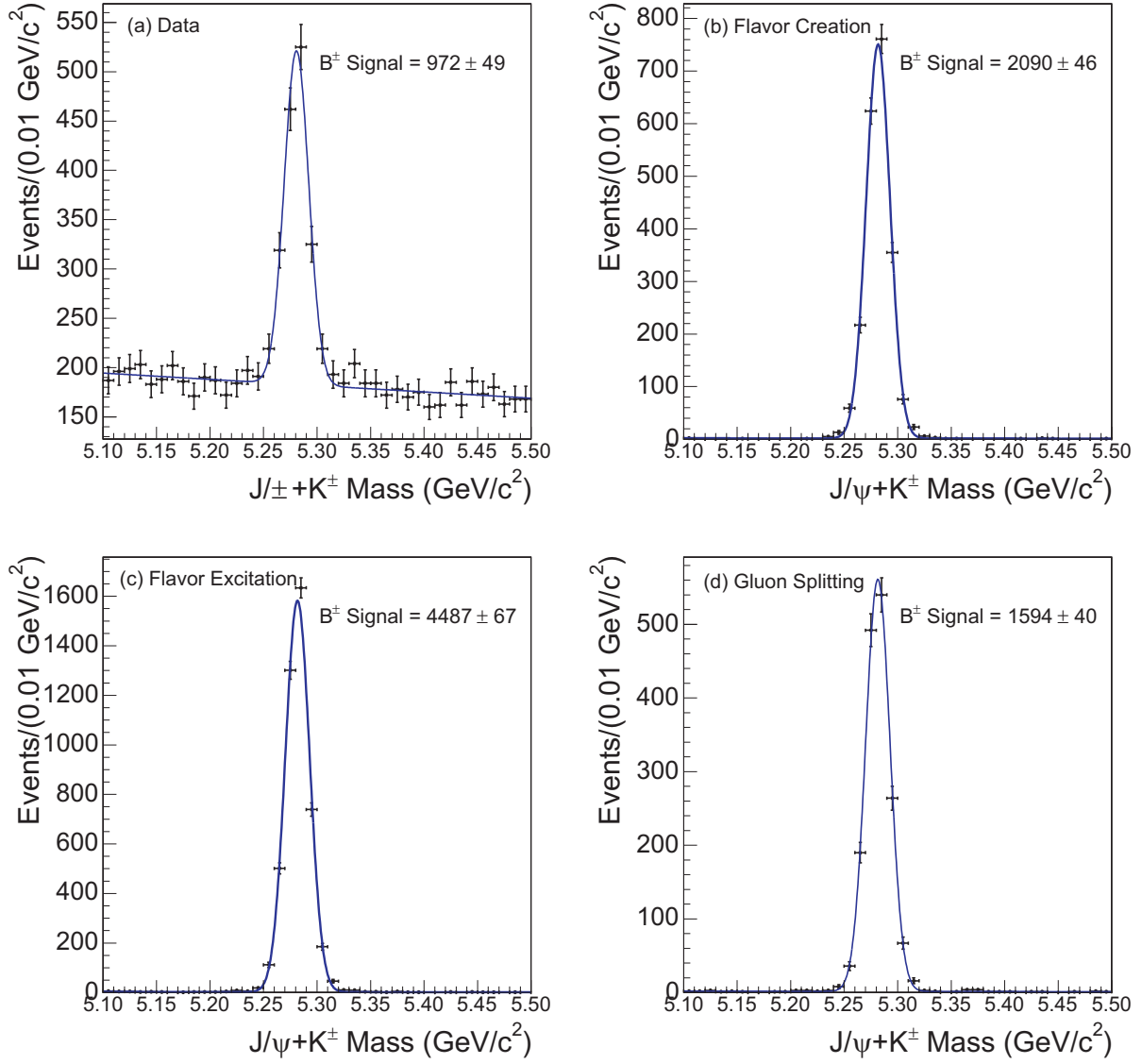


Figure 64: Fitted $B^\pm \rightarrow J/\psi + K^\pm$ mass distributions for data (a), flavor creation (b), flavor excitation (c), and gluon splitting (d).

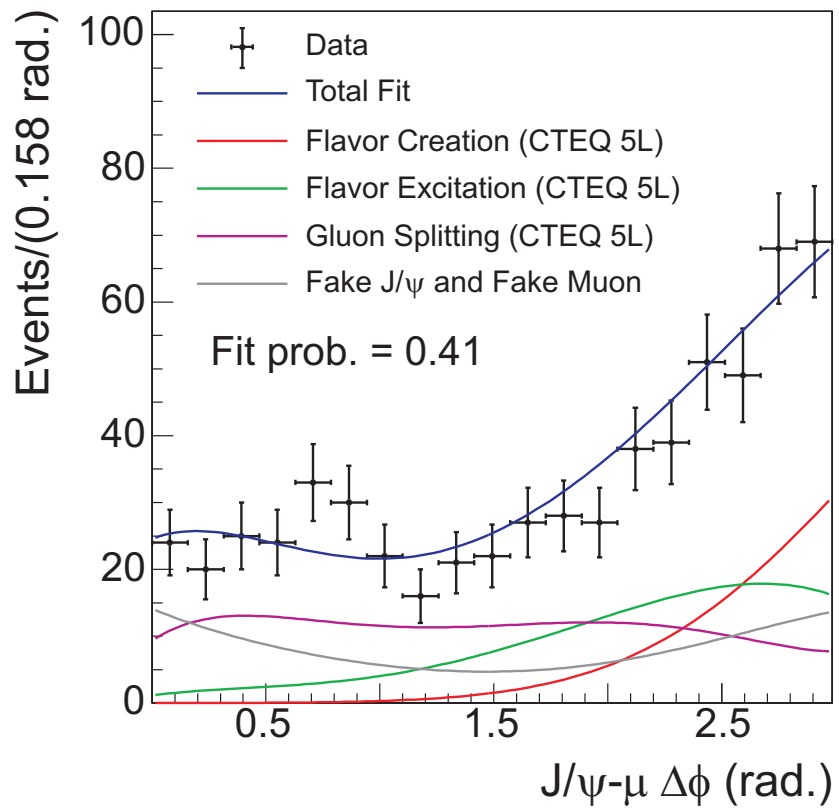


Figure 65: Fitted $\Delta\phi$ for $J/\psi + \mu^\pm$ events.

7.3.2 $b\bar{b}$ tuning crosscheck

The tuning of the PYTHIA $b\bar{b}$ sample using the fitted parameters S_{FE} , S_{GS} and C_{norm} is checked by studying the distributions of $d_0^{l-J/\psi}$ for the “unvertexed” $J/\psi + l^\pm$ samples. A comparison of the predicted $d_0^{l-J/\psi}$ distributions to those seen in data will either expose flaws in the $b\bar{b}$ background method or confirm its accuracy. This check is especially useful for the electron channel since the tuning was carried out with the muon channel only.

The other $J/\psi + l^\pm$ backgrounds sources contribute events to the $d_0^{l-J/\psi}$ distributions and their contributions are determined using the same methods outlined for the lifetime measurement. The $d_0^{l-J/\psi}$ cut is removed from the “unvertexed” sample to show the clear excess of events at small values which can be attributed to B_c decays. The $b\bar{b}$ component of the $d_0^{l-J/\psi}$ distribution is predicted using the PYTHIA $b\bar{b}$ sample normalized by Eq. (7.20). The resulting predicted and measured distributions are shown in Figure 66. There is good agreement in the region where the $b\bar{b}$ dominates, as well as a clear excess at small values where B_c events are expected.

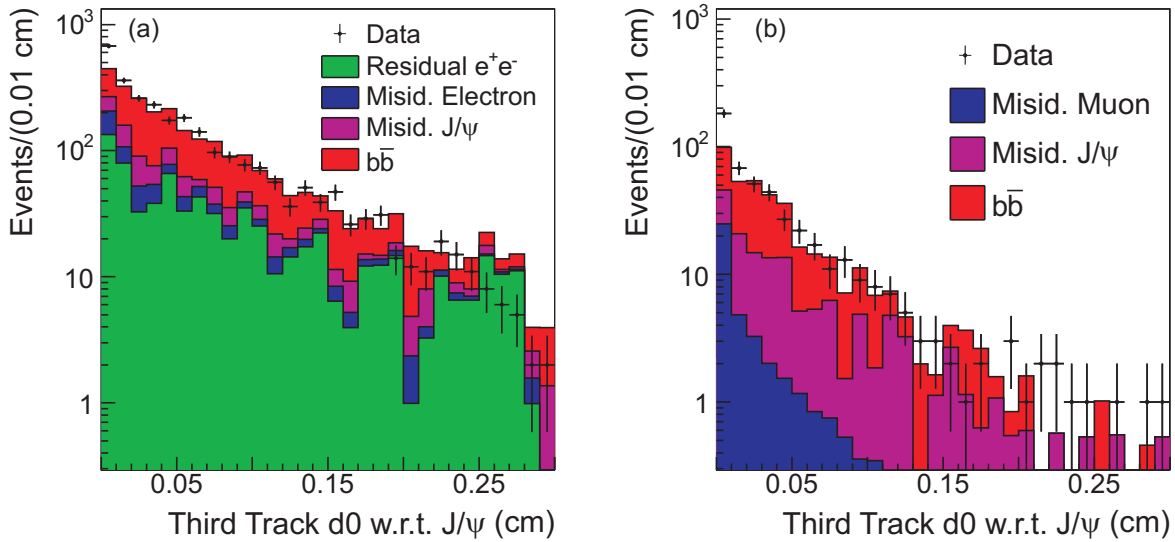


Figure 66: Impact parameter of the third lepton with respect to the J/ψ for the “unvertexed” electron (a) and muon (b) channel samples.

7.3.3 Normalization of the $b\bar{b}$ background

The normalization of the $b\bar{b}$ backgrounds for the lifetime measurement are carried out using Eq. 7.20. $B^\pm \rightarrow J/\psi + K^\pm$ events are selected in data and the PYTHIA sample using cuts similar to the B_c candidate selection, but with the third lepton requirements removed and the application of an $L_{xy}/\sigma_{L_{xy}} > 3.0$ cut to remove the prompt background. The fits for the electron channel are shown in Figure 67, and the muon channel fits are shown in Figure 68.

Candidate $J/\psi + l^\pm$ events are selected by applying the B_c selection cuts to the PYTHIA sample, and identifying the events as FC, GS, or FE. Table 17 lists the number of $J/\psi + l^\pm$ candidates in the PYTHIA sample, the number of $B^\pm \rightarrow J/\psi + K^\pm$ decays in the PYTHIA sample and data, and the predicted $b\bar{b}$ background for both the electron and muon channels.

7.3.4 $b\bar{b}$ ct^* fits

The ct^* of the $b\bar{b}$ background is modeled with candidate events from the tuned PYTHIA sample where the reweighting based on S_{FE} and S_{GS} is carried out by random rejection of events. For both electron channel and muon channel samples the ct^* distributions are fitted with a PDF of the form

$$F_{b\bar{b}}(ct^*, \sigma) = \left[\frac{f_+}{c\tau_+} e^{-\frac{ct_i^*}{c\tau_+}} \theta(ct^*) + \frac{(1-f_+)}{c\tau_{++}} e^{-\frac{ct_i^*}{c\tau_{++}}} \theta(ct^*) \right] \otimes \frac{1}{\sqrt{2\pi}s\sigma} e^{-\frac{1}{2}\left(\frac{ct^*}{s\sigma}\right)^2}. \quad (7.25)$$

Since the $b\bar{b}$ sample contains no prompt J/ψ component, the PDF only includes exponential components that describe a positive proper time distribution. The fitted ct^* projections for both channels are shown in Figure 69, and the fitted parameters and their errors are listed in Table 18.

7.3.5 $b\bar{b}$ σ_{ct^*} fits

The σ_{ct^*} of the $b\bar{b}$ background is modeled with candidate events from the same tuned sample that is used for the ct^* fits. The PDF that is fitted to the samples is chosen to give good

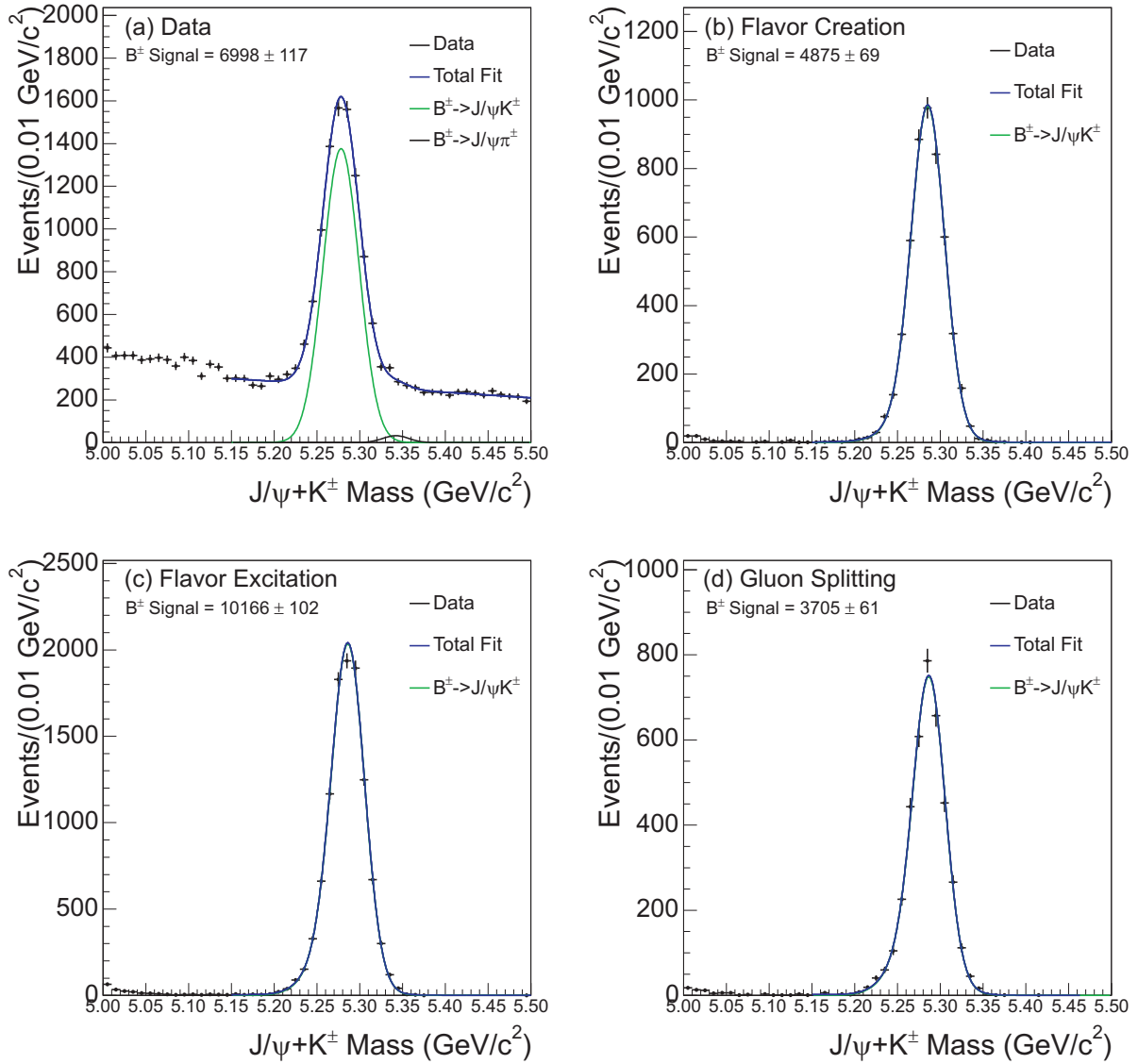


Figure 67: Electron channel fitted $B^\pm \rightarrow J/\psi + K^\pm$ mass distributions for data (a), flavor creation (b), flavor excitation (c), and gluon splitting (d).

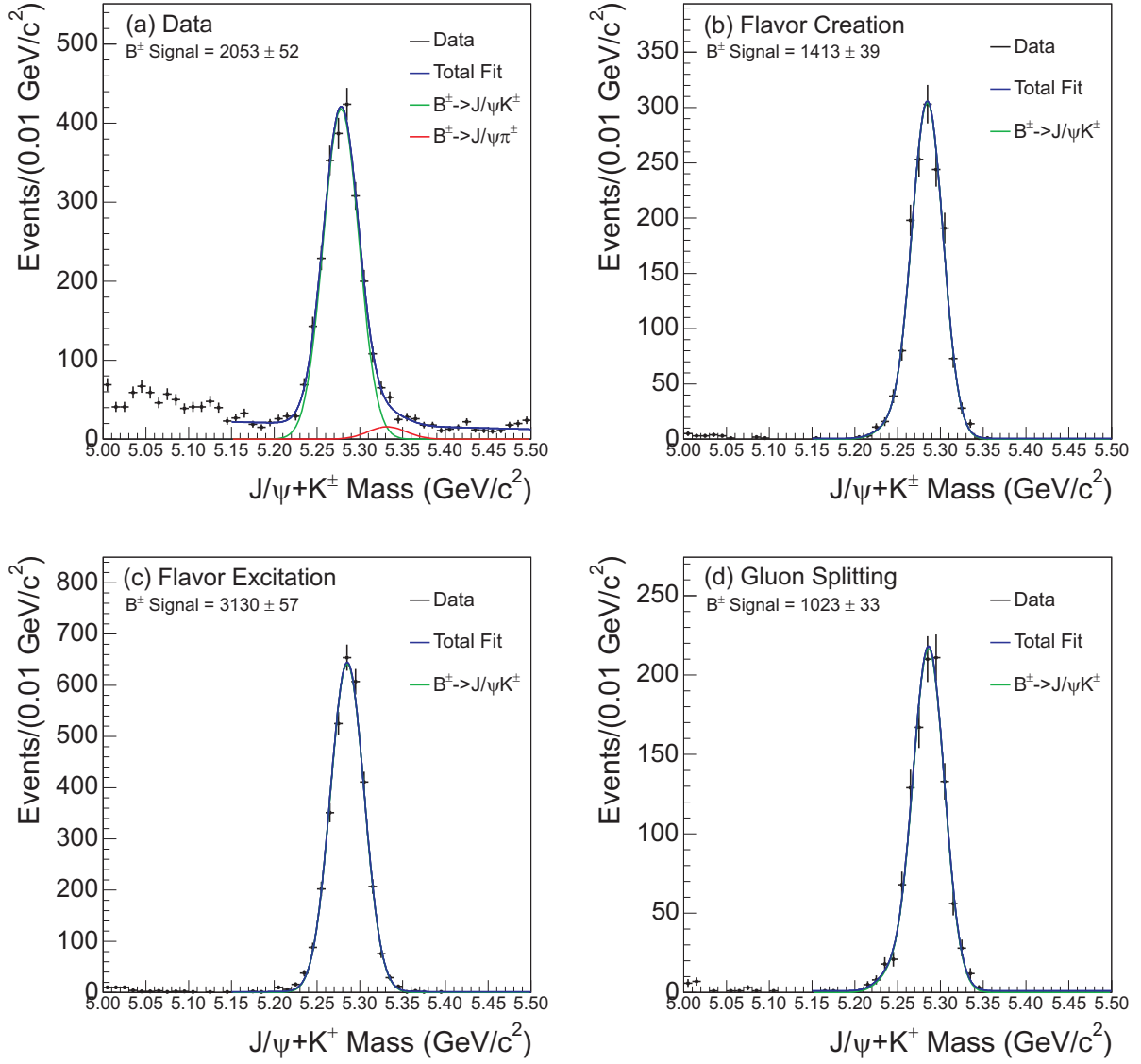


Figure 68: Muon channel fitted $B^\pm \rightarrow J/\psi + K^\pm$ mass distributions for data (a), flavor creation (b), flavor excitation (c), and gluon splitting (d).

	Electron Channel		Muon Channel	
	$N_{b\bar{b}}$	N_{B^\pm}	$N_{b\bar{b}}$	N_{B^\pm}
FC	15	4875 ± 69	5	1413 ± 39
FE	142	10166 ± 102	56	3130 ± 57
GS	320	3705 ± 61	119	1023 ± 33
Data	222.5 ± 11.2	6998 ± 117	77.5 ± 11.9	2053 ± 52

Table 17: Numbers used to determine the $b\bar{b}$ background normalization and the predicted normalizations (first and third columns in the last row).

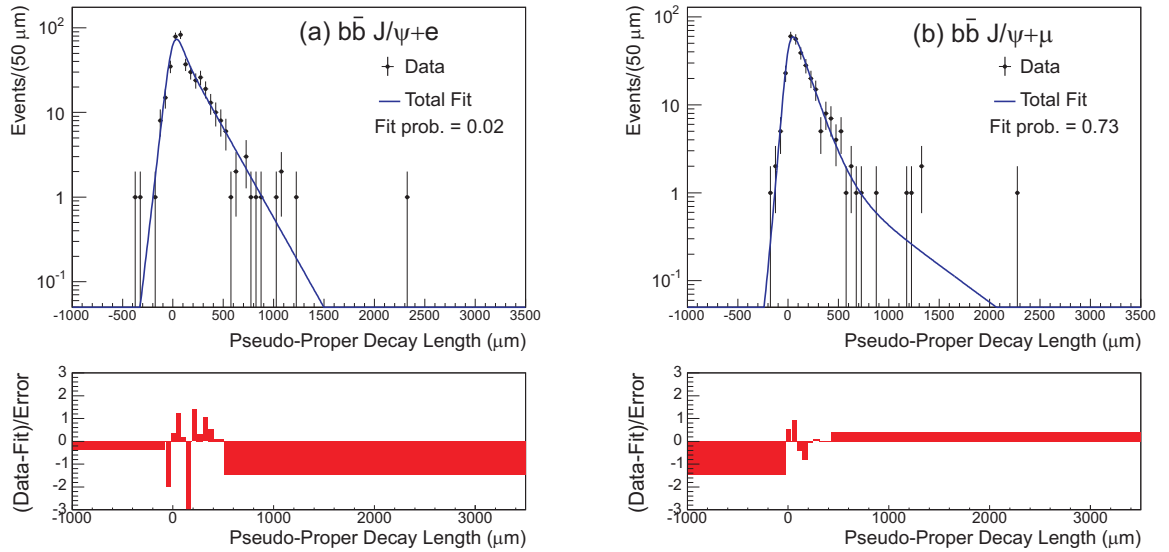


Figure 69: Fitted ct^* distributions of the PYTHIA $b\bar{b}$ events for the electron (a) and muon (b) channels.

Parameter	Electron Channel		Muon Channel	
	Value	Error	Value	Error
s	1.69	0.07	1.31	0.05
$c\tau_+$ (μm)	20.8	11.4	121	15
f_+	0.29	0.07	0.90	0.07
$c\tau_{++}$ (μm)	205	18	516	214

Table 18: Parameters from the $b\bar{b} ct^*$ fits.

agreement with the fitted events:

$$P_{b\bar{b}}(\sigma) = \frac{1}{\sqrt{2\pi}P_0} e^{-\frac{1}{2}\left(\frac{\sigma}{P_0}\right)^2} \otimes \left[\frac{1}{P_1} e^{-\frac{(\sigma-P_2)}{P_1}} \theta(\sigma - P_2) \right]. \quad (7.26)$$

The fitted σ_{ct^*} projections for both channels are shown in Figure 70, and the fitted parameters and their errors are listed in Table 19.

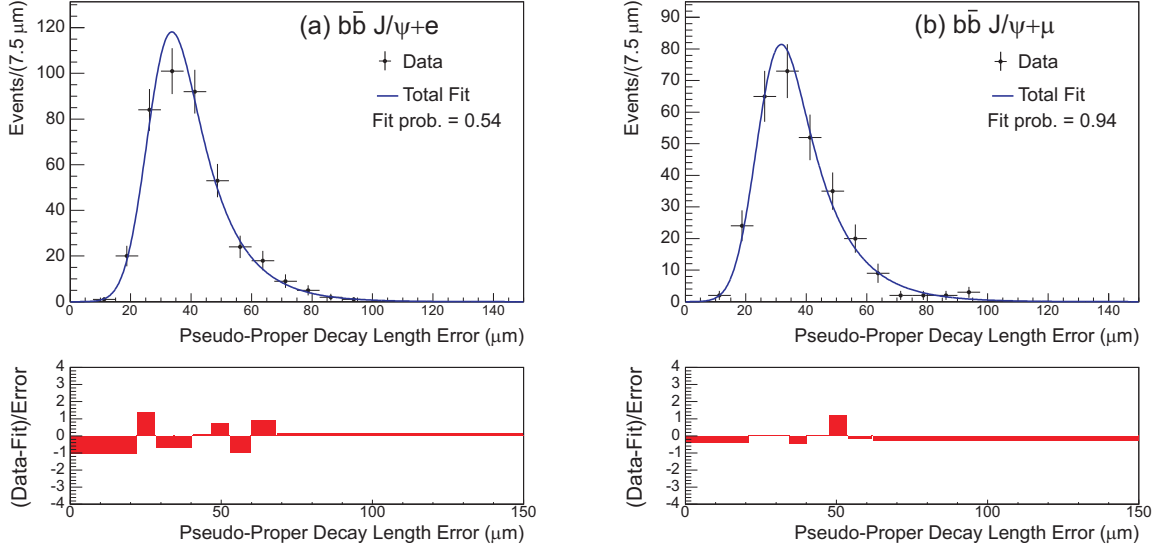


Figure 70: Fitted σ_{ct^*} distributions of the PYTHIA $b\bar{b}$ events for the electron (a) and muon (b) channels.

	Electron Channel		Muon Channel	
Parameter	Value	Error	Value	Error
P_0 (μm)	6.4	0.6	6.3	0.8
P_1 (μm)	12.0	1.0	12.6	1.2
P_2 (μm)	27.3	0.9	25.3	1.0

Table 19: Parameters from $b\bar{b}$ σ_{ct^*} fits.

7.4 RESIDUAL e^+e^- BACKGROUND

As discussed previously, electrons and positrons are created in pairs when a photon converts [94] or a light neutral meson decays to a final state that includes e^+e^- ². When identified by the presence of the oppositely charged partner track, e^+e^- candidates are vetoed. Since this procedure does not identify all e^+e^- pairs, a residual background remains and must be modeled.

To determine the properties of this background, a PYTHIA simulation of $B \rightarrow J/\psi + X$ decays is generated where the event can contain a photon or a light neutral meson. Events with an e^+e^- pairs are selected using truth information, and all cuts for the selection of $J/\psi + e^\pm$ candidates are applied. The ratio of e^+e^- vetoed by the Δ_{xy} and $\Delta\cot(\theta)$ cuts relative to e^+e^- pairs identified using the truth information is a measure of the veto efficiency. Using events from data that have been vetoed and the veto efficiency as determined by the simulation, it is possible to model the residual e^+e^- events that were not vetoed.

Since the efficiencies for e^+e^- removal are measured using a PYTHIA simulated sample, the measurement is sensitive to differences between data and simulation in reconstructing the partner track. To identify and correct for any difference, studies are carried out that compare the efficiency for identifying a certain class of conversion electrons in data and the simulation.

7.4.1 e^+e^- identification efficiency

A PYTHIA Monte Carlo simulation generated with the msel=5 setting and Tune A for the underlying event, as described in Appendix A, provides the e^+e^- candidates for the efficiency measurement. Events containing either a photon conversion or a light neutral meson decaying to e^+e^- are selected, and after applying the analysis cuts, the sample is split into these two classes. For both classes, the efficiency to identify e^+e^- pairs using the veto cuts on Δ_{xy} and $\Delta\cot(\theta)$ are measured as a function of the electron p_T , as shown in Figure 71.

²Among the light neutral meson decays, e^+e^- pairs are most commonly produced by the π^0 Dalitz decay $\pi^0 \rightarrow e^+ + e^- + \gamma$ which has a branching fraction of 1.2%. Other sources include $\eta \rightarrow e^+ + e^- + \gamma$, $\omega \rightarrow \pi^0 + e^+ + e^-$, and $\phi \rightarrow e^+ + e^-$.

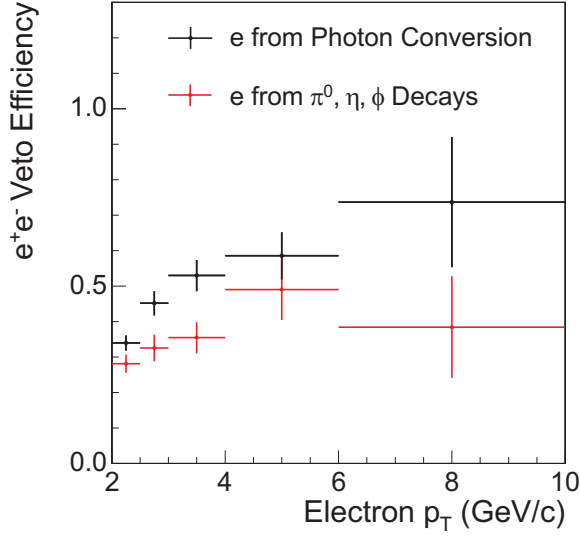


Figure 71: Efficiency for identifying $J/\psi + e$ events where the electron comes from an e^+e^- pair. Efficiencies come from a PYTHIA Monte Carlo simulation.

7.4.2 Sources of e^+e^-

To accurately determine the residual background, it is necessary to know the relative fraction of e^+e^- pairs from photon conversion and neutral light meson decays, since the two sources have different veto efficiencies. A measurement of the relative fraction is carried out using the measured radius of origin, R_{ee} , for e^+e^- pairs. Since conversions happen when a photon interacts with material, conversion e^+e^- pairs will originate at radii beyond the beam pipe, which is located at $r = 1.25$ cm. Neutral light mesons, on the other hand, have a lifetime typical of strong interactions and tend to come from the primary $p\bar{p}$ interaction vertex or secondary decay vertices. Therefore, one expects the distribution of R_{ee} for neutral light meson decays to be peaked near zero, while the distribution from photon conversions is distributed throughout the detector. Figure 72 shows a comparison of R_{ee} for the sources, as modeled by the PYTHIA sample, verifying the expectation. Since the R_{ee} distributions of the two e^+e^- sources are so different, R_{ee} can be used to measure the fractions of the two sources in data.

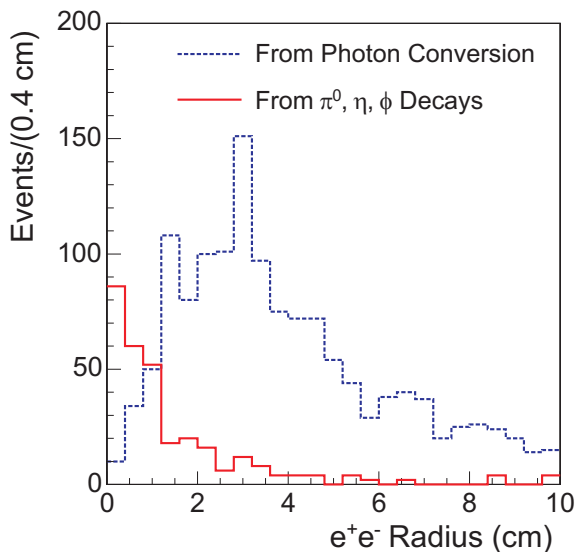


Figure 72: R_{ee} of e^+e^- pairs in PYTHIA.

The sample of vetoed $J/\psi+e^\pm$ events in data has an R_{ee} distribution that is a combination of the R_{ee} distributions of the two e^+e^- sources. Since the R_{ee} distribution for conversion events is irregular due to the distribution of material in the detector, a simple counting method is used for measuring the relative fractions, instead of a fit to the data. The fraction of events with $r < 1.0$ cm is used to measure the fractions of the two sources. The following equation describes number of e^+e^- events with < 1.0 cm in terms of the two sources:

$$N_{data}^R = F_{conv}^R \times N_{conv}^D + F_{\pi^0}^R \times N_{\pi^0}^D. \quad (7.27)$$

Here, N_{data}^R is the number of e^+e^- events in data with $r < 1.0$ cm, F_{conv}^R and $F_{\pi^0}^R$ are the fractions of conversions and light meson decays in the PYTHIA sample that have $r < 1.0$ cm, and N_{conv}^D and $N_{\pi^0}^D$ are the numbers of e^+e^- from the two sources in data. Dividing both sides of Eq. (7.27) by the total number of events gives the same equation written in fractions:

$$F_{data}^R = F_{conv}^R \times F_{conv}^D + F_{\pi^0}^R \times F_{\pi^0}^D. \quad (7.28)$$

Since $F_{conv}^D + F_{\pi^0}^D = 1$, it is possible to solve for $F_{\pi^0}^D$, the fraction of e^+e^- events in data from light neutral meson decays:

$$F_{\pi^0}^D = \frac{F_{conv}^R - F_{data}^R}{F_{conv}^R - F_{\pi^0}^R}. \quad (7.29)$$

Figure 73 shows R_{ee} for $J/\psi + e^\pm$ events in data where the electron is identified as coming from e^+e^- . This distribution is used to determine the fraction F_{data}^R . The fractions F_{conv}^R and $F_{\pi^0}^R$ come from the PYTHIA distributions shown in Figure 72. Evaluating Eq. (7.29) yields the fraction of e^+e^- from neutral meson decays, $F_{\pi^0}^D = 0.140 \pm 0.047$. As a consistency check, the fraction of e^+e^- is also directly measured in the PYTHIA sample using truth information and is found to be 0.1, which is consistent with the measured value from data.

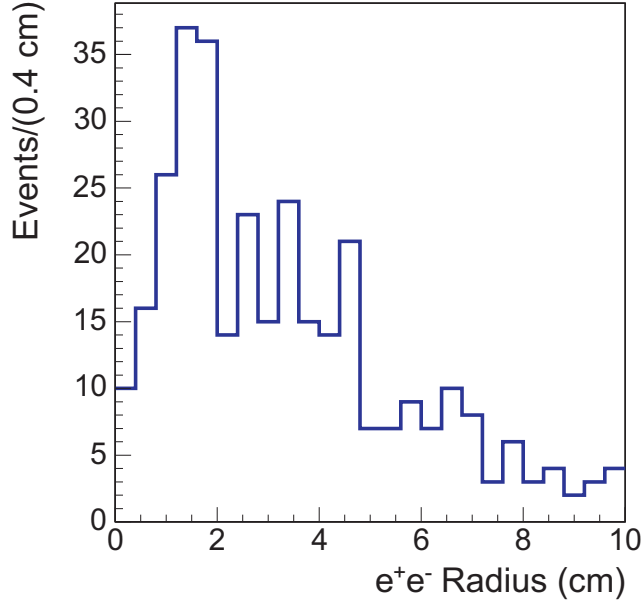


Figure 73: R_{ee} of identified e^+e^- pairs in $J/\psi + e^\pm$ candidate events in data.

7.4.3 Checking the veto efficiency with signed impact parameter

The efficiency for identifying conversion events in the PYTHIA sample can be compared to the efficiency in data by looking at the signed impact parameter d_0^{sign} of conversion candidates in data [95]. The signed impact parameter is defined as the impact parameter d_0 of a track

times its charge q . The impact parameter is the distance of closest approach to the z axis from the helix that describes a particles trajectory. The measured d_0 is set to a positive or negative value such that the sign of d_0 is the opposite of the sign of L_z , the z component of the particles angular momentum about the origin of the lab coordinate system. When photons convert, the e^+e^- tracks tend to make a very small angle relative to the photon direction. In the majority of the cases where the photon originates at the primary vertex, the sign of the impact parameter of the track is largely determined by the charge of the track, as illustrated in Figure 74. In this case, tracks from positrons have positive d_0 and tracks from electrons have negative d_0 . Multiplying d_0 by q gives the quantity d_0^{sign} that will be positive for the tracks of pairs e^+e^- created by converting photons that originate at the primary interaction point.

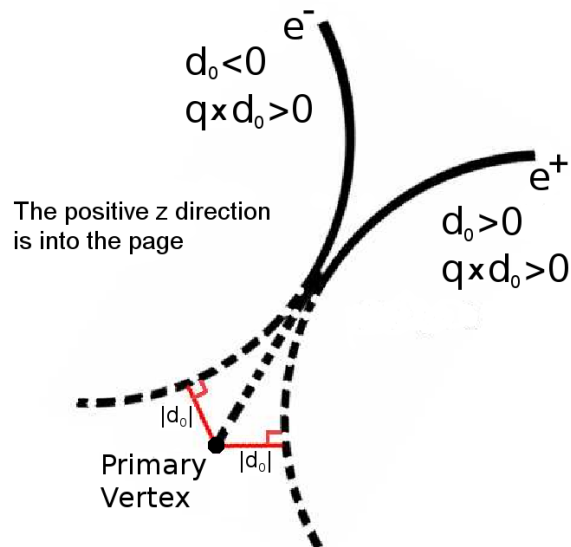


Figure 74: Illustration of a photon conversion where the photon originates at the primary vertex.

Electrons from other sources, however, have impact parameters that are more strongly determined by the opening angle of the decay at which the electron originates, leaving very little asymmetry in the d_0^{sign} distribution. Figure 75 shows d_0^{sign} for electrons in the various sources of $J/\psi + e^\pm$. The samples shown here are similar to the B_c candidate samples used

for the lifetime measurement, but the vertex probability, opening angle, e^+e^- veto, and mass cuts have been removed to increase the sample sizes.

Figure 76 shows the d_0^{sign} for $J/\psi + e^\pm$ events in data, which is a combination of the sources shown in Figure 75. The expected asymmetry is present, and a count of the size of the asymmetry gives a measurement of the number of conversion electrons where the photon originates from the primary interaction point. Applying the e^+e^- veto cuts and recounting the asymmetry gives a count of conversion events that survived the veto. In practice the contributions to the asymmetry by other sources shown in Figure 75 should be subtracted. Since the normalization of $J/\psi + e^\pm$ events from B_c decays is unknown, only the $|d_0^{sign}| > 0.1$ cm regions are used, excluding the B_c events. Fig. 77 shows the efficiency for removing conversion events that are counted from the asymmetry and compares it to the expected efficiency in PYTHIA. All bins but the lowest p_T bin are in good agreement. In the lowest p_T bin a correction of 0.86 applied to the PYTHIA sample gives good agreement, and this correction is applied to all e^+e^- veto efficiency measurements from the PYTHIA sample and used to determine a systematic uncertainty.

7.4.4 Residual e^+e^- normalization

The normalization of the residual e^+e^- backgrounds is determined using the vetoed events and veto efficiency with the following equation:

$$N_{res} = \sum_i F_{\pi^0}^D \frac{(1 - \epsilon_{\pi^0}(p_{Ti}))}{\epsilon_{\pi^0}(p_{Ti})} N_{veto}(p_{Ti}) + (1 - F_{\pi^0}^D) \frac{(1 - \epsilon_{conv}(p_{Ti}))}{\epsilon_{conv}(p_{Ti})} N_{veto}(p_{Ti}). \quad (7.30)$$

Here, the efficiencies and number of vetoed events are evaluated for each p_T bin and the expression is summed over the p_T bins. Care must be taken to avoid double counting with the misidentified J/ψ background. To this end, the above equation is applied to the J/ψ sideband regions and the number of events with misidentified J/ψ and residual e^+e^- electrons is subtracted. This procedure yields a residual e^+e^- background of 416.8 ± 41.5 events based on 368 vetoed events in the J/ψ signal region. The uncertainty in the background normalization includes the statistical uncertainty in the number of vetoed events, the statistical uncertainty in the veto efficiencies, and the uncertainty in the fraction of e^+e^- pairs from light neutral mesons decays.

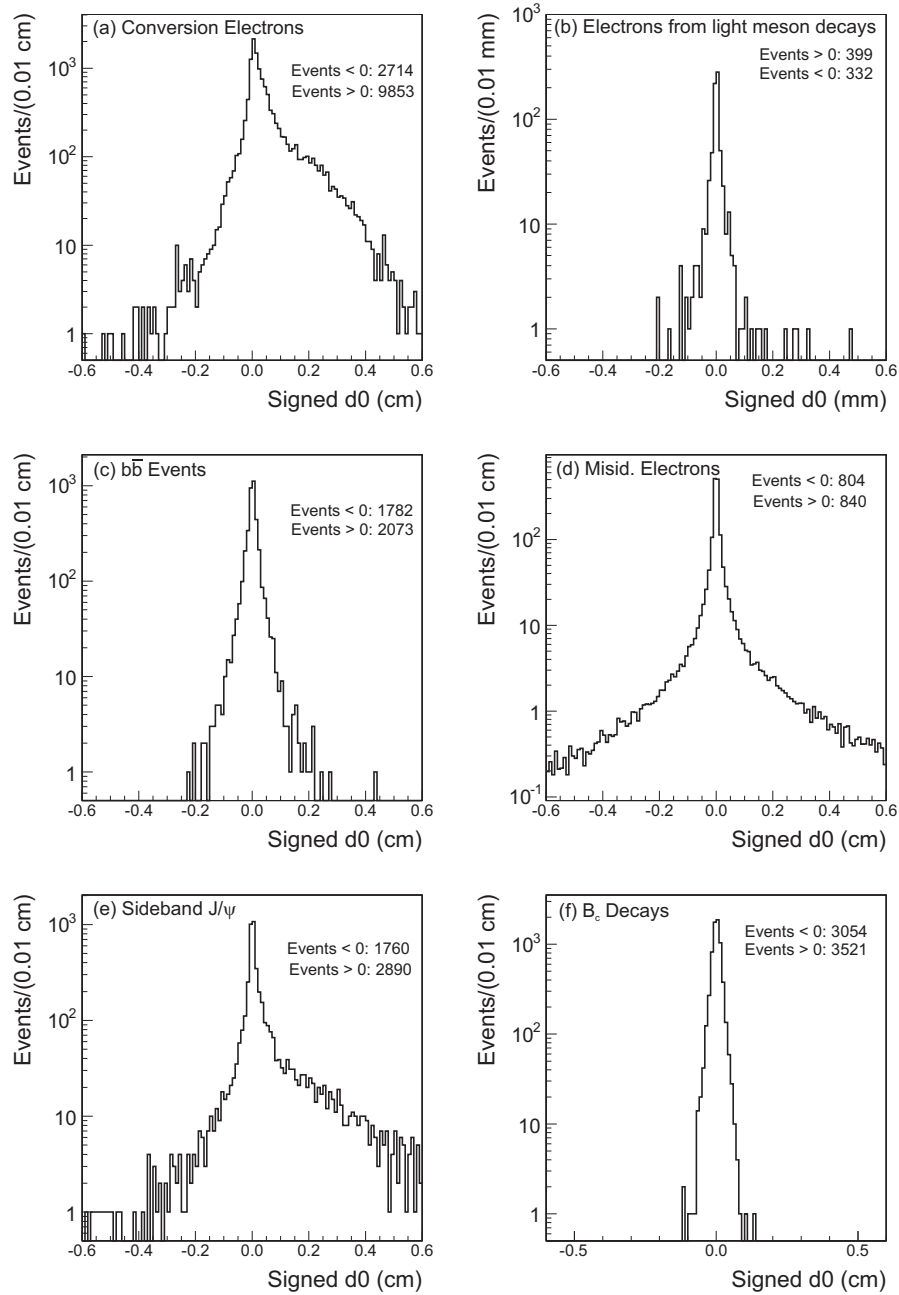


Figure 75: d_0^{sign} for electrons in “unvertexed” $J/\psi + e^\pm$ events from the sources: conversion electrons in PYTHIA (a), light neutral meson decays in PYTHIA (b), $b\bar{b}$ events in PYTHIA (c), misidentified electron events (d), misidentified J/ψ events (e), and B_c decays in the BGENERATOR sample (f). For each plot the number of events with $d_0^{sign} > 0$ and < 0 are listed.

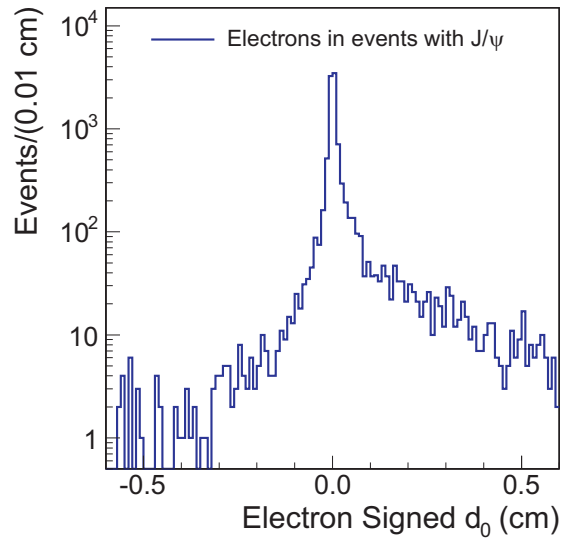


Figure 76: d_0^{sign} for electrons in “unvertexed” $J/\psi + e^\pm$ events in data.

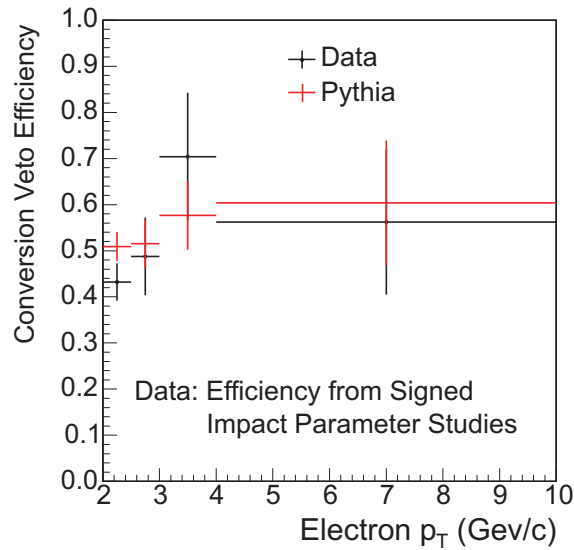


Figure 77: Efficiency of the e^+e^- veto in data determined using d_0^{sign} asymmetries, compared to the efficiency from PYTHIA.

7.4.5 Residual e^+e^- ct^* fit

The vetoed e^+e^- events are used to model the ct^* of the residual e^+e^- background, by applying the same efficiencies used to calculate the normalization of the background. The weighting factor is defined as:

$$W_{RC} = F_{\pi^0}^D \frac{(1 - \epsilon_{\pi^0})}{\epsilon_{\pi^0}} + (1 - F_{\pi^0}^D) \frac{(1 - \epsilon_{conv})}{\epsilon_{conv}} \quad (7.31)$$

Since the weighting of events shows some ct^* and σ_{ct^*} dependence, as illustrated by Fig. 78, the likelihood fits include the weighting factor in the fit model, as outlined in Section 5.4.1.

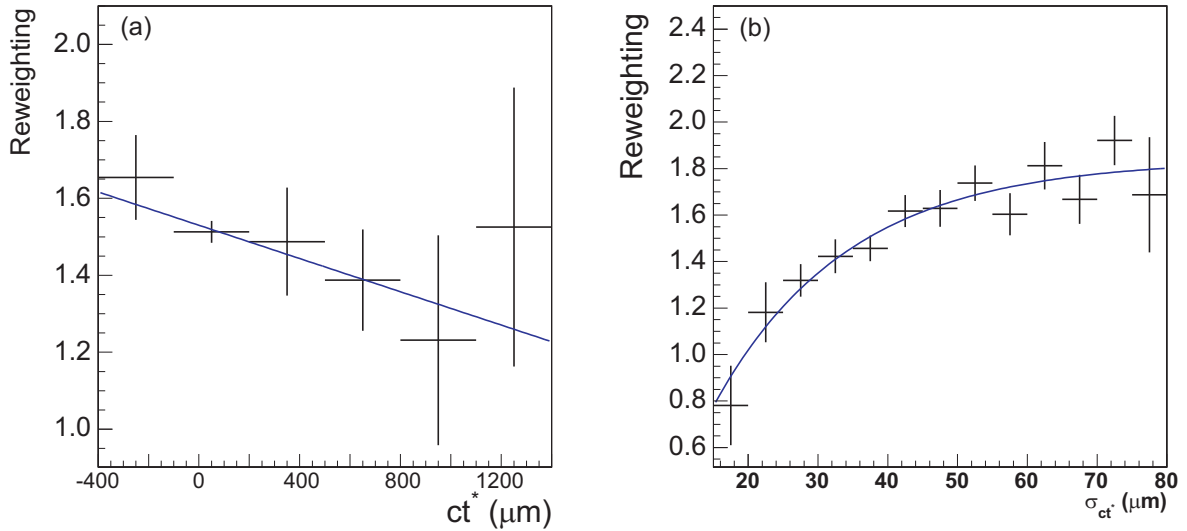


Figure 78: e^+e^- veto efficiency as a function of ct^* (left) and σ_{ct^*} (right).

As mentioned in the previous section, double counting with the misidentified J/ψ background must be avoided. To do this, the misidentified J/ψ events with residual e^+e^- should be modeled by a fit of e^+e^- vetoed J/ψ sideband events with the appropriate weighting applied. The misidentified J/ψ model can then be included to the fit of events in the J/ψ signal region, along with a model for the events with true J/ψ . Unfortunately, the vetoed e^+e^- events in the J/ψ sidebands are not numerous enough for a fit of their ct^* distribution to constrain any but the simplest model. Therefore, the ct^* distribution of all $J/\psi(\mu^+\mu^-) + e^\pm$

events in the J/ψ sideband regions is used. Figure 79 shows the ct^* model for sideband $J/\psi + e^\pm$ events overlaid on those events where the electron is identified as part of an e^+e^- pair. While the χ^2 probability is only 6%, alternate attempts to fit this distribution do not return significantly better probabilities.

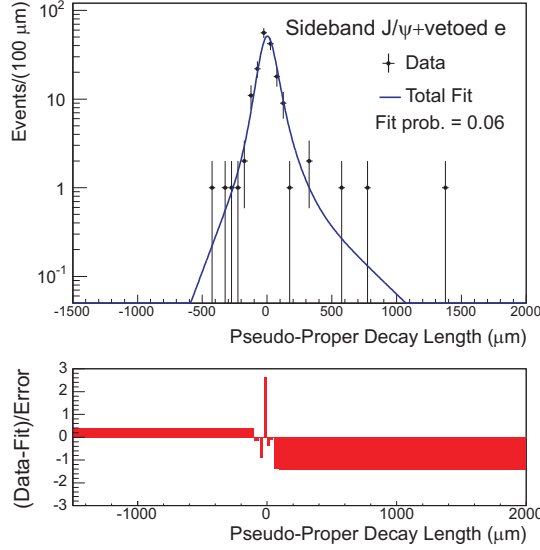


Figure 79: Fit ct^* for sideband $J/\psi + e$ events overlaid on the sub-sample where the electrons are identified as e^+e^- electrons.

With a model for the misidentified J/ψ contribution to the residual e^+e^- background, the events in the J/ψ signal region can be fitted. As previously mentioned the e^+e^- reweighting $W_{RC}(ct^*)$ is included in the fit model:

$$L = e^{-\frac{1}{2}V_W^T C_W^{-1} V_W} \prod_i \frac{A(\sigma_{ct^*i})}{W_{RC}(ct^*)} F_{RC}(ct^*_i, \sigma_{ct^*i}). \quad (7.32)$$

V_W is the vector containing the variation of the parameters that describe $W_{RC}(ct^*)$ around their fitted values from the fit shown in Figure 78. C_W is the covariance matrix for the parameters that describe $W_{RC}(ct^*)$. The $A(\sigma_{ct^*i})$ term is defined to satisfy the normalization condition

$$\int_{-\infty}^{\infty} \frac{A(\sigma_{ct^*i})}{W_{RC}(ct^*)} F_{RC}(ct^*, \sigma_{ct^*i}) d(ct^*) = 1 \quad (7.33)$$

and depends on the parameters that describe $F_{RC}(ct^*, \sigma_{ct^*i})$. The PDF describing the distribution of ct^* for residual e^+e^- events is

$$F_{RC}(ct^*, \sigma_{ct^*}) = f_{sig}[f_0\delta(ct^*) + \frac{f_+}{c\tau_+}e^{\frac{-ct^*}{c\tau_+}}\theta(ct^*)] \otimes \frac{1}{\sqrt{2\pi}s\sigma_{ct^*}}e^{-\frac{1}{2}(\frac{ct^*}{s\sigma_{ct^*}})^2} \quad (7.34)$$

$$+(1 - f_{sig})F_{FJ}(ct^*, \sigma_{ct^*}).$$

$F_{MJ}(ct^*, \sigma_{ct^*})$ is the previously fitted misidentified J/ψ distribution. f_{sig} is the fraction of J/ψ signal events, and f_0 and f_+ are the prompt and long lived fractions of the residual $e^+e^- ct^*$ model. The fit to data is shown in Figure 80 and the fitted parameter values are listed in Table 20.

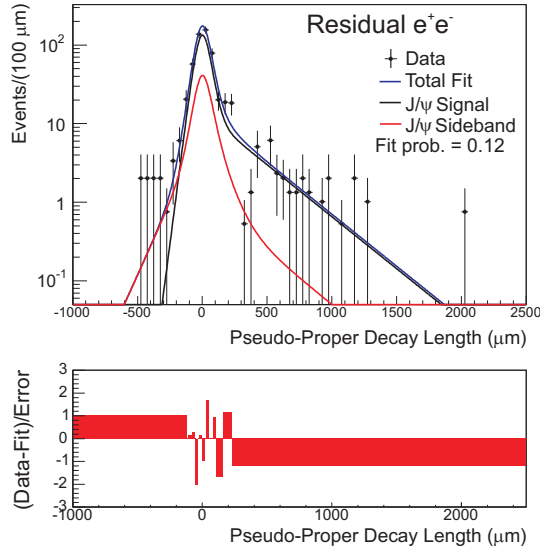


Figure 80: Fitted function overlaid on the ct^* distribution of identified e^+e^- reweighted for veto efficiencies. Red is the constrained misidentified J/ψ component.

7.4.6 Residual $e^+e^- \sigma_{ct^*}$ fit

The same procedure that was used for the ct^* fit is followed while fitting the σ_{ct^*} distribution. The vetoed events in the J/ψ sideband regions are fitted with a PDF of the form:

$$P_{MJ}(\sigma_{ct^*}) = \frac{1}{\sqrt{2\pi}P_0}e^{-\frac{1}{2}(\frac{\sigma_{ct^*}}{P_0})^2} \otimes \frac{1}{P_1}e^{-\frac{(\sigma_{ct^*}-P_2)}{P_1}}\theta(\sigma_{ct^*} - P_2). \quad (7.35)$$

Parameter	Value	Error
s	1.31	0.02
f_0	0.790	0.067
f_+	0.221	0.040
$c\tau_+$ (μm)	328	53
f_{sig}	0.776	0.027

Table 20: Fitted parameters from the residual $e^+e^- ct^*$ fit.

The resulting fitted distribution is shown in Figure 81 and the fitted parameters are listed in Table 21.

The events in the J/ψ signal region are fitted by a model that includes the misidentified J/ψ events as well as signal J/ψ events. The PDF is:

$$P_{RC}(\sigma_{ct^*}) = F_{sig} \frac{1}{\sqrt{2\pi}P_0} e^{-\frac{1}{2}\left(\frac{\sigma_{ct^*}}{P_0}\right)^2} \otimes \frac{1}{P_1} e^{-\frac{(\sigma_{ct^*}-P_2)}{P_1}} \theta(\sigma_{ct^*} - P_2) + (1 - F_{sig})P_{MJ}(\sigma_{ct^*}) \quad (7.36)$$

The resulting fitted events are shown in Figure 82 and the fitted parameters are listed in Table 22.

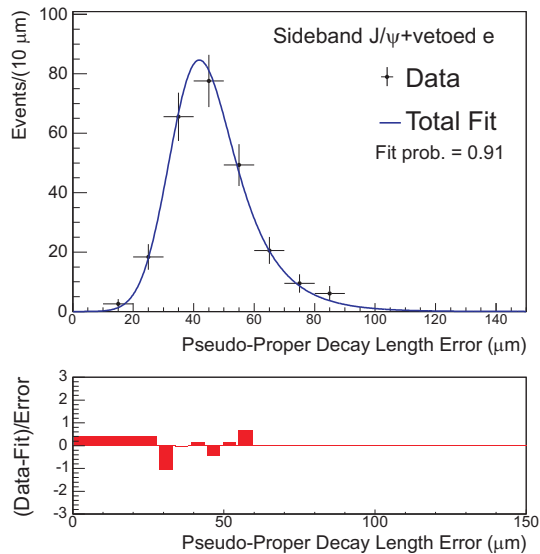


Figure 81: Fitted function overlaid on the σ_{ct^*} of identified e^+e^- events in the J/ψ mass sidebands reweighted for veto efficiencies.

Parameter	Value	Error
P_0 (μm)	8.17	1.04
P_1 (μm)	11.6	1.9
P_2 (μm)	34.9	1.7

Table 21: Fitted parameters from the σ_{ct^*} fit of e^+e^- events in J/ψ sidebands.

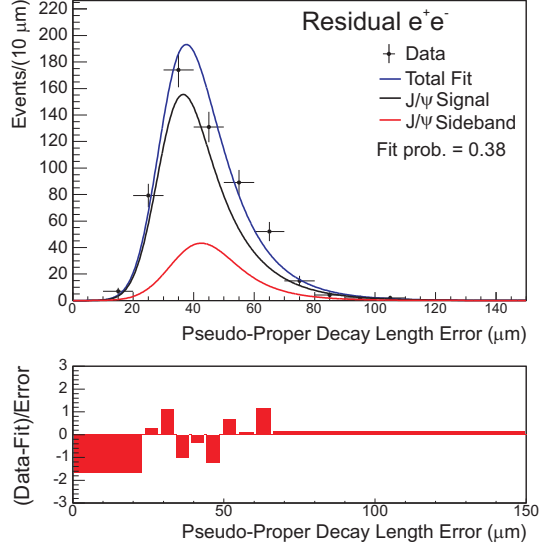


Figure 82: Fitted function overlaid on the σ_{ct^*} distribution of identified e^+e^- events in the J/ψ mass signal region reweighted for veto efficiencies.

Parameter	Value	Error
P_0 (μm)	6.60	0.77
P_1 (μm)	12.9	1.5
P_2 (μm)	29.9	1.3

Table 22: Fitted parameters from the residual e^+e^- σ_{ct^*} fit.

7.5 PROMPT J/ψ BACKGROUND

The prompt J/ψ background is not directly constrained by any simulated or data samples. The model for the ct^* distribution of prompt events is simply a Gaussian resolution function with per event scaled errors ($s\sigma_{ct^*}$) of the form:

$$F_{PR}(ct^*, \sigma) = \frac{1}{\sqrt{2\pi}s\sigma_{ct^*}} e^{-\frac{1}{2}\left(\frac{ct^*}{s\sigma_{ct^*}}\right)^2} \quad (7.37)$$

The single parameter s is extracted from a fit of ct^* in the J/ψ +track samples and is $s = 1.21 \pm 0.02$ and $s = 1.20 \pm 0.02$ for the electron and muon channels respectively. The effect of the choice of resolution function is studied as a systematic uncertainty.

Determination of the σ_{ct^*} PDF for prompt events presents a problem because there is no sample consisting of prompt events only that can be studied. However, a large component of the J/ψ +track sample is prompt J/ψ , and events with negative ct^* are almost exclusively prompt. If the misidentified J/ψ component of the negative ct^* events is constrained, the remainder will be prompt events. These events are used to model the σ_{ct^*} distribution for prompt J/ψ events. The sideband J/ψ +track as well the J/ψ signal component of the J/ψ +track sample are modeled with a PDF of the form:

$$P_{XX}(\sigma) = \frac{1}{\sqrt{2\pi}P_0} e^{-\frac{1}{2}\left(\frac{\sigma_{ct^*}}{P_0}\right)^2} \otimes \left[\frac{P_5}{P_1} e^{-\frac{(\sigma_{ct^*}-P_2)}{P_1}} \theta(\sigma_{ct^*} - P_2) + \frac{(1-P_5)}{P_3} e^{-\frac{(\sigma_{ct^*}-P_4)}{P_3}} \theta(\sigma_{ct^*} - P_4) \right]. \quad (7.38)$$

The constrained parameters from the sideband fits are propagated to the fit of the signal region which is fitted with J/ψ signal and constrained sideband components. The sideband region fits are shown in Figure 83, and the signal region fits are shown in Figure 84. The parameters describing the J/ψ signal component of the signal region fit are listed in Table 23 and used to model the prompt J/ψ background.

The normalization of the prompt J/ψ backgrounds is not constrained and is allowed to float freely in the B_c average lifetime fit.

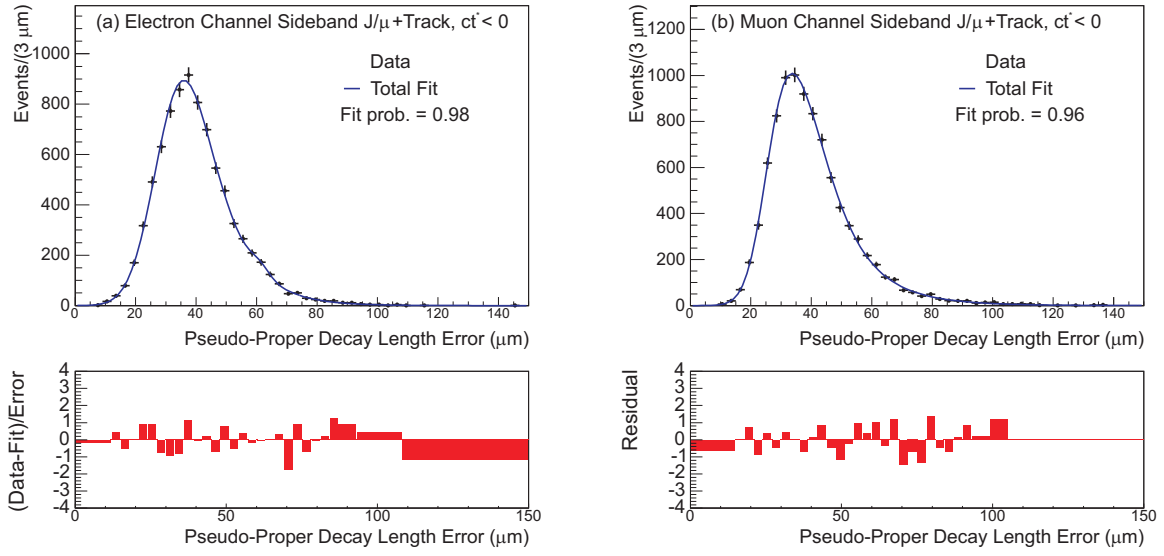


Figure 83: Fitted σ_{ct^*} projections for $ct^* < 0$ sideband J/ψ +track events for the electron channel (a) and muon channel (b).

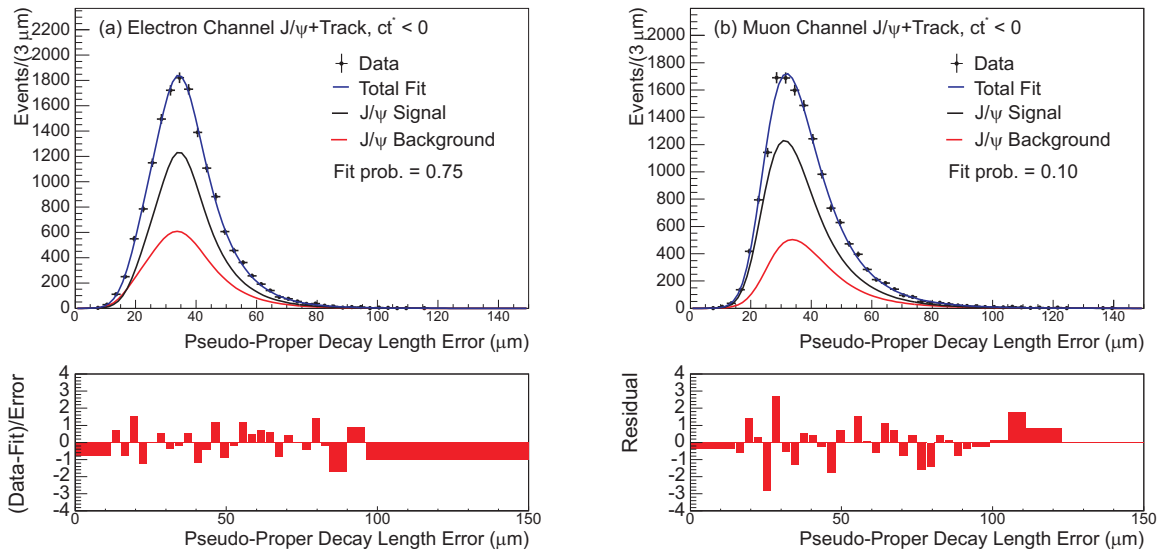


Figure 84: Fitted σ_{ct^*} projections for $ct^* < 0$ J/ψ +track events for the electron channel (a) and muon channel (b).

Parameter	Electron Channel		Muon Channel	
	Fit Value	Error	Fit Value	Error
P_0 (μm)	4.86	0.35	4.86	0.56
P_1 (μm)	9.56	1.85	11.0	3.3
P_2 (μm)	21.7	0.8	24.0	1.7
P_3 (μm)	9.56	0.45	12.5	4.0
P_4 (μm)	31.0	0.5	31.4	3.7
P_5	0.357	0.065	0.73	0.21

Table 23: Fitted parameters describing σ_{ct^*} in fits of J/ψ +track data with $ct^* < 0$.

7.6 BACKGROUNDS SUMMARY

The total numbers of predicted background and signal candidate events are summarized in Table 24. The excess of candidates in data over the background predictions is expected to consist of the prompt J/ψ background and B_c signal events.

Source	Electron Channel Events	Muon Channel Events
Misidentified Lepton	312.0 ± 4.1	96.1 ± 4.6
Misidentified J/ψ	325.2 ± 10.0	141.5 ± 8.4
$b\bar{b}$	222.5 ± 11.2	77.5 ± 11.9
Residual Conversion	416.8 ± 41.5	-
Candidates	1935	572

Table 24: Summary of background predictions and signal events.

The $J/\psi + l^\pm$ mass distribution is studied by comparing the predicted distributions from signal and background models to the distribution in data. Since there is no model for prompt events, they are removed by applying an $L_{xy}/\sigma_{xy} > 3.0$ cut to the $J/\psi + l^\pm$ system. The mass models for background events are constructed using the methods outlined in the previous

sections. The mass model for signal events is constructed from the BGENERATOR sample of B_c decays. The normalization of the signal component is determined by subtracting the number of predicted background events from the number of data events in the 4 – 6 GeV/c^2 mass window and assuming that the signal accounts for the excess. Figure 85 shows the resulting comparison of predicted and measured mass distributions and no major inconsistencies are seen.

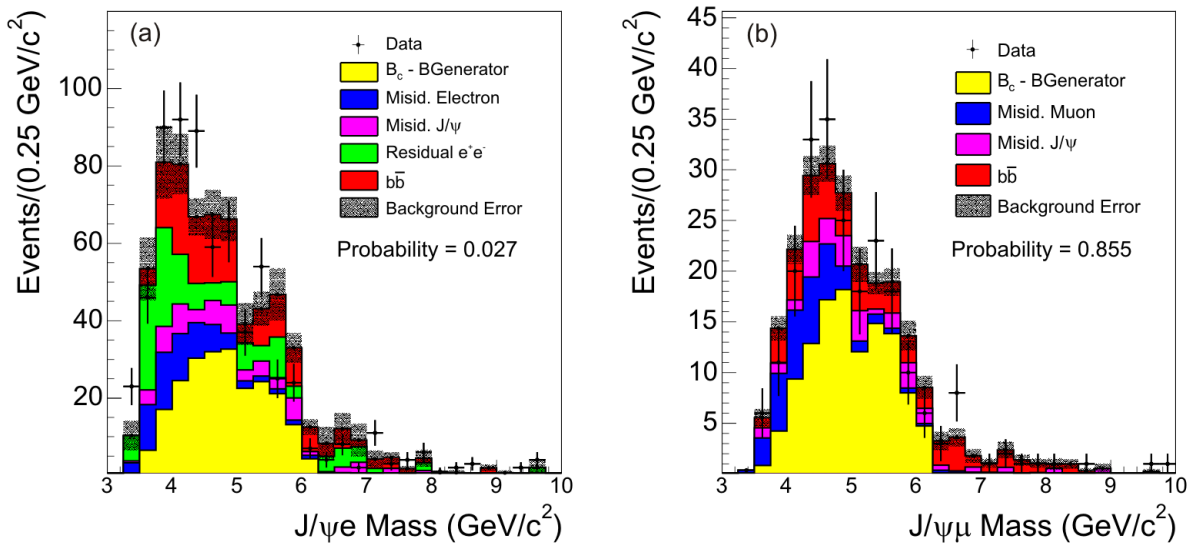


Figure 85: Comparison of predicted and measured $J/\psi + e^\pm$ (a) and $J/\psi + \mu^\pm$ (b) mass distributions for non-prompt events.

8.0 B_c LIFETIME FITTER

The ct^* and σ_{ct^*} PDFs and normalizations describing the background contributions to the B_c candidate samples have been described in the previous chapter. To construct a likelihood function for the lifetime fit, the ct^* and σ_{ct^*} models for the B_c signal events are combined with the background models to give a description of the candidate sample. Separate likelihood functions are constructed for the electron and muon channels and tested using simple Monte Carlo samples. The samples are constructed by randomly generating events that are distributed according to the parameter values, covariance matrices, and the PDFs that are used in the construction of the lifetime likelihood.

8.1 B_c SIGNAL ct^* PDF

As discussed in section 5.1 the ct^* of a given event is related to its proper decay length, ct by the factor K :

$$K = \frac{p_T(J/\psi l)}{\vec{P}(B_c) \cdot \vec{p}_T(J/\psi l) / p_T(J/\psi l)}. \quad (8.1)$$

Assuming that ct for signal events is distributed according to an exponential decay law, the expected distribution of ct^* in terms of the average proper decay length $c\tau$ and the distribution of K , $H(K)$, is

$$F_{B_c}(ct^*, \sigma_{ct^*}) = \int dK H(K) \frac{K}{c\tau} e^{-\frac{Kct^*}{c\tau}} \theta(ct^*) \otimes G(ct^*, \sigma_{ct^*}; s). \quad (8.2)$$

Here, s scales the per event σ_{ct^*} and is constrained by the scale factor from the J/ψ +track ct^* fit. The BGENERATOR sample of B_c decays, generated with an input $c\tau$ of $140\mu m$ is used

to model the distribution of $H(K)$ for signal events. The resulting K factor distributions for the electron and muon channels are shown in Figure 86. The distributions are normalized to 1 and used to carry out the previously defined integral discretely during the fit. The signal ct^* PDF rewritten with the integral discretized is

$$F_{B_c}(ct^*, \sigma_{ct^*}) = \sum H(K) \Delta K \frac{K}{c\tau} \exp\left(-\frac{Kct^*}{c\tau}\right) \theta(ct^*) \otimes G(ct^*, \sigma_{ct^*}; s) \quad (8.3)$$

where the step size ΔK is the bin size in Figure 86.

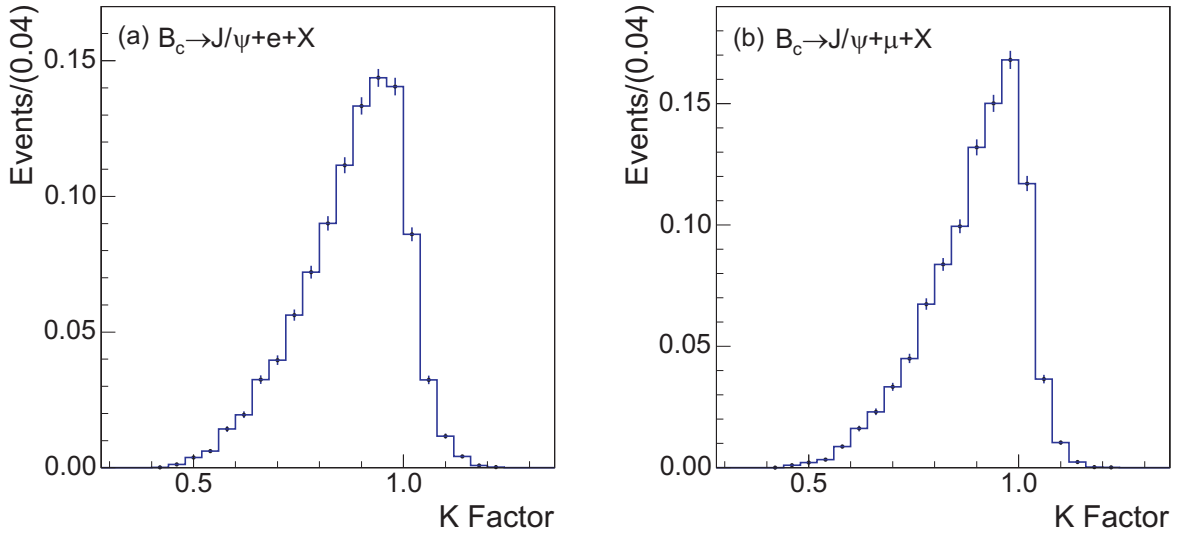


Figure 86: K factor distribution for the electron (a) and muon (a) channels where events are from the BGENERATOR sample of B_c decays.

8.2 B_c SIGNAL σ_{ct^*} PDF

There are two options for modeling the σ_{ct^*} distributions of the B_c events in the lifetime fit. It is possible to fit the σ_{ct^*} distribution of the B_c events in a BGENERATOR sample of B_c decay and propagate the parameters and errors to the lifetime fit of data. This method

may introduce systematic uncertainties related to the accuracy at which the realistic Monte Carlo reproduces the tracking uncertainties that are used to calculate σ_{ct^*} .

To avoid the uncertainties related to possible differences in the tracking resolution between the detector simulation and data, the BGENERATOR sample is not used to model the σ_{ct^*} distribution of B_c events. Instead, σ_{ct^*} is modeled with a function of the form used for many of the backgrounds, and the parameters are allowed to float in the B_c lifetime fit of data. The functional form is:

$$P_{B_c}(\sigma_{ct^*}) = \frac{1}{\sqrt{2\pi}P_0} e^{-\frac{1}{2}\left(\frac{\sigma}{P_0}\right)^2} \otimes \frac{1}{P_1} e^{-\frac{(\sigma_{ct^*}-P_2)}{P_1}} \theta(\sigma_{ct^*} - P_2) \quad (8.4)$$

8.3 CONSTRUCTION OF LIKELIHOOD

Having defined the signal and background PDFs, the likelihood function for all B_c candidates can be constructed. For a sample of N_{sig} B_c candidates that varies with Poisson statistics around the mean ν , the extended likelihood for the electron channel is of the form:

$$\begin{aligned} L = & \frac{e^{-\nu} \nu^{N_{sig}}}{N_{sig}!} \times e^{(-\frac{1}{2} V_p^T C_p^{-1} V_p)} \times e^{(-\frac{1}{2} \frac{(N_{MJ} - \bar{N}_{MJ})^2}{E_{MJ}^2})} \times \\ & e^{(-\frac{1}{2} \frac{(N_{ML} - \bar{N}_{ML})^2}{E_{ML}^2})} \times e^{(-\frac{1}{2} \frac{(N_{b\bar{b}} - \bar{N}_{b\bar{b}})^2}{E_{b\bar{b}}^2})} \times e^{(-\frac{1}{2} \frac{(N_{RC} - \bar{N}_{RC})^2}{E_{RC}^2})} \times \\ & \prod_i^{N_{sig}} [f_{B_c} P_{B_c}(\sigma_{ct^*i}) F_{B_c}(ct_i^*, \sigma_{ct^*i}) + f_{MJ} P_{MJ}(\sigma_{ct^*i}) F_{MJ}(ct_i^*, \sigma_{ct^*i}) + \\ & f_{ML} P_{ML}(\sigma_{ct^*i}) F_{ML}(ct_i^*, \sigma_{ct^*i}) + f_{b\bar{b}} P_{b\bar{b}}(\sigma_{ct^*i}) F_{b\bar{b}}(ct_i^*, \sigma_{ct^*i}) + \\ & f_{RC} P_{RC}(\sigma_{ct^*i}) F_{RC}(ct_i^*, \sigma_{ct^*i}) + f_{PR} P_{PR}(\sigma_{ct^*i}) F_{PR}(ct_i^*, \sigma_{ct^*i})] \end{aligned} \quad (8.5)$$

Here, f_{B_c} , f_{MJ} , f_{ML} , $f_{b\bar{b}}$, f_{RC} , and f_{PR} are the fractions of the B_c , misidentified J/ψ , misidentified lepton, $b\bar{b}$, residual e^+e^- and prompt J/ψ components, respectively. For each component, $P_{B_c \dots PR}$ and $F_{B_c \dots PR}$ are the PDFs for σ_{ct^*} and ct^* , respectively. V_p is a vector containing the deviation of all previously fitted parameters from their previously fitted values, and C_p is the covariance matrix that describes the uncertainties on the previously fitted values of the parameters. N_{MJ} , N_{ML} , $N_{b\bar{b}}$, and N_{RC} are the normalization for each background and

related to the fractions by $N_{MJ} = \nu f_{MJ}$. The background normalizations are constrained by the predicted values \bar{N}_{MJ} , \bar{N}_{ML} , $\bar{N}_{b\bar{b}}$, and \bar{N}_{RC} and their uncertainties E_{MJ} , E_{ML} , $E_{b\bar{b}}$, and E_{RC} . The likelihood for the muon channel is of a similar form, but all of the residual e^+e^- terms (those with subscript RC) are removed.

Bringing the N_{sig} factors of ν inside the product transforms the fractions $f_{B_c \dots P_R}$ to the numbers $N_{B_c \dots P_R}$. Taking $-2\ln(L)$ yields:

$$\begin{aligned}
-2\ln(L) = & \sum_i^{N_{sig}} [-2\ln(N_{B_c} P_{B_c}(\sigma_{ct^*i}) F_{B_c}(ct_i^*, \sigma_{ct^*i}) + N_{MJ} P_{MJ}(\sigma_{ct^*i}) F_{MJ}(ct_i^*, \sigma_{ct^*i}) + \\
& N_{ML} P_{ML}(\sigma_{ct^*i}) F_{ML}(ct_i^*, \sigma_{ct^*i}) + N_{b\bar{b}} P_{b\bar{b}}(\sigma_{ct^*i}) F_{b\bar{b}}(ct_i^*, \sigma_{ct^*i}) + \\
& N_{RC} P_{RC}(\sigma_{ct^*i}) F_{RC}(ct_i^*, \sigma_{ct^*i}) + N_{PR} P_{PR}(\sigma_{ct^*i}) F_{PR}(ct_i^*, \sigma_{ct^*i}))] + \\
& V_p^T C_p^{-1} V_p + \frac{(N_{MJ} - \bar{N}_{MJ})^2}{E_{MJ}^2} + \frac{(N_{ML} - \bar{N}_{ML})^2}{E_{ML}^2} + \\
& \frac{(N_{b\bar{b}} - \bar{N}_{b\bar{b}})^2}{E_{b\bar{b}}^2} + \frac{(N_{RC} - \bar{N}_{RC})^2}{E_{RC}^2} + \\
& 2(N_{B_c} + N_{MJ} + N_{ML} + N_{b\bar{b}} + N_{RC} + N_{PR}) + 2\ln(N_{sig}!)
\end{aligned} \tag{8.6}$$

The unconstrained parameters in the fit are N_{B_c} and N_{PR} , which set the normalization of the B_c and prompt J/ψ components, the B_c average proper decay time $c\tau$, which is a parameter in $F_{B_c}(ct_i^*, \sigma_{ct^*i})$, and the parameters that describe $P_{B_c}(\sigma_{ct^*i})$.

8.3.1 Lifetime fitter checks

To check for biases in the fitter, simple Monte Carlo samples of B_c candidate events are generated using the background determinations from Chapter 7 and a signal model based on the BGENERATOR distributions for K factors and σ_{ct^*} . For the background components, parameters are generated using a weighted rejection of randomly generated parameter values that are compared to the multidimensional Gaussian distribution that has widths defined by the covariance matrix of the parameters. Events are then generated according to the background ct^* and σ_{ct^*} models and the randomly generated parameters. The number of events generated for each background is varied according to the uncertainties of the background determinations. For the parameters that do not have estimates, assumptions must

be made. The normalizations N_{B_c} and N_{PR} are assumed to account for 60% and 40% of the excess events, respectively. The average proper decay length of B_c events is varied over a large range with trials generated at values of 80 μm , 140 μm , and 200 μm , corresponding to 3σ deviations around the previously measured CDF value [2]. The $P_{B_c}(\sigma_{ct^*i})$ model is taken directly from the BGENERATOR B_c sample.

For each input lifetime 1000 trials are generated and fitted. The fitted B_c average proper decay time for each trial, $c\tau_{meas}$, and its error $\sigma_{c\tau}$ are recorded and a pull is constructed:

$$c\tau_{pull} = \frac{c\tau_{meas} - c\tau_{input}}{\sigma_{c\tau}} \quad (8.7)$$

If the fitter is unbiased for measurements of the B_c average proper decay length, the pull distribution for all trials should be a Gaussian with mean 0 and width 1. Figures 87 and 88 show the pull distributions for trials run on the electron channel and muon channel fitters respectively. In all cases the pulls show no significant deviation from the expected Gaussians.

To check that the reconstruction of the per event ct^* does not contain any pathologies that might bias the fitted lifetime, the B^\pm lifetime is measured using $B^\pm \rightarrow J/\psi + K^\pm$ candidates from the same reconstruction code that is used to collect the B_c candidates. Figure 89 shows the resulting fit of the proper decay length. The measured value 494 ± 16 μm is in good agreement with the world average of 502 μm [15].

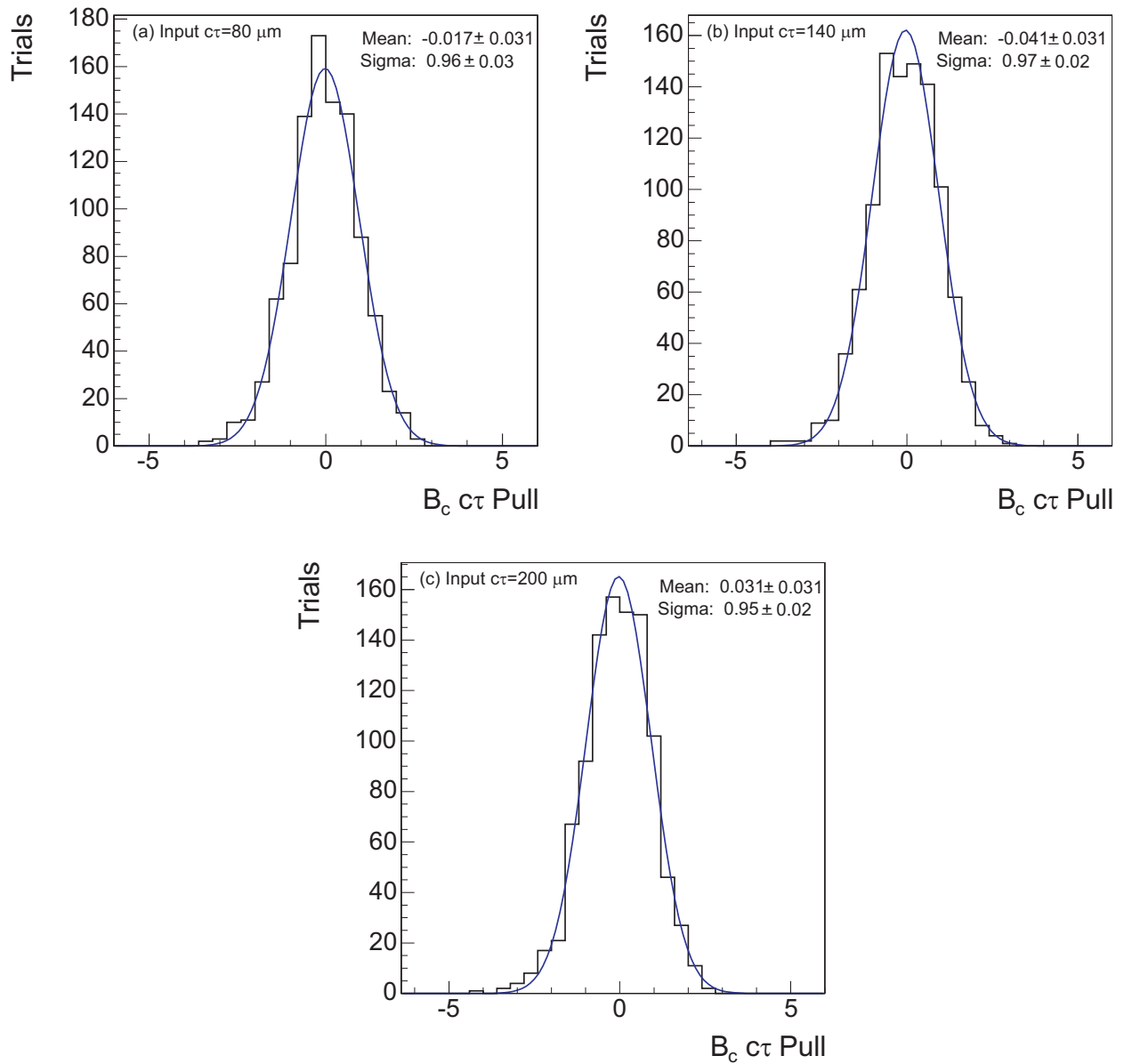


Figure 87: Pulls of measured $c\tau$ for ~ 1000 simple Monte Carlo trials with input $c\tau$ values of 80 (a), 140 (b), and 200 (c) μm . Fits were carried out with the electron channel fitter.

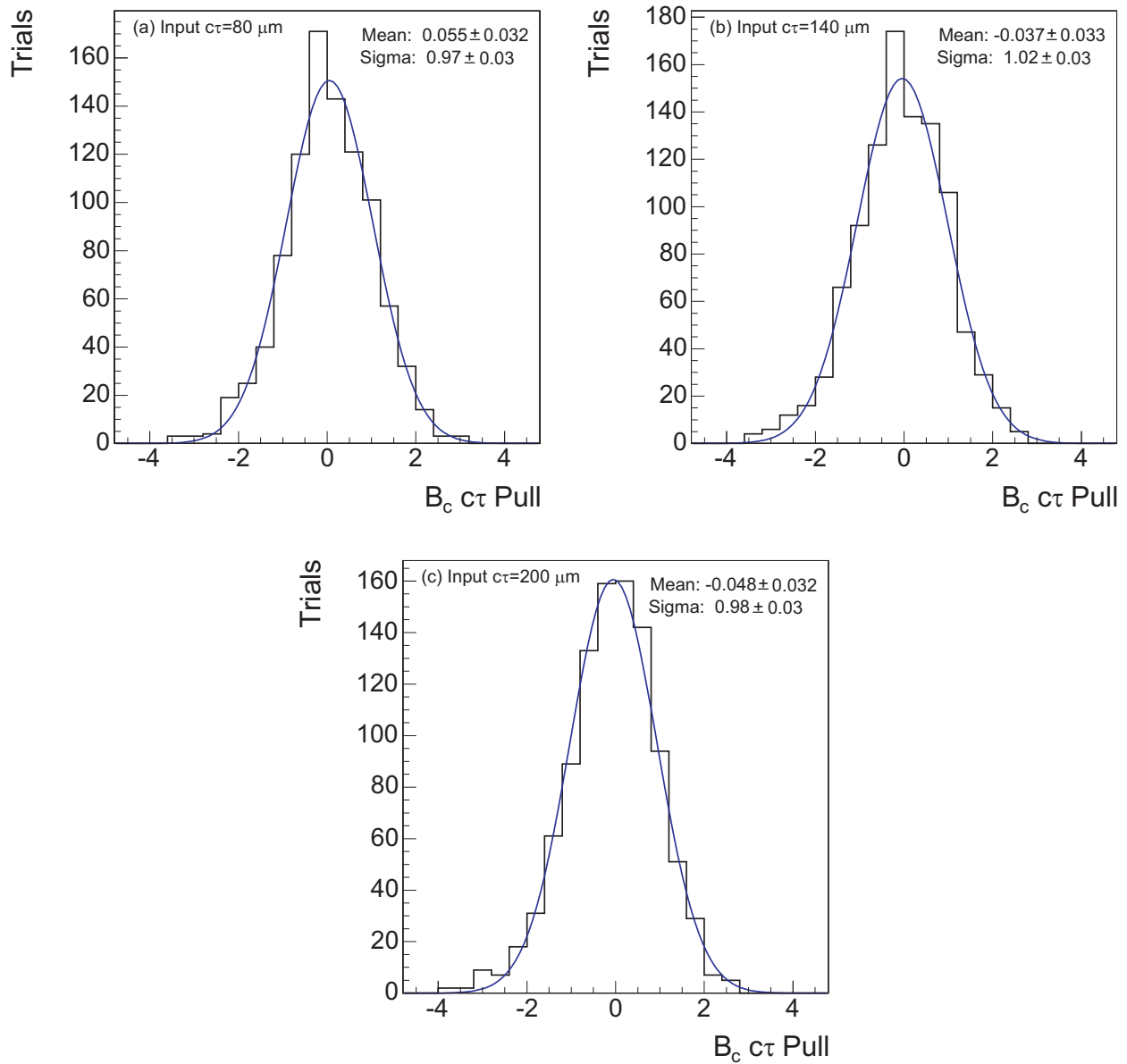


Figure 88: Pulls of measured $c\tau$ for ~ 1000 simple Monte Carlo trials with input $c\tau$ values of 80 (a), 140 (b), and 200 (c) μm . Fits were carried out with the muon channel fitter.

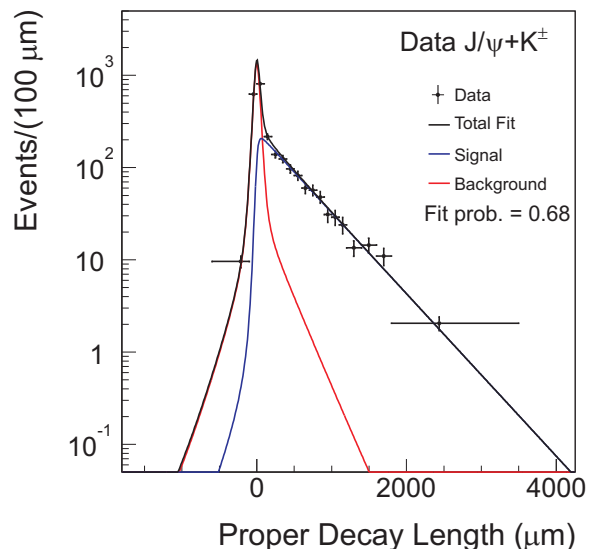


Figure 89: Fit of ct for $B^\pm \rightarrow J/\psi + K^\pm$ candidates.

9.0 B_c AVERAGE LIFETIME FIT

In the previous chapter the lifetime fitters' performance were verified to be unbiased on large sets of simple Monte Carlo samples. The unbiased fitters are used to fit the data, and the resulting parameters and their uncertainties, including the B_c average proper decay length, are discussed here. A number of cross checks are performed to verify that the physics described by the fitted parameters is consistent with the data.

The electron and muon channel candidates are fitted separately, and a combination of the two channels into a single value for the B_c average proper decay length is presented.

9.1 FIT RESULTS

The minimization of the parameters in the lifetime fit are carried out with the MIGRAD algorithm which returns parabolic (symmetric) errors for all parameters by probing the derivatives of the minimization function in the region near the minimum. After the MIGRAD minimization, the MINOS algorithm is applied to the parameter describing the B_c average proper decay length. The MINOS algorithm provides a full scan of $-2\ln(L)$ for varying values of the parameter, returning asymmetric uncertainties if the $-2\ln(L)$ contour is not symmetric. The quoted MINOS statistical uncertainties correspond to a 1 unit increase in $-2\ln(L)$ since this would represent a 1σ deviation (68% confidence range) of the likelihood were it parabolic.

There are six free parameters in the fits, and they are listed in Table 25. The fitted values for the B_c average proper decay length $c\tau$ are $121.7_{-16.3}^{+18.0} \mu\text{m}$ and $179.1_{-27.2}^{+32.6} \mu\text{m}$ for the electron channel and muon channel fits respectively. In addition to the free parameters,

	Electron Channel		Muon Channel	
Parameter	Value	Error	Value	Error
$B_c c\tau$ (μm)	121.7	$^{+18.0}_{-16.3}$	179.1	$^{+32.6}_{-27.2}$
N_{B_c}	342.7	44.0	138.6	20.9
N_{PR}	281.0	54.4	112.9	22.6
$B_c \sigma_{ct^*}$ Parameters				
P_0 (μm)	5.96	0.81	4.85	0.82
P_1 (μm)	11.1	2.0	9.8	2.5
P_2 (μm)	23.6	1.4	21.2	1.2

Table 25: Free parameters from the fits in both electron and muon channels. All errors are from the MIGRAD algorithm, except for the $c\tau$ errors which are calculated with the MINOS algorithm.

the fits include a number of constrained parameters. The fitted values of the constrained parameters for the electron channel are listed in Tables 26 and 27. The fitted values of the constrained parameters for the muon channel are listed in Tables 28 and 29. Fit projections for ct^* and σ_{ct^*} are plotted and compared to the data points as shown in Figures 90 and 91. For each fit projection, a χ^2 probability is calculated by binning events in bins of at least 16 events and comparing the number of events per bin to the integral of the fit projection. All probabilities are > 0.10 , and no inconsistencies are seen.

9.2 FIT RESULT CROSS-CHECKS

The parameters describing the σ_{ct^*} distributions for B_c events are determined by the lifetime fits. From Figure 91 it is clear that the fit chooses the parameters such that the σ_{ct^*} functions for B_c events are peaked at lower values than the σ_{ct^*} functions for the other fit components.

Parameter	Value	Error
s B_c /Prompt σ_{ct^*} scale factor	1.212	0.020
N_{MJ} Misidentified J/ψ Normalization	330	16
Misidentified J/ψ ct^* Parameters		
s	1.302	0.059
f_0	0.632	0.047
$c\tau_{++}$ (μm)	316	85
f_{++}	0.056	0.023
$c\tau_-$ (μm)	105	14
f_-	0.144	0.023
$c\tau_+$ (μm)	84	19
f_+	0.163	0.045
Misidentified J/ψ σ_{ct^*} Parameters		
P_0 (μm)	7.30	0.44
P_1 (μm)	11.15	0.68
P_2 (μm)	32.62	0.63
N_{ML} Misidentified Electron Normalization	313.0	4.6
Misidentified Electron ct^* Parameters		
f_0	0.830	0.011
$c\tau_{++}$ (μm)	678	29
f_{++}	0.0636	0.0040
$c\tau_+$ (μm)	138	17
f_+	0.0837	0.0057
$c\tau_-$ (μm)	109	26
f_-	0.0202	0.0047
s	1.274	0.012
Misidentified Electron σ_{ct^*} Parameters		
P_0 (μm)	4.37	0.12
P_1 (μm)	10.5	1.6
P_2 (μm)	22.52	0.31
P_3 (μm)	10.43	0.39
P_4 (μm)	32.19	0.25
P_5	0.353	0.042

Table 26: Constrained parameters from the fit of the electron channel events.

Parameter	Value	Error
$N_{b\bar{b}}$ $b\bar{b}$ Normalization	224	11
$b\bar{b}$ ct^* Parameters		
s	1.717	0.067
$c\tau_+$ (μm)	19	11
$c\tau_{++}$ (μm)	206	17
f_+	0.288	0.064
$b\bar{b}$ σ_{ct^*} Parameters		
P_0 (μm)	6.29	0.62
P_1 (μm)	12.11	0.90
P_2 (μm)	27.27	0.81
N_{RC} Residual e^+e^- Normalization	429	50
Residual e^+e^- ct^* Parameters		
s	1.311	0.019
$c\tau_+$ (μm)	362	44
f_0	0.785	0.065
f_+	0.215	0.036
Residual e^+e^- σ_{ct^*} Parameters		
P_0 (μm)	6.91	0.77
P_1 (μm)	11.9	1.1
P_2 (μm)	29.3	1.1
Prompt σ_{ct^*} Parameters		
P_0 (μm)	4.84	0.22
P_1 (μm)	9.5	1.7
P_2 (μm)	21.81	0.74
P_3 (μm)	9.54	0.42
P_4 (μm)	31.10	0.49
P_5	0.367	0.062

Table 27: Continuation of constrained parameters from the fit of the electron channel events.

Parameter	Value	Error
s B_c /Prompt σ_{ct^*} scale factor	1.202	0.020
N_{MJ} Misidentified J/ψ Normalization	142.5	8.1
Misidentified J/ψ ct^* Parameters		
s	1.35	0.11
f_0	0.788	0.062
$c\tau_+$ (μm)	390	67
f_+	0.140	0.030
$c\tau_-$ (μm)	231	80
f_-	0.076	0.023
Misidentified J/ψ σ_{ct^*} Parameters		
P_0 (μm)	5.99	0.77
P_1 (μm)	15.2	1.1
P_2 (μm)	25.59	0.96
N_{ML} Misidentified Muon Normalization	97.52	4.50
Misidentified Muon ct^* Parameters		
f_0	0.677	0.022
$c\tau_{++}$ (μm)	658	28
f_{+++}	0.207	0.013
$c\tau_+$ (μm)	117	38
f_+	0.085	0.010
$c\tau_-$ (μm)	100	26
f_-	0.0259	0.0084
s	1.167	0.019
Misidentified Muon σ_{ct^*} Parameters		
P_0 (μm)	4.829	0.096
P_1 (μm)	11.68	0.23
P_2 (μm)	22.8	0.12
P_3 (μm)	8.81	0.62
P_4 (μm)	31.63	0.52
P_5	0.799	0.015

Table 28: Constrained parameters from the fit of the muon channel events.

Parameter	Value	Error
$N_{b\bar{b}}$ $b\bar{b}$ Normalization	78.6	6.3
$b\bar{b}$ ct^* Parameters		
s	1.310	0.046
$c\tau_+$ (μm)	120	11
$c\tau_{++}$ (μm)	575	136
f_+	0.900	0.044
$b\bar{b}$ σ_{ct^*} Parameters		
P_0 (μm)	6.23	0.65
P_1 (μm)	12.87	0.81
P_2 (μm)	25.04	0.67
Prompt σ_{ct^*} Parameters		
P_0 (μm)	4.84	0.21
P_1 (μm)	10.97	0.39
P_2 (μm)	23.94	0.57
P_3 (μm)	12.7	1.6
P_4 (μm)	31.1	1.8
P_5	0.724	0.087

Table 29: Continuation of constrained parameters from the fit of the muon channel events.

As a cross-check, the fitted σ_{ct^*} functions are compared to the σ_{ct^*} distributions predicted by the BGENERATOR sample of B_c decays. Figure 92 shows the fitted functions overlaid on the distributions from BGENERATOR. The overall structure of the fitted functions are consistent with the distributions predicted by the BGENERATOR sample, including the peak values of the distributions.

The predicted $J/\psi + l^\pm$ mass distributions were compared to data in Section 7.9. A similar procedure can be followed to compare the mass distributions, where the background normalizations are determined by the fit results. Mass templates are constructed for the backgrounds using the same methods outlined in Chapter 7. Since no method exists for constructing a mass template for the prompt J/ψ background, a $ct^* > 120 \mu\text{m}$ cut is applied to remove the prompt events. Mass templates for the B_c signal events are modeled using the BGENERATOR sample of B_c decays. The normalizations for the background and signal components are determined by integrating the various components of the fit function in the region $ct^* > 120 \mu\text{m}$. The resulting predicted mass distributions are compared to data as

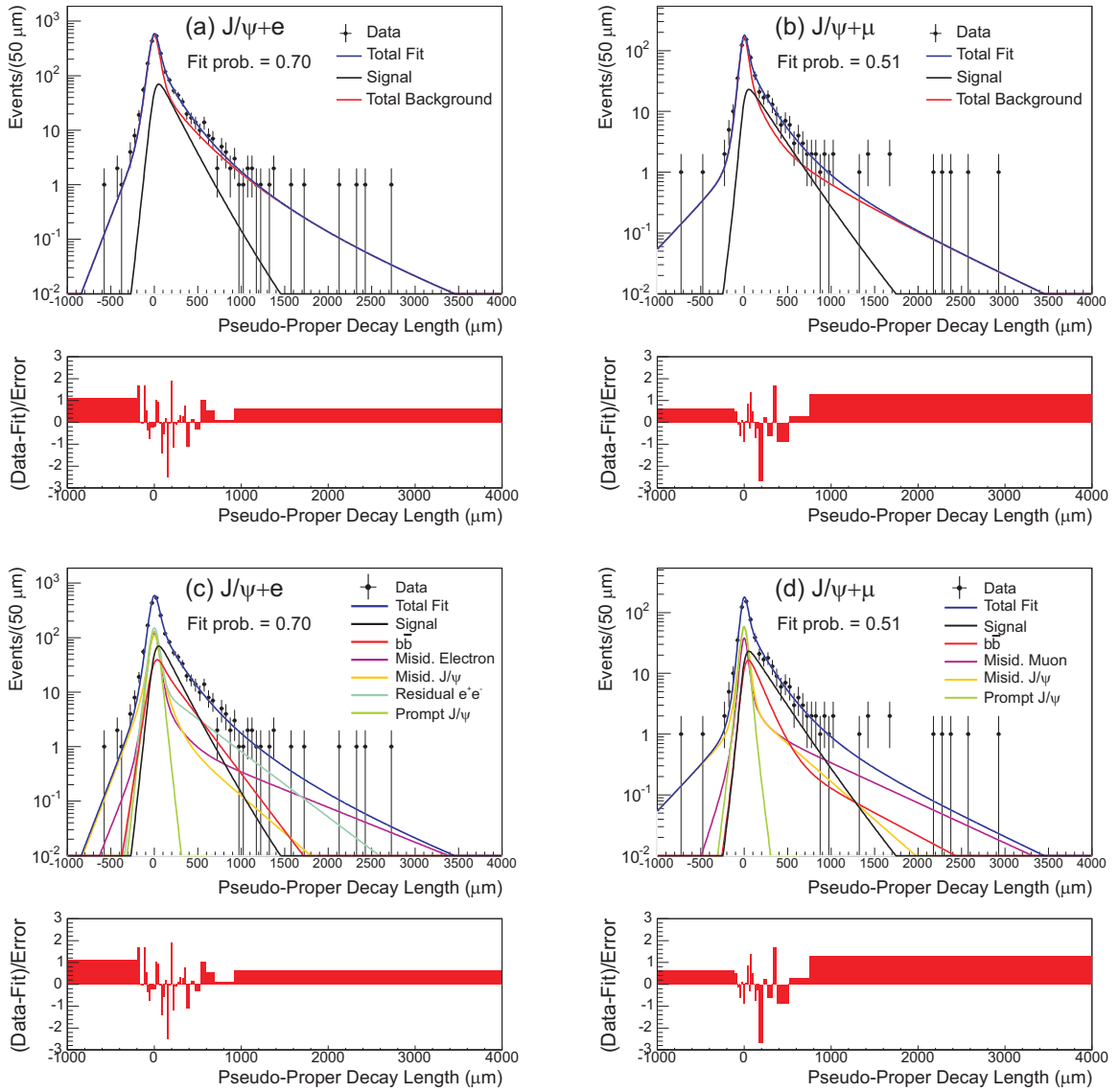


Figure 90: ct^* fit projections for the electron channel (a,c) and muon channel (b,d) fits. The backgrounds are plotted as a single function (a) and (b) and broken out (c) and (d).

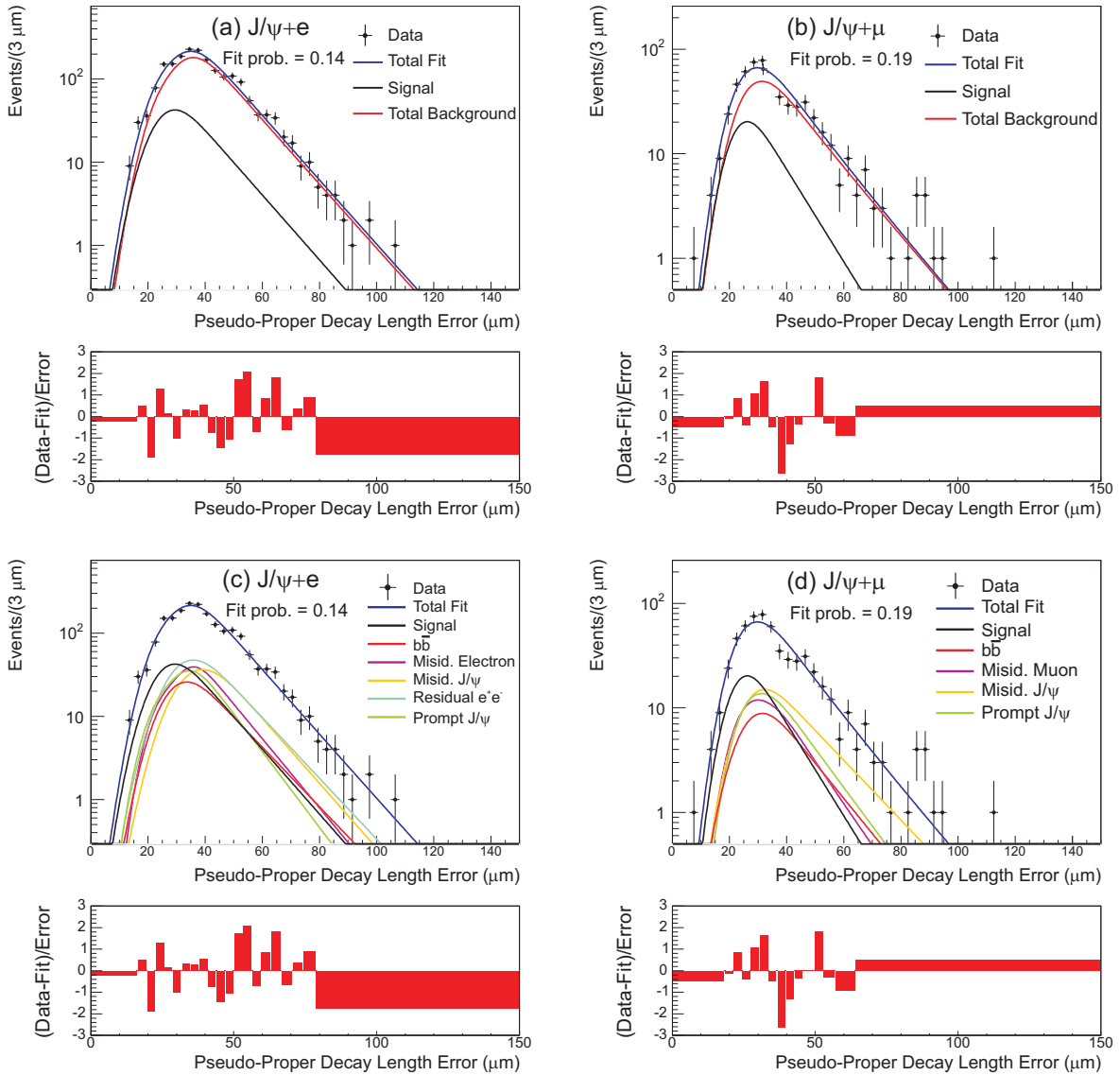


Figure 91: σ_{ct^*} fit projections for the electron channel (a,c) and muon channel (b,d) fits. The backgrounds are plotted as a single function in (a) and (b) and broken out in (c) and (d).

shown in Figure 93. The agreement between the predicted and measured mass distributions is good.

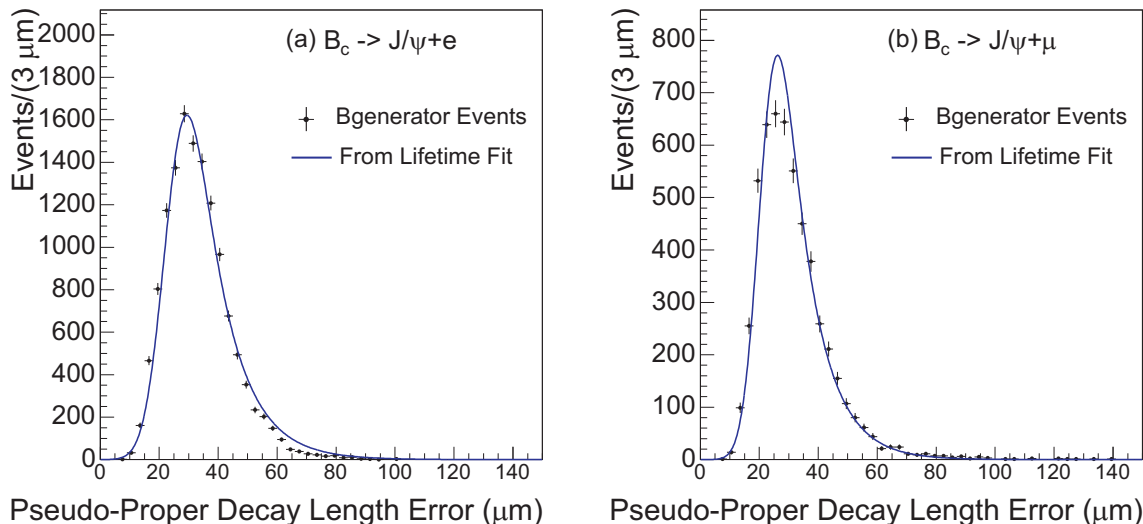


Figure 92: Fitted σ_{ct^*} functions compared to the σ_{ct^*} distributions from the BGENERATOR sample of B_c decays for the electron (a) and muon (b) channels.

In addition to determining the B_c average proper decay length, the fit also determines the B_c yields for both the electron and muon channels. They are 342.7 ± 44.0 and 138.6 ± 20.9 events, respectively. Given the efficiencies for reconstructing candidate events, are the relative yields in the electron and muon channels consistent? This question can be answered by studying the BGENERATOR B_c sample where B_c decays to electron and muon final states are generated in equal proportion. The resulting yields of electron and muon final states are 13112 and 5284 events respectively. The relative yield for the two channels as predicted by the BGENERATOR sample is 2.48. The relative yield from the fit to data is 2.47 ± 0.49 , which is in good agreement with the predicted relative yield from BGENERATOR

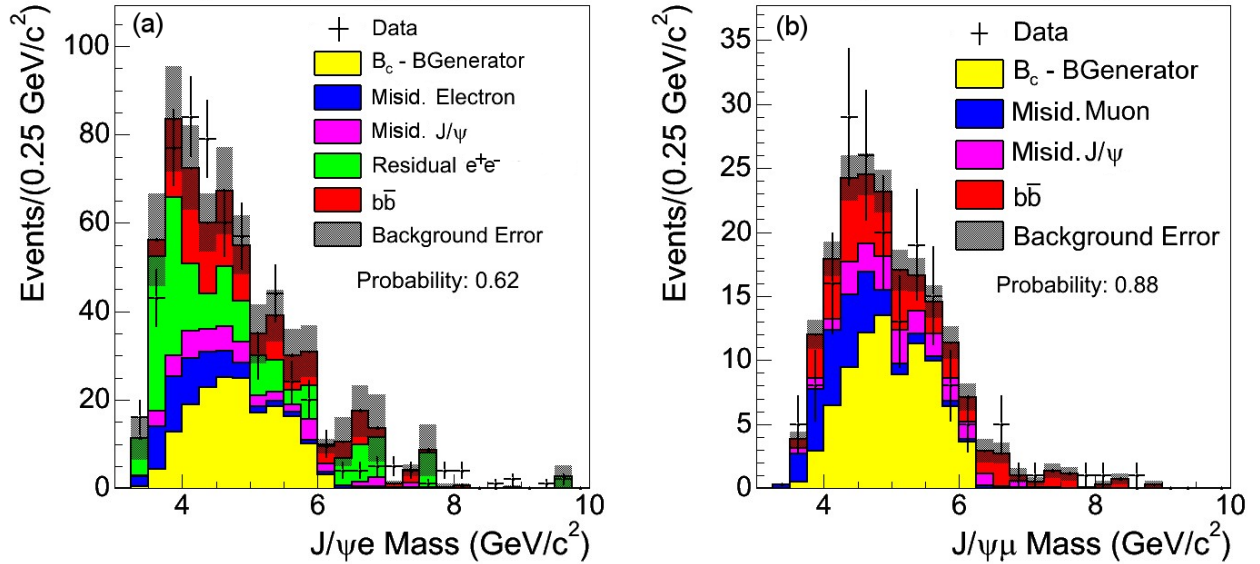


Figure 93: Predicted $J/\psi + l$ mass distributions for the electron channel (a) and the muon channel (b). The histograms for the predicted components are stacked.

9.3 COMBINING THE ELECTRON AND MUON CHANNEL FITS

The fitted values for the B_c average proper decay length from the electron channel and muon channel fits can be combined to give a single measured value. Since the likelihoods are constructed as probabilities, the likelihoods are combined by taking their product, or in the case of $-2\ln(L)$ their sum. The sum $-2\ln(L_e) - 2\ln(L_\mu)$ is carried out by evaluating the MIGRAD minimum at points in a parameter space consisting of the parameters that are common to the two likelihoods. For each likelihood and at each point in the space, the common parameters are fixed, while $-2\ln(L)$ is minimized by varying the remaining parameters. This provides a contour of dimension equal to the number of common parameters. The two contours for the two channels are then added creating a combined countour where the properties of the minimum describe the fitted values and statistical uncertainties of the common parameters.

Since the only parameter common to the electron and muon channel fits is the B_c average proper decay length $c\tau$, the MIGRAD minimum is evaluated at various values of $c\tau$ for each

channel. The resulting contours for the electron and muon channels are shown in Figure 94. These contours are equivalent to those used by the MINOS algorithm to compute the statistical uncertainties. The two contours are added and the resulting contour is shown in Figure 95. The minimum value of the combined contour is $142.5 \mu\text{m}$ and the statistical uncertainties are evaluated by finding the $c\tau$ values corresponding to a 1 unit change in the contour. The combined measurement of the average proper decay length with statistical uncertainty is $c\tau = 142.5^{+15.8}_{-14.8}(\text{stat.}) \mu\text{m}$. In terms of an average proper decay time, this is $\tau = 0.475^{+0.053}_{-0.049}$ ps.

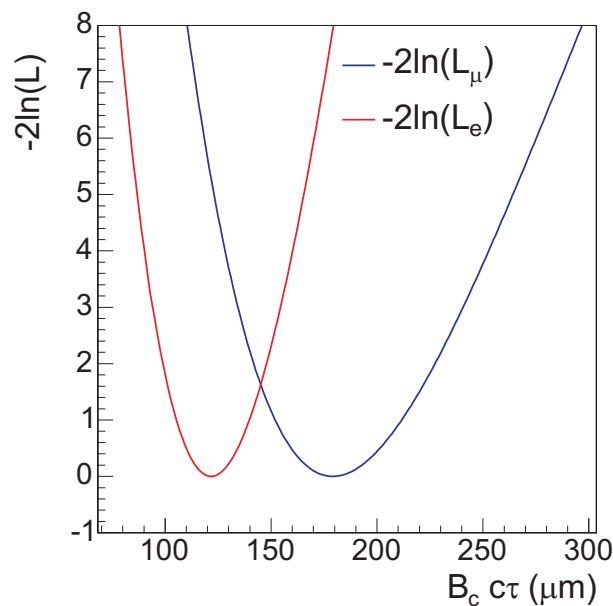


Figure 94: $-2\ln(L)$ contours for the electron and muon channels. For each point, the $c\tau$ is fixed while the other parameters are minimized with MIGRAD.

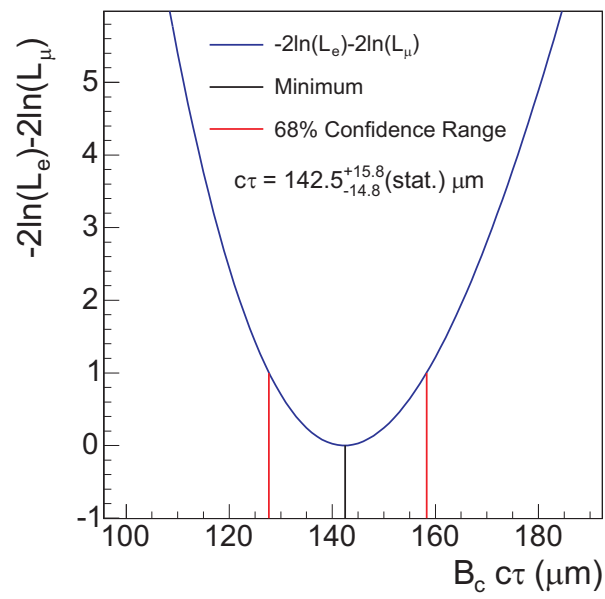


Figure 95: Combined likelihood for the electron and muon channels.

10.0 SYSTEMATIC UNCERTAINTIES

The goal of a robust measurement is to apply procedures for selecting and modeling events where the variation of the procedures within uncertainties does not significantly change the measured central value and the procedures do not introduce any biases in the measured central value. An example from this thesis is the choice of the $Z_{\mu}^{pull} > -1.0$ cut which minimizes the uncertainty due to variations in the proton fraction model for the J/ψ +track sample. To the extent that procedural uncertainties remain they must be evaluated. The evaluation of these systematic uncertainties is discussed in this chapter.

The procedure for determining the systematic uncertainties is similar to the method of simple Monte Carlos used in Section 7.3.1 to check for biases in the fitters. For the systematic studies, the trials are not generated with the same PDFs that are used in the fitter. Instead, the signal or background model that corresponds to the systematic uncertainty being studied is modified in a manner that probes the configuration space corresponding to the systematic uncertainty. The modified model is used while generating toys, and the unmodified fitter is used to fit events. The difference in the mean measured average proper decay length from the input value gives a measurement of the systematic uncertainty. This procedure is carried out for each of the sources of error studied.

The systematic uncertainties are measured for trials generated with B_c average proper decay length values of 128, 143, and 158 μm , corresponding to the measured value and $\pm 1\sigma$ of statistical uncertainty. The systematics are evaluated for the electron and muon channels separately, and a weighted combination is constructed using the most conservative model to account for possible correlations of the systematic uncertainties between the two channels. The total systematic uncertainty for each input $c\tau$ is the sum in quadrature of the individual combined uncertainties, and the largest value of the total systematic uncertainty among the

input $c\tau$ values is chosen as the systematic uncertainty for the measurement.

10.1 THE B_c SPECTRUM

The production spectrum of B_c mesons created in $p\bar{p}$ collisions at the Tevatron has not been measured experimentally. The K factors used in the lifetime fit are modeled with the BGENERATOR Monte Carlo sample of B_c decays where the B_c mesons are generated using η and p_T spectra based on theoretical calculations.

The dependence of the measured lifetime on the B_c spectrum is modeled by using spectra that are harder or softer in their p_T distributions and generating new BGENERATOR Monte Carlo samples. The new samples are used to construct new K factor distributions. For the case of the hard spectrum, the B_c are generated with the spectrum that describes the production of light B mesons. A comparison of the spectra can be seen in Figure 96. For the soft spectrum, the inverse of the transformation from the B_c to B spectrum is applied to the B_c spectrum and the resulting spectrum is used to generate B_c .

Figure 97 shows a comparison of the new K factor distributions for the hard and soft spectra as well as the nominal distribution. The K factor distributions for the hard and soft spectra are used to generate trials, and the shifts in the measured average proper decay length are listed in Table 30.

10.2 B_c DECAY MODES

The BGENERATOR sample used to model B_c signal events also requires as an input the B_c branching fractions for decays to $J/\psi(\mu^+\mu^-)+l^\pm+X$ final states. The branching fractions are listed in Appendix A and based on theoretical predictions. The variation of the theoretical predictions of the branching fractions can be significant [50], so a systematic uncertainty should be assigned. A conservative variation of the branching fractions is to double or halve the rate of the $J/\psi(\mu^+\mu^-)+l^++\mu_l$ branching fraction relative to the rate of all other sources

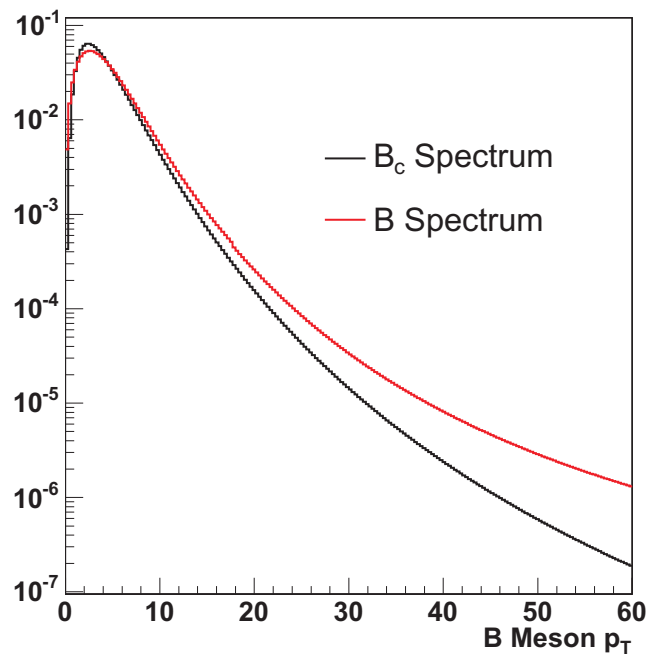


Figure 96: Comparison of B_c and B meson p_T spectra that are used while generating events in BGENERATOR.

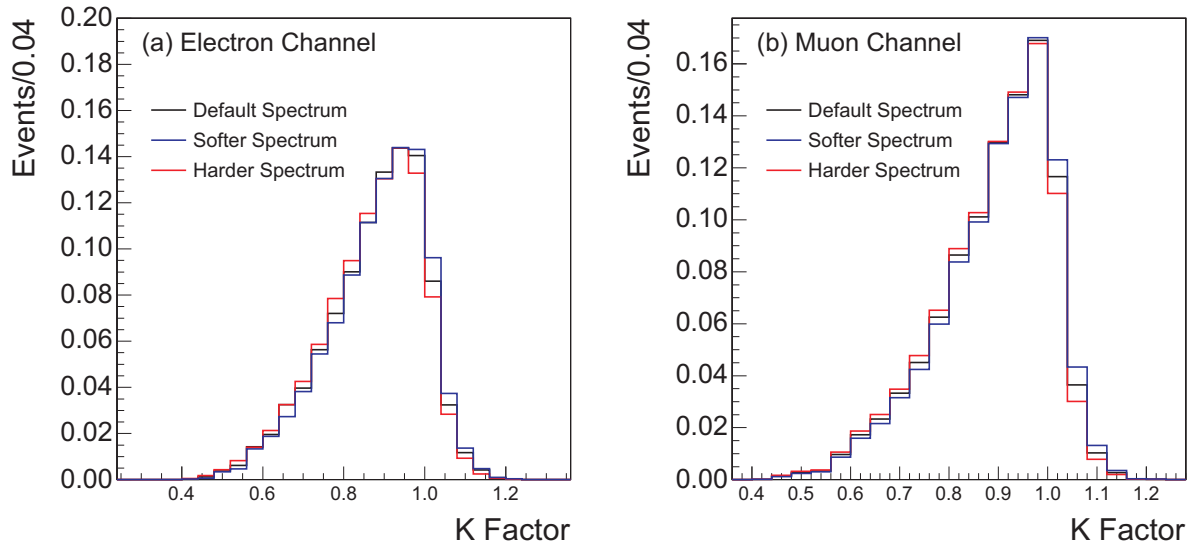


Figure 97: Comparison of electron (a) and muon (b) channel K factor distributions for simulated B_c events with varied p_T spectra.

	Systematic Shift (μm)		
Systematic	$c\tau = 128 \mu\text{m}$	$c\tau = 143 \mu\text{m}$	$c\tau = 158 \mu\text{m}$
Electron Channel			
Harder Spectrum	+1.1	+1.4	+1.4
Softer Spectrum	-1.1	-1.0	-1.2
Muon Channel			
Harder Spectrum	+0.8	+0.9	+1.1
Softer Spectrum	-0.0	-1.0	-1.0

Table 30: Shifts in the average proper decay length for systematic studies of the B_c spectrum.

of $J/\psi(\mu^+\mu^-) + l^\pm + X$. Figure 98 shows what effect adjusting the branching fractions has on the K factors distributions. These K factor distributions for adjusted branching fractions are used to generate trials, and the resulting systematic shifts in the average proper decay length are listed in Table 31.

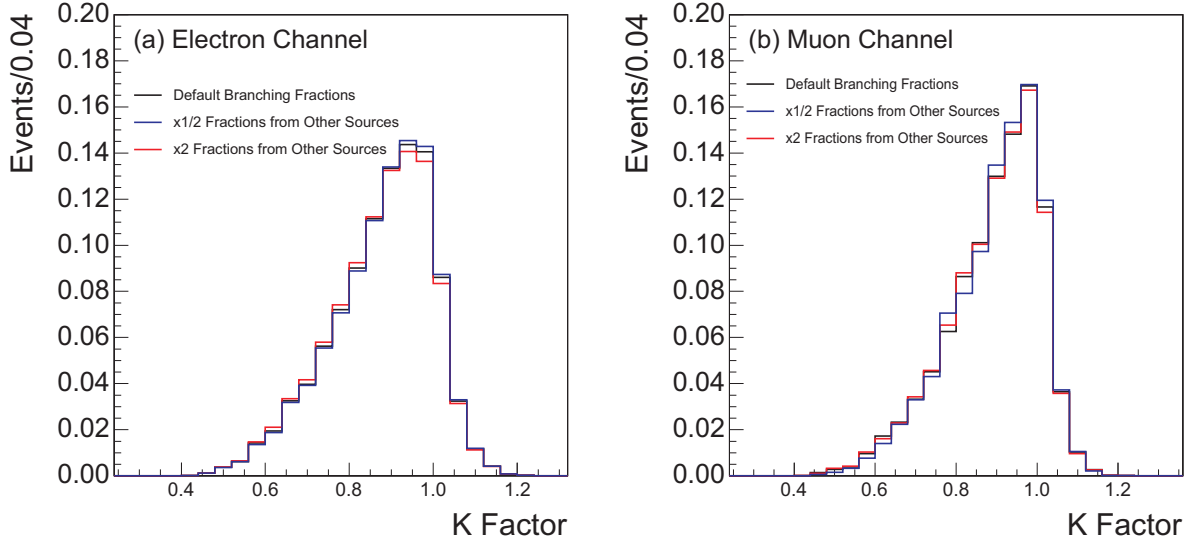


Figure 98: Comparison of the electron (a) and muon (b) channel K factor for default and adjusted branching fractions.

10.3 MISIDENTIFIED J/ψ ct^* MODEL

The ct^* for the misidentified J/ψ background is modeled with sideband J/ψ events where an additional third lepton is present. Since the sample of events used for the ct^* model is small, any long lived exponential components are not well determined by a fit to the events. A related sample with large statistics consists of events with J/ψ candidates selected from the J/ψ mass sideband and an additional third track with no lepton requirement. This large sample can be fitted to give an alternative model of the ct^* in the long lived regions, as shown in Figure 99. The models from fits of the sideband J/ψ +track events are not in

Systematic Shift (μm)			
Systematic	$c\tau = 128 \mu\text{m}$	$c\tau = 143 \mu\text{m}$	$c\tau = 158 \mu\text{m}$
Electron Channel			
Halved Fractions	-0.2	+0.1	-0.3
Doubled Fractions	+0.6	+0.8	+0.6
Muon Channel			
Halved Fractions	-0.6	-0.7	-0.7
Doubled Fractions	+0.3	+0.2	+0.3

Table 31: Shifts in the average proper decay length for systematic studies of the B_c branching fractions.

good agreement with the sample of sideband J/ψ +lepton events, but they can be modified by adjusting the relative fraction of prompt and long lived components to show good agreement. The adjusted models are overlaid on sideband $J/\psi + l$ events and shown Figure 100. These new models are used to generate events for a trials, and the resulting shifts in the measured average proper decay length are listed in Table 32.

10.4 $b\bar{b}$ SCALE FACTORS

As described in Section 7.3.1, the relative normalizations of the QCD processes that produce $b\bar{b}$ pairs in the PYTHIA Monte Carlo are tuned using the $\Delta\phi$ correlation between the J/ψ and μ coming from opposite b quarks. The tuning enhances the gluon splitting component by $\sim 40\%$ while decreasing the amount of flavor creation and flavor excitation to compensate. As a check on the systematic uncertainty related to the tuning, the $b\bar{b}$ is modeled with two other sets of scale factors: the untuned PYTHIA sample is used where scale factors are by definition 1, and the gluon splitting component is increased by 1σ from 1.42 ± 0.21 to 1.63. The number of predicted $b\bar{b}$ events vary as described in Table 33.

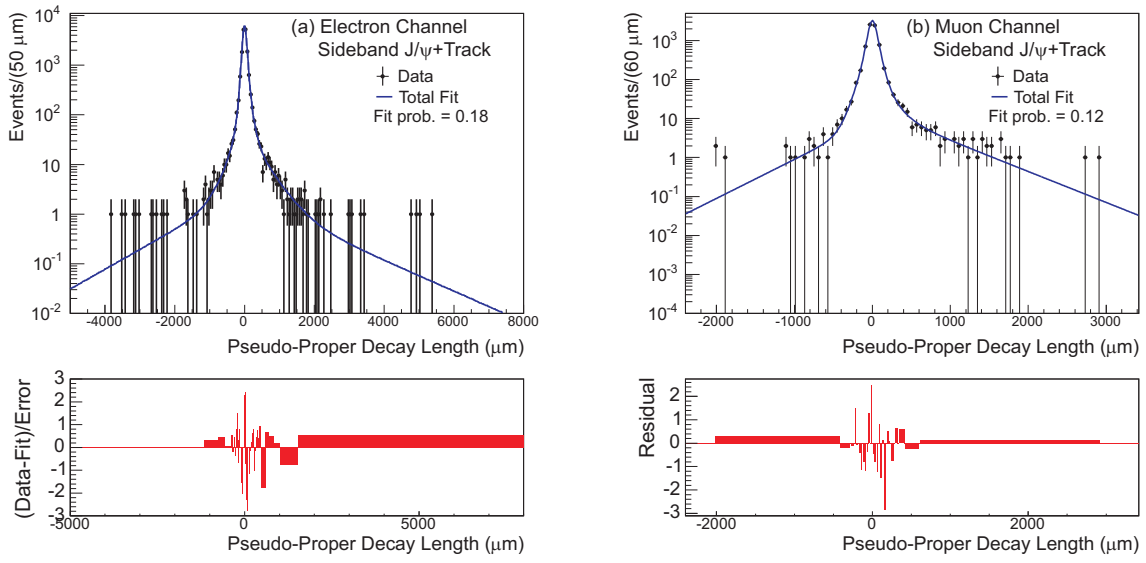


Figure 99: Fitted ct^* distributions for sideband J/ψ +track events for the electron channel (a) and muon channel (b) cuts.

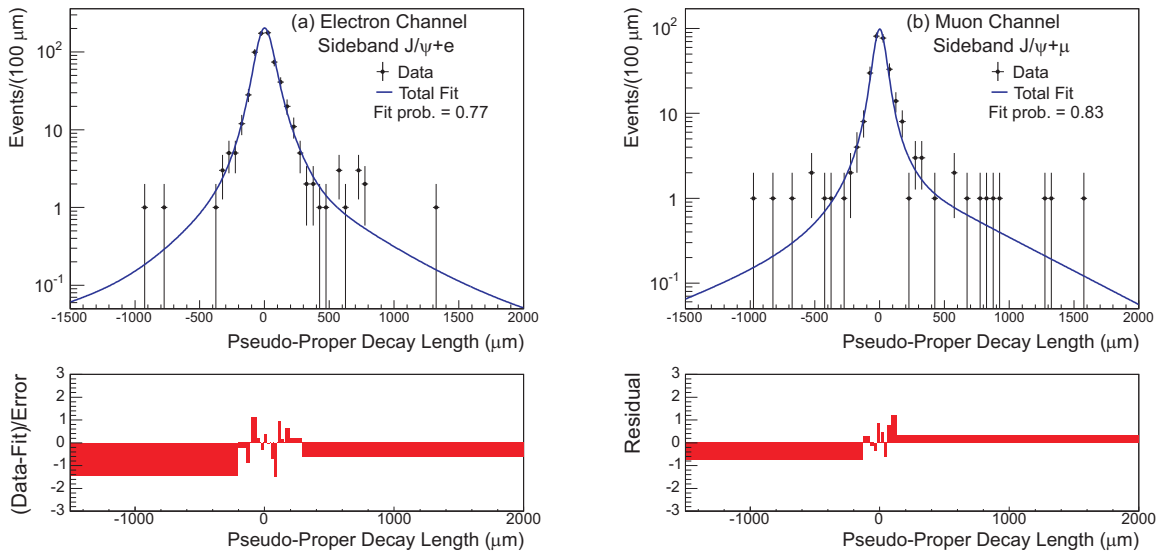


Figure 100: ct^* distributions for electron (a) and muon (b) channel sideband $J/\psi + l$ events with the adjusted functions from the sideband J/ψ +track samples.

Systematic	Systematic Shift (μm)		
	$c\tau = 128 \mu\text{m}$	$c\tau = 143 \mu\text{m}$	$c\tau = 158 \mu\text{m}$
Electron Channel			
Sideband J/ψ +track Inspired Template	+0.7	+1.0	+1.1
Muon Channel			
Sideband J/ψ +track Inspired Template	-1.0	-0.9	-0.4

Table 32: Shifts in the average proper decay length for systematic studies of the shape of the ct^* distribution for misidentified J/ψ events.

$b\bar{b}$ Normalization Predictions			
Channel	Untuned Pythia	Nominal Scale Factors	GS $+1\sigma$
Electron Channel	160.8	222.5	245.4
Muon Channel	56.5	77.5	86.8

Table 33: Variation of the predicted $b\bar{b}$ normalization for variations in the factors that scale the relative fractions of QCD processes in the $b\bar{b}$ production.

The models with adjusted scale factors are used to generate trials and the resulting shifts in the measured average proper decay length are listed in Table 34.

Systematic	Systematic Shift (μm)		
	$c\tau = 128 \mu\text{m}$	$c\tau = 143 \mu\text{m}$	$c\tau = 158 \mu\text{m}$
Electron Channel			
Unscaled PYTHIA QCD Processes	-3.9	-3.4	-1.8
+1 σ GS Scaling	+1.5	+1.1	+0.8
Muon Channel			
Unscaled PYTHIA QCD Processes	+0.2	+1.9	+3.9
+1 σ GS Scaling	+1.2	+0.6	+0.2

Table 34: Shifts in the average proper decay length for systematic studies of the tuning of the PYTHIA $b\bar{b}$ sample.

10.5 $b\bar{b}$ TRACK PARAMETER ERRORS

The short lifetime of the $b\bar{b}$ background compared to typical B lifetimes is due to the fact that the J/ψ and third lepton do not originate from the same b quark. This is because the probability for the J/ψ and third lepton to appear to be from the same vertex falls off as the L_{xy} of the J/ψ increases. In effect, the vertex probability cut shapes the ct^* distribution of $b\bar{b}$ events. Since calculating a vertex probability depends on the error matrices of the vertexed tracks' parameters, the shaping of the $b\bar{b}$ background may be different in data and simulation if the typical uncertainties for track parameters differ.

The muons from J/ψ decays in J/ψ +track events are used to compare tracking uncertainties between the data and simulated PYTHIA events. The error distributions of the J/ψ muons' track parameters for the data and simulation are shown in Figure 101. There are minor disagreements in some of the distributions, particularly the z_0 error, so an iterative reweighting of events is applied. The iterative process begins with the z_0 distribution, and

a reweighting of events is applied to give good agreement between data and the simulation. The same procedure is applied iteratively, cycling through the parameters twice, after which the agreement between the data and simulation, as measured by the χ^2 agreement does not improve. Figure 102 shows the level of agreement between the reweighted simulation and data.

Applying the reweighting to the Pythia $b\bar{b}$ events changes the normalization of the electron channel $b\bar{b}$ background from 222.5 to 240.3 events and the muon channel $b\bar{b}$ background from 77.5 to 83.7 events. The reweighted PYTHIA samples are used to generate trials, and the systematic shifts in the measured average proper decay length are listed in Table 35.

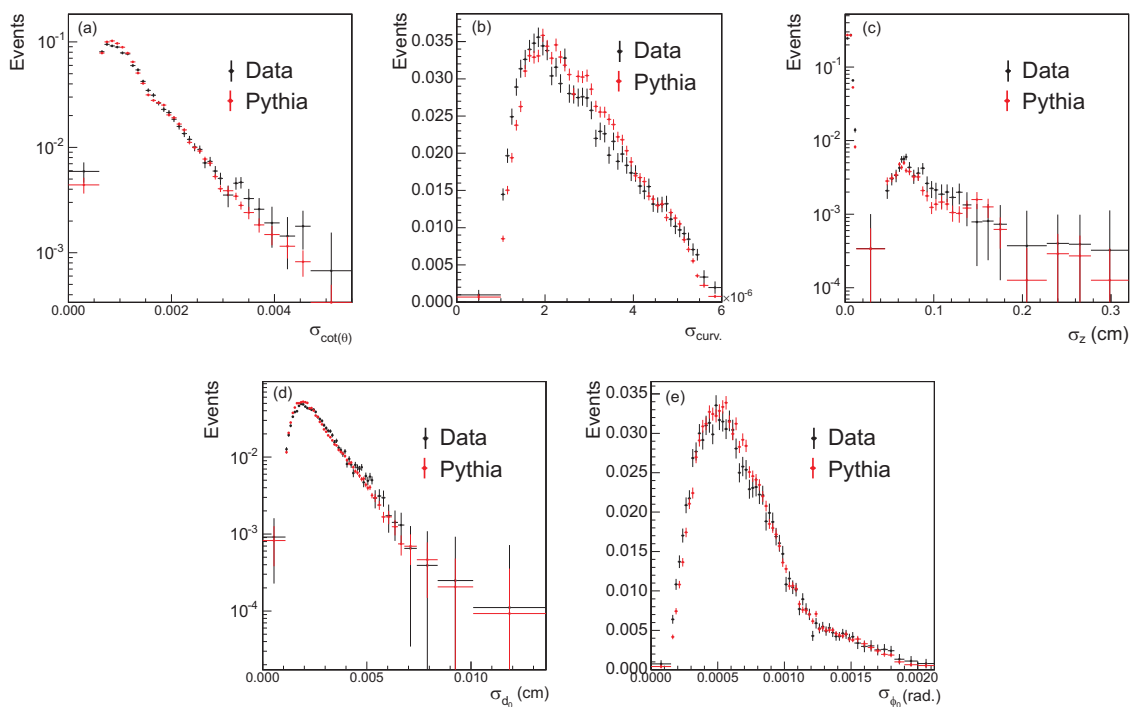


Figure 101: Comparison of track parameter errors for J/ψ legs in J/ψ +track samples for both PYTHIA and data. Variables are $\cot(\theta)$ error (a), curvature error (b), z_0 error (c), d_0 error (d), and ϕ_0 error (e).

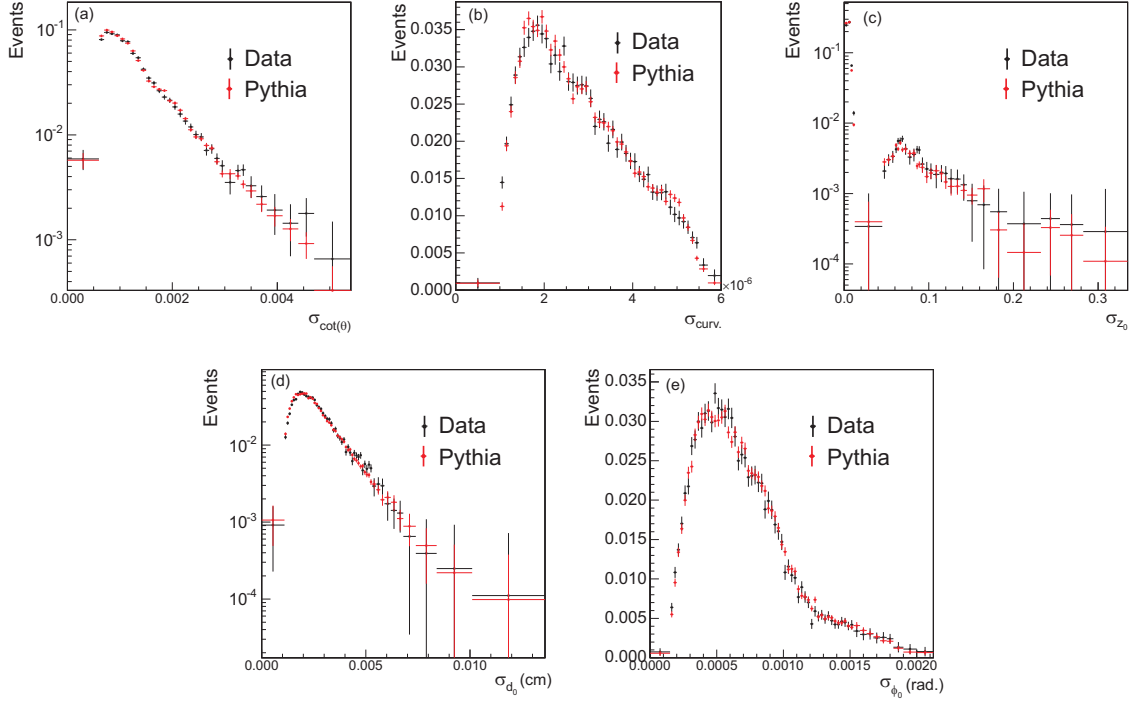


Figure 102: Comparison of track parameter errors for J/ψ legs in J/ψ +track samples for both PYTHIA and data after reweighting is applied to the PYTHIA sample. Variables are $\cot(\theta)$ error (a), curvature error (b), z_0 error (c), d_0 error (d), and ϕ_0 error (e).

	Systematic Shift (μm)		
Systematic	$c\tau = 128 \mu\text{m}$	$c\tau = 143 \mu\text{m}$	$c\tau = 158 \mu\text{m}$
Electron Channel			
Reweighted Track Parameter Errors	+1.2	+1.0	+0.5
Muon Channel			
Reweighted Track Parameter Errors	+1.8	+1.4	+1.2

Table 35: Shifts in the average proper decay length for systematic studies of the track parameters uncertainties in the PYTHIA $b\bar{b}$ sample.

10.6 RESOLUTION FUNCTIONS

The ct^* of prompt J/ψ and B_c events are modeled using resolution functions that are a single Gaussian. The uncertainty due to the choice of resolution function is studied using ct^* fits of the J/ψ +track samples. The fits of the J/ψ +track samples using a resolution function consisting of a single Gaussian provides the scale factors s that scale the per event σ_{ct^*} measurements in the prompt J/ψ and B_c ct^* models. The J/ψ +track samples can also be fitted with the sum of two Gaussians used as the resolution function:

$$F(ct^*, \sigma_{ct^*}) = \frac{(1 - F_1)}{\sqrt{2\pi}s_0\sigma_{ct^*}} e^{-\left(\frac{ct^*}{s_0\sigma_{ct^*}}\right)^2} + \frac{F_1}{\sqrt{2\pi}s_1\sigma_{ct^*}} e^{-\left(\frac{ct^*}{s_1\sigma_{ct^*}}\right)^2}. \quad (10.1)$$

The fitted parameters for both channels and both resolution function models are listed in Table 36. Figure 103 shows a comparison of the single and double Gaussian resolution functions. The double Gaussian resolution functions are used while generating trials and, the observed shifts in the measured average proper decay length are listed Table 37. The behaviour of the shifts as the input $c\tau$ varies appears to be unpredictable, swinging between positive and negative values. A closer examination of the simple Monte Carlo fits reveals that in some ranges the effect of the events generated by the second Gaussian is accounted for by adjusting the normalization and shape of the B_c component of the fit, while in others they are accounted for by adjusting the normalizations and shapes of the backgrounds. The preferred behavior is dependent on the input value of $c\tau$. As a cross-check, this systematic error is also evaluated by fitting the events in data while adjusting the resolution model used in the fitter. This returns shifts of $1.9 \mu\text{m}$ and $3.5 \mu\text{m}$ for the electron and muon channels respectively. The size of these shifts is consistent with those seen by the simple Monte Carlo studies.

10.7 B_c σ_{ct^*} FUNCTIONAL FORM

The σ_{ct^*} of B_c events in the lifetime fit is modeled with the functional form:

$$P_{B_c}(\sigma_{ct^*}) = \frac{1}{\sqrt{2\pi}P_0} e^{-\frac{1}{2}\left(\frac{\sigma_{ct^*}}{P_0}\right)^2} \otimes \frac{1}{P_1} e^{-\frac{(\sigma_{ct^*} - P_2)}{P_1}} \theta(\sigma_{ct^*} - P_2) \quad (10.2)$$

	Electron Channel		Muon Channel	
Parameter	Single Gaussian	Double Gaussian	Single Gaussian	Double Gaussian
s_0	1.21 ± 0.02	1.12 ± 0.01	1.20 ± 0.02	1.11 ± 0.02
s_1	-	2.41 ± 0.11	-	2.47 ± 0.24
F_1	-	0.16 ± 0.02	-	0.14 ± 0.04

Table 36: Parameters describing the single Gaussian and double Gaussian resolution functions from fits of the J/ψ +track sample.

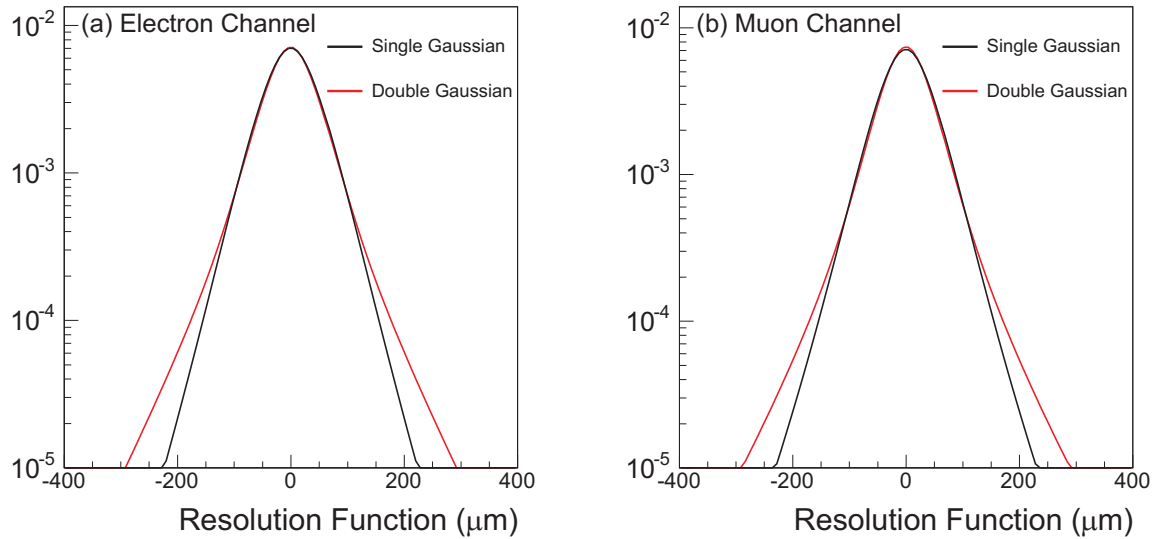


Figure 103: Plot of single and double Gaussian resolution functions for the electron (a) and muon (b) channels.

Systematic Shift (μm)			
Systematic	$c\tau = 128 \mu\text{m}$	$c\tau = 143 \mu\text{m}$	$c\tau = 158 \mu\text{m}$
Electron Channel			
Double Gaussian resolution	-0.6	-3.0	-4.7
Muon Channel			
Double Gaussian resolution	-5.5	+3.5	+1.8

Table 37: Shifts in the average proper decay length for systematic studies of the choice of resolution function used while modeling the prompt J/ψ and B_c ct^* .

In Section 9.2 the functions from the lifetime fits were compared to the σ_{ct^*} distributions of B_c events from BGENERATOR. The comparison showed that the qualitative agreement between the fitted functions and simulated events is quite good. A quantitative measure of the agreement is difficult because the simulated sample has small statistical uncertainties while the functions are fitted to a data sample with considerably larger statistical uncertainties. Fits to the σ_{ct^*} distributions from the BGENERATOR simulated sample show that one needs a PDF for σ_{ct^*} with more degrees of freedom for the fit to have a reasonable probability, given the large statistics in the sample. The PDF used for fitting the high statistics BGENERATOR samples is:

$$\begin{aligned}
P_{B_c}(\sigma_{ct^*}) = & \frac{1}{\sqrt{2\pi}P_0} e^{-\frac{1}{2}\left(\frac{\sigma_{ct^*}}{P_0}\right)^2} \otimes \frac{P_6}{P_1} e^{-\frac{(\sigma_{ct^*}-P_2)}{P_1}} \theta(\sigma_{ct^*} - P_2) + \\
& \frac{1}{\sqrt{2\pi}P_3} e^{-\frac{1}{2}\left(\frac{\sigma_{ct^*}}{P_3}\right)^2} \otimes \frac{(1-P_6)}{P_4} e^{-\frac{(\sigma_{ct^*}-P_5)}{P_4}} \theta(\sigma_{ct^*} - P_5)
\end{aligned} \tag{10.3}$$

The fitted σ_{ct^*} distributions from BGENERATOR samples can be seen in Figure 104 and the parameters are listed in Table 38. The BGENERATOR based models are used while generating the trials, and the observed systematic shifts in the average proper decay length are listed Table 39.

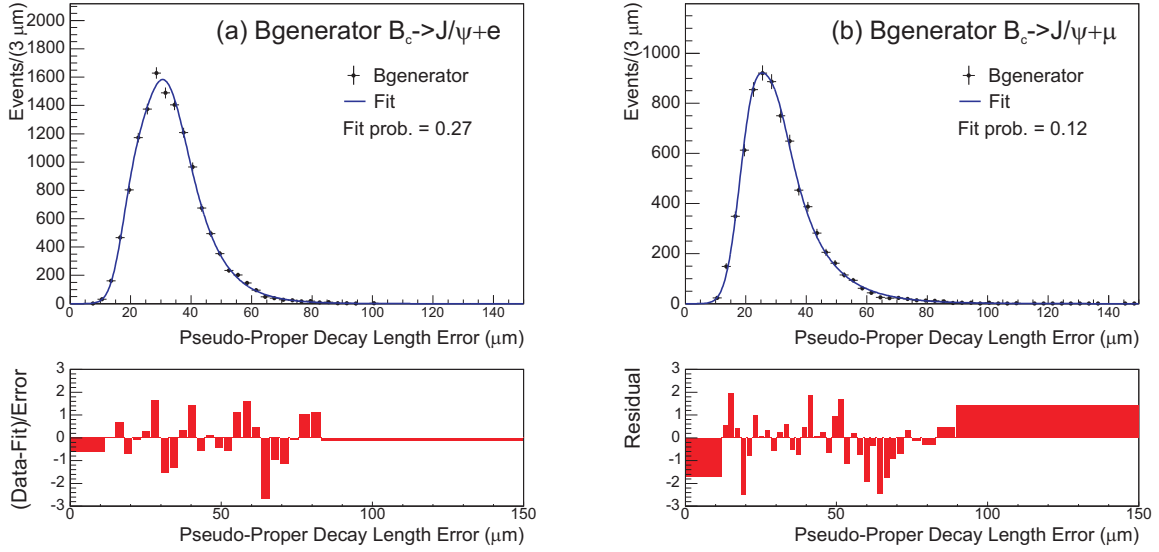


Figure 104: Fits σ_{ct^*} distributions for B_c events from BGENERATOR for electron (a) and muon (b) channel final states.

	Electron Channel		Electron Channel	
Parameter	Fit Value	Error	Fit Value	Error
P_0	3.48	0.29	3.56	0.74
P_1	17.14	1.74	12.85	0.97
P_2	5.71	0.58	27.5	2.2
P_3	8.61	0.27	4.10	0.39
P_4	7.99	0.37	7.99	0.80
P_5	26.2	0.59	19.26	0.93
P_6	0.265	0.068	0.34	0.14

Table 38: Parameters from the σ_{ct^*} fits of B_c events from BGENERATOR.

Systematic Shift (μm)			
Systematic	$c\tau = 128 \mu\text{m}$	$c\tau = 143 \mu\text{m}$	$c\tau = 158 \mu\text{m}$
Electron Channel			
$B_c \sigma_{ct^*}$ Function	+0.5	+0.6	+0.6
Muon Channel			
$B_c \sigma_{ct^*}$ Function	+0.1	0.0	0.0

Table 39: Shifts in the average proper decay length for systematic studies of the choice of σ_{ct^*} model for B_c decays.

10.8 J/ψ +TRACK PROTON FRACTION

Appendix C contains a discussion of the dependence of the misidentified muon background on the different models of the proton fraction of third tracks in the J/ψ +track sample. The uncertainty related to choice of proton fractions is modeled by assuming the proton fraction is flat in p_T , rather than the nominal model where it decreases with p_T . Since protons are misidentified as muons with a rate that is effectively 0, this decreases the misidentified muon background from 96.1 to 92.5 events. The misidentified muon model with flat proton fractions is used while generating trials, and the measured shifts in the average proper decay length of the B_c are listed in Table 40.

Systematic Shift (μm)			
Systematic	$c\tau = 128 \mu\text{m}$	$c\tau = 143 \mu\text{m}$	$c\tau = 158 \mu\text{m}$
Flat Proton Fraction	+1.3	+1.3	+1.4

Table 40: Shifts in the average proper decay length for systematic studies of the choice of proton fraction model for third tracks in the J/ψ +track sample.

10.9 DECAY-IN-FLIGHT CORRECTION

As discussed in Section 7.2.1.1, a correction is made to the probabilities for hadrons to be misidentified as muons because some of the decay-in-flight events in the D^0 sample will not reconstruct inside the D^0 mass window due to kinks in the decay-in-flight tracks. The correction is done using a BGENERATOR sample of D^0 decays where the number of decay-in-flight events that fall outside the mass peak are counted. The events outside the mass peak are normalized to data using the number of events in the D^0 distribution where no muon requirement has been applied to either D^0 leg. The correction depends on the ability of the simulation to model correctly the tracking and muon efficiencies for the decay-in-flight tracks.

The single track reconstruction efficiency for data relative to simulation has been studied by CDF collaborators and measured to be 87.8% [96]. The correction is scaled by this relative efficiency. The CMUP muon reconstruction efficiency in data has also been measured by CDF collaborators and is 90% [88]. The 10% inefficiency in CMUP muon reconstruction is taken as the maximum difference between the reconstruction efficiency in data and the simulation, and a 10% correction is applied to the decay-in-flight correction. After applying these two adjustments to the decay-in-flight correction, the number of misidentified muon background events is 92.5 compared to the nominal value of 96.1. The adjusted misidentified muon background model is used while generating trials, and the measured shifts in the average proper decay length are listed in Table 41.

	Systematic Shift (μm)		
Systematic	$c\tau = 128 \mu m$	$c\tau = 143 \mu m$	$c\tau = 158 \mu m$
DIF Correction	+1.3	+1.3	+1.4

Table 41: Shifts in the average proper decay length for systematic studies of the decay-in-flight correction for events falling outside the D^0 mass window.

10.10 J/ψ MASS SIDEBANDS AND THE MISIDENTIFIED J/ψ BACKGROUND

The J/ψ sidebands provide the events used to model the misidentified J/ψ background. As discussed in Section 7.1.1 and shown in Figure 105, the distribution of events in the lower sideband for the muon channel shows a possible structure around $3.0 \text{ GeV}/c^2$. Although there is no known physics source that could cause an excess of events in this region, the structure is studied and a systematic uncertainty is determined.

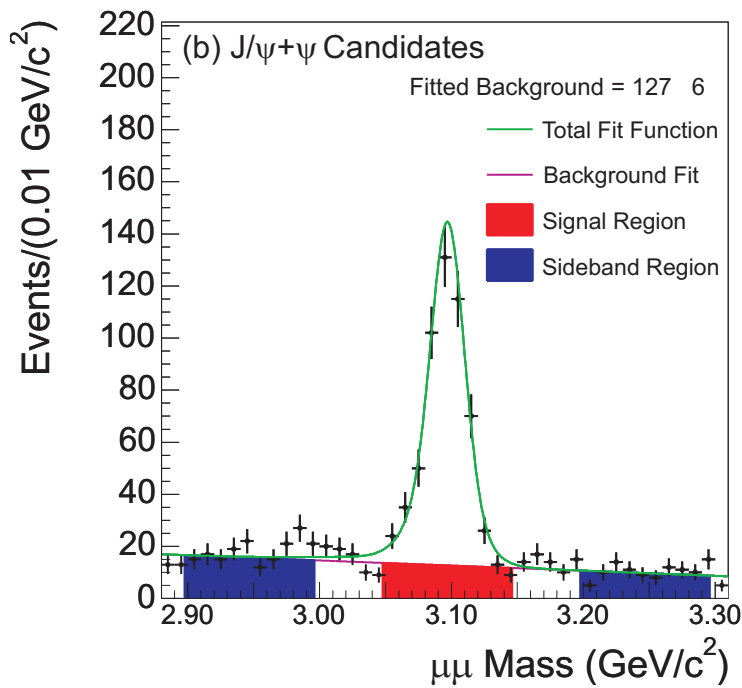


Figure 105: Fit of J/ψ candidate mass distribution for $J/\psi + \mu$ events.

Since a similar structure is not seen in the electron channel events, sources of events unique to the muon channel are studied as a possible source of the structure. The most obvious source are events where one of muons from the J/ψ decay has been identified as the third track, while another track in the event takes its place as a J/ψ leg. These events are enhanced since the muon requirement for the third track is more strict than that for the J/ψ legs. The presence of these events in the sample is seen by plotting the invariant mass

of the third muon with the J/ψ leg of opposite charge and looking near the J/ψ mass. As seen in Figure 106 a peak is present, indicating events where the swap has taken place.

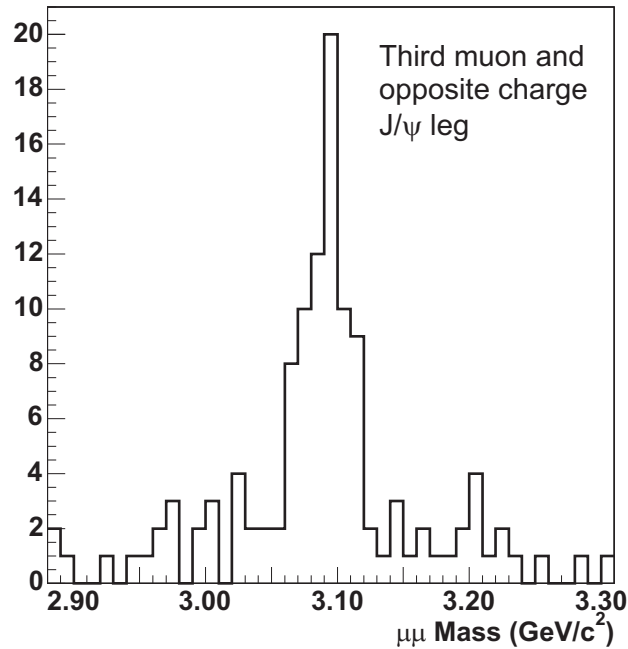


Figure 106: Invariant mass of third muon and oppositely charged J/ψ legs for events in the J/ψ sideband region.

The presence of the mass peak in the swapped distribution suggests a method for dividing the $J/\psi + \mu$ candidate events. Those events with masses in the swapped distribution that fall within $50 \text{ MeV}/c^2$ of the J/ψ mass comprise one sample, while those that do not comprise the other. The resulting J/ψ mass distributions (with no swapped tracks) for the two samples are shown in Figure 107. The bump at $3.0 \text{ GeV}/c^2$ may be enhanced in the case where the third track appears to be a J/ψ leg, although the statistics are too low for a definitive answer. There is no physical model that explains why a bump should be present at $3.0 \text{ GeV}/c^2$, but a phenomenological model can be applied and used to determine a systematic uncertainty.

To study the systematic uncertainty, the assumption is made that among events where a J/ψ decay product is identified as the third track, there is a source of events with a mass peak around $3.0 \text{ GeV}/c^2$. The mass distribution for those events is refit with an additional

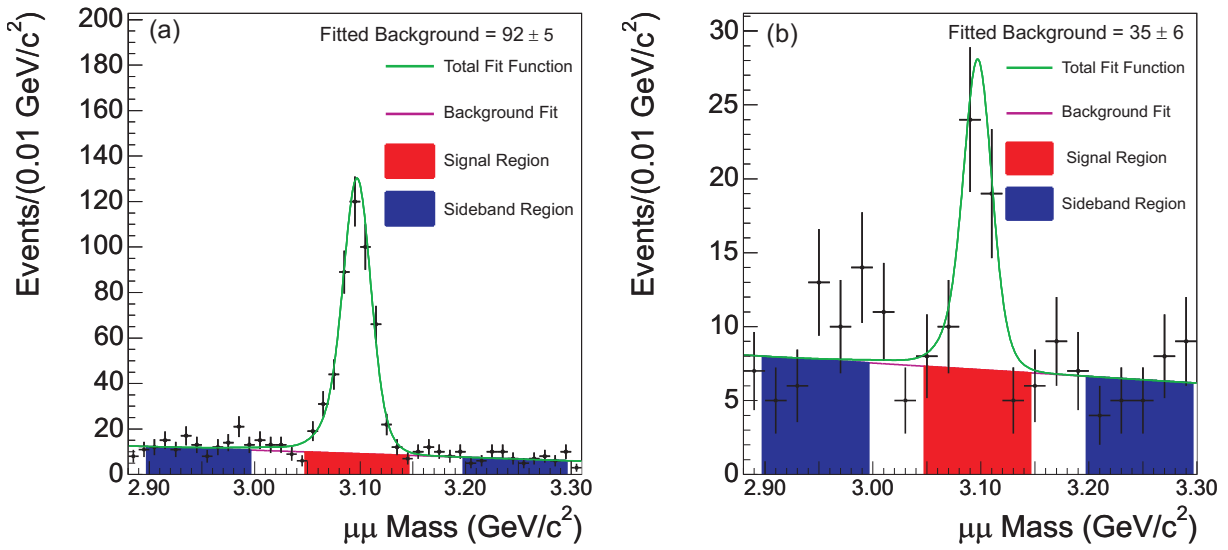


Figure 107: Fit of the J/ψ mass for $J/\psi + \mu$ events split into two types. (a) The third muon does not reconstruct to within $50 \text{ MeV}/c^2$ of the J/ψ mass with the oppositely charged J/ψ leg. (b) The third muon does reconstruct to within $50 \text{ MeV}/c^2$ of the J/ψ mass with the oppositely charged the J/ψ leg.

Gaussian component, and the fitted distribution is shown in Figure 108. The fit returns 29 ± 3 background events under the J/ψ mass peak, compared to 35 ± 6 events when the additional Gaussian is not included. The number of background events is calculated by integrating the background models in the J/ψ mass signal window. The fitted value of 29 ± 3 events is added 92 ± 5 events from the fit of events where third track is not one of the J/ψ decay products. This gives a background of 121 ± 6 events for the misidentified J/ψ which can be compared to the 142 ± 8 events measured by simply counting events in the sideband regions.

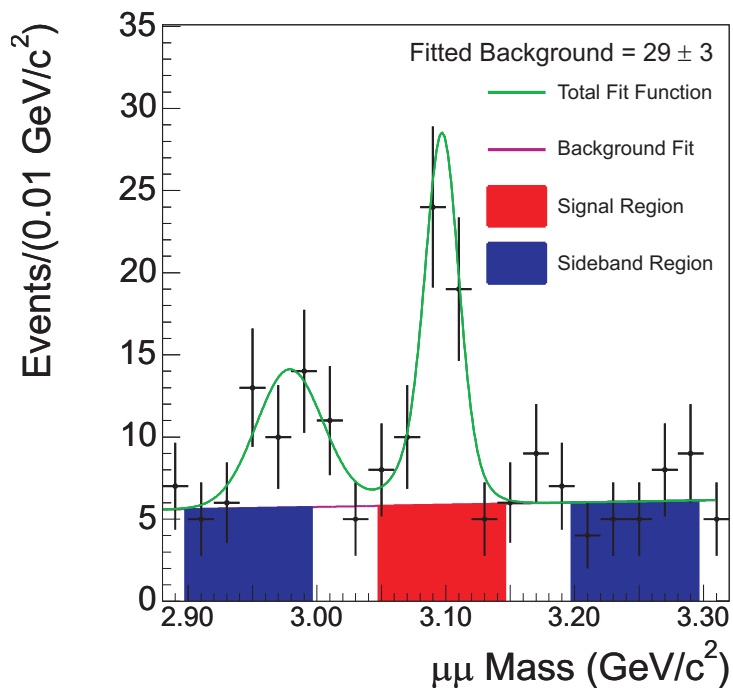


Figure 108: Fit of the J/ψ mass for $J/\psi + \mu$ events where the third muon does reconstruct to within $50 \text{ MeV}/c^2$ of the J/ψ mass with the oppositely charged the J/ψ leg. An additional Gaussian is added to fit the bump in the lower sideband.

For the systematic study, the contribution of events in the lower sideband to the ct^* model of misidentified J/ψ events should be removed. Refitting the ct^* distribution using only events in the upper sideband accomplishes this. The resulting ct^* fit compared to the fit including both sidebands is shown in Figure 109. The fitted parameters are listed in Table 42. The parameters as determined by both sideband or the upper sideband only are

consistent.

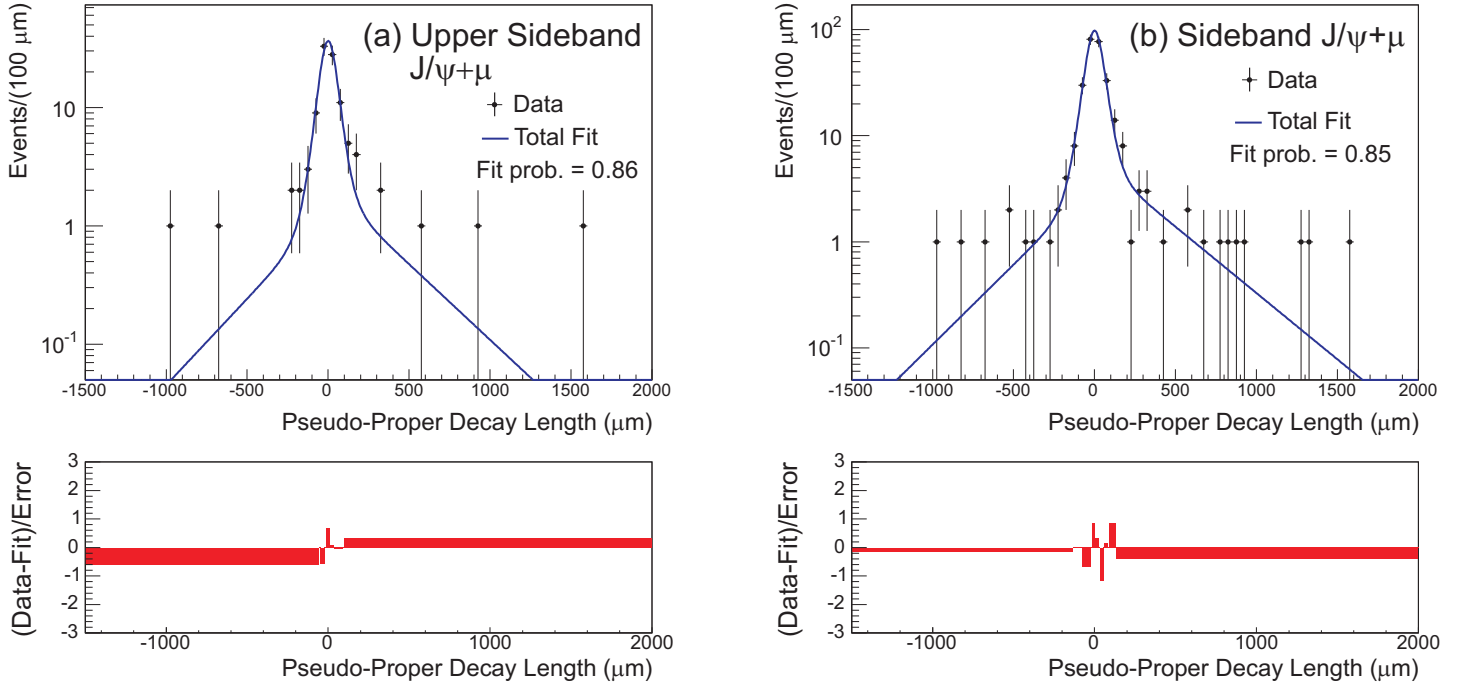


Figure 109: Fitted ct^* for sideband $J/\psi + \mu$ events using only the upper sideband (a) and using both sidebands (b).

The ct^* model from the upper J/ψ sideband and the background of 121 ± 6 events are used while generating trials. The measured shifts in the average proper decay length are listed in Table 43.

10.11 MISIDENTIFIED ELECTRON METHOD

In Section 7.2 the size of the misidentified electron background is determined by weighting events in the J/ψ +track with misidentification probabilities. The selected J/ψ +track events have the $Z_e^{pull} > -1.3$ cut applied to the third track, while the particle fractions for the third track are calculated on a J/ψ +track sample that does not have the $Z_e^{pull} > -1.3$ cut applied. The particle fractions are then adjusted using Z_e^{pull} cut efficiencies measured from electrons,

Parameter	Upper Sideband	Both Sidebands
Error Scale Factor	1.32 (fixed)	1.32 ± 0.10
Prompt Fraction	0.79 ± 0.10	0.79 ± 0.06
Pos. Lifetime	340 ± 111	347 ± 168
Pos. Fraction	0.13 ± 0.05	0.14 ± 0.03
Neg. Lifetime	289 ± 139	288 ± 85
Neg. Fraction	0.073 ± 0.039	0.069 ± 0.023

Table 42: Fitted parameters from sideband $J/\psi + \mu ct^*$ fits using only the upper sideband or both sidebands.

	Systematic Shift (μm)		
Systematic	$c\tau = 128 \mu m$	$c\tau = 143 \mu m$	$c\tau = 158 \mu m$
Misidentified J/ψ Model	-1.6	-1.4	-1.4

Table 43: Shifts in the average proper decay length for systematic studies of the sideband J/ψ events used while determining the misidentified J/ψ background for the muon channel.

pions, kaons, and protons from the conversion, tagged D^0 , and Λ samples. For the case of the tagged D^0 and Λ samples, most of the tracks used for the efficiency calculation are XFT trigger tracks, while the third tracks in the J/ψ +track sample are not biased by the J/ψ trigger to be XFT tracks. One may be concerned that the efficiencies calculated using XFT tracks are different than the efficiency for a sample of track that includes many non-XFT tracks.

A second method for weighting the events in the J/ψ +track sample is to remove the Z_e^{pull} cut and instead include the efficiency of the Z_e^{pull} cut directly in the determination of the misidentification rates. The misidentification rates are then be applied directly to the J/ψ +track sample where the Z_e cut has not been applied. This method is actually more sensitive to measured efficiencies since they enter the weighting as a multiplicative factor. In the nominal method of recalculating the particle fractions, outlined in Section 7.2.2.4, the efficiencies are present in both the numerator and denominator of the recalculated fraction, suppressing the effect of any systematic uncertainty. The method outlined here yields a misidentified lepton background of 295.9 ± 3.3 events compared to 312.0 ± 4.1 events for the nominal method. The misidentified lepton determined with the Z_e^{pull} cut efficiency included in the misidentification rates is used while generating trials, and the measured systematic shifts in the average proper decay length are listed in in Table 44.

	Systematic Shift (μm)		
Systematic	$c\tau = 128 \mu\text{m}$	$c\tau = 143 \mu\text{m}$	$c\tau = 158 \mu\text{m}$
Misidentified electron calculation	-0.3	-0.2	-0.3

Table 44: Shifts in the average proper decay length for systematic studies of the method for handling the Z_e cut in the misidentified electron calculation.

10.12 e^+e^- VETO EFFICIENCY

As discussed in section 7.4.3 the conversion electron veto efficiency is studied using the signed impact parameter of electrons, suggesting a multiplicative correction of 0.86 to the e^+e^- veto efficiency in the $p_T = 2.0 - 2.5$ GeV/ c bin. Since this correction is based on a discrepancy of only $\sim 1.5\sigma$, a systematic uncertainty is evaluated for the case of no correction. Without the correction the residual e^+e^- is 370.4 ± 40.9 events, compared to 416.8 ± 41.5 with the correction. The background model without the correction is used while generating trials resulting in the observed shifts in the B_c average proper decay length that are listed in Table 45.

	Systematic Shift (μm)		
Systematic	$c\tau = 128 \mu\text{m}$	$c\tau = 143 \mu\text{m}$	$c\tau = 258 \mu\text{m}$
No adjustment	-2.1	-2.0	-2.2

Table 45: Shifts in the average proper decay length for systematic studies of the correction to the conversion veto efficiency in the $p_T = 2.0 - 2.5$ GeV/ c region.

10.13 SILICON DETECTOR ALIGNMENT

A systematic uncertainty is applied to account for uncertainties in the alignment of the silicon detectors. Based on previous work by CDF collaborators, an uncertainty of $2.0 \mu\text{m}$ [97] is applied to both channels at all $c\tau$ values.

10.14 COMBINING SYSTEMATIC UNCERTAINTIES

The systematic uncertainties are evaluated for the two channels separately and must be combined into a single systematic uncertainty for the combined $c\tau$ measurement. The weighted

sum of the measured $c\tau$ for the muon and electron channels is defined as:

$$c\tau_{total} = \left(\frac{c\tau_e}{E_e^2} + \frac{c\tau_\mu}{E_\mu^2} \right) / \left(\frac{1}{E_e^2} + \frac{1}{E_\mu^2} \right) \quad (10.4)$$

In this equation, $c\tau_e$ and $c\tau_\mu$ are the measured lifetimes and E_e and E_μ are the statistical errors. Taking the derivative with respect to $c\tau_e$ yields:

$$\frac{d(c\tau_{total})}{d(c\tau_e)} = \frac{E_\mu^2}{E_e^2 + E_\mu^2} \quad (10.5)$$

Using the derivatives with respect to $c\tau_e$ and $c\tau_\mu$, one can write an equation for combining systematics uncertainties that are evaluated for both channels, S_e and S_μ :

$$S_{total} = \sqrt{\frac{d(c\tau_{total})}{d(c\tau_e)}^2 S_e^2 + \frac{d(c\tau_{total})}{d(c\tau_\mu)}^2 S_\mu^2 + 2 \frac{d(c\tau_{total})}{d(c\tau_e)} \frac{d(c\tau_{total})}{d(c\tau_\mu)} S_e S_\mu} \quad (10.6)$$

The the last term in the equation is present for the case where the systematic errors S_e and S_μ are positively correlated with coefficient 1. The term should not be present if the errors are uncorrelated.

For each systematic uncertainty that is evaluated for both the electron and muon channels, the systematics are combined in the most conservative method possible, by ignoring the signs of the systematic uncertainties and assuming that the systemics uncertainties for the two channels are correlated. For systematic uncertainties that only apply to the electron or muon channel, the uncertainty in the other channel is simply 0. Table 46 lists the systematic uncertainties for both channels evaluated at the varied input $c\tau$ values and includes the combined uncertainties for each systematic. For each value of $c\tau$ the systematics are added in quadrature to give a total systematic uncertainty. The largest total systematic uncertainty of $5.5 \mu\text{m}$ is seen for $c\tau = 158 \mu\text{m}$ and is taken as the systematic uncertainty for the combined $c\tau$ measurement.

Description	Systematic Shift (μm)								
	$c\tau = 128 \mu\text{m}$			$c\tau = 143 \mu\text{m}$			$c\tau = 158 \mu\text{m}$		
	e	μ	Total	e	μ	Total	e	μ	Total
<i>b\bar{b}</i> QCD Processes									
Default Pythia	-3.9	0.2	2.8	-3.4	1.9	2.9	-1.8	3.9	2.4
Fitted $+1\sigma$	1.5	1.2	1.4	1.1	0.6	1.0	0.8	0.2	0.6
Pythia Track Errors	1.2	1.8	1.4	1.0	1.4	1.1	0.5	1.2	0.7
B_c Spectrum									
Hard	1.1	0.8	1.0	1.4	0.9	1.3	1.4	1.1	1.3
Soft	-1.1	-0.8	1.0	-1.0	-1.0	1.0	-1.2	-1.0	1.1
B_c Branching Fractions									
$\times 2$ Rates	0.6	0.3	0.5	0.8	0.2	0.6	0.6	0.3	0.5
$\times 1/2$ Rates	-0.2	-0.6	0.3	0.1	-0.7	0.3	-0.3	-0.7	0.3
$B_c \sigma_{ct^*}$	0.5	0.1	0.4	0.6	0.0	0.4	0.6	0.0	0.4
Misid. $J/\psi ct^*$	0.7	-1.0	0.6	1.0	-0.9	0.7	1.1	-0.4	0.8
Resolution Function	-0.6	-5.5	2.1	-3.0	3.5	3.2	-4.7	1.8	3.8
Silicon Alignment	2.0	2.0	2.0	2.0	2.0	2.0	2.0	2.0	2.0
Misid. J/ψ Normalization	-	-1.6	0.5	-	-1.4	0.4	-	-1.4	0.4
J/ψ +track p Fraction	-	1.3	0.4	-	1.3	0.4	-	1.4	0.4
Decay-in-flight Correction	-	1.3	0.4	-	1.3	0.4	-	1.4	0.4
Residual e^+e^- Eff.	-2.1	-	1.5	-2.0	-	1.4	-2.2	-	1.5
Misid. Electron Method	-0.3	-	0.2	-0.2	-	0.1	-0.3	-	0.2
Total in Quadrature			4.9	5.4			5.5		

Table 46: Summary of systematic uncertainties for the electron and muon channels listed in the columns labeled e and μ respectively. The columns labeled Total contain the combined systematic uncertainties of the two channels.

11.0 CONCLUSION

This thesis has presented a measurement of the B_c averaged proper decay length (time).

$$c\tau = 142.5_{-14.8}^{+15.8}(\text{stat.}) \pm 5.5(\text{syst.}) \mu\text{m}$$

$$\tau = 0.475_{-0.049}^{+0.053}(\text{stat.}) \pm 0.018(\text{syst.}) \text{ ps}$$

The significance of the measurement can be understood by comparing to previous measurements of the B_c lifetime as well as theoretical predictions. Of particular interest is whether this measurement, on its own or in combination with others, can provide any constraints on the theoretical predictions of the lifetime.

11.1 COMPARISON TO OTHER MEASUREMENT

Previous measurements of the B_c lifetime have been carried out by CDF in Run I and CDF and D0 in Run II. The measured values are listed in Table 47. The measurement presented in this thesis is consistent with the previously measured values of the B_c lifetime. Including statistical and systematic uncertainties, the measurement presented in this thesis provides a precision similar to that of the D0 Run II measurement. While the D0 Run II result has higher statistical precision, owing to the greater muon acceptance of the D0 detector, they have considerably larger systematic uncertainties. This is because they use the mass distribution of candidate events to constrain the normalizations of background contributions, and there are considerable systematic uncertainties associated with modeling the mass distributions.

Experiment	Int. Lumi.	Decay Mode	Measured τ
CDF Run I	110 pb ⁻¹	$J/\psi + l^\pm + X$	$0.46_{-0.16}^{+0.18}(stat.) \pm 0.03(syst.)$ ps [1]
CDF Run II	360 pb ⁻¹	$J/\psi + e^\pm + X$	$0.463_{-0.065}^{+0.073}(stat.) \pm 0.036(syst.)$ ps [2]
D0 Run II	1.4 fb ⁻¹	$J/\psi + \mu^\pm + X$	$0.448_{-0.036}^{+0.038}(stat.) \pm 0.032(syst.)$ ps [3]
CDF Run II	1.0 fb ⁻¹	$J/\psi + l^\pm + X$	$0.475_{-0.049}^{+0.053}(stat.) \pm 0.018(syst.)$ ps

Table 47: Listing of the measurements of the B_c average proper decay time τ .

A combination of the most precise measurements from each experiment can provide the most precise experimental value which can then be compared to theoretical predictions of the B_c lifetime. Figure 110 shows a comparison of the CDF Runs I&II and the D0 Run II measurements. A weighted average based on the total uncertainties is taken, and the uncertainties are combined to give a combined measurement of $\tau = 0.459 \pm 0.037$ ps. This represents an improvement by a factor > 4 in the precision of the measured lifetime since the first measurement carried out by CDF Run I.

11.2 COMPARISON TO THEORETICAL PREDICTIONS

Does the combined measured value of the B_c lifetime $\tau = 0.459 \pm 0.037$ ps provide a constraint for theoretical models used to predict the lifetime? In Chapter 3 three predictions using various models were presented: $\tau = 0.4 - 0.7$ ps using the optical theorem [5], $\tau = 0.48 \pm 0.05$ ps using three point QCD sum rules [6], and $\tau = 0.59 \pm 0.06$ ps using the light front constituent quark model [7]. Among these predictions, the experimental value falls the furthest from the prediction in the light front constituent quark model. In this model, one source of uncertainty is the choice of quark model wave function which is either modeled by solving the nonrelativistic Schrodinger equation or the semi-relativistic Salpeter equation. The semi-relativistic model provides a lower value of the lifetime $\tau = 0.57$ ps compared to the nonrelativistic model $\tau = 0.65$ ps. Not surprisingly, the more sophisticated model is

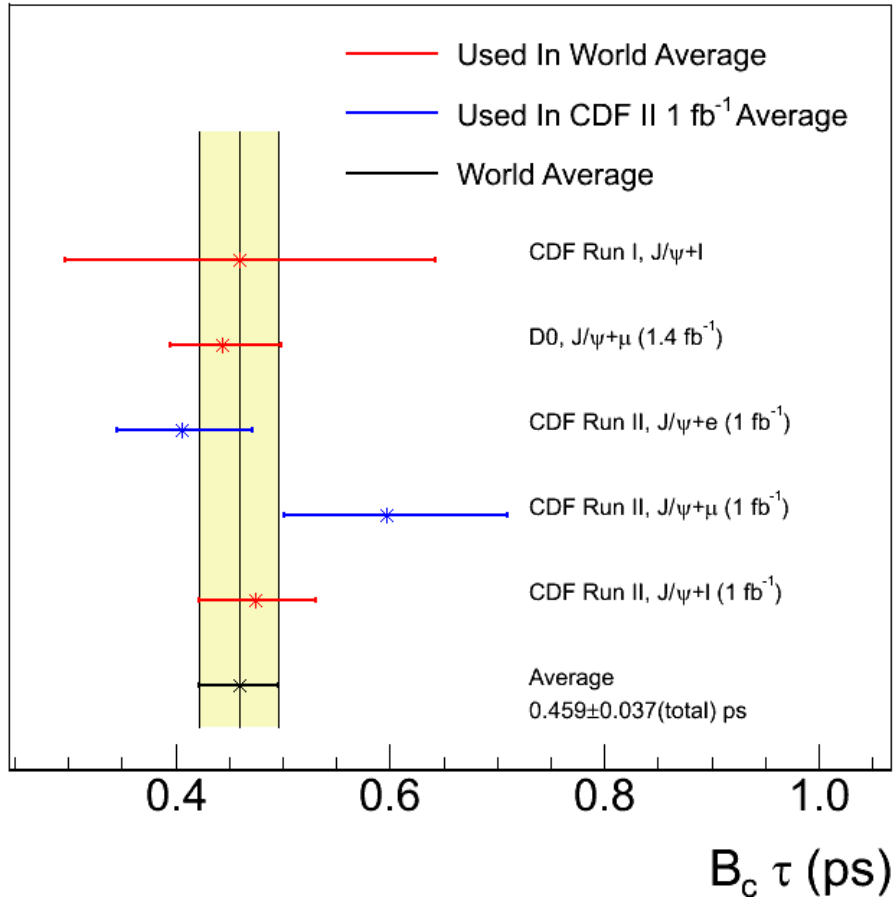


Figure 110: Comparison of the B_c average proper decay time for the CDF Run I, D0 Run II, and CDF Run II experiments. The weighted average is taken assuming no correlations in the uncertainties.

in better agreement. The other major source of uncertainty is the threshold value for the hadron continuum used when calculating the inclusive rate $\Gamma(H_Q \rightarrow X' l \nu_l)$ where H_Q is the heavy quark and X' represent the hadron continuum including resonance above the lowest vector and pseudoscalar states. The choice of threshold value can lead to a predicted lifetime as low as 0.53 ps in the semi-relativistic model. This brings the theoretical prediction to within 2σ of the measured value.

The prediction of the B_c lifetime using the optical theorem is largely dependent on the charm quark mass with the quoted range corresponding to variations of $m_c = 1.4 - 1.6$ GeV/ c^2 . This corresponds to a variation of the bottom quark mass as well, since the bottom quark mass is constrained to give $\tau_{B_d} \approx 1.55$ ps for a given choice of the charm quark mass. The experimental result suggests a charm quark mass near the higher end of the mass range. This is consistent with the fact that a large charm quark mass is needed in the OPE approach to reproduce the D^0 lifetime [5].

The prediction of the lifetime using sum rules, $\tau = 0.48 \pm 0.05$, depends on the heavy quark masses and the scale for hard gluon corrections when estimating the hadron decay widths from the semileptonic decay widths in the factorization approach. The current precision of the measured lifetime does not allow for any strong constraint on the theoretical prediction, but the measured lifetime does suggest that the choice of scale for the hard gluon corrections was reasonable.

11.3 PROSPECTS FOR FUTURE MEASUREMENTS

A number of prospects exist for new or improved measurements of the B_c lifetime over the coming years. As of October 2008 CDF has collected ~ 4 fb $^{-1}$ of integrated luminosity and another ~ 2 fb $^{-1}$ is expected before the end of data taking. An update of the measurement presented in this thesis with the full sample of data should provide a factor of 2 or more decrease in the statistical uncertainties. Unfortunately, measured quantities such as dE/dx , which is used prominently in this measurement, require calibrations as new data is collected. Because of this, the processing time between raw data and fully calibrated data can be

considerable. However, there are prospects for improving the statistics of the measurement without increasing size of the dataset. The choice of CMUP muons as third muons limits the third track acceptance to $|\eta| < 0.6$ and $p_T > 3.0 \text{ GeV}/c^2$ for the muon channel. If the muon likelihoods based on CMU and CMX detector information were used, the acceptance could be increased to $|\eta| < 1.0$ and $p_T > 2.0 \text{ GeV}/c^2$, giving approximately twice the B_c events in the muon channel.

The semileptonic decay modes are not the only possible source of events for a lifetime measurement in current data from CDF. The decay mode $B_c^\pm \rightarrow J/\psi + \pi^\pm$ has been studied with 2.4 fb^{-1} of integrated luminosity, and the mass was measured with 108 ± 15 signal events [43]. Figure 111 shows the mass distribution from this measurement and one can see an excess of events in the lower sideband below the fitted mass peak. The excess is likely due to partially reconstructed B_c decays including $B_c^\pm \rightarrow J/\psi + l^\pm + X$ decays where the lepton is identified as a pion. A measurement of the lifetime will have include a model of the partially reconstructed events to understand their contribution under the mass peak. Since these events are from B_c decays, they can be used in the lifetime measurement. A recent measurement of the B_s^0 lifetime using partially and fully reconstructed modes proved quite successful [98].

CDF collaborators are currently pursuing a measurement of the lifetime in the $B_c^\pm \rightarrow J/\psi + \pi^\pm$ decay mode. A confirmation of current results in the semileptonic modes is important since the fully reconstructed mode requires different methods for modeling signal and background events. The presence of a narrow mass peak from signal events constrains the signal yield and allows nearby mass sidebands to be used in the modeling of the background events. Since the events are fully reconstructed, no K factors are needed to model unmeasured B_c decay products. Due to the differences in methodology, the systematic uncertainties of a measurement in the fully reconstructed mode will be quite different than those in previous measurements in the semileptonic mode. This makes the fully reconstructed mode particularly interesting as a verification of current experimental results.

After the shutdown of the Tevatron, the primary experiment for studying B_c will be the LHCb experiment at the Large Hadron Collider (LHC). For similar luminosities, the LHC should produce ~ 10 times the number of B_c that are produced at the Tevatron [99]. If the

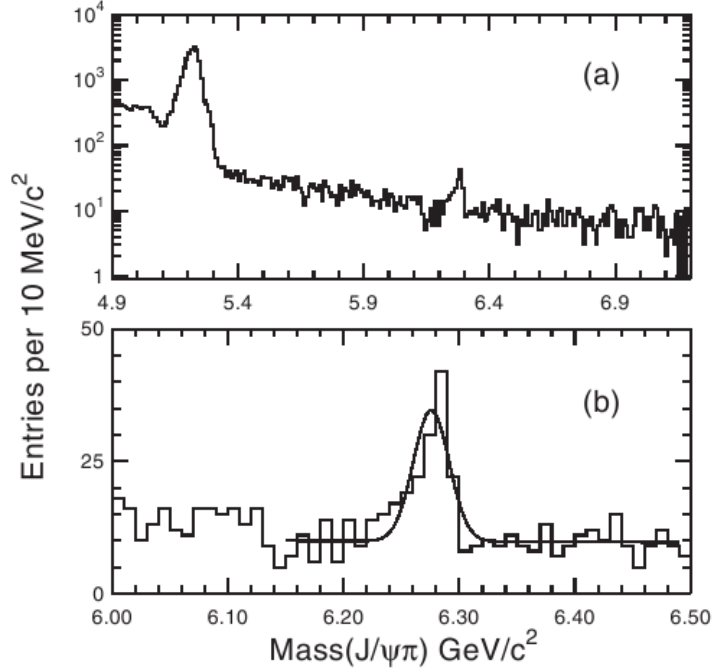


Figure 111: Reconstructed $J/\psi + \pi^\pm$ for B_c candidates.

LHC achieves a factor of ~ 100 times the integrated luminosity of the Tevatron, the total number of B_c candidates would be ~ 1000 times larger. This would allow for measurements of the B_c lifetime at the $\sim 1 \mu\text{m}$ or less level of precision. Such precise measurements would provide constraints to the bottom and charm quark masses as well as the normalization point of the nonleptonic weak Lagrangian [99].

With such large statistics, many more B_c properties will be measured at LHCb, including branching fractions for decays through the b quark, c quark, and annihilation modes. Leptonic decays through the annihilation mode provide a means for measuring the leptonic constant f_{B_c} , although the measurement will be difficult in the dominant decay mode $B_c^+ \rightarrow \tau^+ \nu_\tau$ due to the challenges of τ reconstruction. The hadronic decays in the annihilation mode allow for a measurement of a_1 , which contains the hard gluon corrections that are present in the hadronic mode but not the leptonic mode. Many other possibilities for the study of the B_c are opened with greater statistics, including the measurement of direct

CP violation [100] in B_c decays.

11.4 CONCLUDING REMARKS

A procedure for measuring the B_c lifetime has been presented in this thesis. The measured value is in good agreement with previous measurements, and can be combined with previous measurements to give an experimental value with precision of ~ 0.037 ps. At this level of precision, the experimental value begins to provide a check on theoretical predictions. Numerous opportunities remain to improve the precision of the lifetime measurement including improvements to the method described in this thesis, a measurement in the $B_c^\pm \rightarrow J/\psi + \pi^\pm$ decay mode, and measurements that will be made at LHCb. Given these prospects, this measurement helps provide a useful starting point for future measurements of the properties of the B_c meson.

APPENDIX A

MONTE CARLO SIMULATION SAMPLES

A number of Monte Carlo simulated samples of B_c and $b\bar{b}$ events are used in the analysis. A description of the samples follows.

A.1 BGENERATOR SAMPLE OF B_C DECAYS

Signal B_c events are modeled using a simulated sample of B_c generated with BGENERATOR and passed through the standard detector simulation. The generation and decay of B_c requires two inputs: a spectrum that describes the p_T vs. η distribution of B_c produced in $\sqrt{s} = 1.96$ TeV $p\bar{p}$ collisions, and the table of branching fractions for B_c decays to states with a J/ψ meson and a third lepton.

The B_c spectrum is based on theoretical predictions [101, 102] and was validated for use with BGENERATOR by CDF collaborators studying $B_c \rightarrow J/\psi\pi$ decays [103]. The predicted momentum spectrum of the B_c is soft compared to the lighter B mesons, as illustrated by Figure 112 which compares the p_T projection of spectra for B_c and B mesons.

The decay table which describes the branching fractions for B_c is also based on theoretical estimates [49]. Of the possible B_c decays, only those that produce J/ψ mesons and third leptons are used, and decays are forced to $J/\psi(\mu^+\mu^-) + l + X$ states 100% of the time. For cases that involve intermediate decays, the intermediate decays are forced to the desired final states, and the branching fractions for the intermediate decays are propagated to the

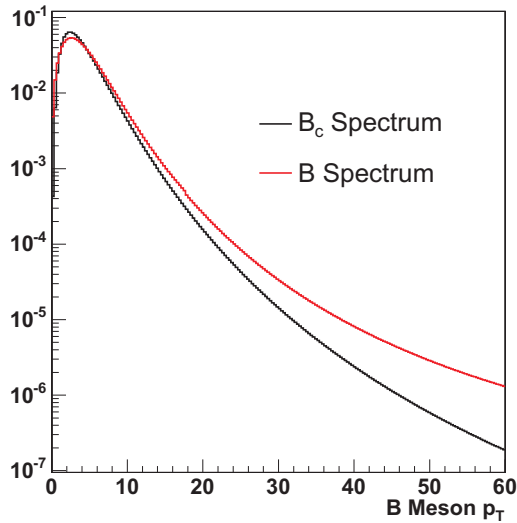


Figure 112: Comparison of the B_c and B meson spectra used when generating events with BGENERATOR.

top level B_c branching fraction. For example, B_c is predicted to decay to $\psi(2S) + \mu + \nu_{\mu}$ 0.094% of the time. The $\psi(2s)$ subsequently decays to $J/\psi + X$ 58% so when the $\psi(2s)$ is forced to decay to $J/\psi + X$, an additional factor of 0.58 is applied to 0.094%. Table A.1 lists the B_c branching fractions that are input to the simulation, where the total decay fraction is normalized 1, and the subsequent contributions to the selected $J/\psi(\mu^+\mu^-) + l^\pm$ samples.

A total of 20 million B_c events are generated, and decayed to $J/\psi(\mu^+\mu^-) + e^\pm$ and $J/\psi(\mu^+\mu^-) + \mu^\pm$ final states with equal probability. After selection, the yields for the muon and electron channels are 5284 and 13112 respectively. The lower muon yield is due to the smaller p_T and η acceptance for the third muon selection compared to the electron selection.

Fraction of $J/\psi + l + X$ Events			
Decay	Input to Simulation	After $J/\psi + \mu$ Selection	After $J/\psi + e$ Selection
$J/\psi l \nu_l$	0.8581	0.9710	0.9629
$J/\psi \tau \nu_\tau$	0.0370	0.0085	0.0114
$\psi(2S) l \nu_l$	0.0235	0.0164	0.0187
$B_s l \nu_l$	0.0226	0.0000	0.0002
$B_s^* l \nu_l$	0.0271	0.0000	0.0000
$B^0 l \nu_l$	0.0009	0.0000	0.0000
$B^{0*} l \nu_l$	0.0018	0.0000	0.0000
$J/\psi D_s$	0.0054	0.0010	0.0014
$J/\psi D_s^*$	0.0217	0.0028	0.0041
$J/\psi D^0$	0.0005	0.0000	0.0002
$J/\psi D^{0*}$	0.0014	0.0001	0.0002

Table 48: Estimates of the fraction of $J/\psi(\mu^+\mu^-)+l^\pm$ events from different B_c decays, where the branching fractions to the final states include all branching fractions to intermediate states.

A.2 PYTHIA $b\bar{b}$ SAMPLE

For studies of the background where the J/ψ and third lepton originate from opposite $b\bar{b}$ jets, a realistic Monte Carlo of $b\bar{b}$ production is needed. For this purpose, PYTHIA is used to generate $b\bar{b}$ events in the "msel=1" mode where all $2 \rightarrow 2$ processes, with the addition of initial and final state radiation, are included [37].

The decay table applied to the $b\bar{b}$ sample is designed to decay B mesons containing a \bar{b} quark to states with a J/ψ while decaying the opposite jet to all physically allowed states according to their experimentally or theoretically determined branching fractions. Events containing a J/ψ and an additional muon, electron or kaon are selected at the generator level and run through the standard simulation process.

The creation of $b\bar{b} J/\psi(\mu^+\mu^-) + l^\pm$ candidates is suppressed by two factors with the consequence that many events must be generated to create samples of reasonable size. Because all $2 \rightarrow 2$ processes are included, the rate of $b\bar{b}$ production is suppressed by a factor of ~ 1000 relative to the all inelastic interactions produced. There is an additional suppression of candidate events due to the fact that the J/ψ and third lepton do not originate from the same decay vertex, and the rate at which they appear to originate from the same vertex is quite low. For the case of $b\bar{b} J/\psi(\mu^+\mu^-) + \mu^\pm$ events, a previously generated sample of $b\bar{b}$ was re-decayed, providing a sample of 180 candidate events. For the $b\bar{b} J/\psi(\mu^+\mu^-) + e^\pm$ events, a new sample was required to account for the larger p_T and η acceptance in the selection. 240,000,000 were generated providing a sample 410 $J/\psi(\mu^+\mu^-) + e^\pm$ candidates.

A.3 PYTHIA e^+e^- SAMPLE

PYTHIA is also used to generate samples with J/ψ from B decays that also contain e^+e^- pairs from photon conversion or the decay of light neutral mesons. These samples are used to study the efficiency for identifying and vetoing e^+e^- pairs in events where one of the electrons can make a vertex with the J/ψ .

Events are generated in two steps: the "msel=5" setting generates a $b\bar{b}$ pair, and the

"msel=2" setting generates an additional inelastic interaction in the event to give more realistic detector occupancy. The events are generated with the same decay table used for the $b\bar{b}$ generation and events with a J/ψ and a photon or light neutral meson with $p_T > 1.7$ GeV/ c are selected and run through the simulation. A sample of 75,000,000 generated events provides 1711 candidate events with a J/ψ and an e^+e^- pair where one of the electrons makes a vertex with the J/ψ .

APPENDIX B

ASSOCIATED DATA SAMPLES SELECTION

In addition to the $J/\psi(\mu^+\mu^-) + l^\pm$ sample containing signal candidates, the analysis uses a number a data samples, to study signal and background efficiencies. The selection of these data samples are discussed in the following sections.

B.1 CONVERSION ELECTRON SAMPLE

Understanding the efficiency of the electron likelihood ratio employed for electron identification requires a sample of unbiased electrons to which the likelihood ratio can be applied. Photon conversions, $\gamma \rightarrow e^+e^-$ when the photon interact with material [94], are the ideal sample. Since the conversion pair typically has a small mass and opening angle, the events are easily selected. In addition to the kinematic properties, electron or trigger selection can be applied to one of the conversion tracks while leaving the other unbiased.

The selection of conversion candidates begins with the "ELECTRON_CENTRAL_8" trigger path which requires a $p_T > 8 \text{ GeV}/c$ track with an associated $8 \text{ GeV}/c^2$ energy deposit in the CEM. The trigger track is identified, and oppositely charged tracks that originate from the same point with small opening angle are selected to form photon conversion candidates. Table 49 list the cuts used for selection.

Figure 113 shows the candidate events before the $\Delta\cot(\theta)$ cut is applied, and the large peak at zero is expected for the conversion signal. The sidebands of the $\Delta\cot(\theta)$ distribution

Selection Requirement	Value
Trigger Track p_T	$> 8.0 \text{ GeV}/c$
Trigger Track E_T^{em}	$> 8.0 \text{ GeV}/c^2$
Second Track p_T	$> 2.0 \text{ GeV}/c$
Second Track hit requirements	Identical to B_c candidate electron selection
Two Track xy Displacement	$ \Delta_{xy} < 0.2 \text{ cm}$
Conversion Radius	$< 12 \text{ cm}$
CES Wedge	Two tracks point to different CES wedges
Two Track polar opening angle	$ \Delta \cot(\theta) < 0.01$

Table 49: Cuts applied to select photon conversion candidates.

are used to subtract out the background contributions. With all cuts applied, the likelihood ratio can be applied to the second track and its performance studied. The second track sample can also be used as a sample of electrons for dE/dx or TOF studies.

B.2 TAGGED D^0 SAMPLE

The rates at which pions and kaons are misidentified as leptons can be studied using samples of pions and kaons identified by the decay chain that produces them. The decay $D^{*+} \rightarrow D^0(K^-\pi^+)\pi^+ + c.c.$ identifies the pion and kaon from the D^0 decay by the charge of the soft pion from the D^{*+} decay.

The D^0 candidates are selected from data collected with two track hadronic triggers. The simplest of these triggers selects two oppositely charged XFT+SVT tracks with $p_T > 1.5 \text{ GeV}/c$, impact parameters $> 100 \mu\text{m}$, and opening angle $< 90^\circ$. The exact details of the trigger mix in the two track hadronic triggers varies with time, but always includes events with two XFT+SVT tracks with impact parameter cuts to ensure that they likely originate from a displaced vertex.

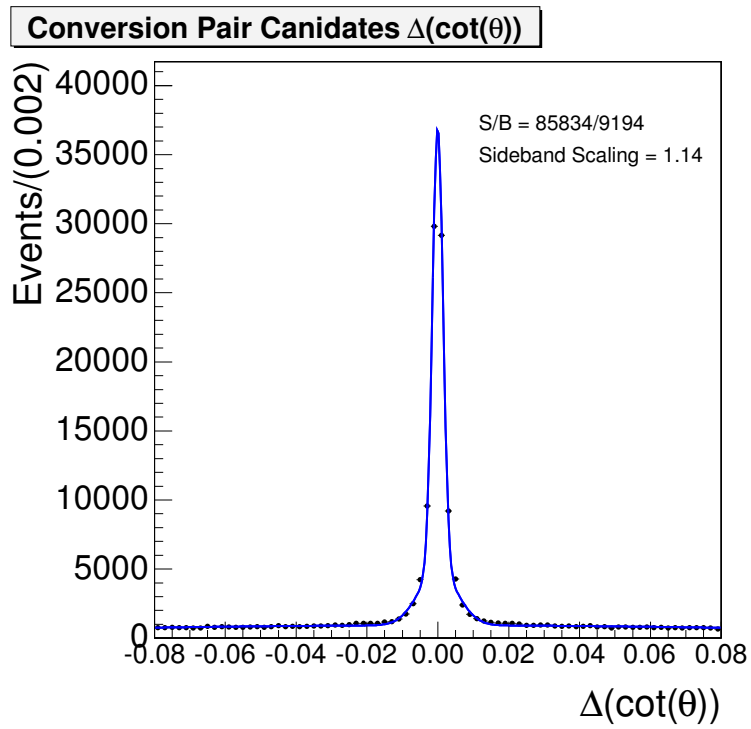


Figure 113: $\Delta\cot(\theta)$ for conversion pair candidates.

The offline selection of the tagged D^0 decays is listed in Table 50. The D^0 leg that is being studied, whether it is the pion or kaon leg, will always have identical tracking requirements as applied to the third track in the $J/\psi(\mu^+\mu^-) + l^\pm$ sample, excluding the lepton requirements. Figure 114 illustrates the reduction of backgrounds by selecting on the $D^{*+} - D^0$ mass difference as well as the resulting tagged D^0 mass distribution.

Selection Requirement	Value
D^0 legs p_T	π or K $p_T > 2.0$ GeV/ c
D^0 leg track requirements	Identical to $J/\psi + l$ selection, but no lepton ID
D^0 p_T	> 3.0 GeV/ c
K/π $\Delta\phi$	> 0.035 and < 2.36
K/π Δz	< 8 cm
D^0 Vertex Prob.	> 0.001
D^0 L_{xy}	> 0.01 cm
$ M(D^0) - 1.865 $	< 0.1 GeV/ c^2
D^* Vertex Prob.	> 0.001
$D^0/\text{soft } \pi$ $\Delta\phi$	< 0.7854
$ [M(D^*) - M(D^0)] - 0.1457 $	< 0.002 GeV/ c^2
$Q(\pi) * Q(\text{soft } \pi)$	$= 1$

Table 50: Cuts applied to two track hadronic trigger datasets to skim D^{*+} tagged D^0 decays.

B.3 Λ SAMPLE

The decay $\Lambda^0 \rightarrow p^+\pi^- + c.c.$ offers a source of protons for studies of lepton misidentification rates. Since the mass of the Λ^0 , 1.116 GeV/ c^2 , is only slightly larger than the sum of the p and π masses, $0.938 + 0.140 = 1.078$ GeV/ c^2 , the p and π have small momenta in the Λ rest frame. When a large boost is applied to move to the lab frame, the more massive particle,

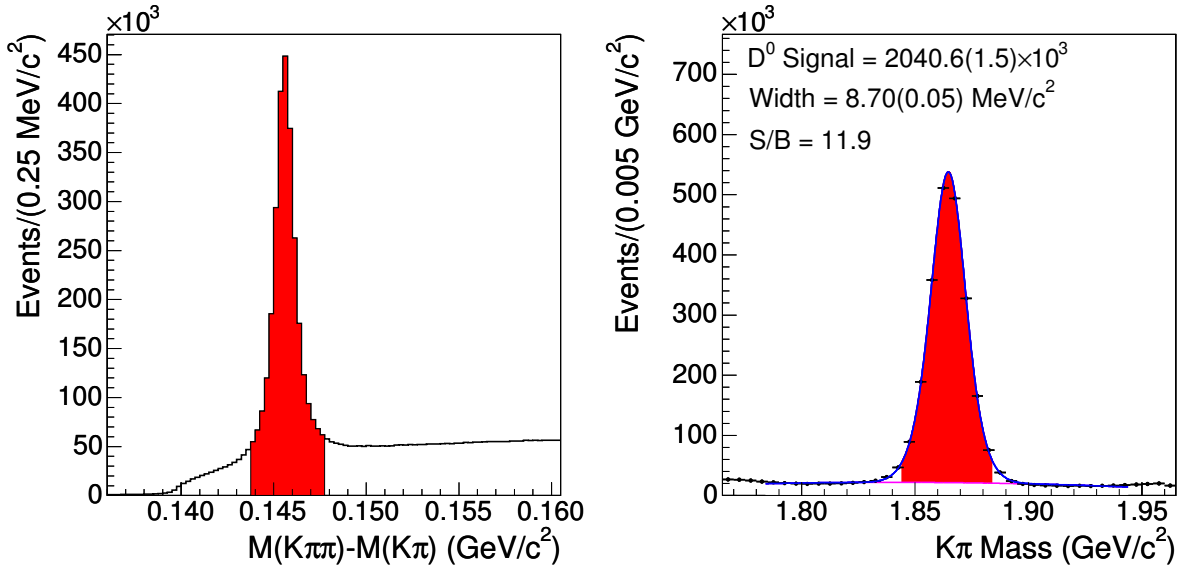


Figure 114: Left: Invariant mass difference between the D^{*+} and D^0 systems. Right: Invariant mass of the D^0 system after all cuts are applied.

the p , has a larger momentum. Therefore, a sample of protons can be identified as the Λ^0 decay product with the largest momentum.

The Λ candidates are collected from the same two track trigger sample as the tagged D^0 sample. The event selection listed in Table 51 gives a sample with the mass distribution seen in Figure 115.

Selection Requirement	Value
Proton Leg p_T	$p_T > 2.0 \text{ GeV}/c$
Pion Leg p_T	$p_T > 0.4 \text{ GeV}/c$
Proton track requirements	Identical to $J/\psi + l$ selection, but no lepton ID
Proton d_0	$> 0.012 \text{ cm}$
$p\pi \Delta z$	$< 8 \text{ cm}$
Λ Vertex Prob.	> 0.01
ΛL_{xy}	$> 0.85 \text{ cm}$
$ M(\Lambda) - 1.116 $	$< 0.04 \text{ GeV}/c^2$

Table 51: Cuts applied to two track hadronic trigger datasets to skim Λ decays.

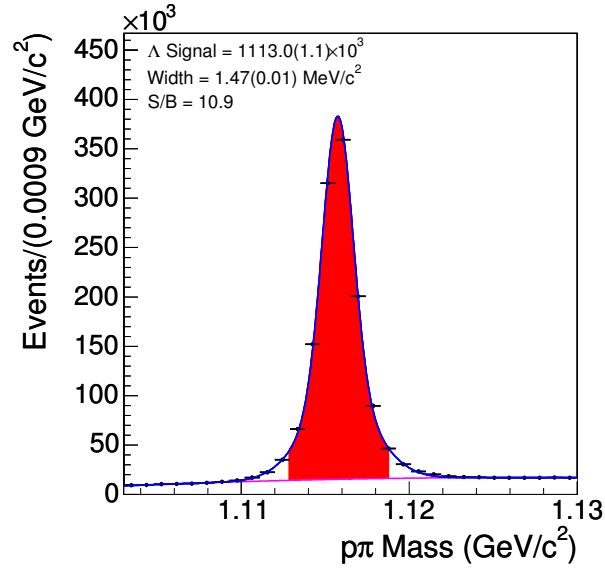


Figure 115: Invariant mass of Λ^0 candidates after selection is applied.

APPENDIX C

THIRD TRACK PROTON STUDIES

As discussed in Chapter 7, the misidentified muon background is modeled using J/ψ +track events that are selected using the same cuts as the B_c selection, but with the lepton identification cuts for the third lepton removed. Calculation of the background require the determination of the fractions of third tracks in the J/ψ +track sample that are pions, kaons, and protons. These fractions are measured using TOF and dE/dx information when the third track momentum is < 3.0 GeV/ c . For momenta > 3.0 GeV/ c dE/dx information only is used. For the < 3.0 GeV/ c region, protons and kaons are clearly differentiated by the TOF information, but above 3.0 GeV/ c it is difficult to separate the contributions from protons and kaons. Proton fractions above 3.0 GeV/ c must be constrained by using a model to extrapolate the proton fraction from the < 3.0 GeV/ c region to the higher momentum region. One possible model assumes that the proton fraction is flat with momentum. Another possibility is to study the momentum dependence of the proton fraction in a realistic Monte Carlo simulation of PYTHIA generated B decays. Figure 116 shows the momentum dependent proton fraction for third tracks in the J/ψ +track sample as determined by the realistic PYTHIA based simulation. Here, the fraction of protons in the 2 – 3 GeV/ c bin is scaled such that the simulation agrees with data, and the same scaling is applied to all bins.

The PYTHIA model of proton fractions is only a rough estimation. The main sources of J/ψ +proton events in PYTHIA are events where the proton comes from the fragmentation process or the decay of a B baryon. The fraction of protons from fragmentation depends on

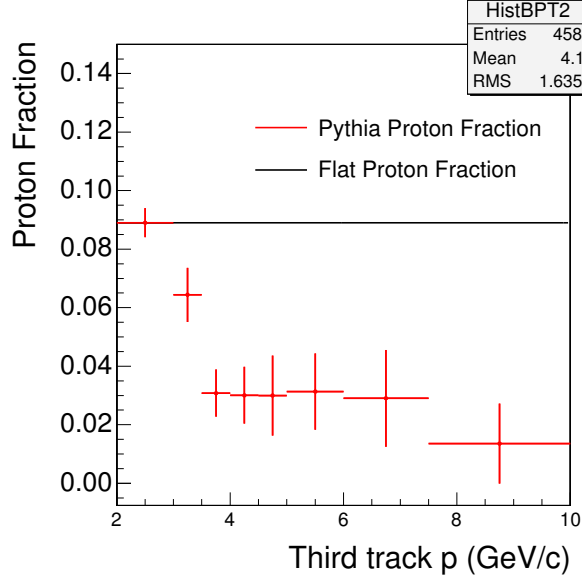


Figure 116: Proton fraction of third tracks in the PYTHIA J/ψ +track sample.

the Lund model [33], which PYTHIA uses to model fragmentation. The fraction of protons from B baryon decays, depends on the branching fractions for B baryons to decay to J/ψ and the production of B baryons relative to B mesons. The B baryon branching fractions, except for $\Lambda_b \rightarrow J/\psi + \Lambda$, have not been measured or have not yet been precisely measured. Considerable uncertainties surrounding the B Baryon fraction and momentum spectrum relative to B mesons at energy scales typical to B_c candidate events [96].

Toy Monte Carlos are used to determine the uncertainties related to the proton fraction in the J/ψ +track sample. The misidentified muon model used while generating toys is constructed using a proton fraction that is flat in momentum. However, the misidentified muon model used in the lifetime fitter is constructed using the momentum dependant proton fraction suggested by the PYTHIA sample. The flat proton fraction model predicts a smaller misidentified muon background, since protons are not misidentified as muons. In fact, the difference between the two models leads to a 20% difference in the predicted normalization of the misidentified muon background. The pull distribution of measured B_c lifetimes in the toy Monte Carlos are shown in Figure 117. The deviation of the pull corresponds to a shift

in the measured lifetime of about $10 \mu\text{m}$.

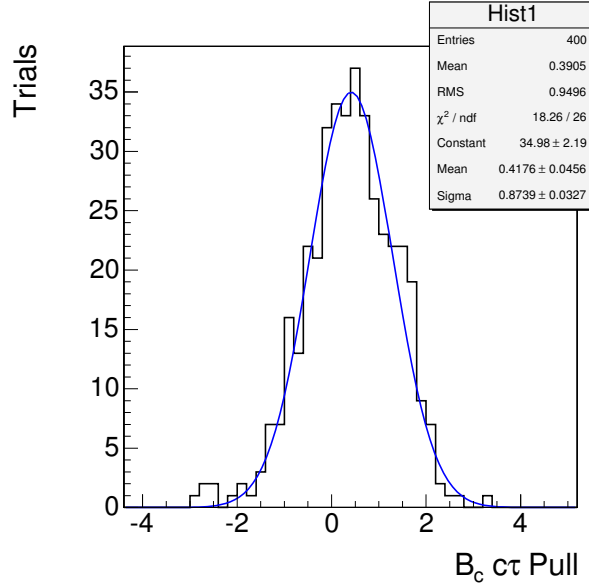


Figure 117: Pull of measured $B_c c\tau$ in toy Monte Carlos where the model for proton fractions is varied.

A single source of systematic uncertainty in the B_c lifetime of $10 \mu\text{m}$ is unacceptable and the uncertainty must be decreased. This can be done by minimizing the kaon and proton contribution of third tracks in the J/ψ +track sample. To achieve this goal a $Z_\mu > -1.0$ cut is applied to third tracks. Having a cut of > -1.0 removes about 15% of signal events (as well as backgrounds with a properly identified third muon). For kaons and protons, however, this cut removes about 75% and 80% of events from the J/ψ +track sample respectively. In addition to minimizing the uncertainty related to the relative amounts of kaons and protons, this cut also reduces the total misidentified muon background by about 50% since it removes 75% of kaons. After applying the cut, the proton fraction toy Monte Carlo study is carried out again. The pull distribution can be seen in Figure 118, and the associated uncertainty is $\sim 2.5 \mu\text{m}$, which is acceptable.

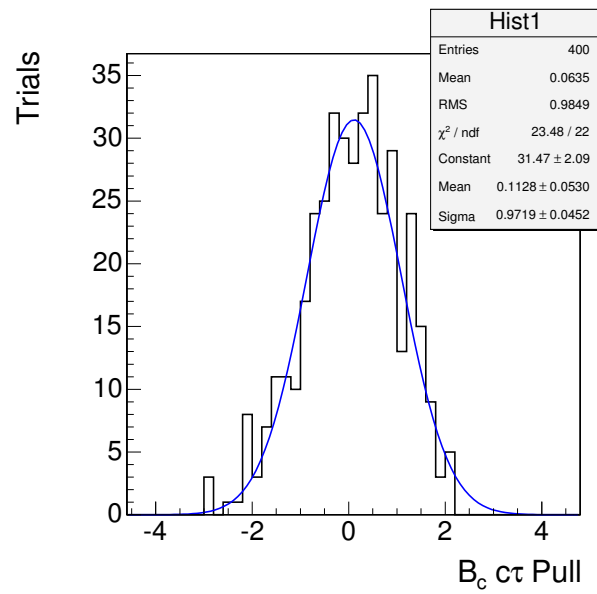


Figure 118: Pull of measured $B_c c\tau$ in toy Monte Carlos where the model for proton fractions is varied after the $Z_\mu > -1.0$ has been applied.

APPENDIX D

MISIDENTIFIED LEPTON FITS

The calculation of the misidentified lepton background is discussed in Section 7.2. The calculation involves the determination of lepton misidentification probabilities using decay products from tagged $D^0 \rightarrow \pi K$ decay and $\Lambda \rightarrow p\pi$ decays. For both cases a large number of mass fits are carried out for various values of p_T and charge of the decay products from which the misidentification probabilities are determined. The fitted mass distributions are shown in this chapter.

The calculation of the misidentified lepton background also depends on the particle composition of third tracks in the J/ψ +track sample. The composition is determined by carrying out two dimensional fits of the TOF and dE/dx of third tracks for momentums $< 3.0 \text{ GeV}/c$ and fits of dE/dx only for momentums $> 3.0 \text{ GeV}/c$. The fits are carried out in bins of third track momentum, third track charge, and ct^* of the J/ψ +track system. The fitted particle identification distributions are also shown in this chapter.

D.1 MASS FITS FOR ELECTRON MISIDENTIFICATION PROBABILITIES

The electron misidentification probability is determined by mass fits of the tagged D^0 and Λ distributions. First the parent distributions, where one of the decay products of the D^0 or Λ passes the same selection as third tracks in the J/ψ +track sample, are fitted. Next, the

daughter distributions, where the decay product must also pass the electron likelihood ratio cut, are fitted. The mass fits are carried out for pions and kaons that are D^0 decay products and protons that are Λ decay products. Events are separated based on the p_T of the decay product and charge of the decay product since the misidentification rates vary depending on these properties of the particle.

The fitted parent distributions for positively and negatively charged pions are shown in Figures 119 and 120 respectively. The parent distributions for positively and negatively charged kaons are shown in Figures 121 and 122. The parent distributions for positively and negatively charged protons are shown in Figures 123 and 124.

The fitted daughter distributions for positively and negatively charged pions are shown in Figures 125 and 126 respectively. The daughter distributions for positively and negatively charged kaons are shown in Figures 127 and 128. The daughter distributions for positively and negatively charged protons are shown in Figures 129 and 130.

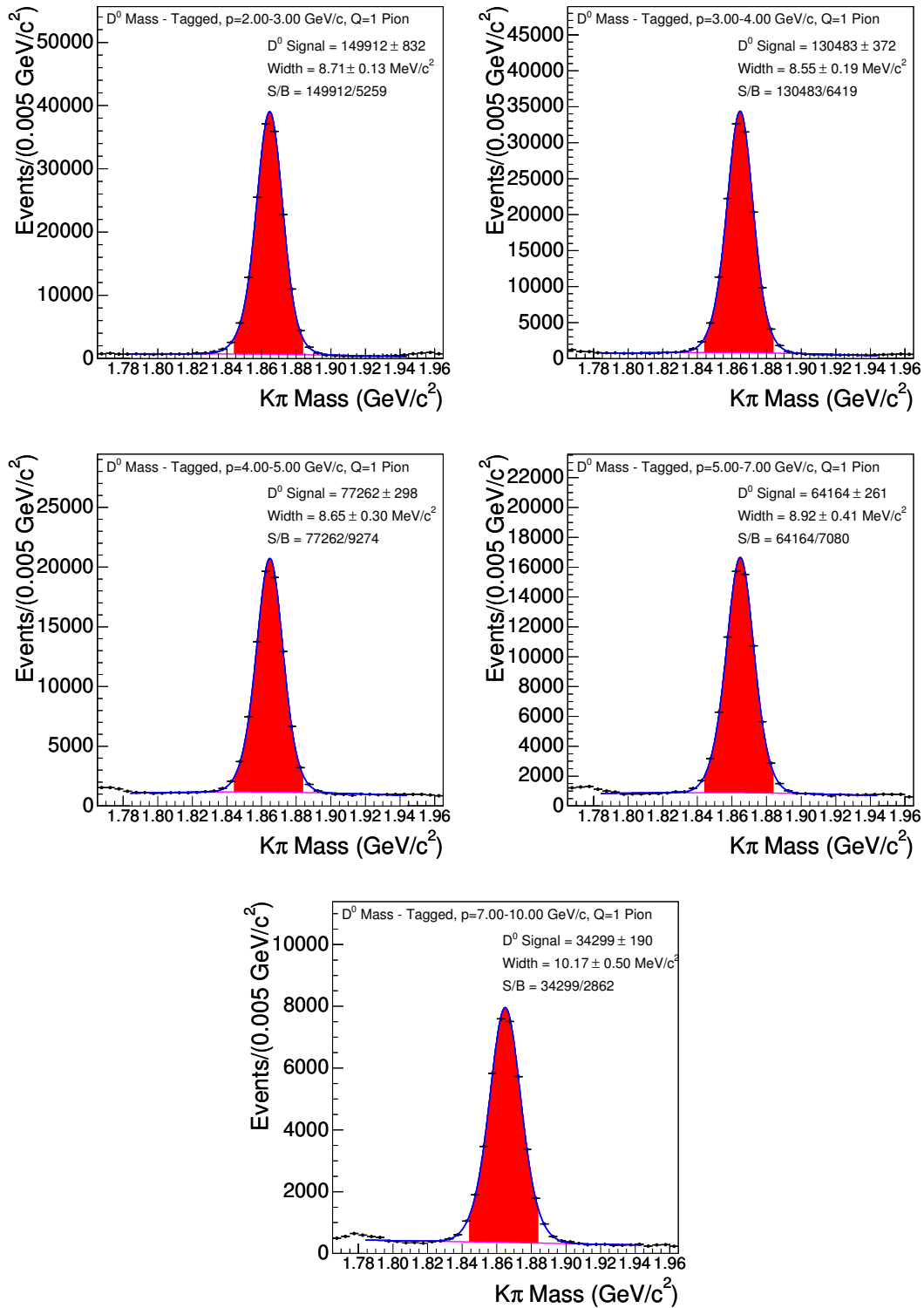


Figure 119: Fitted D^0 mass peaks where the π^+ leg meets the third track requirements. Broken into p_T bins of 2 – 3 GeV/c (top left), 3 – 4 GeV/c (top right), 4 – 5 GeV/c (middle left), 5 – 7 GeV/c (middle right), and > 7 GeV/c (bottom).

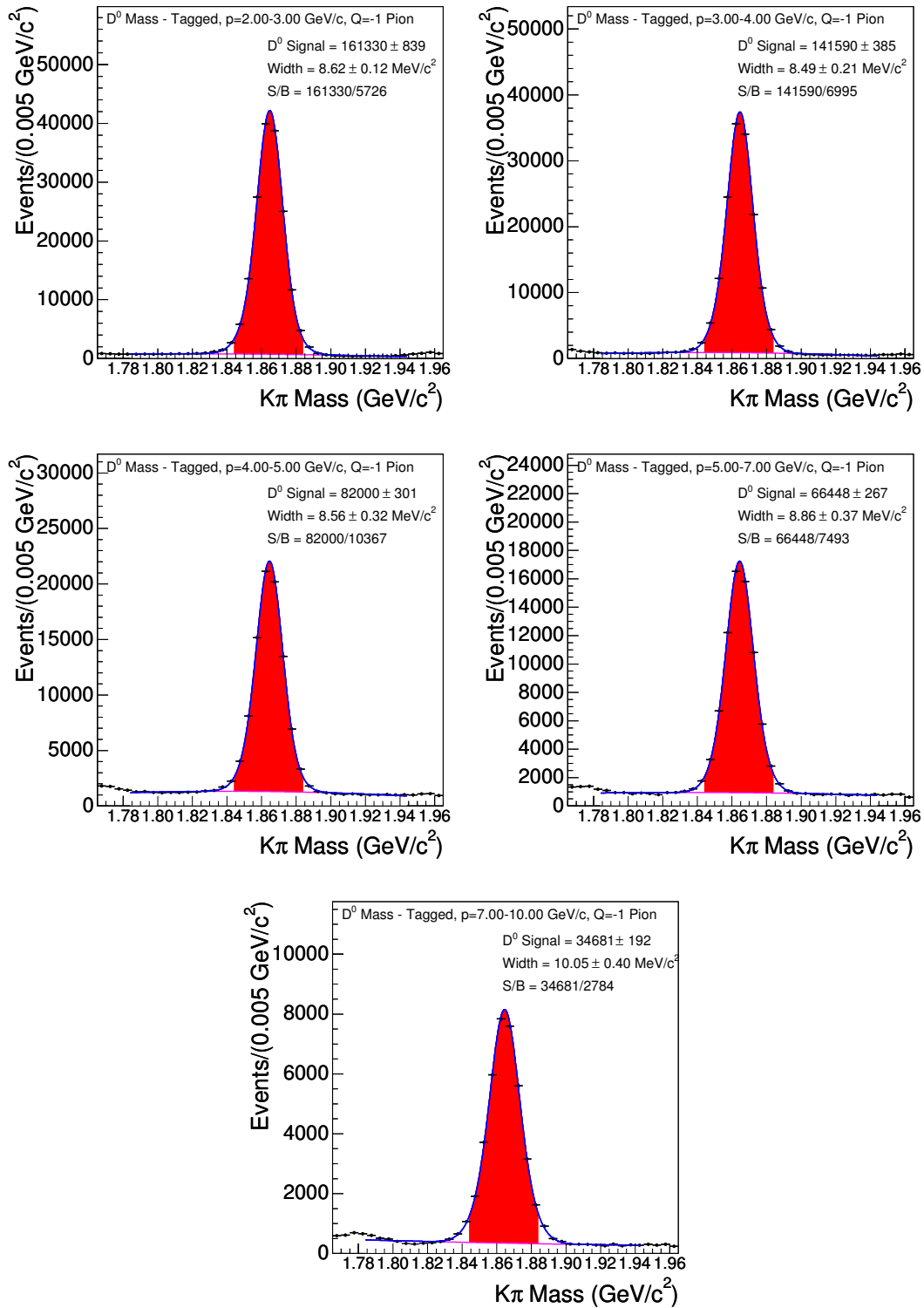


Figure 120: Fitted D^0 mass peaks where the π^- leg meets the third track requirements. Broken into p_T bins of 2 – 3 GeV/c (top left), 3 – 4 GeV/c (top right), 4 – 5 GeV/c (middle left), 5 – 7 GeV/c (middle right), and > 7 GeV/c (bottom).

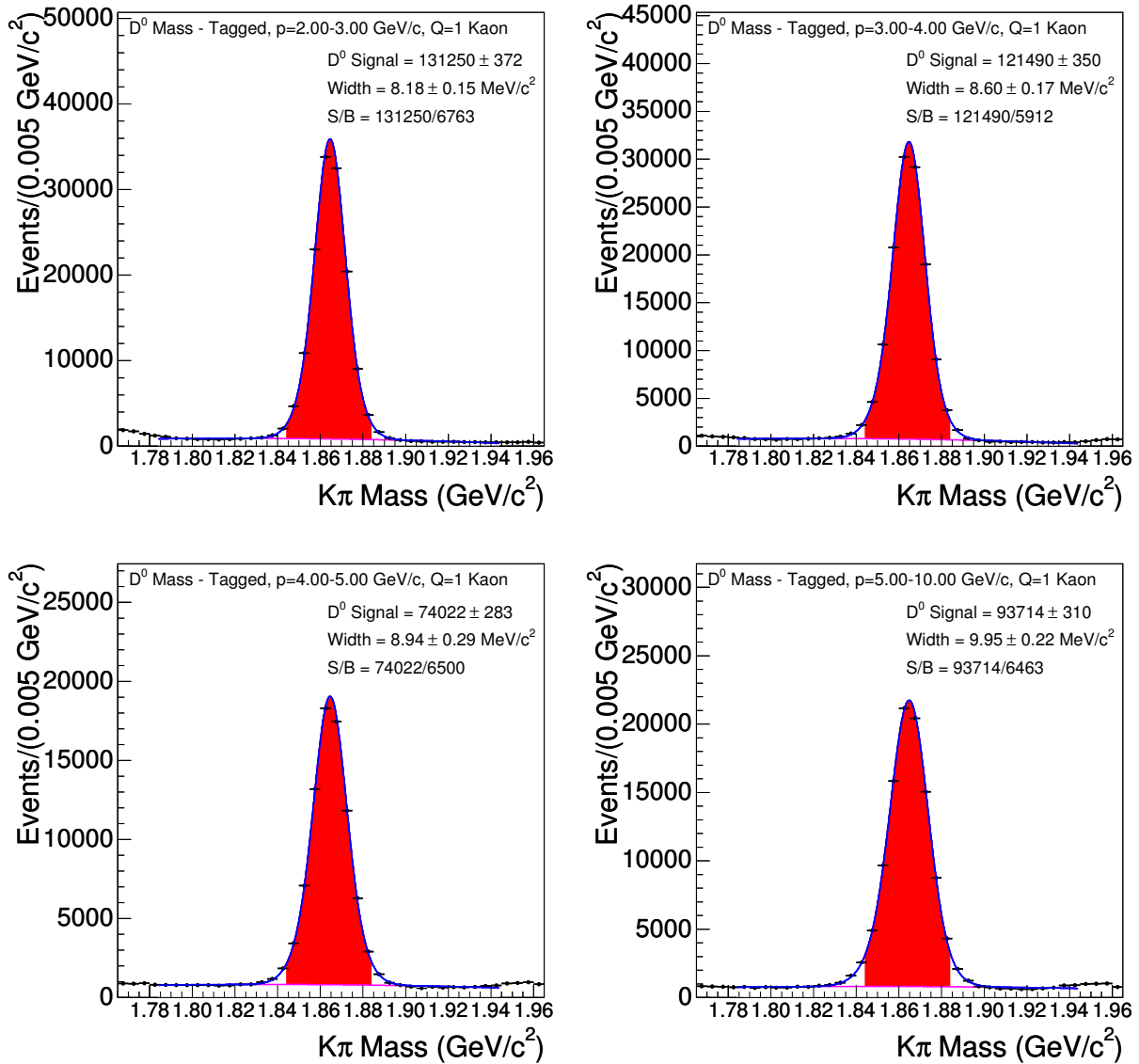


Figure 121: Fitted D^0 mass peaks where the K^+ leg meets the third track requirements. Broken into p_T bins of 2 – 3 GeV/c (top left), 3 – 4 GeV/c (top right), 4 – 5 GeV/c (bottom left), and > 5 GeV/c (bottom right).

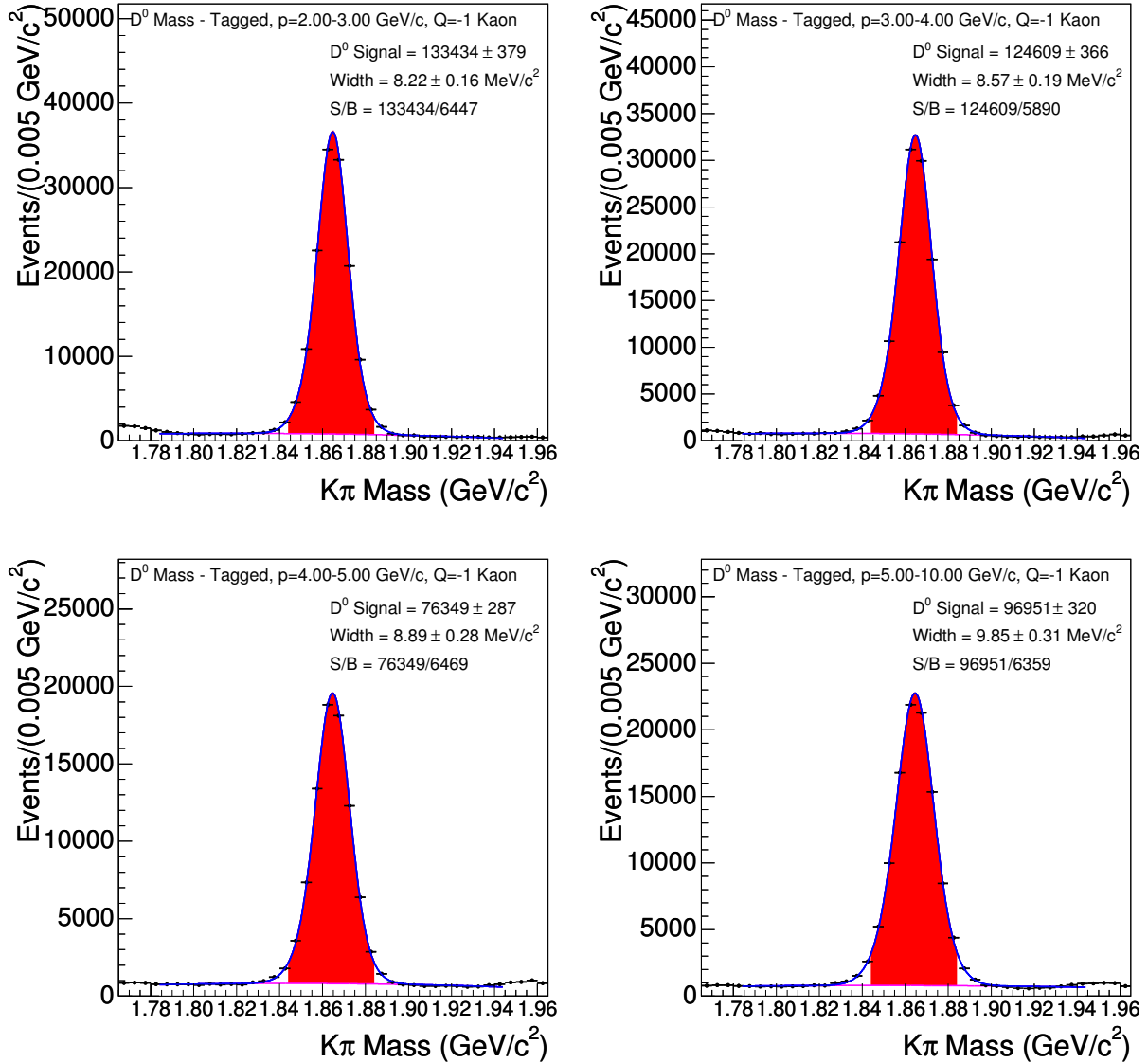


Figure 122: Fitted D^0 mass peaks where the K^- leg meets the third track requirements. Broken into p_T bins of 2 – 3 GeV/c (top left), 3 – 4 GeV/c (top right), 4 – 5 GeV/c (bottom left), and > 5 GeV/c (bottom right)

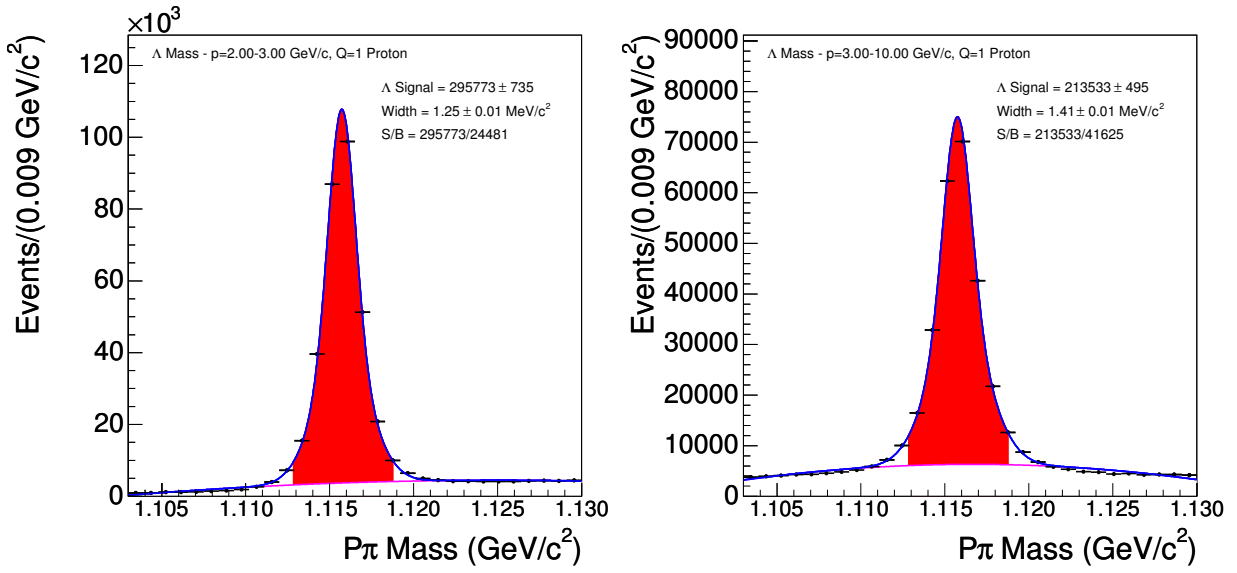


Figure 123: Fitted Λ mass peaks where the p^+ leg meets the third track requirements. Broken into p_T bins of 2 – 3 GeV/c (left) and $> 3 \text{ GeV}/c$ (right).

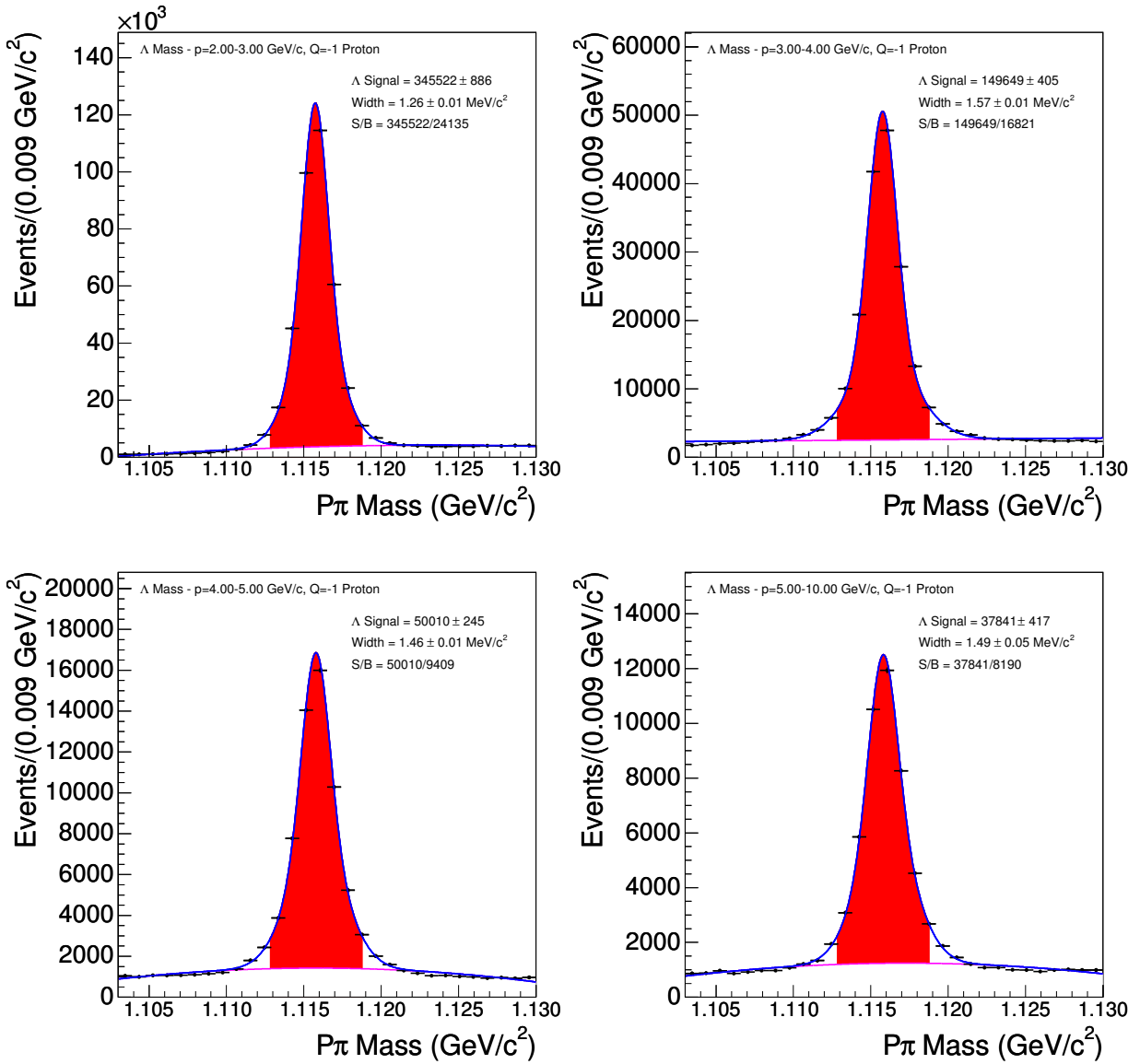


Figure 124: Fitted Λ mass peaks where the p^- leg meets the third track requirements. Broken into p_T bins of 2 – 3 GeV/ c (top left), 3 – 4 GeV/ c (top right), 4 – 5 GeV/ c (bottom left), and > 5 GeV/ c (bottom right)

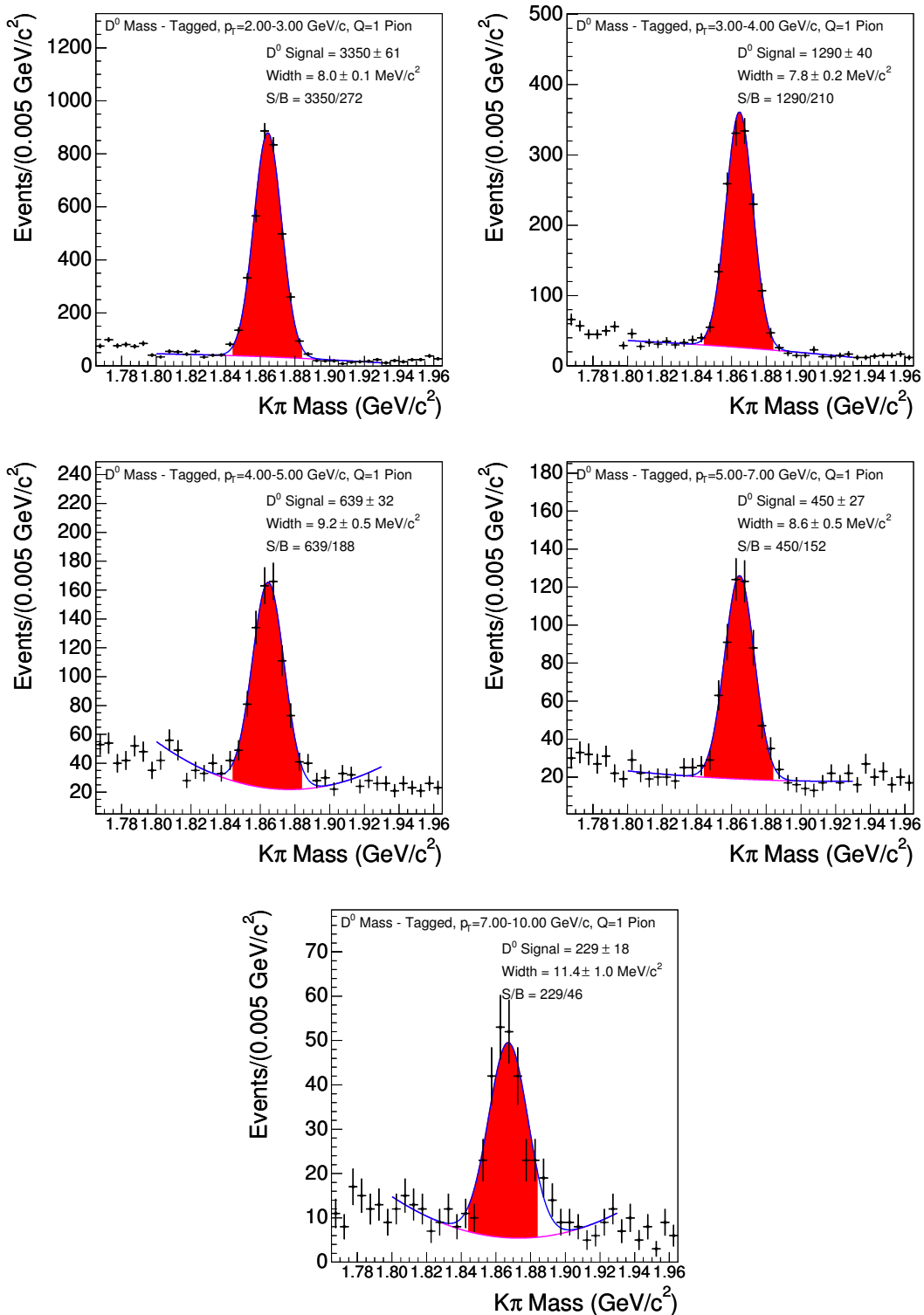


Figure 125: Fitted D^0 mass peaks where the π^+ leg passes electron selection. Broken into p_T bins of 2 – 3 GeV/c (top left), 3 – 4 GeV/c (top right), 4 – 5 GeV/c (middle left), 5 – 7 GeV/c (middle right), and > 7 GeV/c (bottom).

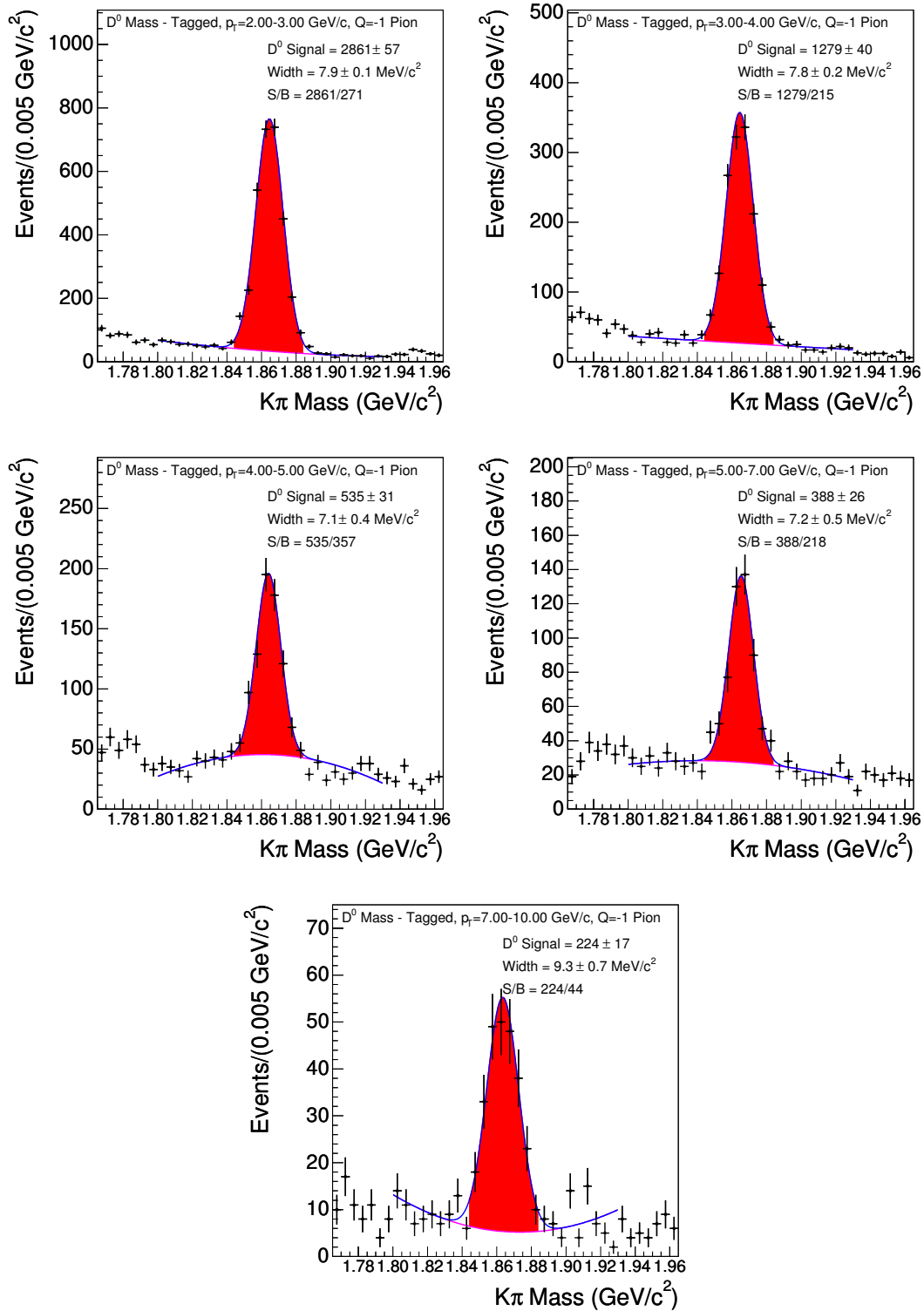


Figure 126: Fitted D^0 mass peaks where the π^- leg passes electron selection. Broken into p_T bins of 2 – 3 GeV/c (top left), 3 – 4 GeV/c (top right), 4 – 5 GeV/c (middle left), 5 – 7 GeV/c (middle right), and $> 7 \text{ GeV}/c$ (bottom).

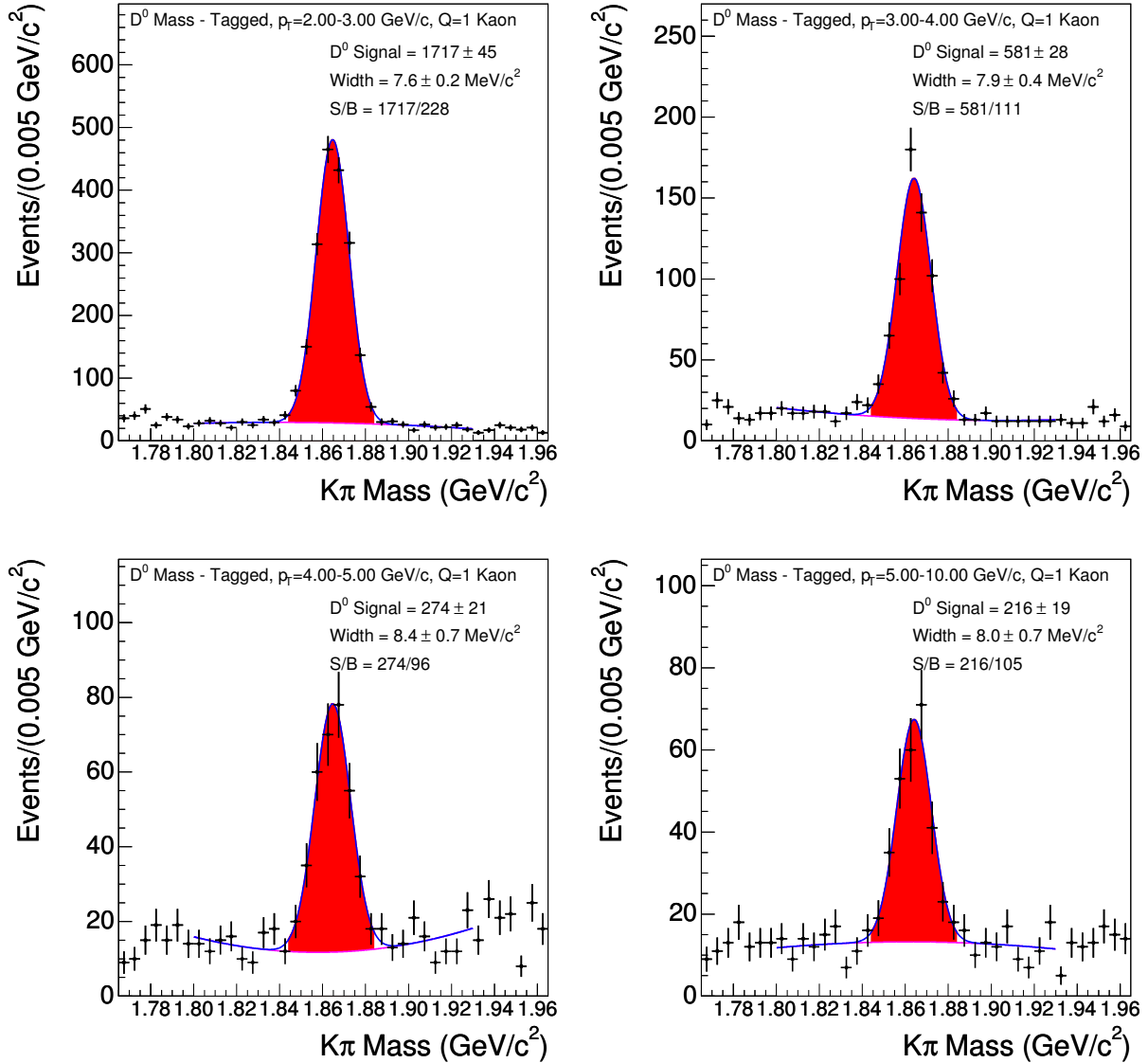


Figure 127: Fitted D^0 mass peaks where K^+ leg passes electron selection. Broken into p_T bins of 2 – 3 GeV/c (top left), 3 – 4 GeV/c (top right), 4 – 5 GeV/c (bottom left), and > 5 GeV/c (bottom right).

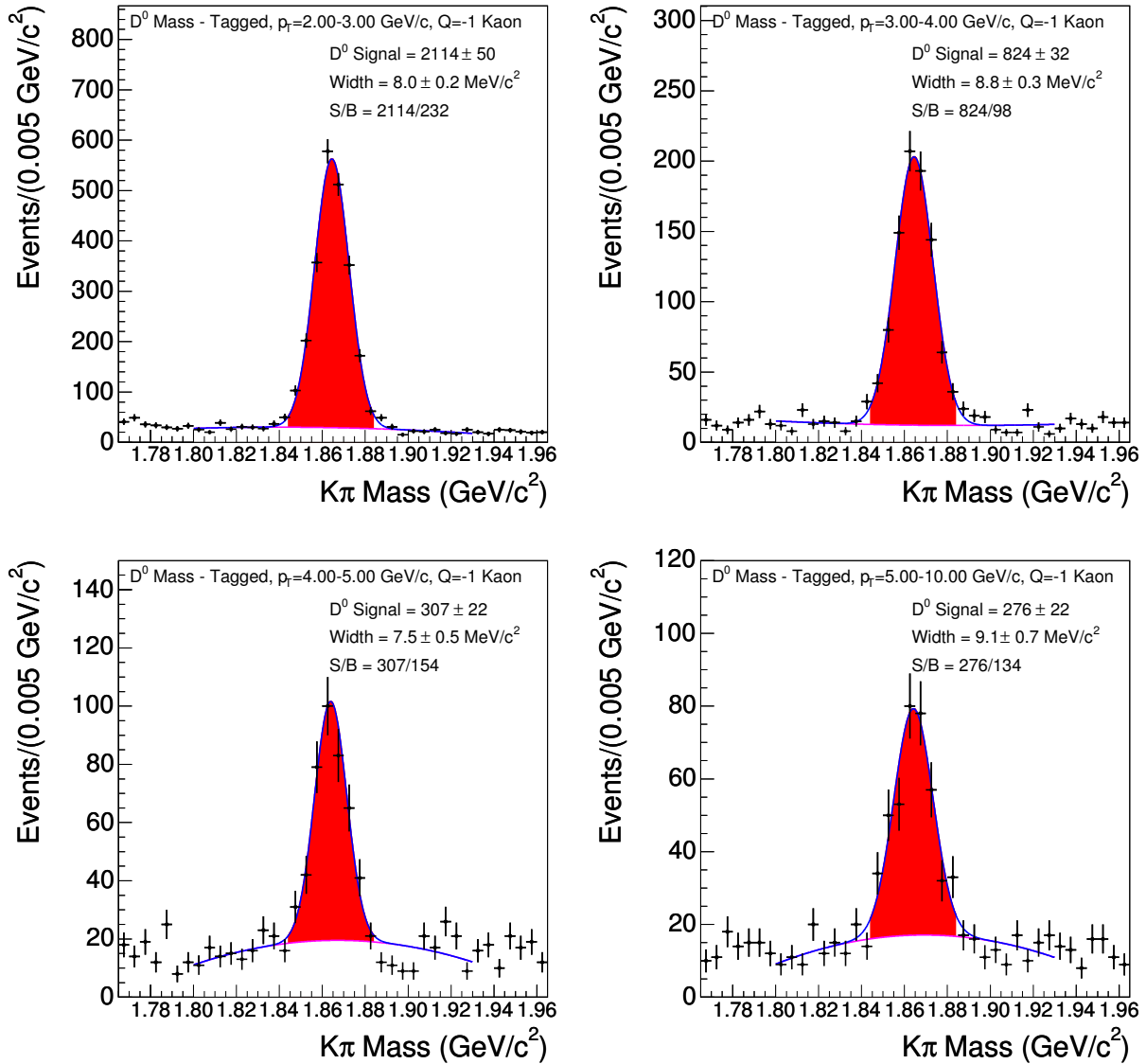


Figure 128: Fitted D^0 mass peaks where K^- leg passes electron selection. Broken into p_T bins of 2 – 3 GeV/c (top left), 3 – 4 GeV/c (top right), 4 – 5 GeV/c (bottom left), and > 5 GeV/c (bottom right)

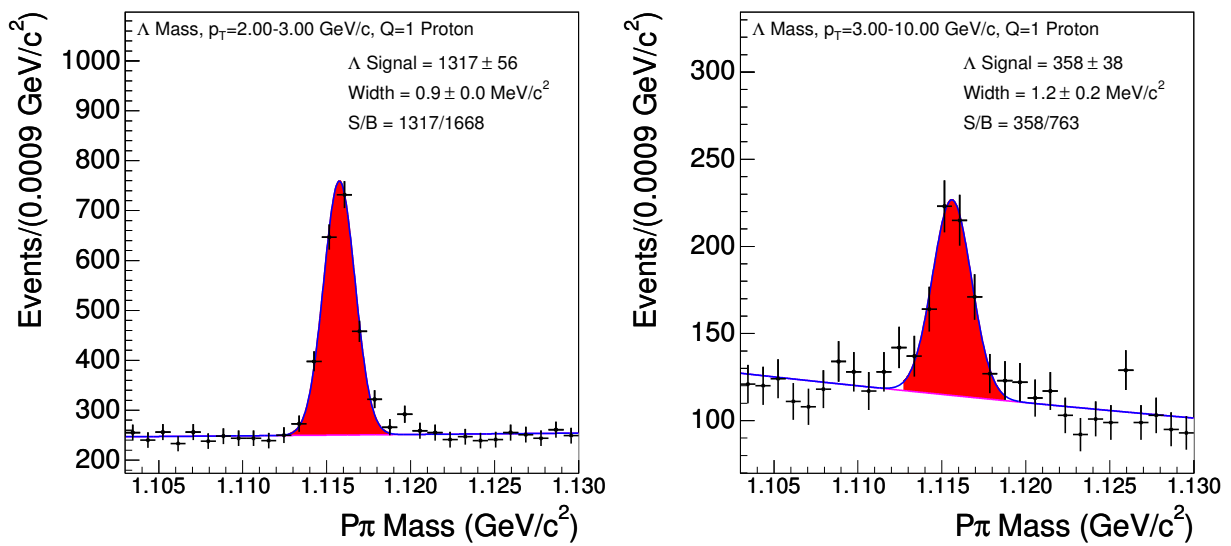


Figure 129: Fitted Λ mass peaks where p^+ leg passes electron selection. Broken into p_T bins of 2 – 3 GeV/ c (left) and > 3 GeV/ c (right).

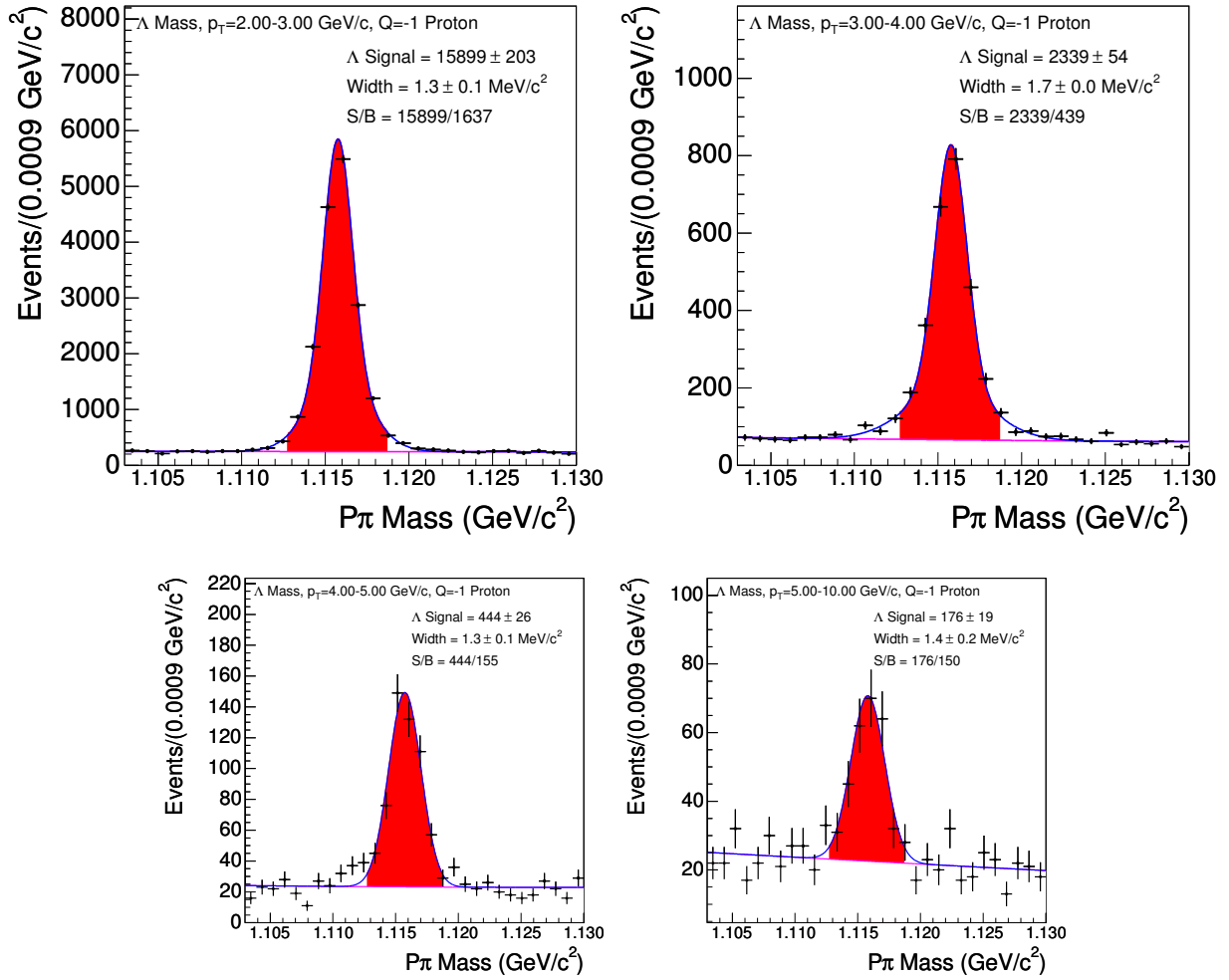


Figure 130: Fitted Λ mass peaks where p^- leg passes electron selection. Broken into p_T bins of 2 – 3 GeV/c (top left), 3 – 4 GeV/c (top right), 4 – 5 GeV/c (bottom left), > 5 GeV/c (bottom right)

D.2 MASS FITS FOR MUON MISIDENTIFICATION PROBABILITIES

The muon misidentification probabilities are determined using the same method that was used for the electron misidentification probabilities. Positively and negatively charged pions are binned together, since no difference is seen in their misidentification probabilities. Positively and negatively charged kaons are binned separately, since there is an expected difference in the punch-through probability due to the difference in the interaction cross sections with materials in the detector.

The fitted parent distributions for pions are shown in Figure 131. The parent distributions for positively and negatively charged kaons are shown in Figure 132.

The fitted daughter distributions for pions are shown in Figure 133. The daughter distributions for positively and negatively charged kaons are shown in Figure 134.

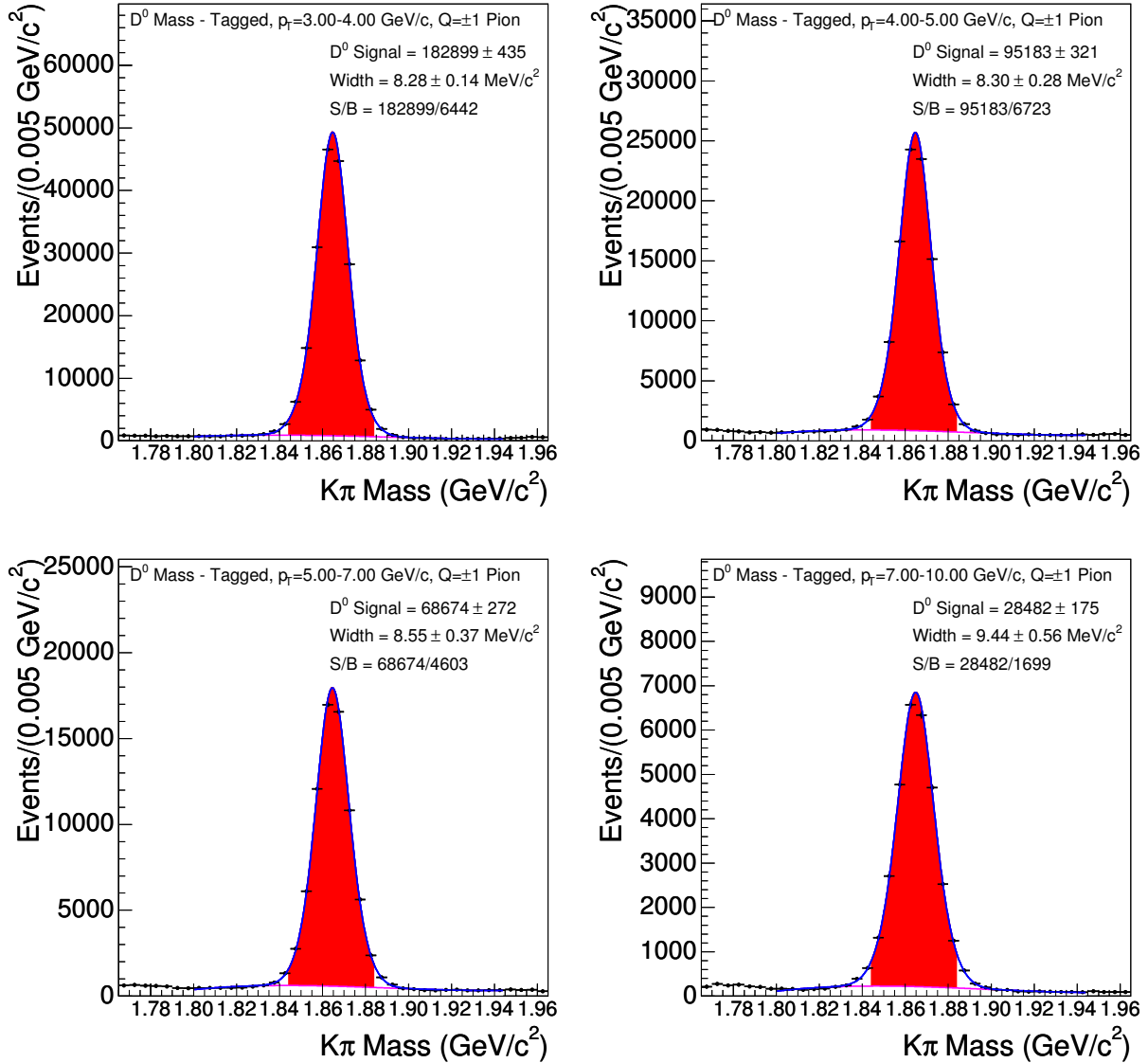


Figure 131: Fitted D^0 mass peaks where the π^\pm leg meets the third track requirements. Broken into p_T bins of 3 – 4 GeV/c (top left), 4 – 5 GeV/c (top right), 5 – 7 GeV/c (bottom left), and > 7 GeV/c (bottom right).

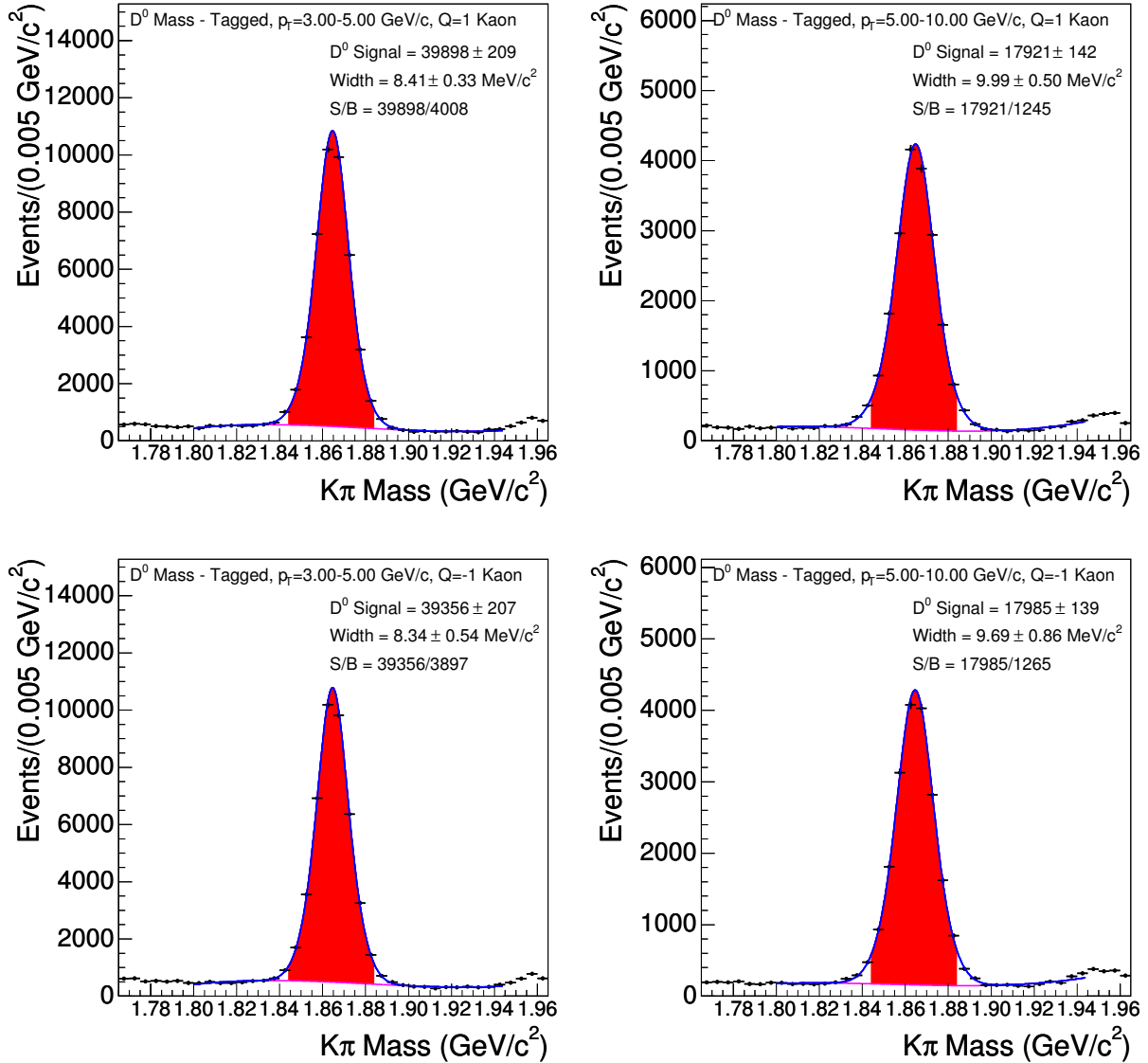


Figure 132: Fitted D^0 mass peaks where the K leg meets the third track requirements. Broken into p_T and q bins of $3 - 5$ GeV/c and $q = 1$ (top left), > 5 GeV/c and $q = 1$ (top right), $3 - 5$ GeV/c and $q = -1$ (bottom left), and > 5 GeV/c and $q = -1$ (bottom right).

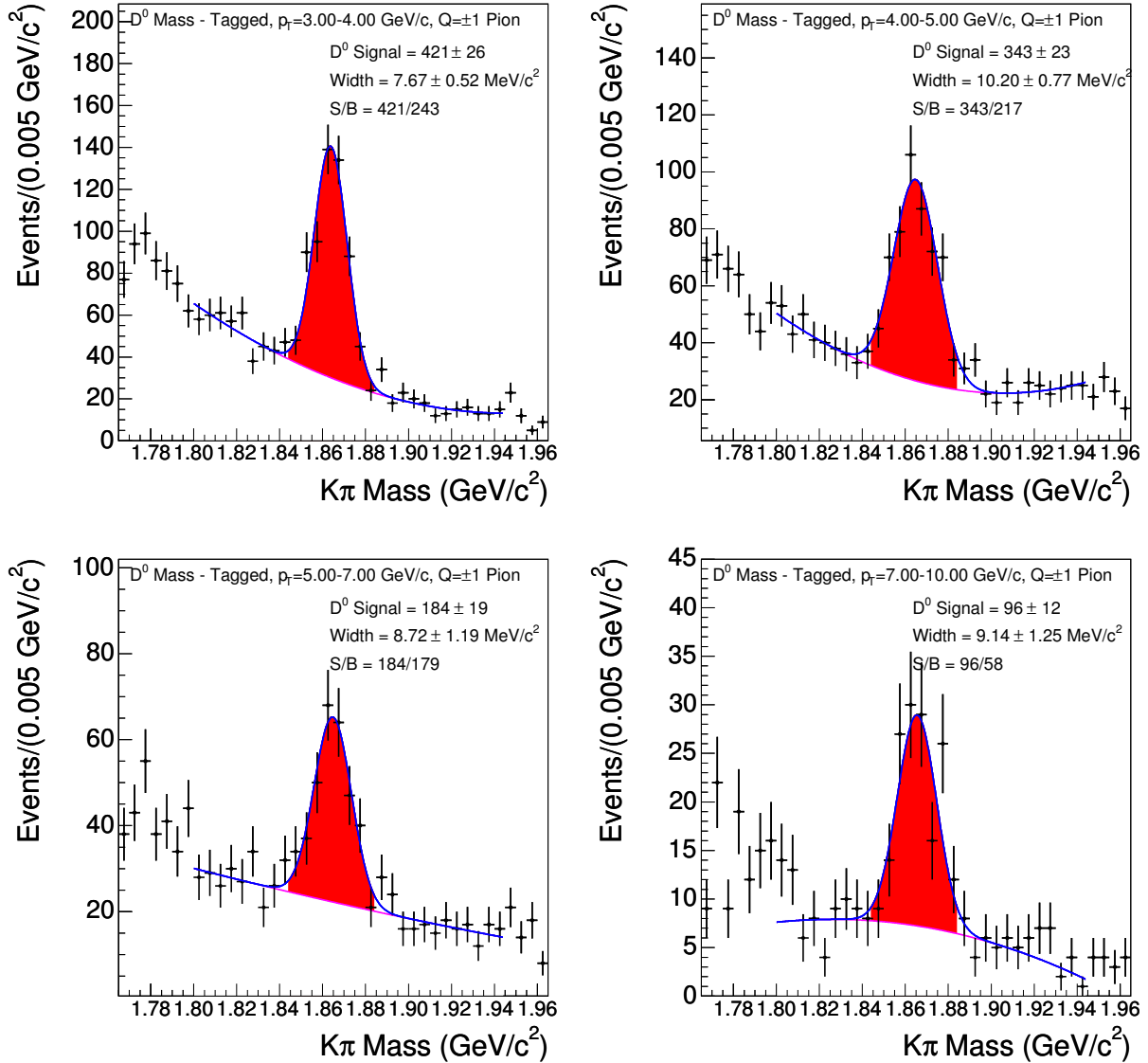


Figure 133: Fitted D^0 mass peaks where the π^\pm leg meets the third muon requirements. Broken into p_T bins of 3 – 4 GeV/c (top left), 4 – 5 GeV/c (top right), 5 – 7 GeV/c (bottom left), and > 7 GeV/c (bottom right).

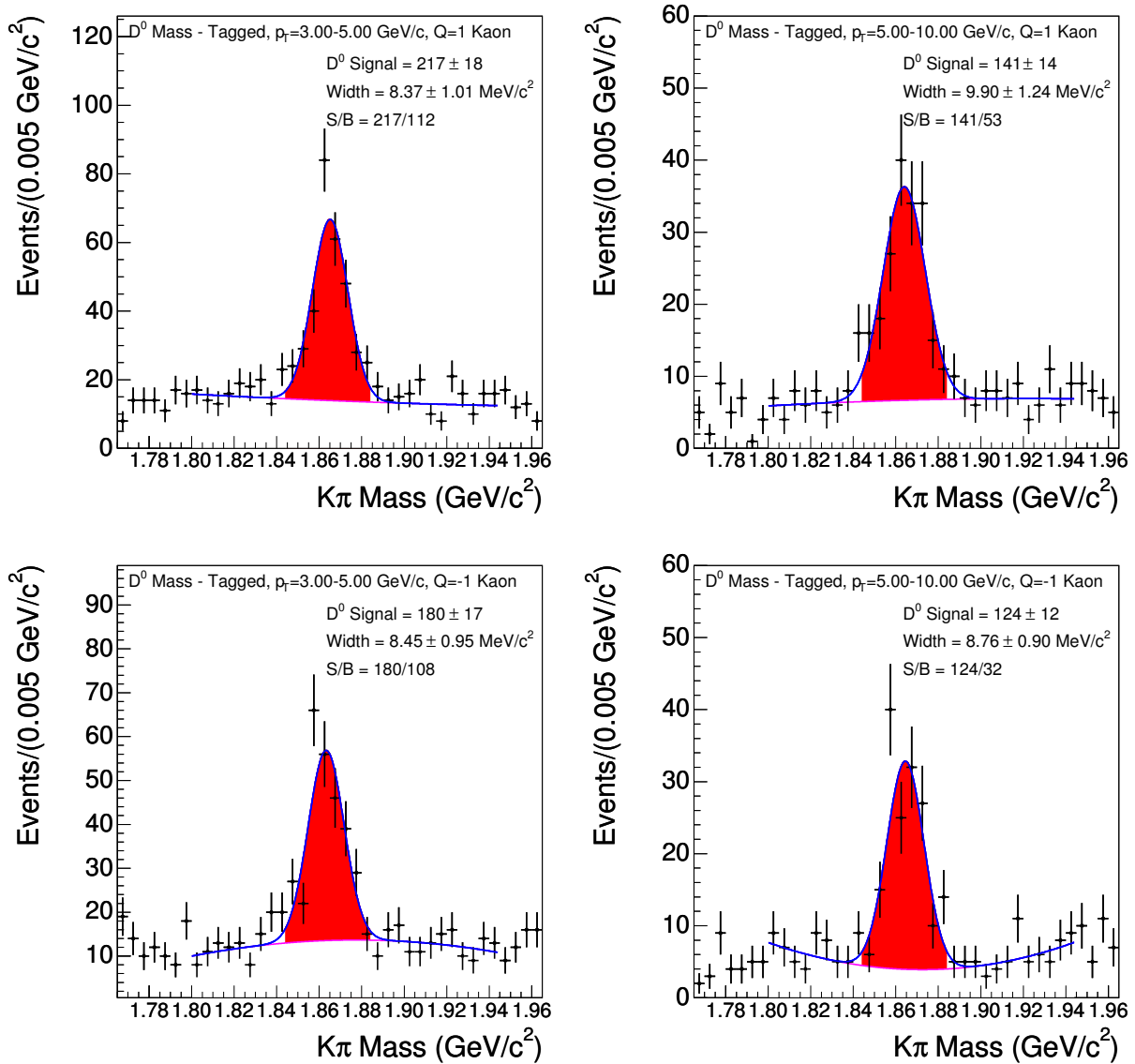


Figure 134: Fitted D^0 mass peaks where the K leg meets the third muon requirements. Broken into p_T and q bins of 3 – 5 GeV/ c and $q = 1$ (top left), > 5 GeV/ c and $q = 1$ (top right), 3 – 5 GeV/ c and $q = -1$ (bottom left), and > 5 GeV/ c and $q = -1$ (bottom right).

D.3 $T_{\pi}^{pull}/Z_{\pi}^{pull}$ FITS FOR THE ELECTRON CHANNEL

The fractional particle composition for third tracks in the electron channel J/ψ +track sample is determined by two dimensional $TOF_{\pi}^{pull}/Z_{\pi}^{pull}$ when the momentum of the third tracks is < 3.0 GeV/ c . For the fits, the events are divided by third track momentum, third track charge, and ct^* of the J/ψ +track system.

The fit projections for positively charged and negatively charged tracks where J/ψ +track $ct^* < 0$ μm are shown in Figures 135 and 136 respectively. The fit projections for positively charged and negatively charged tracks where J/ψ +track $0 < ct^* < 150$ μm are shown in Figures 137 and 138. The fit projections for positively charged and negatively charged tracks where J/ψ +track $ct^* > 150$ μm are shown in Figures 139 and 140.

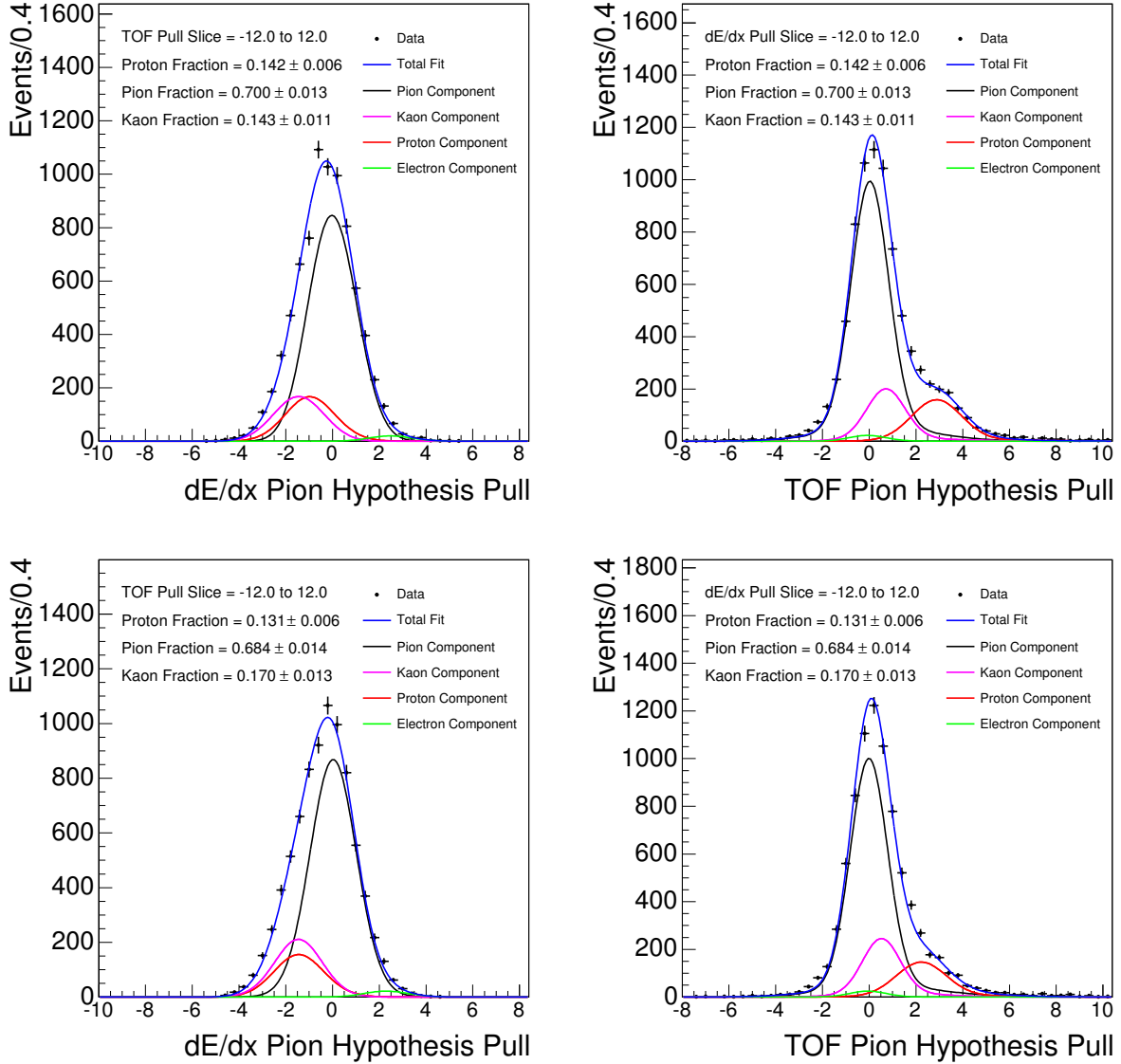


Figure 135: Z_{π}^{pull} (left) and TOF_{π}^{pull} (right) projections of fits of particle fractions in the $p = 2.0 - 2.5 \text{ GeV}/c$ (top) and $p = 2.5 - 3.0 \text{ GeV}/c$ (bottom) momentum bins for positively charged third tracks and $J/\psi + \text{track } ct^* < 0 \mu\text{m}$.

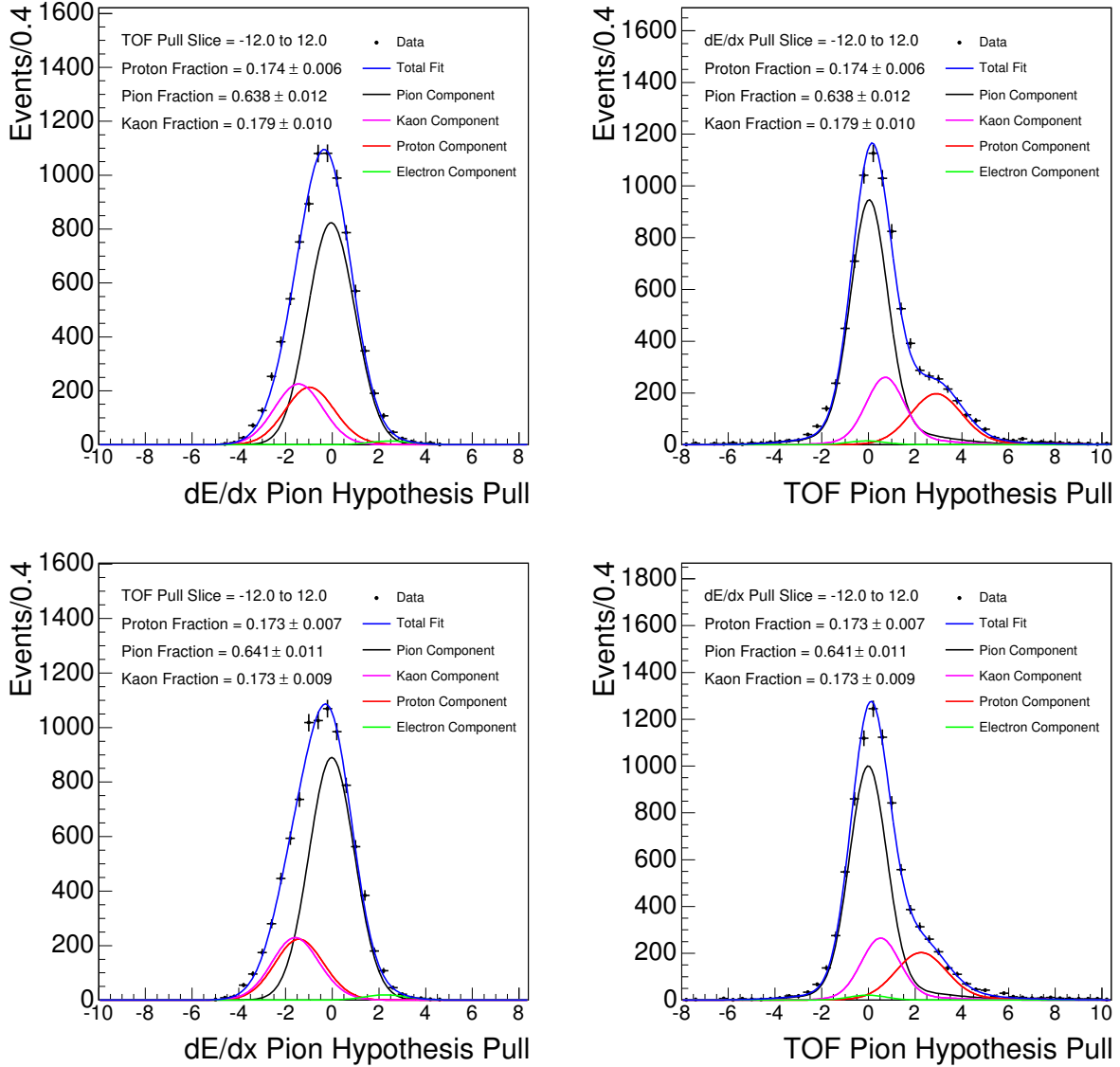


Figure 136: Z_{π}^{pull} (left) and TOF_{π}^{pull} (right) projections of fits of particle fractions in the $p = 2.0 - 2.5 \text{ GeV}/c$ (top) and $p = 2.5 - 3.0 \text{ GeV}/c$ (bottom) momentum bins for negatively charged third tracks and $J/\psi + \text{track } ct^* < 0 \mu\text{m}$.

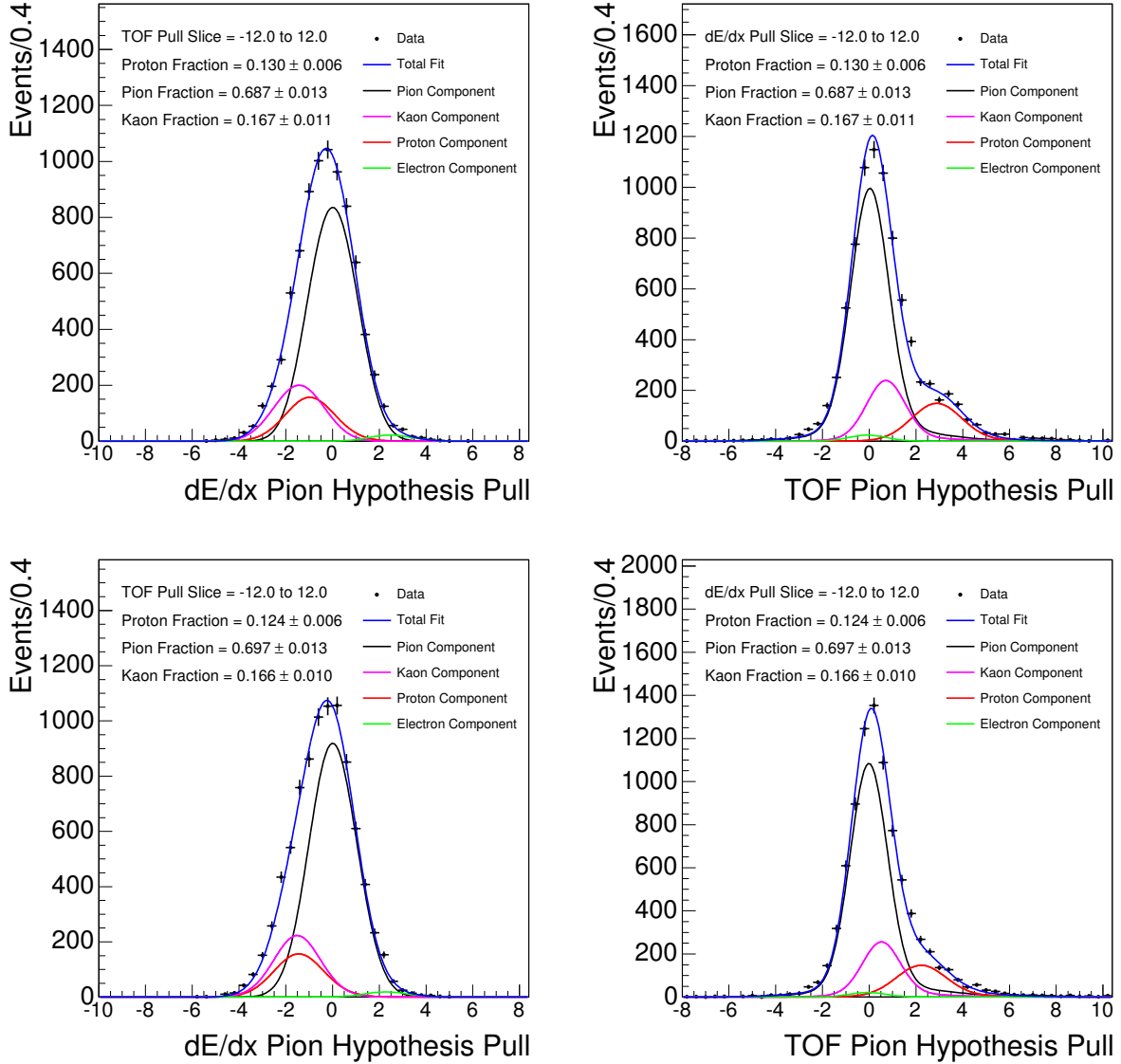


Figure 137: Z_{π}^{pull} (left) and TOF_{π}^{pull} (right) projections of fits of particle fractions in the $p = 2.0 - 2.5 \text{ GeV}/c$ (top) and $p = 2.5 - 3.0 \text{ GeV}/c$ (bottom) momentum bins for positively charged third tracks and $J/\psi + \text{track } 0 < ct^* < 150 \mu\text{m}$.

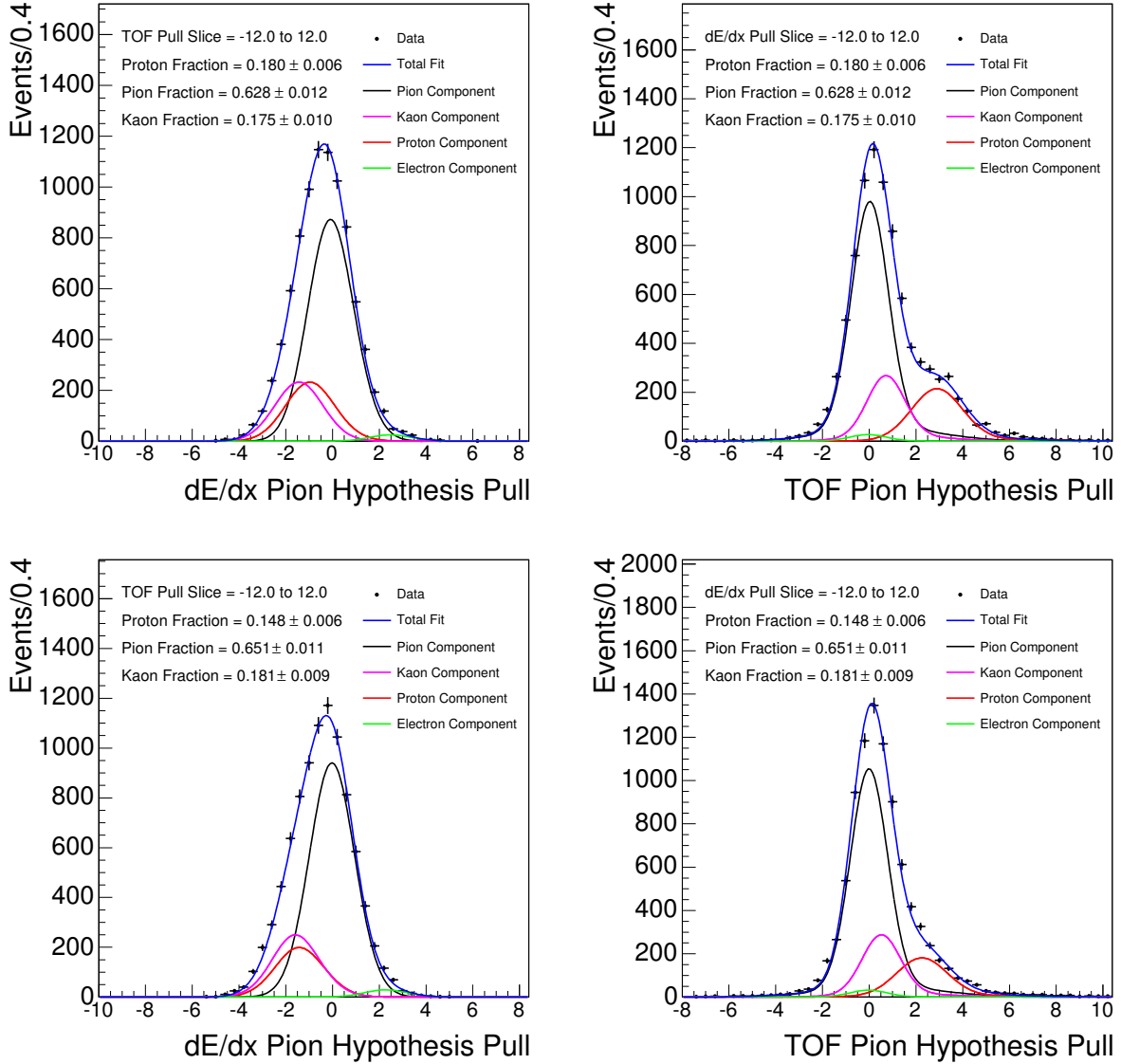


Figure 138: Z_{π}^{pull} (left) and TOF_{π}^{pull} (right) projections of fits of particle fractions in the $p = 2.0 - 2.5$ GeV/c (top) and $p = 2.5 - 3.0$ GeV/c (bottom) momentum bins for negatively charged third tracks and $J/\psi + \text{track } 0 < ct^* < 150 \mu\text{m}$.

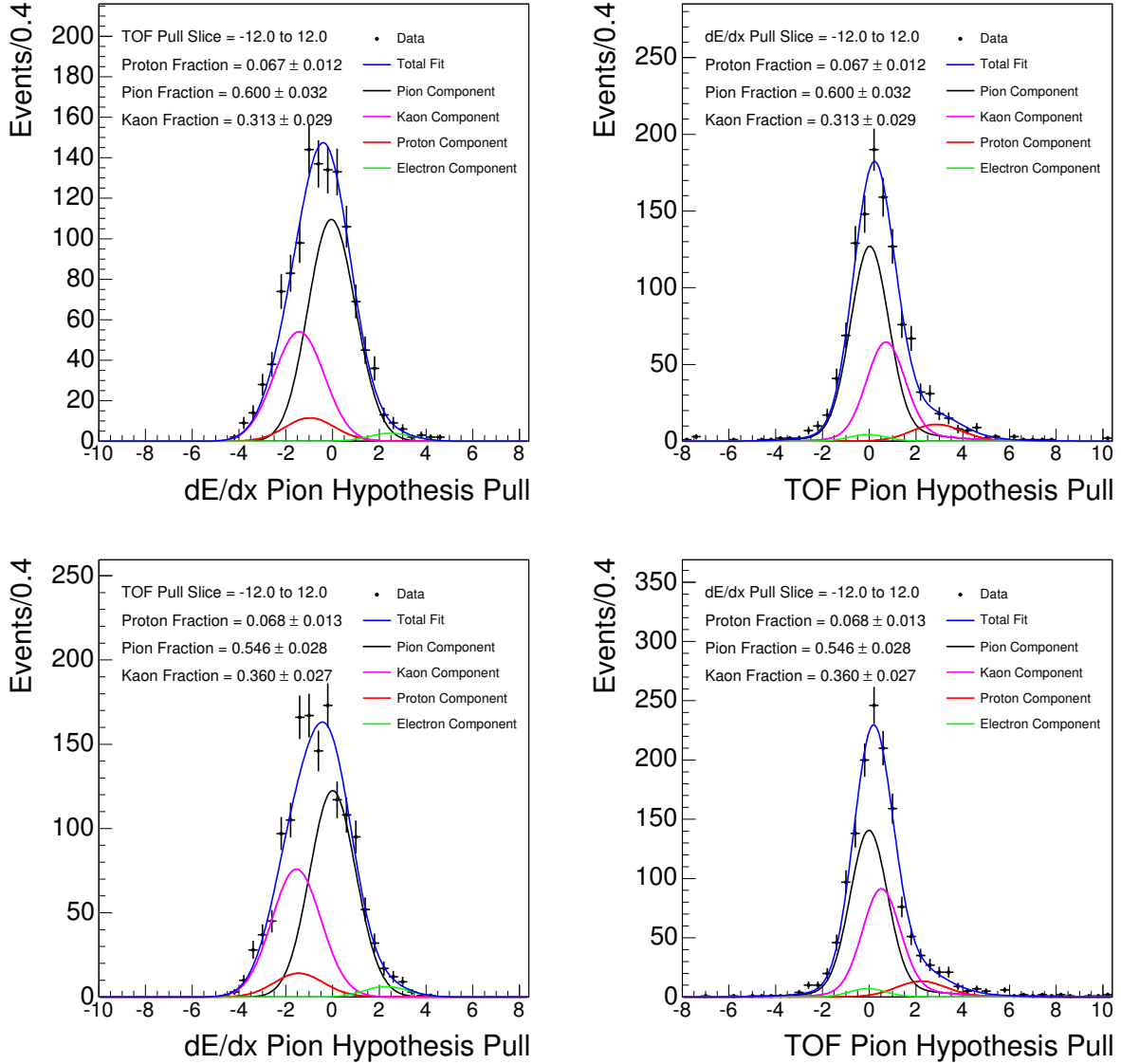


Figure 139: Z_{π}^{pull} (left) and TOF_{π}^{pull} (right) projections of fits of particle fractions in the $p = 2.0 - 2.5$ GeV/c (top) and $p = 2.5 - 3.0$ GeV/c (bottom) momentum bins for positively charged third tracks and $J/\psi + \text{track } ct^* > 150 \mu\text{m}$.

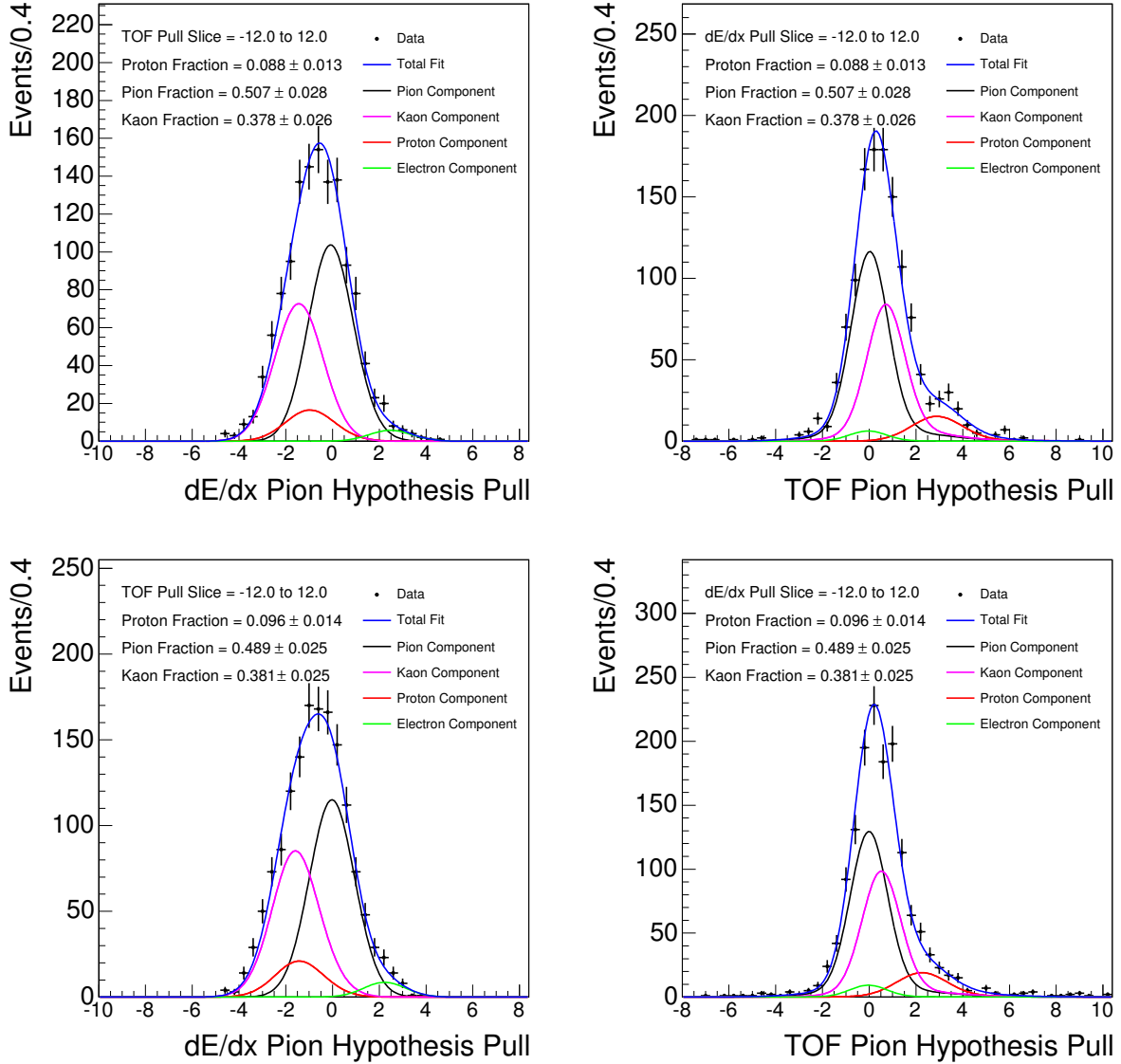


Figure 140: Z_{π}^{pull} (left) and TOF_{π}^{pull} (right) projections of fits of particle fractions in the $p = 2.0 - 2.5 \text{ GeV}/c$ (top) and $p = 2.5 - 3.0 \text{ GeV}/c$ (bottom) momentum bins for negatively charged third tracks and $J/\psi + \text{track } ct^* > 150 \mu\text{m}$.

D.4 $T_{\pi}^{pull}/Z_{\pi}^{pull}$ FITS FOR THE MUON CHANNEL

The fractional particle composition for third tracks in the muon channel J/ψ +track sample is determined by two dimensional $TOF_{\pi}^{pull}/Z_{\pi}^{pull}$ in a similar fashion to the electron channel sample. In the case of the muon channel, the fitted fractions are not used directions, but as a basis for extrapolation the proton fractions to the regions where the third track momentum is $> 3.0 \text{ GeV}/c$.

For J/ψ +track $ct^* < 0 \mu\text{m}$, the fit projections positively charged tracks are shown in Figures 141 and 142, and the fit projections for negatively charged tracks are shown in Figures 143 and 144. For J/ψ +track $0 < ct^* < 150 \mu\text{m}$, the fit projections positively charged tracks are shown in Figures 145 and 146, and the fit projections for negatively charged tracks are shown in Figures 147 and 148. For J/ψ +track $ct^* > 150 \mu\text{m}$, the fit projections positively charged tracks are shown in Figures 149 and 150, and the fit projections for negatively charged tracks are shown in Figures 151 and 152. The proton fractions for the three ct^* regions and their dependence on the third track momentum are summarized in Figure 153.

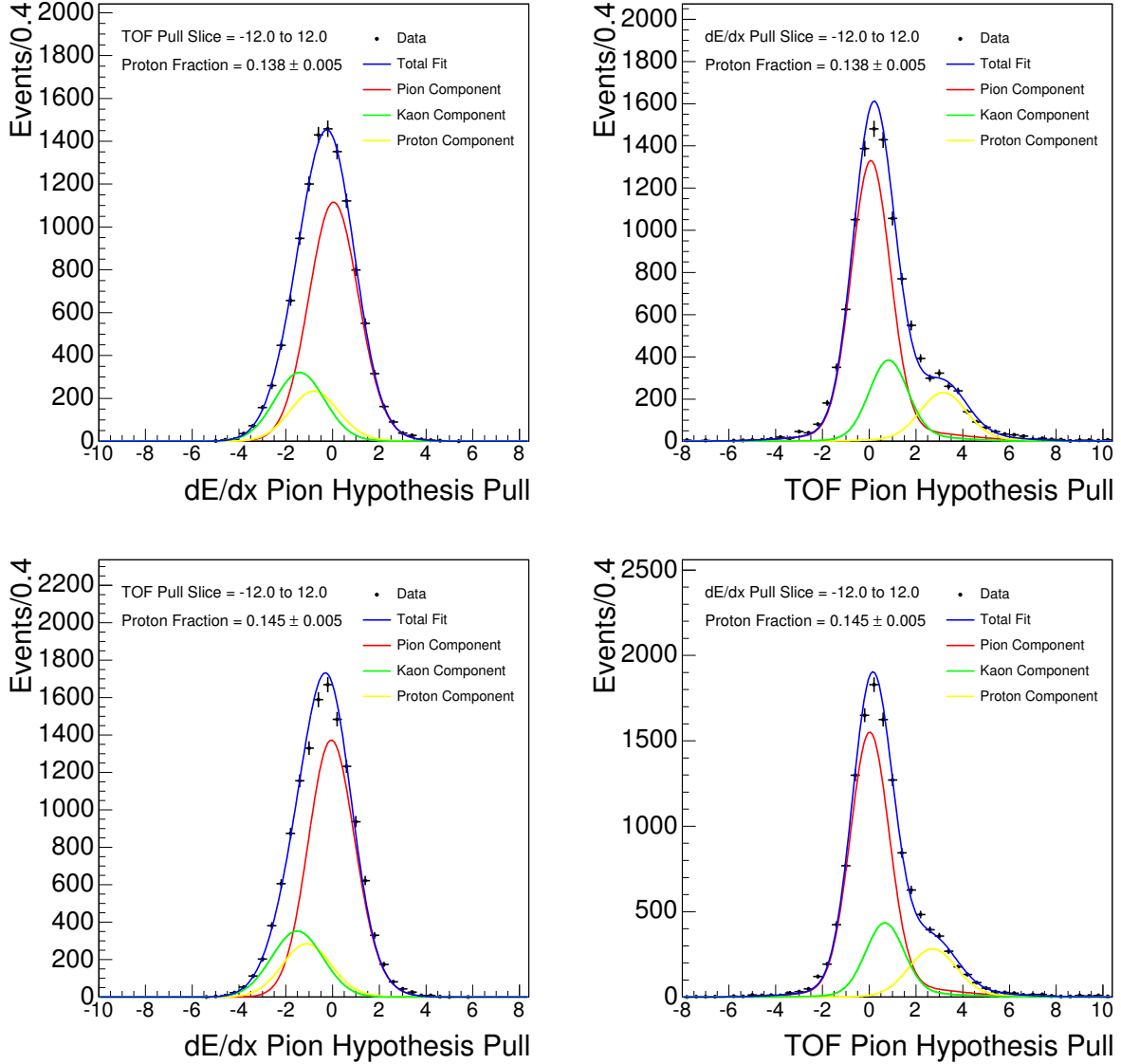


Figure 141: Z_{π}^{pull} (left) and TOF_{π}^{pull} (right) projections of fits of particle fractions in the $p = 2.0 - 2.25$ GeV/c (top) and $p = 2.25 - 2.5$ GeV/c (bottom) momentum bins for positively charged third tracks and $J/\psi + \text{track } ct^* < 0 \mu\text{m}$.

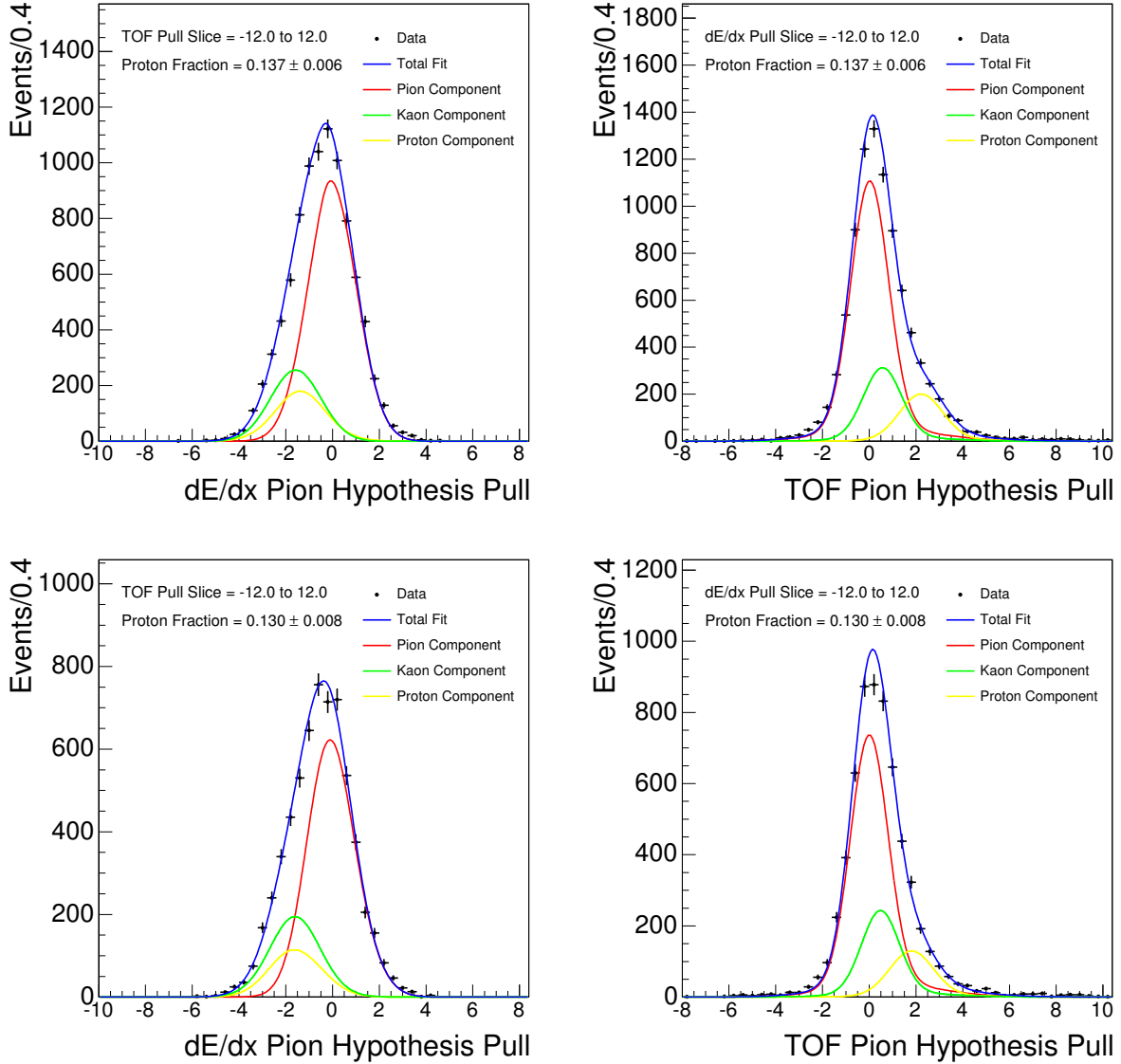


Figure 142: Z_{π}^{pull} (left) and TOF_{π}^{pull} (right) projections of fits of particle fractions in the $p = 2.5 - 2.75$ GeV/c (top) and $p = 2.75 - 3.0$ GeV/c (bottom) momentum bins for positively charged third tracks and $J/\psi + \text{track } ct^* < 0 \mu\text{m}$.

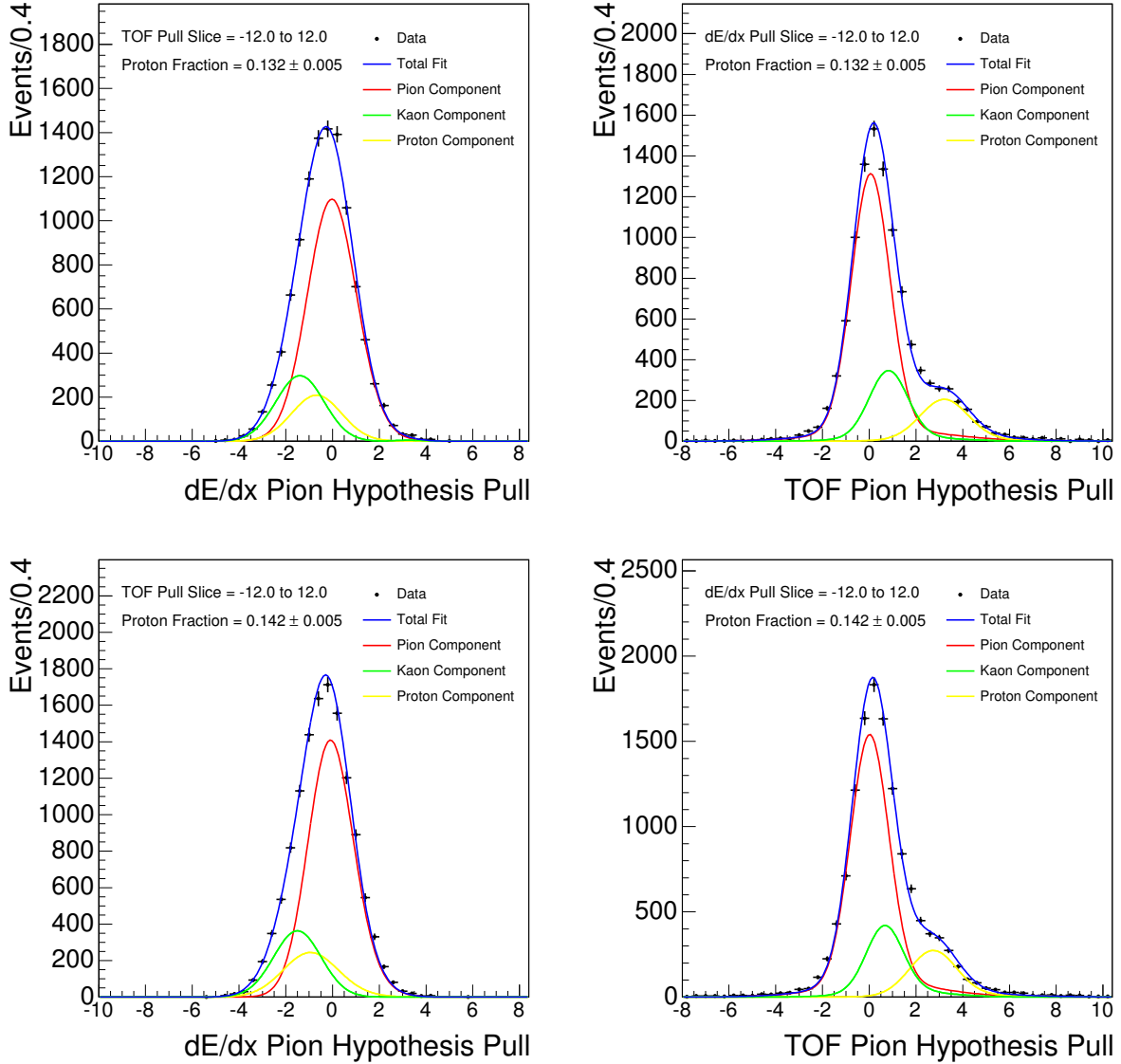


Figure 143: Z_{π}^{pull} (left) and TOF_{π}^{pull} (right) projections of fits of particle fractions in the $p = 2.0 - 2.25$ GeV/c (top) and $p = 2.25 - 2.5$ GeV/c (bottom) momentum bins for negatively charged third tracks and $J/\psi + \text{track } ct^* < 0 \mu\text{m}$.

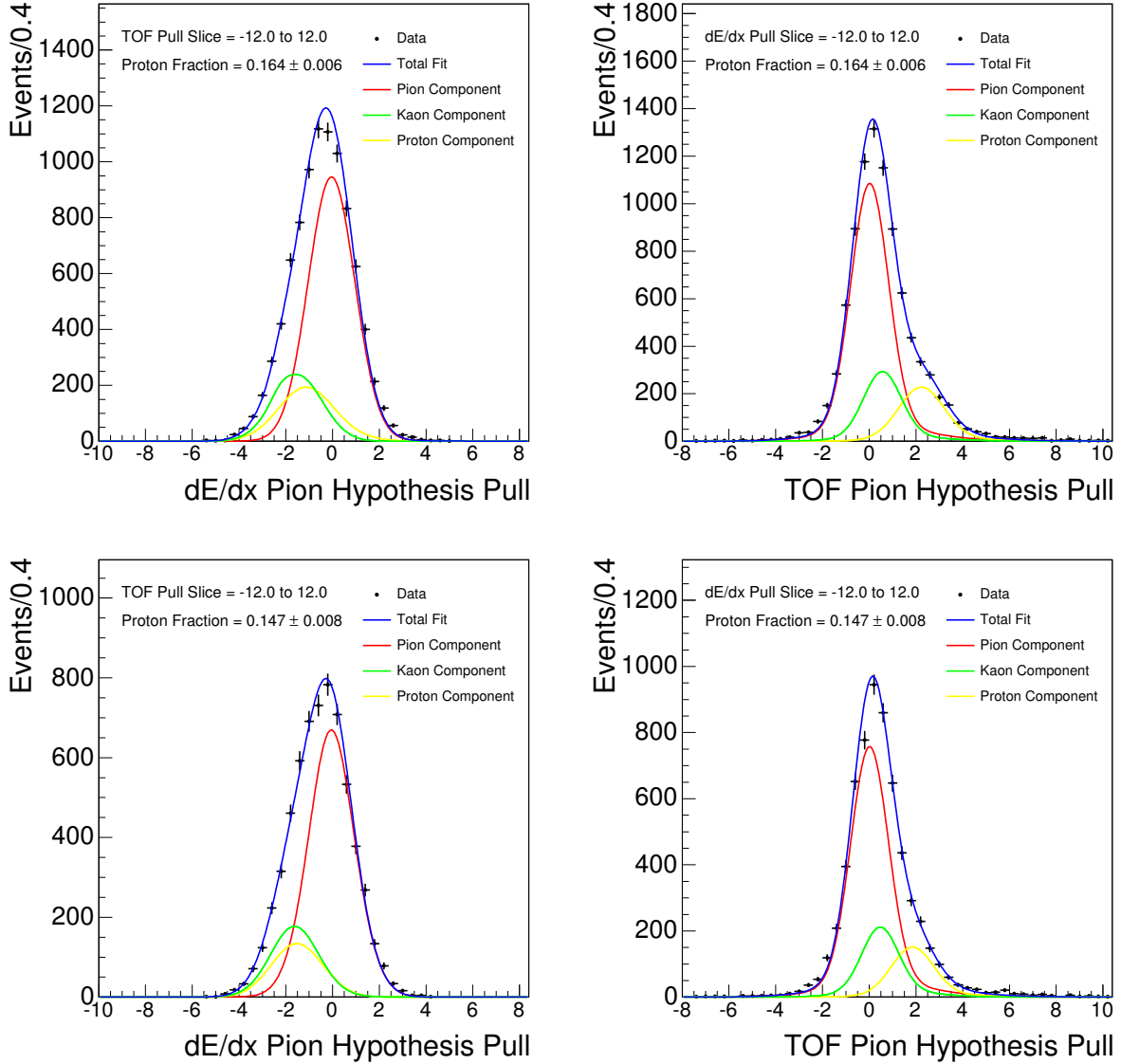


Figure 144: Z_{π}^{pull} (left) and TOF_{π}^{pull} (right) projections of fits of particle fractions in the $p = 2.5 - 2.75$ GeV/c (top) and $p = 2.75 - 3.0$ GeV/c (bottom) momentum bins for negatively charged third tracks and $J/\psi + \text{track } ct^* < 0 \mu\text{m}$.

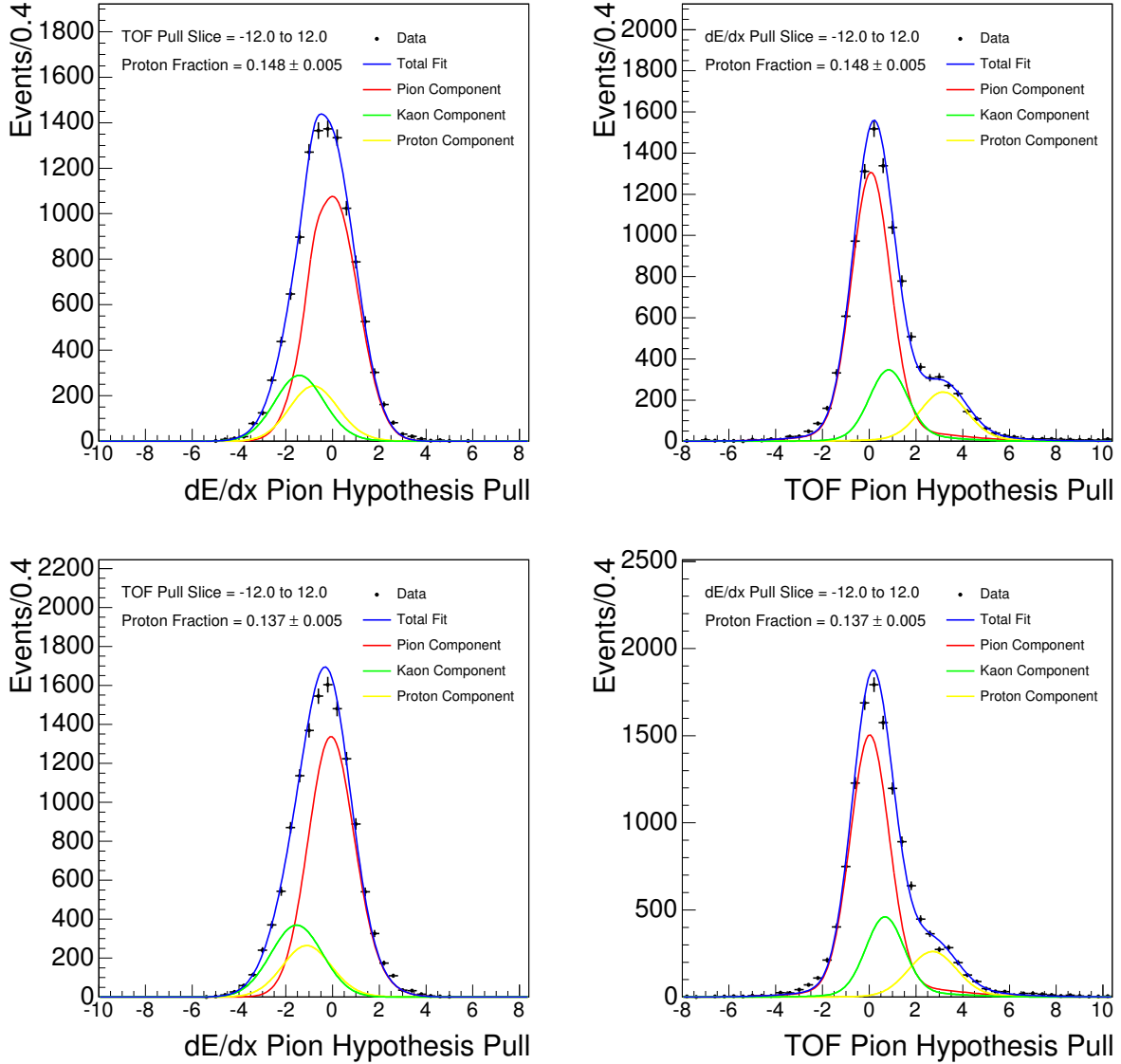


Figure 145: Z_{π}^{pull} (left) and TOF_{π}^{pull} (right) projections of fits of particle fractions in the $p = 2.0 - 2.25$ GeV/c (top) and $p = 2.25 - 2.5$ GeV/c (bottom) momentum bins for positively charged third tracks and $J/\psi + \text{track } 0 < ct^* < 150 \mu\text{m}$.

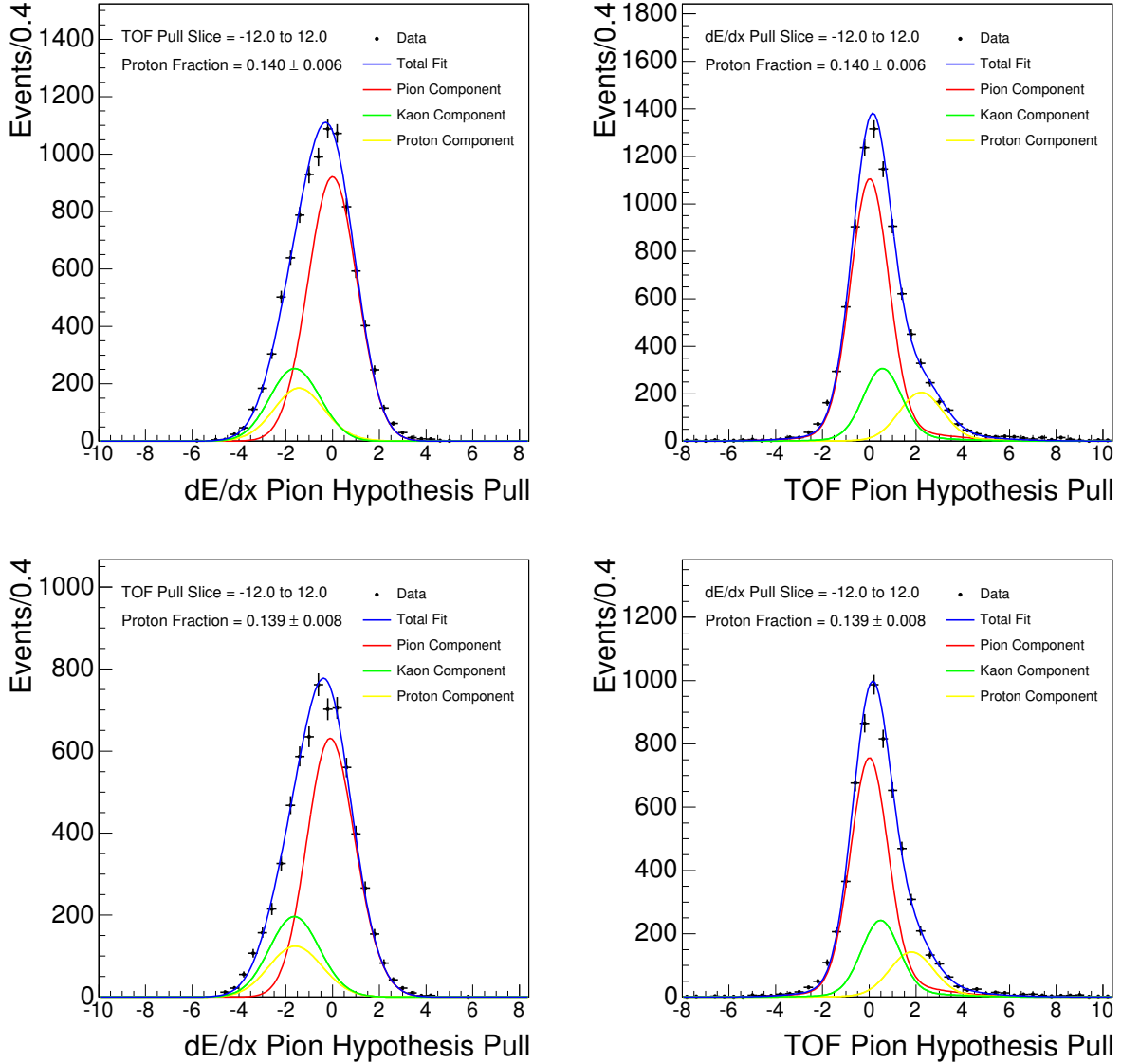


Figure 146: Z_{π}^{pull} (left) and TOF_{π}^{pull} (right) projections of fits of particle fractions in the $p = 2.5 - 2.75$ GeV/c (top) and $p = 2.75 - 3.0$ GeV/c (bottom) momentum bins for positively charged third tracks and $J/\psi + \text{track } 0 < ct^* < 150 \mu\text{m}$.

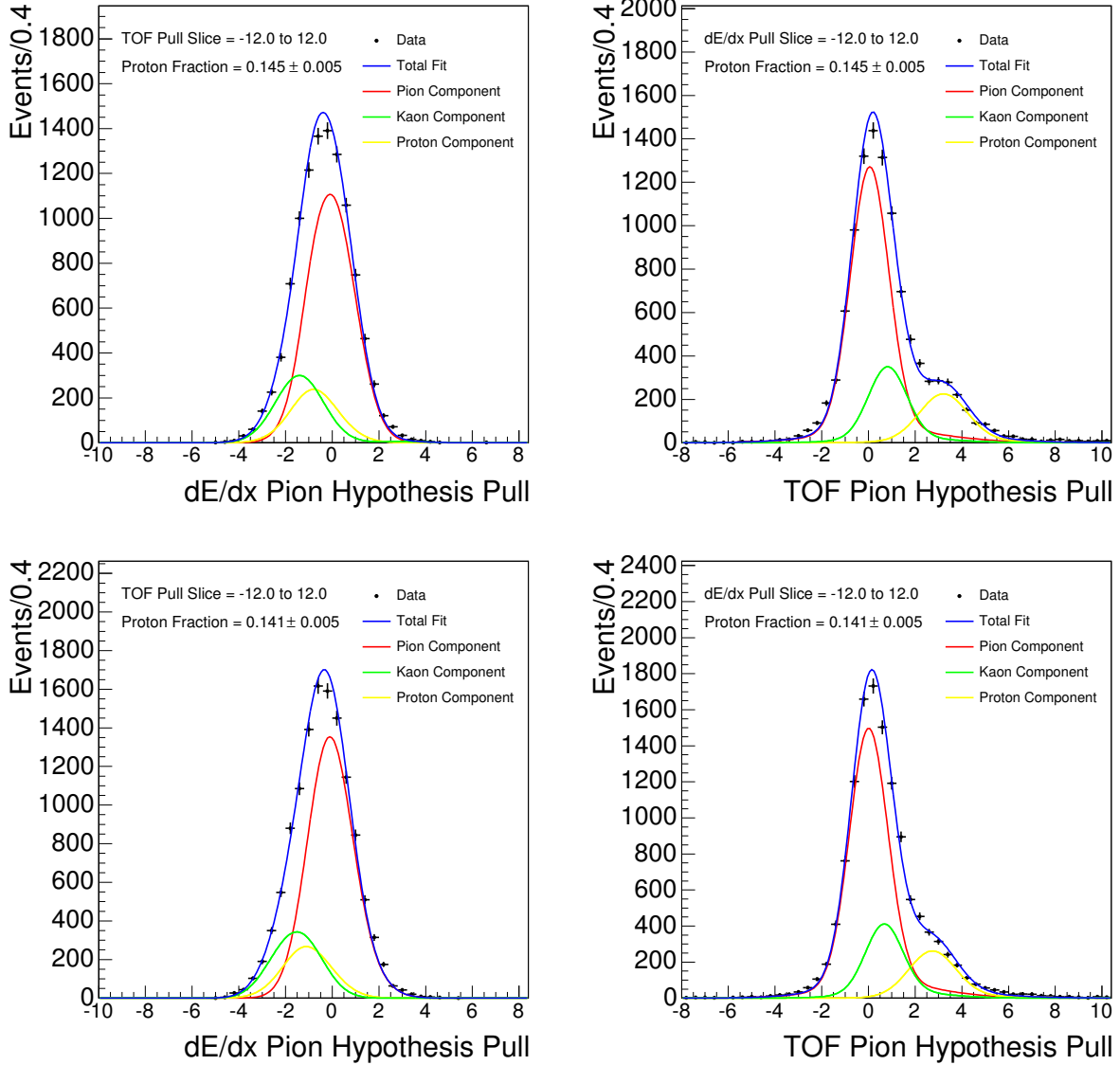


Figure 147: Z_{π}^{pull} (left) and TOF_{π}^{pull} (right) projections of fits of particle fractions in the $p = 2.0 - 2.25$ GeV/c (top) and $p = 2.25 - 2.5$ GeV/c (bottom) momentum bins for negatively charged third tracks and $J/\psi + \text{track } 0 < ct^* < 150 \mu\text{m}$.

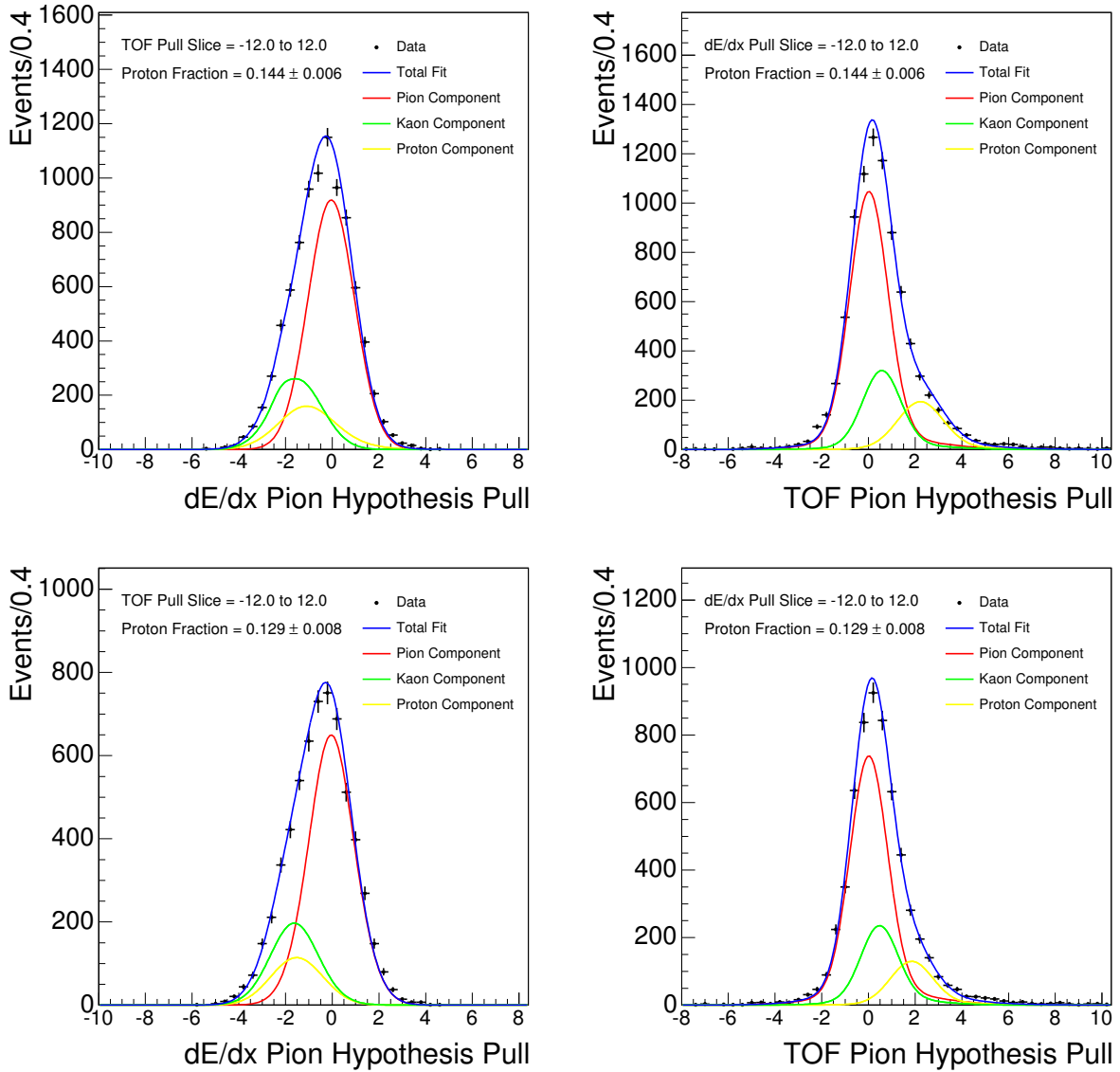


Figure 148: Z_{π}^{pull} (left) and TOF_{π}^{pull} (right) projections of fits of particle fractions in the $p = 2.5 - 2.75$ GeV/c (top) and $p = 2.75 - 3.0$ GeV/c (bottom) momentum bins for negatively charged third tracks and $J/\psi + \text{track } 0 < ct^* < 150 \mu\text{m}$.

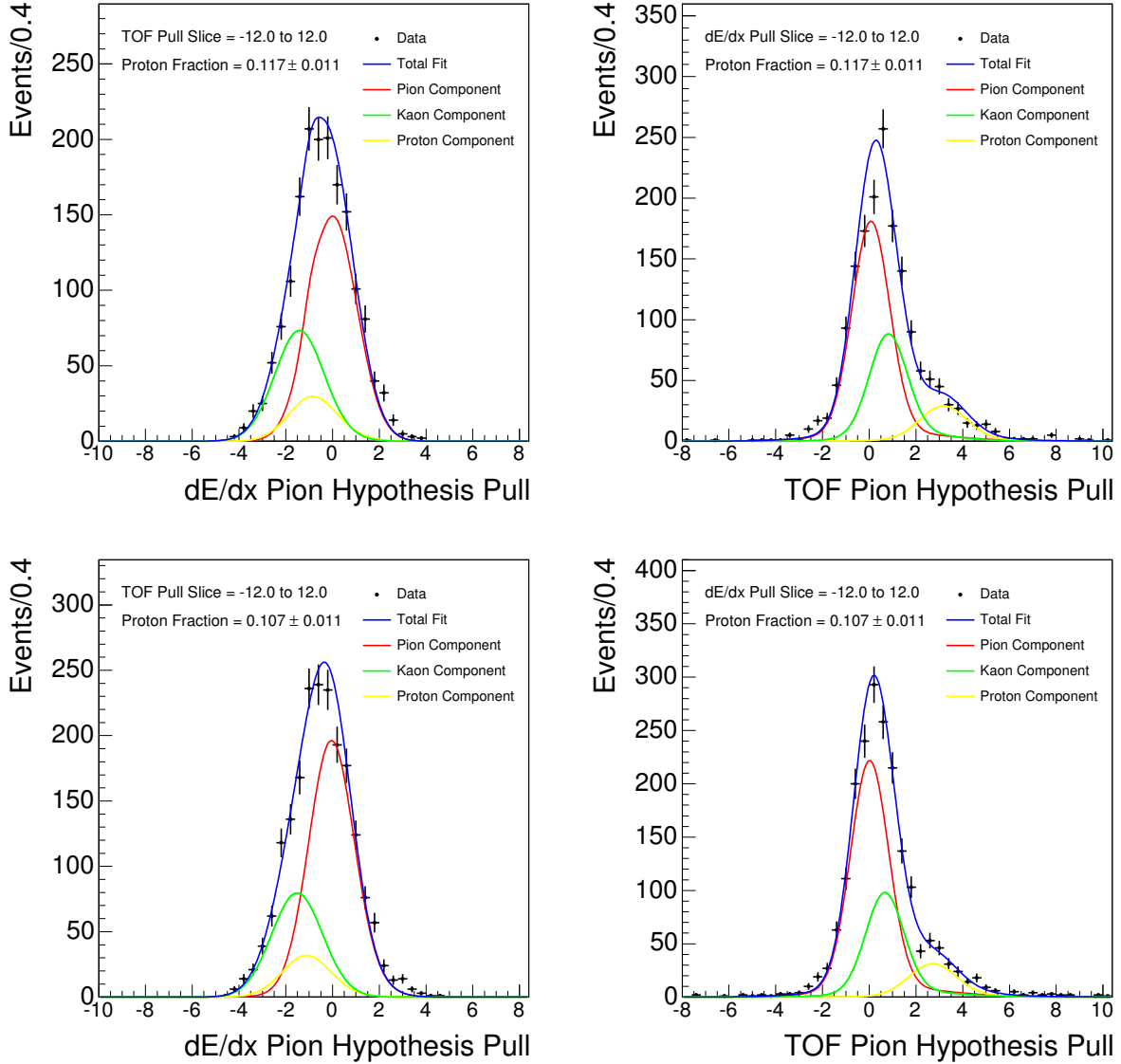


Figure 149: Z_{π}^{pull} (left) and TOF_{π}^{pull} (right) projections of fits of particle fractions in the $p = 2.0 - 2.25$ GeV/c (top) and $p = 2.25 - 2.5$ GeV/c (bottom) momentum bins for positively charged third tracks and $J/\psi + \text{track } ct^* > 150 \mu\text{m}$.

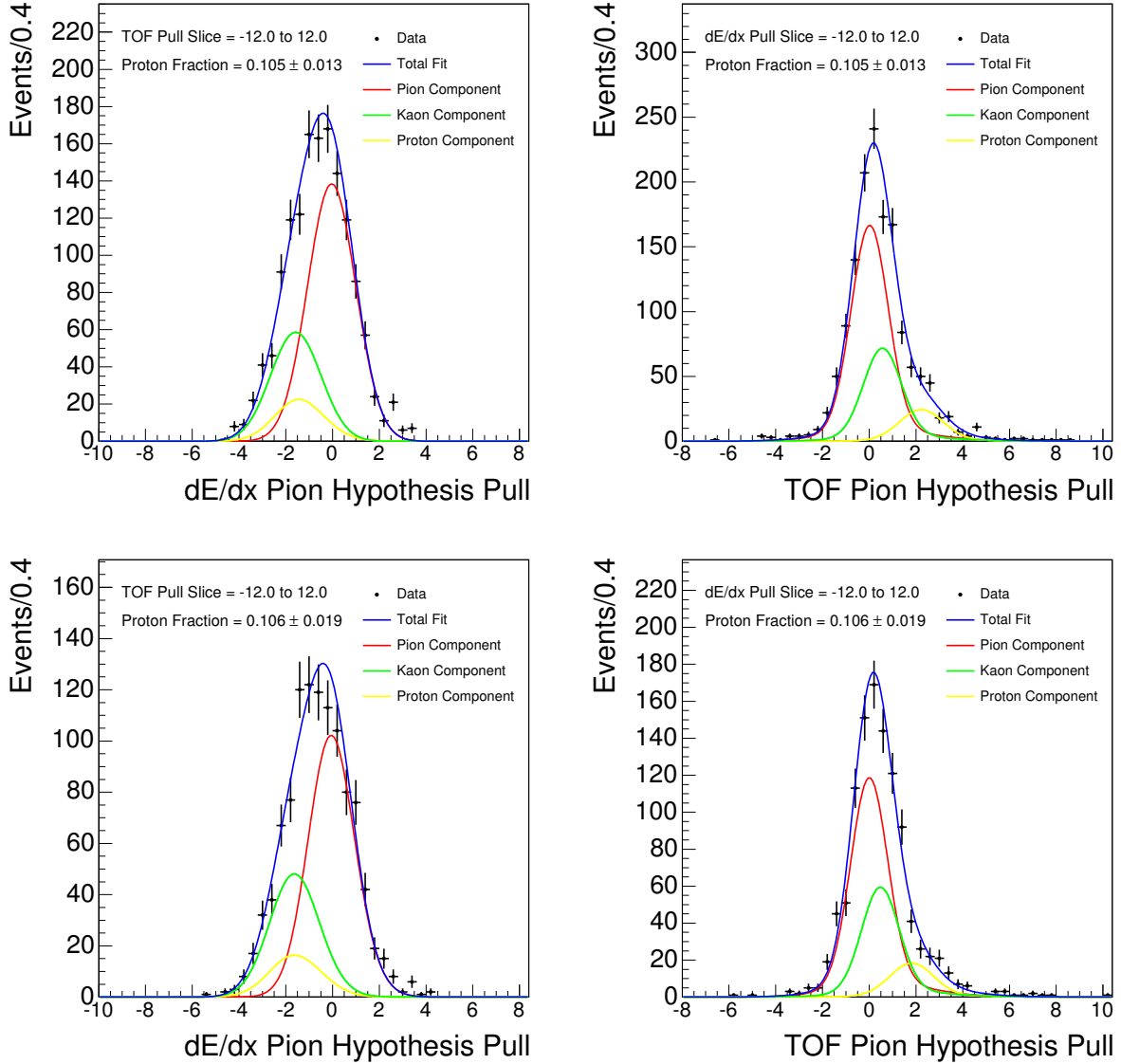


Figure 150: Z_{π}^{pull} (left) and TOF_{π}^{pull} (right) projections of fits of particle fractions in the $p = 2.5 - 2.75$ GeV/c (top) and $p = 2.75 - 3.0$ GeV/c (bottom) momentum bins for positively charged third tracks and $J/\psi + \text{track } ct^* > 150 \mu\text{m}$.

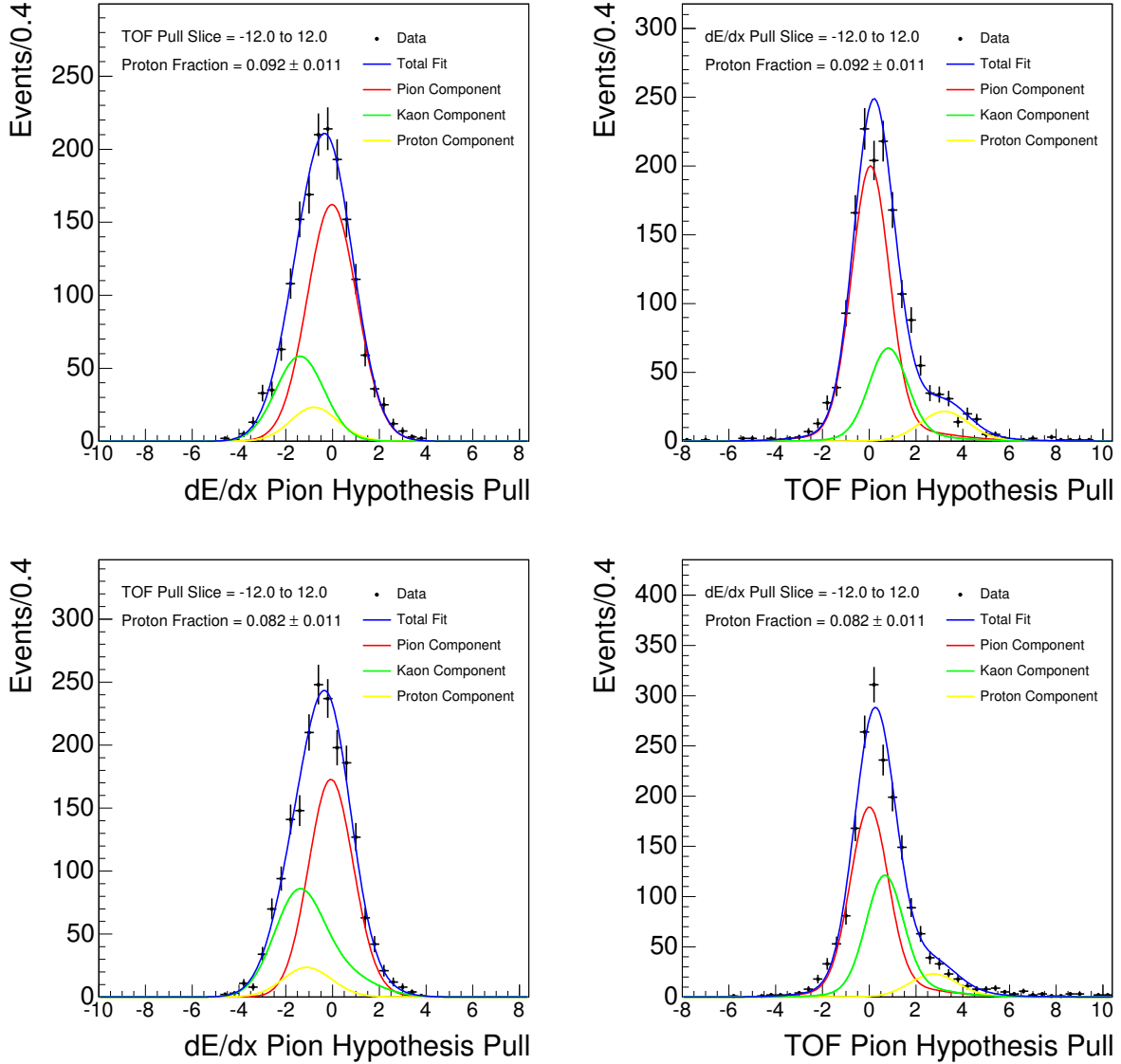


Figure 151: Z_{π}^{pull} (left) and TOF_{π}^{pull} (right) projections of fits of particle fractions in the $p = 2.0 - 2.25$ GeV/c (top) and $p = 2.25 - 2.5$ GeV/c (bottom) momentum bins for negatively charged third tracks and $J/\psi + \text{track } ct^* > 150 \mu\text{m}$.

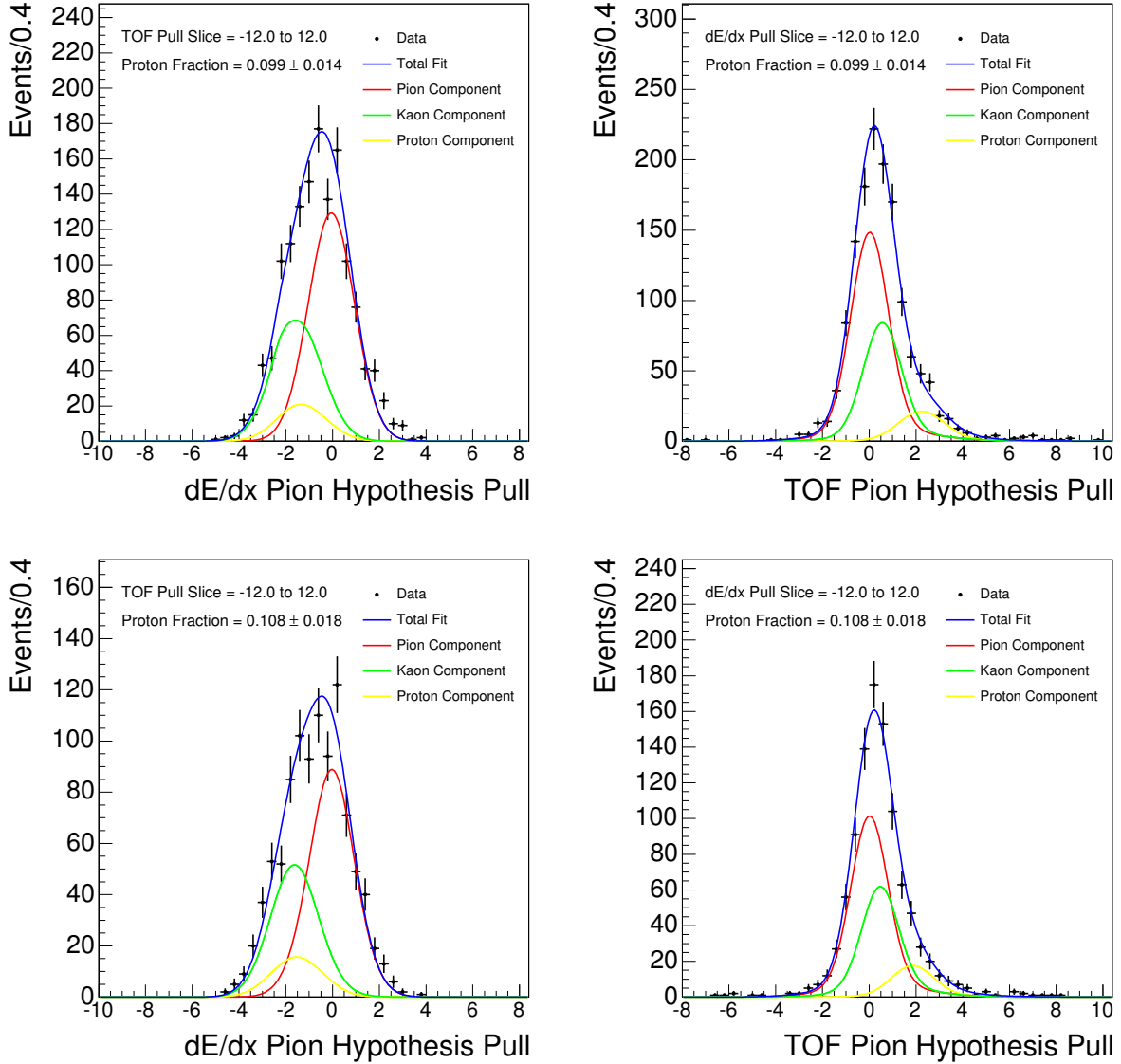


Figure 152: Z_{π}^{pull} (left) and TOF_{π}^{pull} (right) projections of fits of particle fractions in the $p = 2.5 - 2.75$ GeV/c (top) and $p = 2.75 - 3.0$ GeV/c (bottom) momentum bins for negatively charged third tracks and $J/\psi + \text{track } ct^* > 150 \mu\text{m}$.

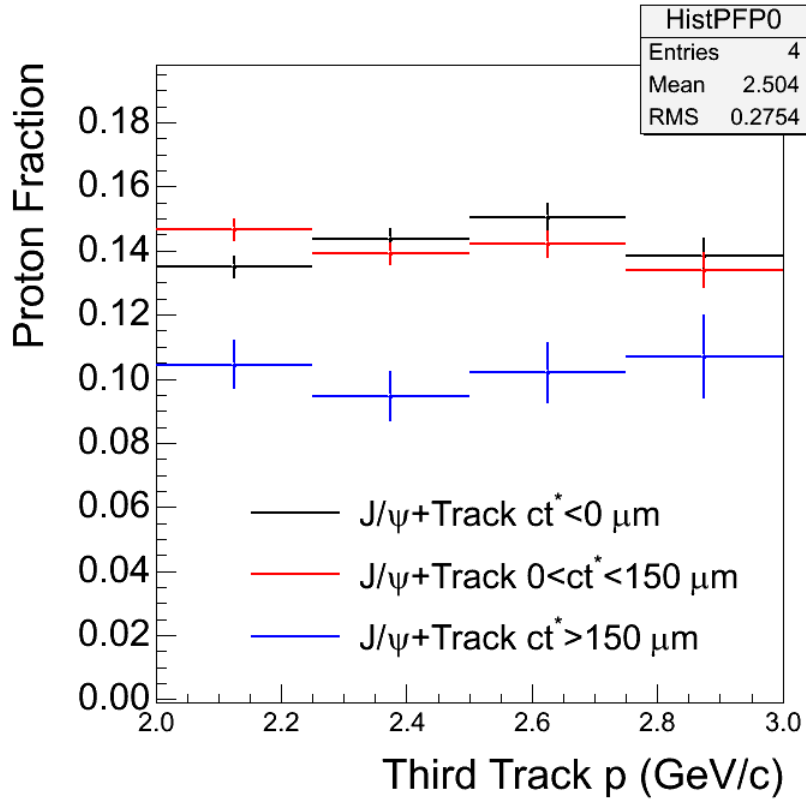


Figure 153: The fraction of $p = 2 - 3 \text{ GeV}/c$ third tracks that are protons for the muon channel $J/\psi + \text{track}$ sample.

D.5 Z_{π}^{pull} FITS FOR THE ELECTRON CHANNEL

The fractional particle composition for third tracks in the electron channel J/ψ +track sample is determined by Z_{π}^{pull} fits when the momentum of the third tracks is $> 3.0 \text{ GeV}/c$. For the fits, the events are divided by third track momentum, third track charge, and ct^* of the J/ψ +track system.

The fit projections for positively charged and negatively charged tracks where J/ψ +track $ct^* < 0 \text{ } \mu\text{m}$ are shown in Figures 154 and 155 respectively. The fit projections for positively charged and negatively charged tracks where J/ψ +track $0 < ct^* < 150 \text{ } \mu\text{m}$ are shown in Figures 156 and 157. The fit projections for positively charged and negatively charged tracks where J/ψ +track $ct^* > 150 \text{ } \mu\text{m}$ are shown in Figures 158 and 159.

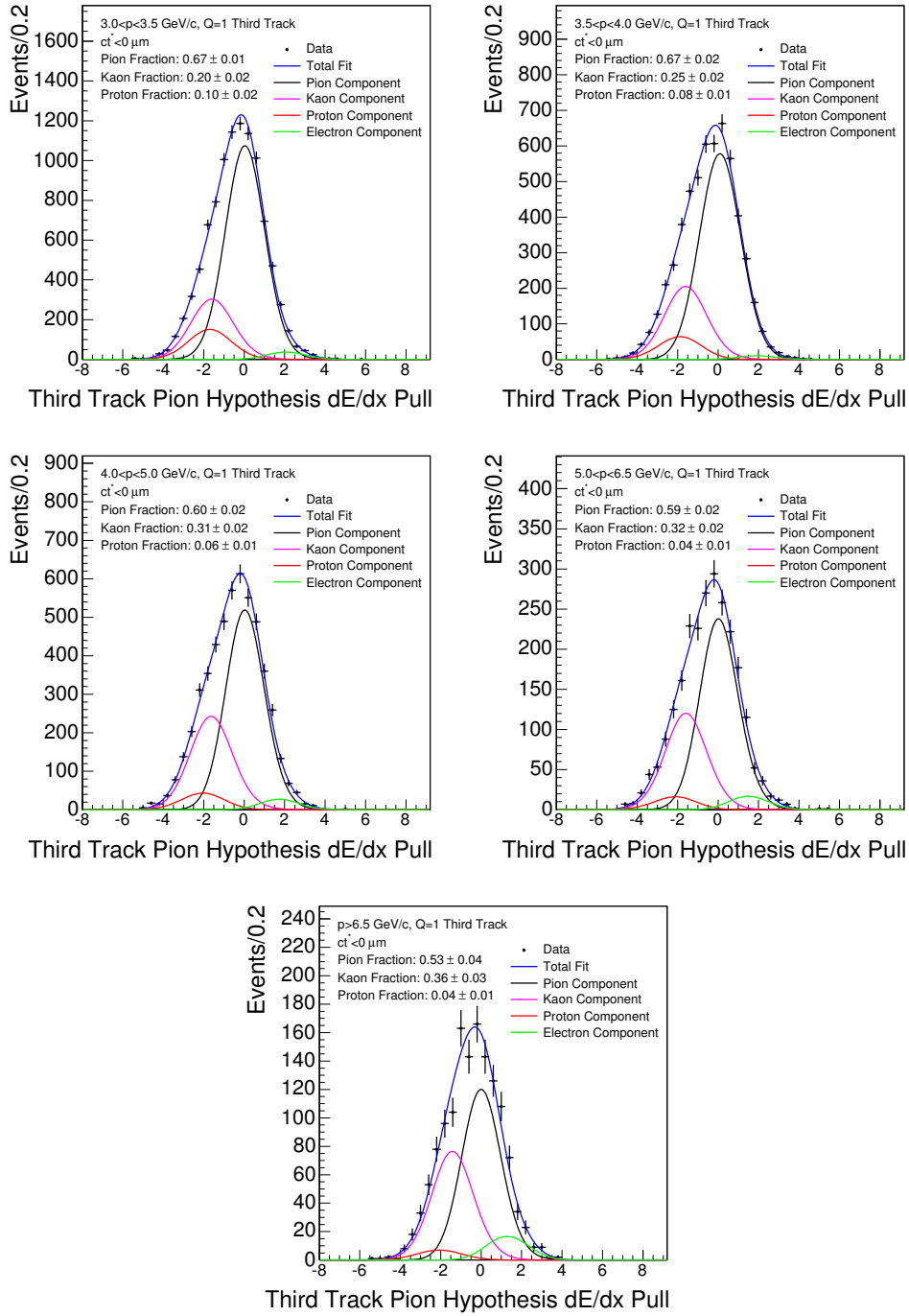


Figure 154: Fitted Z_{π}^{pull} distributions for $q = 1$ and $J/\psi + track ct^* < 0 \mu\text{m}$. Broken into third track momentum bins of 3.0–3.5 GeV/c (top left), 3.5–4.0 GeV/c (top right), 4.0–5.0 GeV/c (middle left), 5.0–6.5 GeV/c (middle right), and > 6.5 GeV/c (bottom).

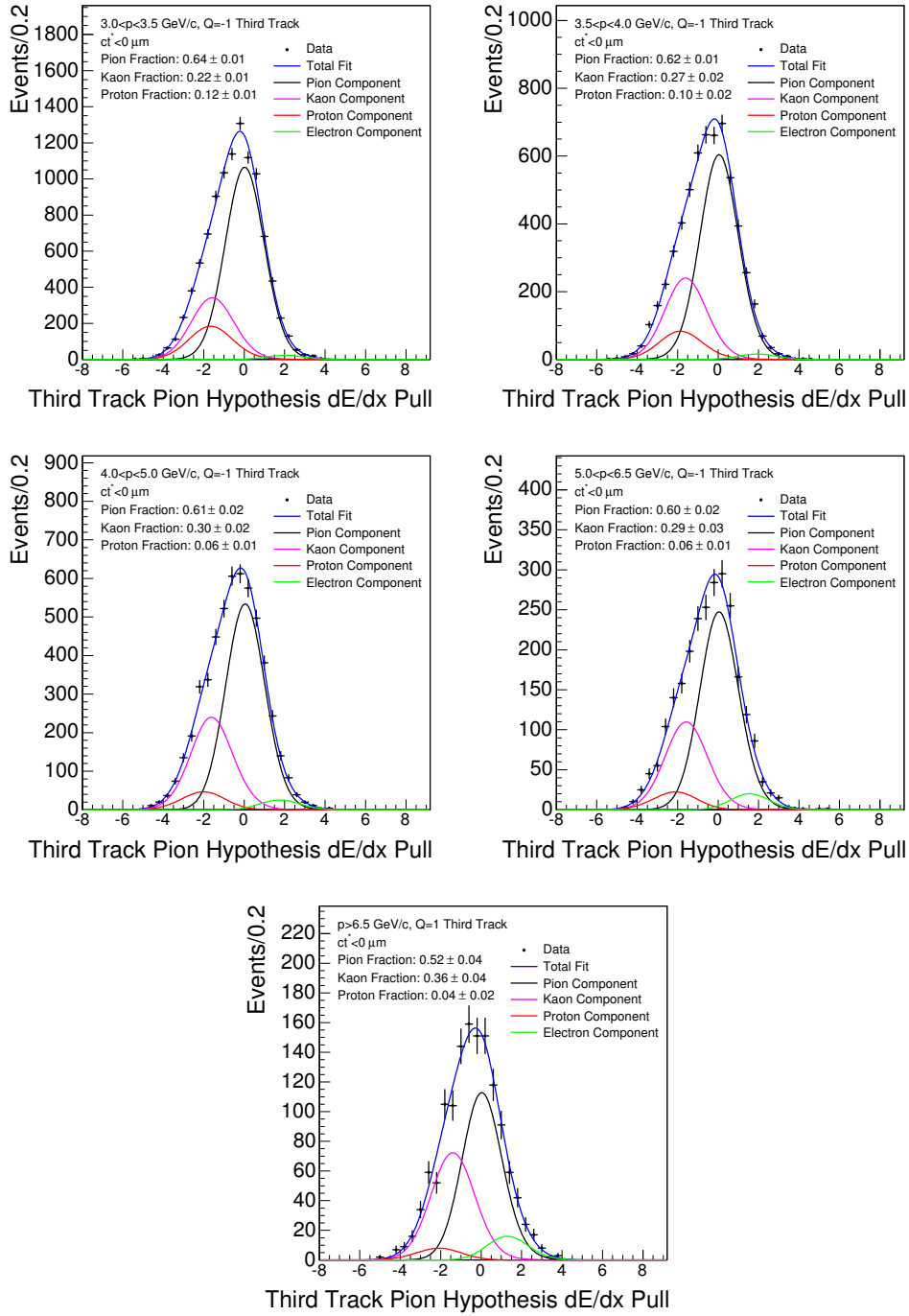


Figure 155: Fitted Z_{π}^{pull} distributions for $q = -1$ and $J/\psi + track ct^* < 0 \mu\text{m}$. Broken into third track momentum bins of 3.0 – 3.5 GeV/c (top left), 3.5 – 4.0 GeV/c (top right), 4.0 – 5.0 GeV/c (middle left), 5.0 – 6.5 GeV/c (middle right), and > 6.5 GeV/c (bottom).

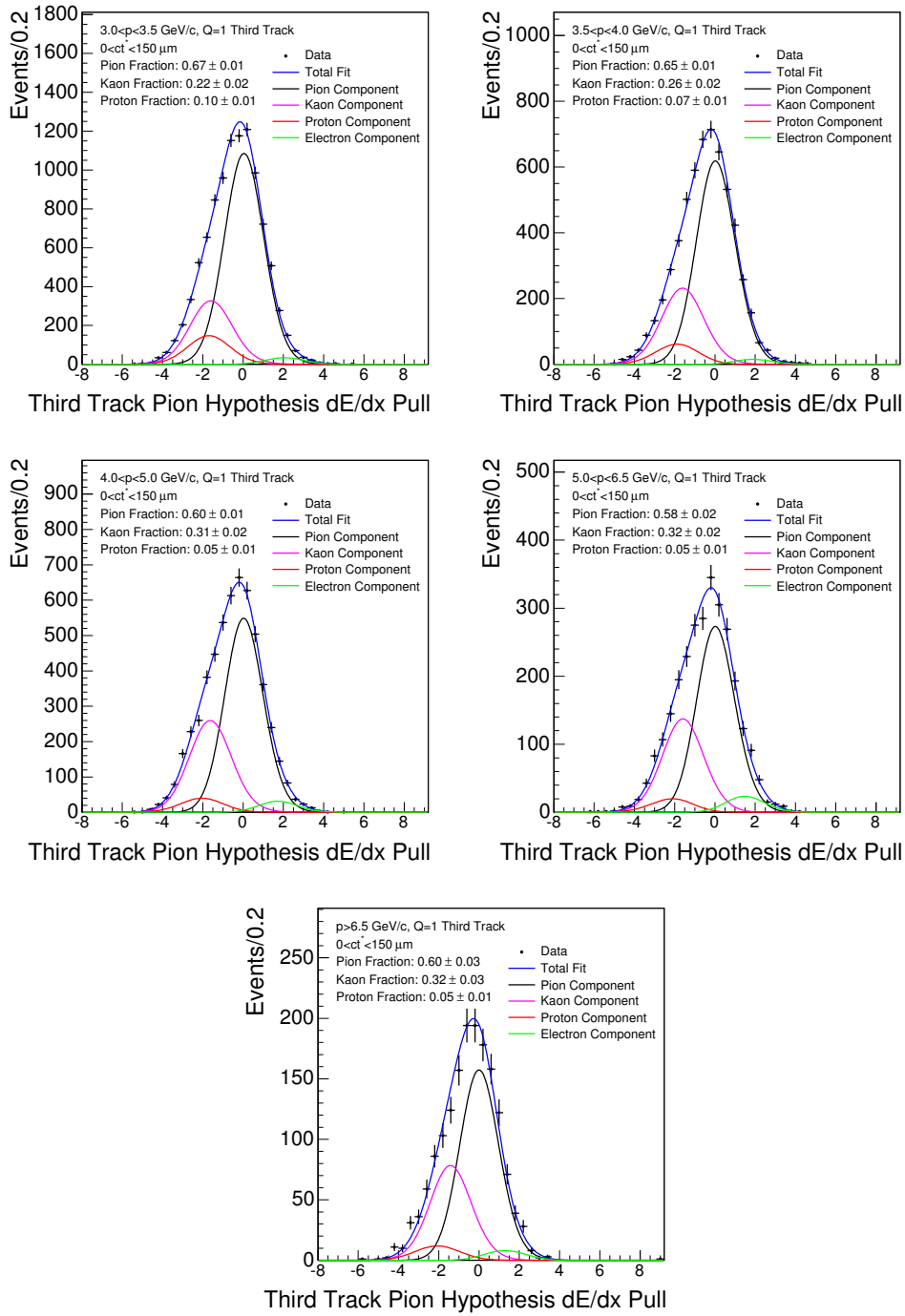


Figure 156: Fitted Z_{π}^{pull} distributions for $q = 1$ and $J/\psi + track\ 0 < ct^* < 150\ \mu\text{m}$. Broken into third track momentum bins of 3.0 – 3.5 GeV/c (top left), 3.5 – 4.0 GeV/c (top right), 4.0 – 5.0 GeV/c (middle left), 5.0 – 6.5 GeV/c (middle right), and > 6.5 GeV/c (bottom).

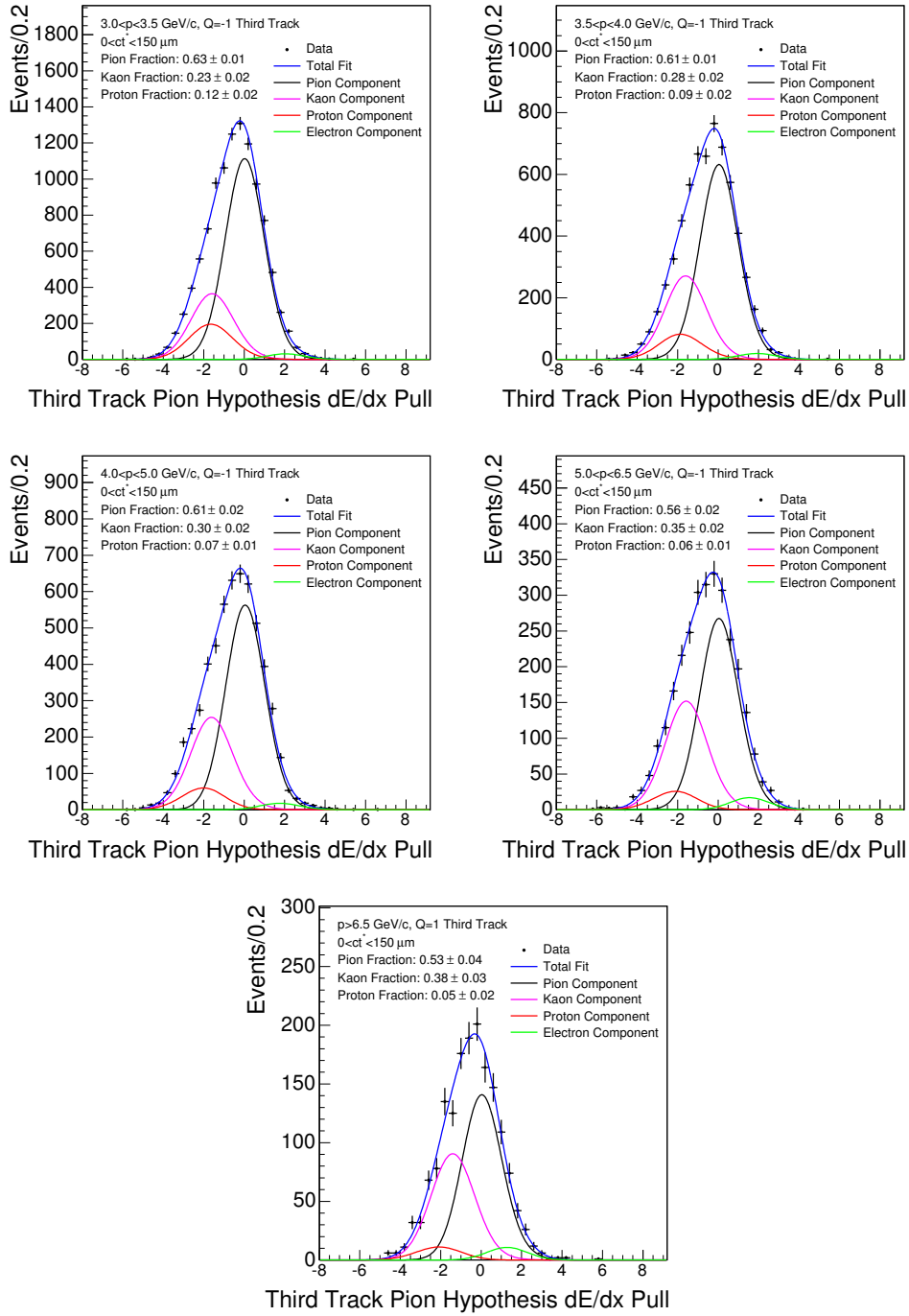


Figure 157: Fitted Z_{π}^{pull} distributions for $q = -1$ and $J/\psi + track$ $0 < ct^* < 150 \mu\text{m}$. Broken into third track momentum bins of 3.0 – 3.5 GeV/c (top left), 3.5 – 4.0 GeV/c (top right), 4.0 – 5.0 GeV/c (middle left), 5.0 – 6.5 GeV/c (middle right), and > 6.5 GeV/c (bottom).

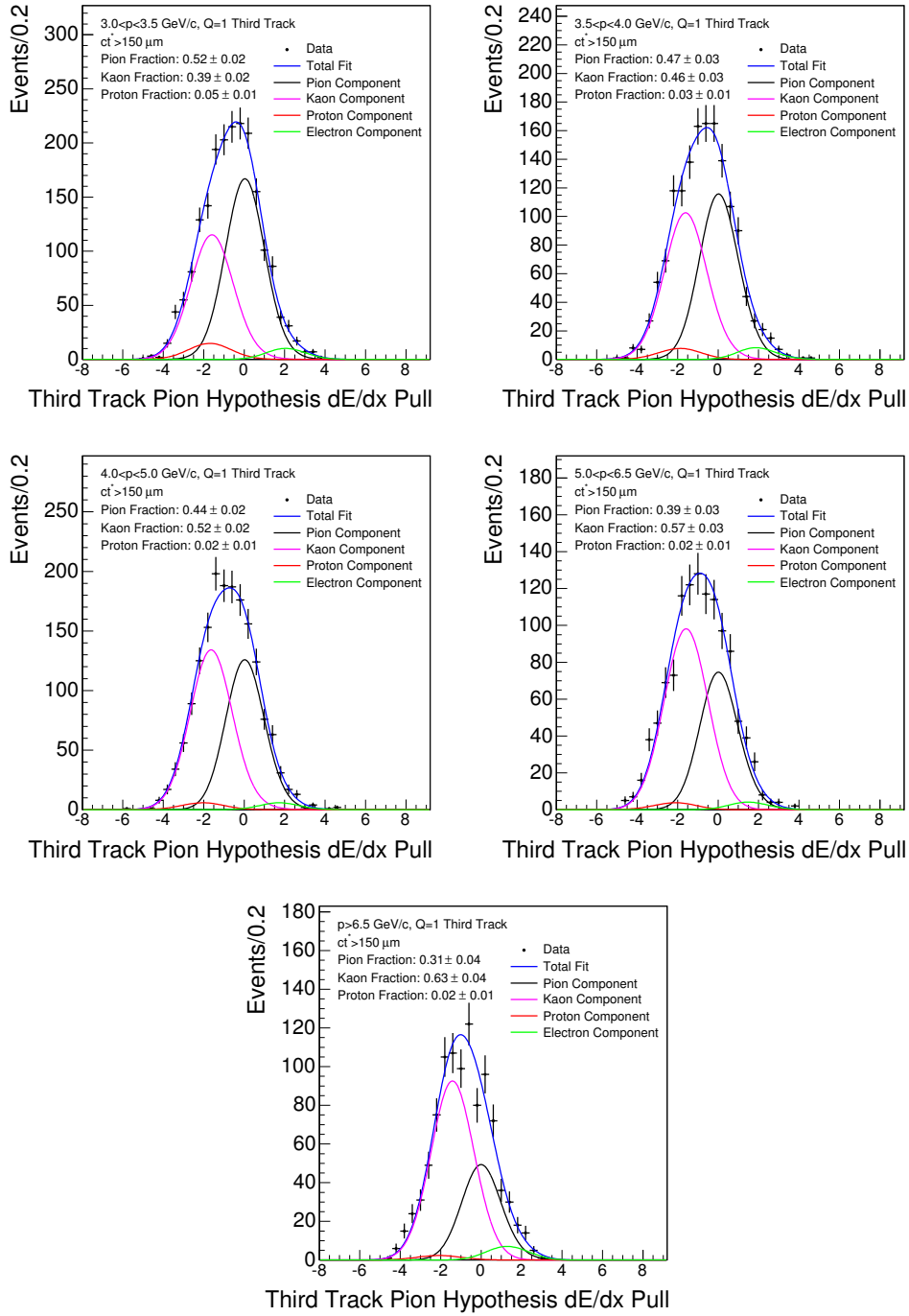


Figure 158: Fitted Z_{π}^{pull} distributions for $q = 1$ and $J/\psi + track ct^* > 150 \mu\text{m}$. Broken into third track momentum bins of 3.0 – 3.5 GeV/c (top left), 3.5 – 4.0 GeV/c (top right), 4.0 – 5.0 GeV/c (middle left), 5.0 – 6.5 GeV/c (middle right), and $> 6.5 \text{ GeV/c}$ (bottom).

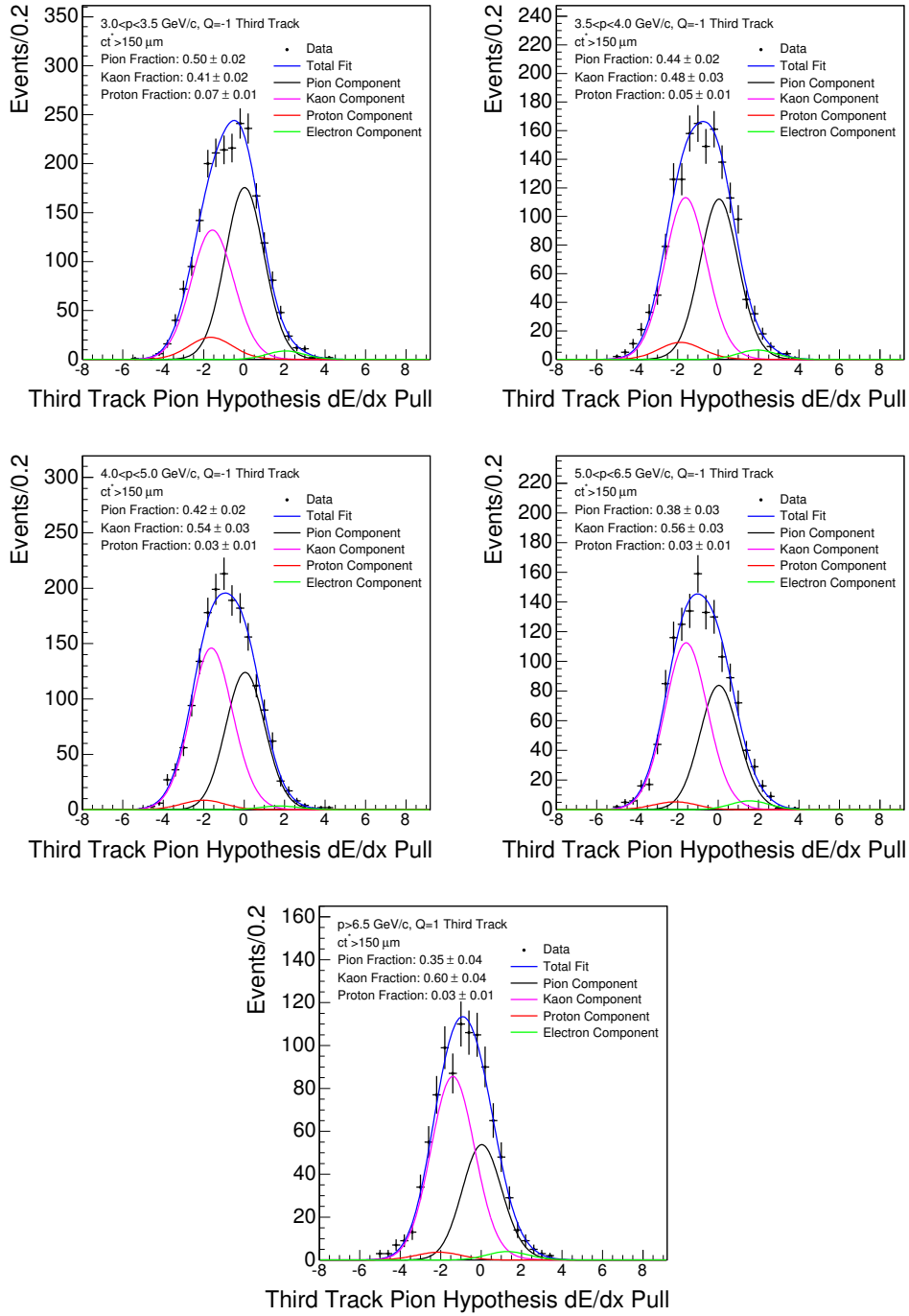


Figure 159: Fitted Z_{π}^{pull} distributions for $q = -1$ and $J/\psi + track ct^* > 150 \mu\text{m}$. Broken into third track momentum bins of 3.0 – 3.5 GeV/c (top left), 3.5 – 4.0 GeV/c (top right), 4.0 – 5.0 GeV/c (middle left), 5.0 – 6.5 GeV/c (middle right), and > 6.5 GeV/c (bottom).

D.6 Z_{π}^{pull} FITS FOR THE MUON CHANNEL

The fractional particle composition for third tracks in the muon channel J/ψ +track sample is determined by Z_{π}^{pull} fits when the momentum of the third tracks is > 3.0 GeV/ c . For the fits, the events are divided by third track momentum, third track charge, and ct^* of the J/ψ +track system.

The fit projections for positively charged and negatively charged tracks where J/ψ +track $ct^* < 0$ μm are shown in Figures 160 and 161 respectively. The fit projections for positively charged and negatively charged tracks where J/ψ +track $0 < ct^* < 150$ μm are shown in Figures 162 and 163. The fit projections for positively charged and negatively charged tracks where J/ψ +track $ct^* > 150$ μm are shown in Figures 164 and 165.

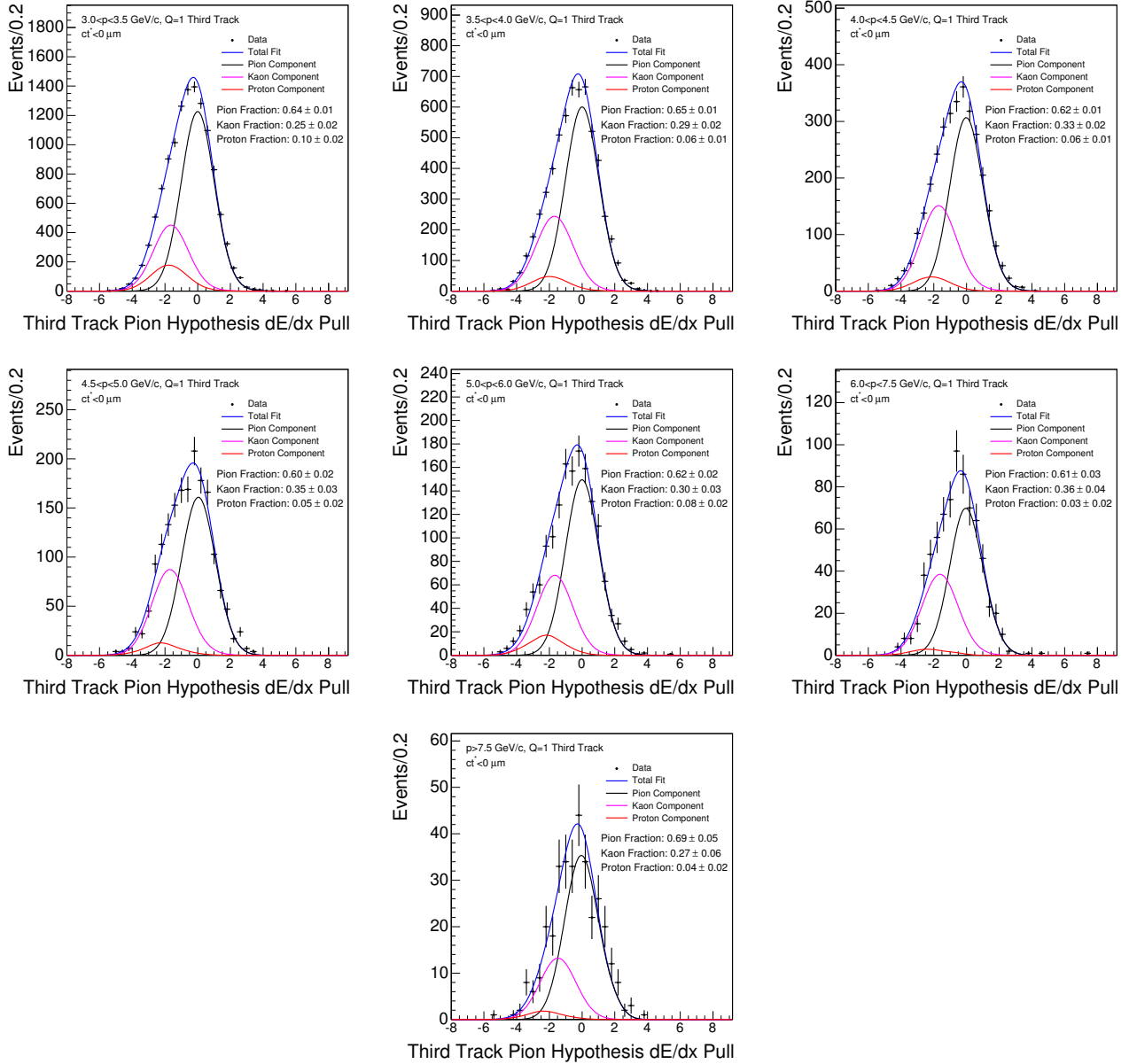


Figure 160: Fitted Z_{π}^{pull} distributions for $q = 1$ and $J/\psi + track ct^* < 0 \mu\text{m}$. Broken into third track momentum bins of 3.0 – 3.5 GeV/c (top left), 3.5 – 4.0 GeV/c (top center), 4.0 – 4.5 GeV/c (top right), 4.5 – 5.0 GeV/c (middle right), 5.0 – 6.0 GeV/c (middle center), 6.0 – 7.0 GeV/c (middle right), and > 7.0 GeV/c (bottom).

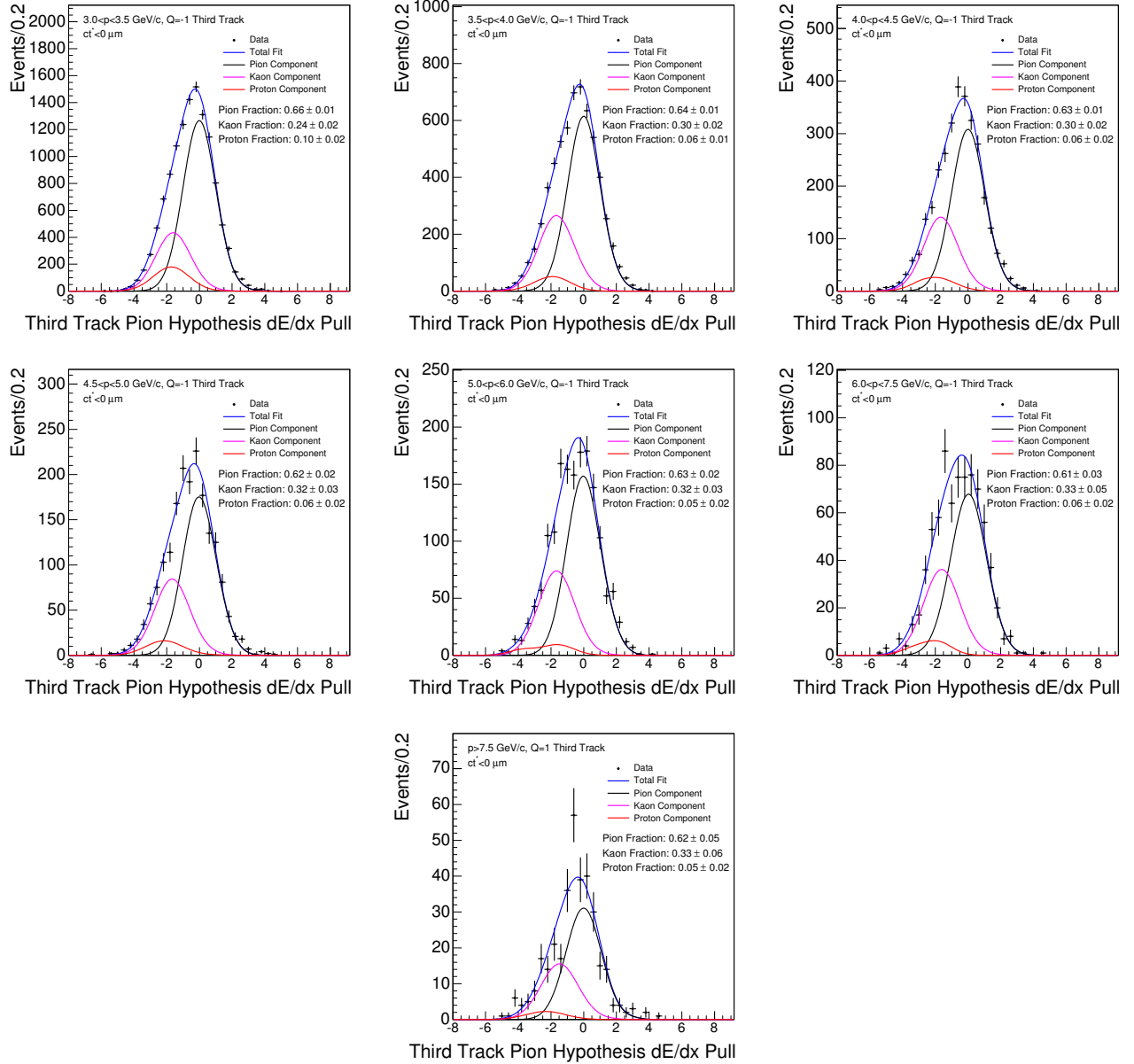


Figure 161: Fitted Z_{π}^{pull} distributions for $q = -1$ and $J/\psi + track\ ct^* < 0\ \mu\text{m}$. Broken into third track momentum bins of 3.0 – 3.5 GeV/c (top left), 3.5 – 4.0 GeV/c (top center), 4.0 – 4.5 GeV/c (top right), 4.5 – 5.0 GeV/c (middle right), 5.0 – 6.0 GeV/c (middle center), 6.0 – 7.0 GeV/c (middle right), and > 7.0 GeV/c (bottom).

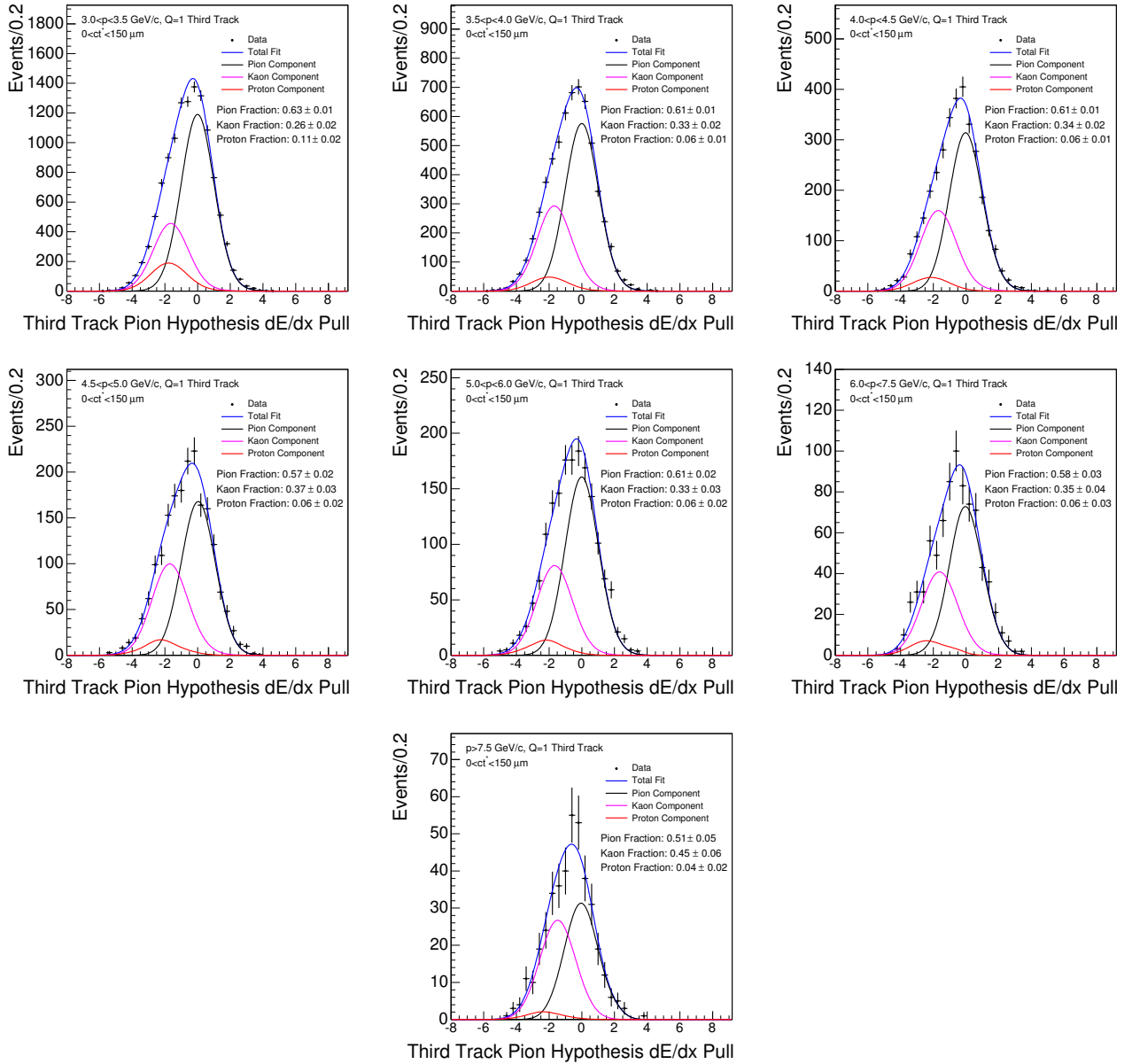


Figure 162: Fitted Z_{π}^{pull} distributions for $q = 1$ and $J/\psi + track$ $0 < ct^* < 150 \mu\text{m}$. Broken into third track momentum bins of 3.0 – 3.5 GeV/c (top left), 3.5 – 4.0 GeV/c (top center), 4.0 – 4.5 GeV/c (top right), 4.5 – 5.0 GeV/c (middle right), 5.0 – 6.0 GeV/c (middle center), 6.0 – 7.0 GeV/c (middle right), and > 7.0 GeV/c (bottom).

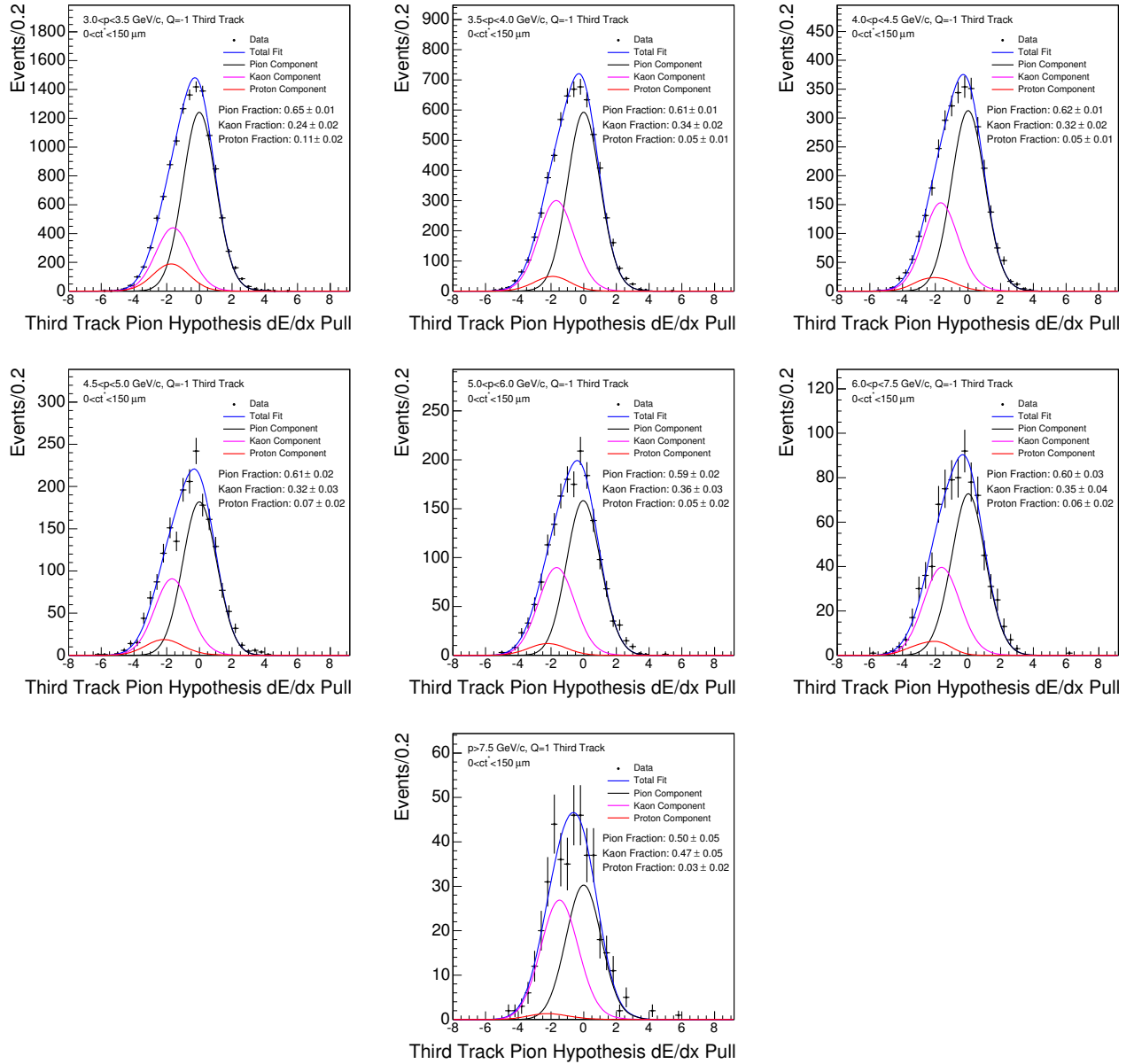


Figure 163: Fitted Z_{π}^{pull} distributions for $q = -1$ and $J/\psi + track$ $0 < ct^* < 150 \mu\text{m}$. Broken into third track momentum bins of 3.0 – 3.5 GeV/c (top left), 3.5 – 4.0 GeV/c (top center), 4.0 – 4.5 GeV/c (top right), 4.5 – 5.0 GeV/c (middle right), 5.0 – 6.0 GeV/c (middle center), 6.0 – 7.0 GeV/c (middle right), and > 7.0 GeV/c (bottom).

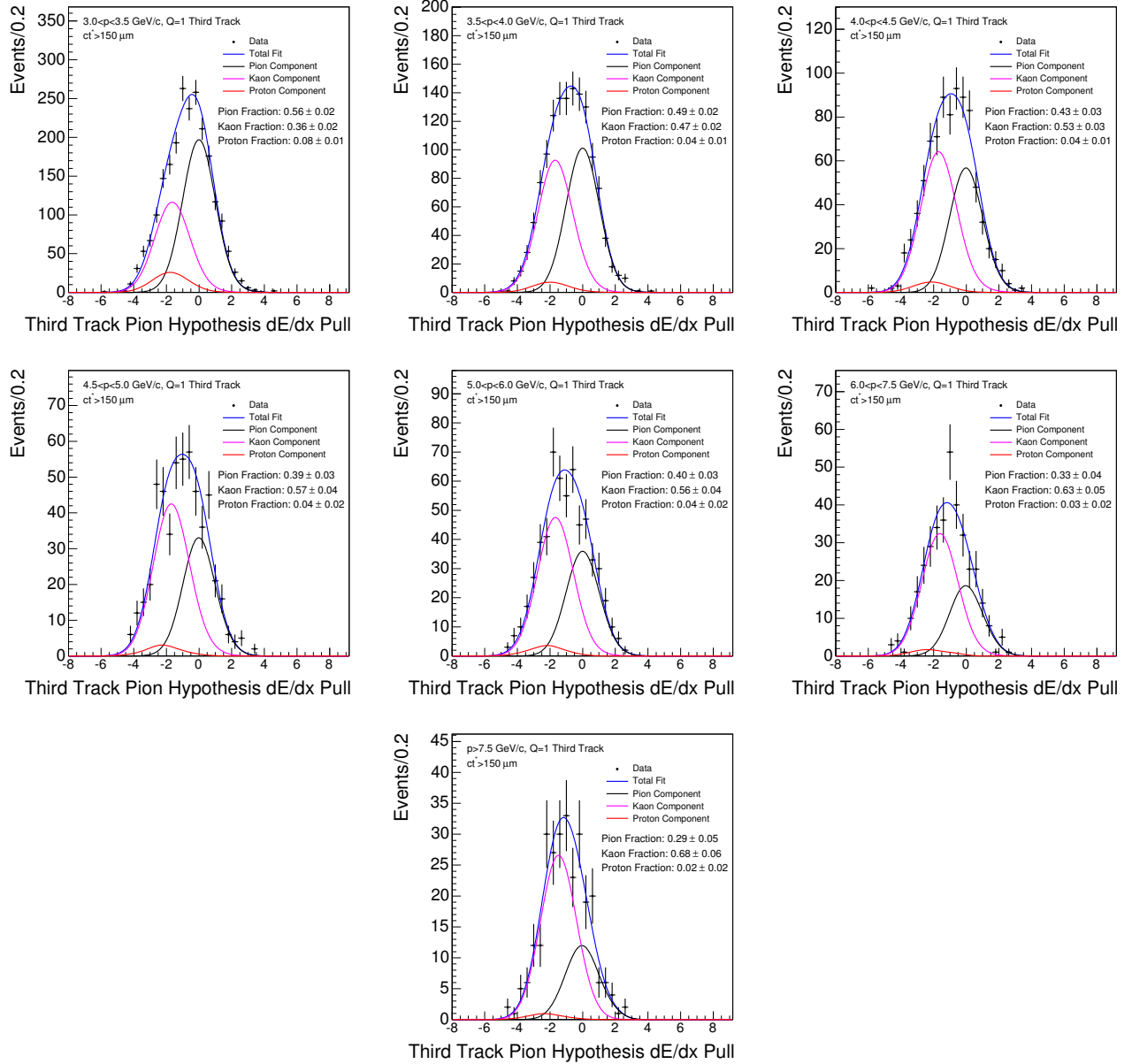


Figure 164: Fitted Z_{π}^{pull} distributions for $q = 1$ and $J/\psi + track\ ct^* > 150\ \mu\text{m}$. Broken into third track momentum bins of 3.0 – 3.5 GeV/c (top left), 3.5 – 4.0 GeV/c (top center), 4.0 – 4.5 GeV/c (top right), 4.5 – 5.0 GeV/c (middle right), 5.0 – 6.0 GeV/c (middle center), 6.0 – 7.0 GeV/c (middle right), and > 7.0 GeV/c (bottom).

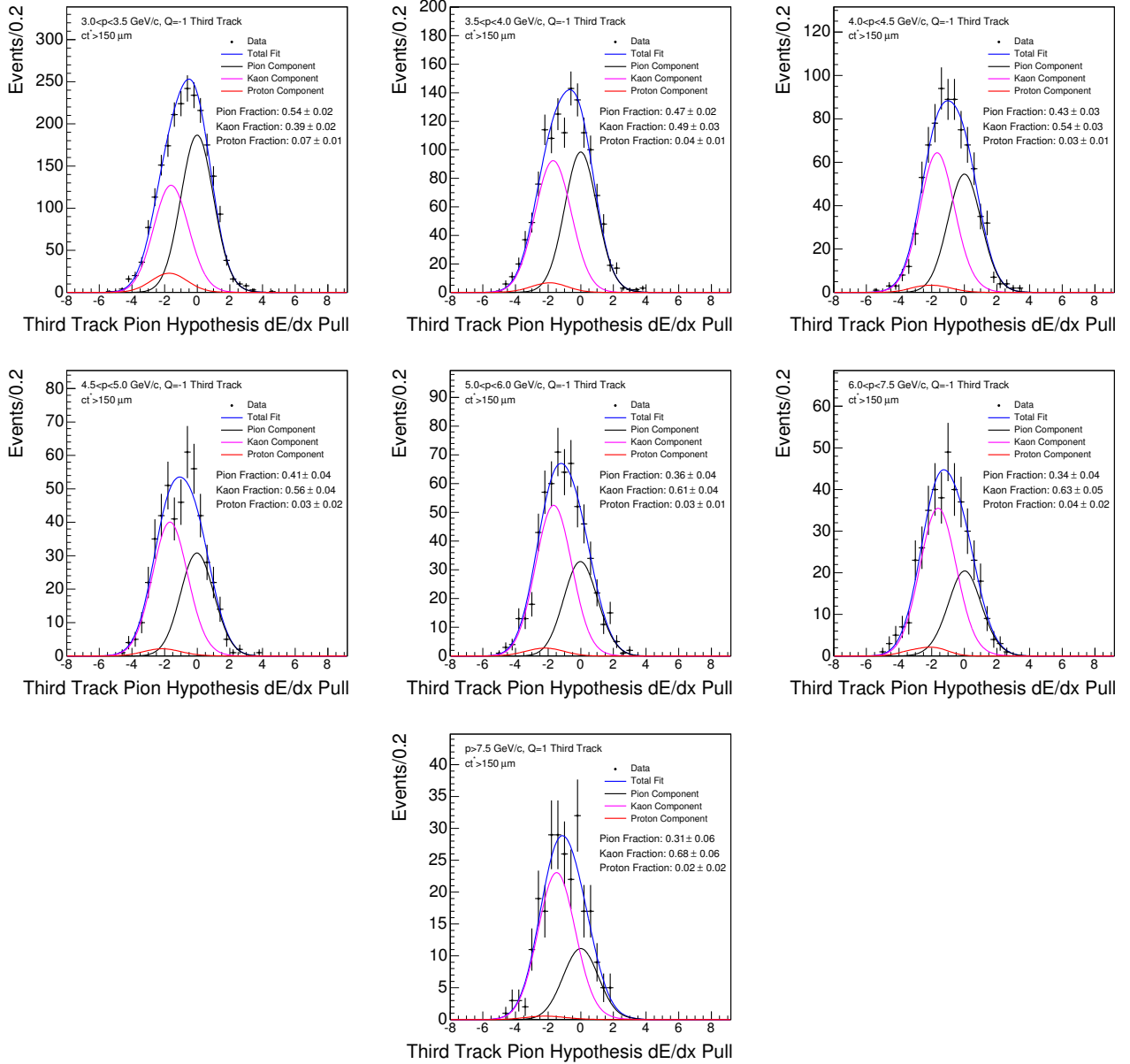


Figure 165: Fitted Z_{π}^{pull} distributions for $q = -1$ and $J/\psi + track\ ct^* > 150\ \mu\text{m}$. Broken into third track momentum bins of 3.0 – 3.5 GeV/c (top left), 3.5 – 4.0 GeV/c (top center), 4.0 – 4.5 GeV/c (top right), 4.5 – 5.0 GeV/c (middle right), 5.0 – 6.0 GeV/c (middle center), 6.0 – 7.0 GeV/c (middle right), and > 7.0 GeV/c (bottom).

BIBLIOGRAPHY

- [1] CDF, F. Abe *et al.*, Phys. Rev. Lett. **81**, 2432 (1998), hep-ex/9805034.
- [2] CDF, A. Abulencia *et al.*, Phys. Rev. Lett. **97**, 012002 (2006), hep-ex/0603027.
- [3] D0, T. D. Collaboration, (2008), arXiv:0805.2614.
- [4] C.-H. Chang and Y.-Q. Chen, Phys. Rev. **D49**, 3399 (1994).
- [5] M. Beneke and G. Buchalla, Phys. Rev. **D53**, 4991 (1996), hep-ph/9601249.
- [6] V. V. Kiselev, A. E. Kovalsky, and A. K. Likhoded, Nucl. Phys. **B585**, 353 (2000), hep-ph/0002127.
- [7] A. Y. Anisimov, I. M. Narodetsky, C. Semay, and B. Silvestre-Brac, Phys. Lett. **B452**, 129 (1999), hep-ph/9812514.
- [8] CDF-II, R. Blair *et al.*, FERMILAB-PUB-96-390-E.
- [9] P. A. M. Dirac, Proc. Roy. Soc. Lond. **A118**, 351 (1928).
- [10] R. P. Feynman, Phys. Rev. **80**, 440 (1950).
- [11] J. S. Schwinger, Phys. Rev. **74**, 1439 (1948).
- [12] S. Tomonaga, Prog. Theor. Phys. **1**, 27 (1946).
- [13] B. C. Odom, D. Hanneke, B. D'Urso, and G. Gabrielse, Phys. Rev. Lett. **97**, 030801 (2006).
- [14] LEP Working Group for Higgs boson searches, R. Barate *et al.*, Phys. Lett. **B565**, 61 (2003), hep-ex/0306033.
- [15] Particle Data Group, S. Eidelman *et al.*, Phys. Lett. **B592**, 1 (2004).
- [16] S. Weinberg, Phys. Rev. Lett. **19**, 1264 (1967).
- [17] A. Salam and J. C. Ward, Phys. Lett. **13**, 168 (1964).

- [18] S. L. Glashow, Nucl. Phys. **22**, 579 (1961).
- [19] P. W. Higgs, Phys. Rev. Lett. **13**, 508 (1964).
- [20] M. Gell-Mann, Phys. Lett. **8**, 214 (1964).
- [21] O. W. Greenberg, Phys. Rev. Lett. **13**, 598 (1964).
- [22] M. Y. Han and Y. Nambu, Phys. Rev. **139**, B1006 (1965).
- [23] D. J. Gross and F. Wilczek, Phys. Rev. **8**, 3633 (1973).
- [24] N. Cabibbo, Phys. Rev. Lett. **10**, 531 (1963).
- [25] M. Kobayashi and T. Maskawa, Prog. Theor. Phys. **49**, 652 (1973).
- [26] M. Beneke, G. Buchalla, M. Neubert, and C. T. Sachrajda, Nucl. Phys. **B591**, 313 (2000), hep-ph/0006124.
- [27] E. Eichten and B. R. Hill, Phys. Lett. **B234**, 511 (1990).
- [28] C. Quigg and J. L. Rosner, Phys. Rept. **56**, 167 (1979).
- [29] G. T. Bodwin, E. Braaten, and G. P. Lepage, Phys. Rev. **D51**, 1125 (1995), hep-ph/9407339.
- [30] A. S. Kronfeld, (2002), arXiv:hep-lat/0205021v2.
- [31] CTEQ, H. L. Lai *et al.*, Eur. Phys. J. **C12**, 375 (2000), hep-ph/9903282.
- [32] B. Andersson, G. Gustafson, G. Ingelman, and T. Sjostrand, Phys. Rept. **97**, 31 (1983).
- [33] B. Andersson, G. Gustafson, and B. Soderberg, Z. Phys. **C20**, 317 (1983).
- [34] F. Gabbiani, A. I. Onishchenko, and A. A. Petrov, Phys. Rev. **D70**, 094031 (2004), hep-ph/0407004.
- [35] Heavy Flavor Averaging Group (HFAG), E. Barberio *et al.*, (2007), arXiv:0704.3575.
- [36] M. P. Hartz, (2008), arXiv:0808.0048.
- [37] T. Sjostrand, S. Mrenna, and P. Skands, JHEP **05**, 026 (2006), hep-ph/0603175.
- [38] C.-H. Chang and Y.-Q. Chen, Phys. Rev. **D48**, 4086 (1993).
- [39] CDF, F. Abe *et al.*, Phys. Rev. Lett. **75**, 1451 (1995), hep-ex/9503013.
- [40] V. V. Kiselev, A. E. Kovalsky, and A. K. Likhoded, Phys. Atom. Nucl. **64**, 1860 (2001).
- [41] HPQCD, I. F. Allison *et al.*, Phys. Rev. Lett. **94**, 172001 (2005), hep-lat/0411027.

- [42] S. Godfrey, Phys. Rev. **D70**, 054017 (2004), hep-ph/0406228.
- [43] CDF Collaboration, T. Aaltonen *et al.*, Physical Review Letters **100**, 182002 (2008).
- [44] M. Chabab, Phys. Lett. **B325**, 205 (1994).
- [45] S. M. Ikhdaïr and R. Sever, Int. J. Mod. Phys. **A21**, 6699 (2006), hep-ph/0702166.
- [46] M. A. Shifman, A. I. Vainshtein, and V. I. Zakharov, Nucl. Phys. **B147**, 385 (1979).
- [47] M. J. Dugan and B. Grinstein, Phys. Lett. **B255**, 583 (1991).
- [48] A. Khodjamirian, (2002), hep-ph/0209166.
- [49] V. V. Kiselev, (2002), hep-ph/0211021.
- [50] M. A. Ivanov, J. G. Korner, and P. Santorelli, Phys. Rev. **D73**, 054024 (2006), hep-ph/0602050.
- [51] A. Abd El-Hady, J. H. Munoz, and J. P. Vary, Phys. Rev. **D62**, 014019 (2000), hep-ph/9909406.
- [52] C. W. Schmidt, Presented at 1993 Particle Accelerator Conference (PAC 93), Washington, DC, 17-20 May 1993.
- [53] M. Popovic and C. Ankenbrandt, AIP Conf. Proc. **448**, 128 (1998).
- [54] H. E. Montgomery, (1999), hep-ex/9904019.
- [55] B. Drendel *et al.*, (2008), <http://www-drendel.fnal.gov/documents/2007-Pbar-Rookie-Book.htm>.
- [56] P. H. Garbincius, (2004), hep-ex/0406013.
- [57] CDF, A. Sill, Nucl. Instrum. Meth. **A447**, 1 (2000).
- [58] CDF, A. A. Affolder *et al.*, Nucl. Instrum. Meth. **A453**, 84 (2000).
- [59] CDF, J. P. Fernandez, Nucl. Instrum. Meth. **A535**, 370 (2004).
- [60] CDF, A. A. Affolder *et al.*, Nucl. Instrum. Meth. **A526**, 249 (2004).
- [61] W. Blum and G. Rolandi, Berlin, Germany: Springer (1993) 348 p.
- [62] S. Vallecorsa *et al.*, CDF Note **6369**.
- [63] CDF-II, D. Acosta *et al.*, Nucl. Instrum. Meth. **A518**, 605 (2004).

- [64] CDF, S. Cabrera *et al.*, Presented at IEEE 2003 Nuclear Science Symposium (NSS) and Medical Imaging Conference (MIC) including Sessions on Nuclear Power Systems, Portland, Oregon, 19-24 Oct 2003.
- [65] CDF, L. Balka *et al.*, Nucl. Instrum. Meth. **A267**, 272 (1988).
- [66] M. Gallinaro *et al.*, IEEE Trans. Nucl. Sci. **52**, 879 (2005), physics/0411056.
- [67] J. K. Mayer, CDF Note **5174**.
- [68] CDF, S. Bertolucci *et al.*, Nucl. Instrum. Meth. **A267**, 301 (1988).
- [69] G. Ascoli *et al.*, Nucl. Instrum. Meth. **A268**, 33 (1988).
- [70] CDF, S. Holm *et al.*, IEEE Trans. Nucl. Sci. **47**, 895 (2000).
- [71] K. Anikeev *et al.*, IEEE Trans. Nucl. Sci. **53**, 653 (2006).
- [72] A. Bardi *et al.*, Nucl. Instrum. Meth. **A485**, 178 (2002).
- [73] Y. S. Chung *et al.*, IEEE Trans. Nucl. Sci. **52**, 1212 (2005).
- [74] E. G. Mario Campanelli, CDF Note **6905**.
- [75] H. Stadie *et al.*, CDF Note **6327**.
- [76] F. James and M. Roos, Comput. Phys. Commun. **10**, 343 (1975).
- [77] J. Boudreau *et al.*, CDF Note **7782**.
- [78] K. Anikeev *et al.*, CDF Note **5092**.
- [79] J. Beringer *et al.*, CDF Note **7917**.
- [80] A. Warburton *et al.*, http://www-cdf.fnal.gov/cdfsim/cdfsim_main.html .
- [81] H.-P. Wellisch *et al.*, <http://wwwasd.web.cern.ch/wwwasd/geant4/G4UsersDocuments/UsersGuides/PhysicsReferenceManual/print/PhysicsReferenceManual.pdf> .
- [82] E. Gerchtein and M. Paulini, (2003), physics/0306031.
- [83] S. Rolli, <http://ncdf70.fnal.gov:8001/trigsim/trgsim.html> .
- [84] G. Giurgiu *et al.*, CDF Note **7043**.
- [85] C. Hays, http://fcdfwww.fnal.gov/internal/WebTalks/Archive/0402/040227_b_physics_analysis_kernel/04_040227_b_physics_analysis_kernel_Chris_Hays_1%_deftrk.022704.pdf .

- [86] J. Morello *et al.*, CDF Note **6932**.
- [87] G. Pope *et al.*, CDF Note **6956**.
- [88] E. Berry *et al.*, CDF Note **8042**.
- [89] M. Aoki *et al.*, CDF Note **7518**.
- [90] V. Tiwari *et al.*, CDF Note **7121**.
- [91] M. Aoki *et al.*, CDF Note **7758**.
- [92] A. A. Affolder, UMI-30-82087.
- [93] K. Lannon and K. Pitts, CDF Note **6354**.
- [94] CDF, D. E. Acosta *et al.*, Phys. Rev. **D70**, 074008 (2004), hep-ex/0404022.
- [95] A. Affolder, CDF Note **6263**.
- [96] K. Gibson, CDF Note **8320**.
- [97] J. Boudreau *et al.*, CDF Note **6387**.
- [98] T. C. Collaboration, (2008), <http://www-cdf.fnal.gov/physics/new/bottom/080207.blessed-bs-lifetime/>.
- [99] I. P. Gouz, V. V. Kiselev, A. K. Likhoded, V. I. Romanovsky, and O. P. Yushchenko, Phys. Atom. Nucl. **67**, 1559 (2004), hep-ph/0211432.
- [100] R. Fleischer and D. Wyler, Phys. Rev. **D62**, 057503 (2000), hep-ph/0004010.
- [101] C.-H. Chang and X.-G. Wu, Eur. Phys. J. **C38**, 267 (2004), hep-ph/0309121.
- [102] C.-H. Chang, C. Driouichi, P. Eerola, and X. G. Wu, Comput. Phys. Commun. **159**, 192 (2004), hep-ph/0309120.
- [103] P. Bussey *et al.*, CDF Note **7018**.